HUNGARIAN
ACADEMY
OF SCIENCES

Light–Matter Interaction towards Ultrastrong Coupling

D.Sc. thesis

András Vukics

MMXXI–MMXXII

LIGHT–MATTER INTERACTION

towards

ULTRASTRONG COUPLING

András Vukics

Wigner Research Centre for Physics

2021–2022

D.Sc. thesis

This thesis was typeset using the LaTeX typesetting system originally developed by Leslie Lamport, based on TeX created by Donald Knuth.

The body text is set 12/14.5pt on a 26pc measure with Minion Pro designed by Robert Slimbach. This neohumanistic font was first issued by Adobe Systems in 1989 and have since been revised. Other fonts include Sans and Typewriter from Donald Knuth's Computer Modern family.

The design is chiefly based on Eivin Uggedal's thesis (cf. http://github.com/jrk/uggedal-thesis) with minor modifications by the author.

To Peter, the best of colleagues,
to Tobias, the best of friends,
and to Viktória, the best of all.

Eloquia Domini, eloquia casta:
argentum igne examinatum,
probatum terræ purgatum septuplum.

(Psalmus 11)

CONTENTS

Contents i

List of Figures iii

Preface v

1 Introduction 1
- 1.1 Quantum optics – a short history 1
- 1.2 Regimes of light-matter coupling 3
- 1.3 The electric-dipole picture and the Dicke phase transition 5
- 1.4 The breakdown of photon blockade 8
- 1.5 Computational aspects 11

The Electric-Dipole Picture in the Ultrastrong-Coupling Regime

2 The electric-dipole picture in arbitrary domains, and a Dicke counter-no-go statement 17
- 2.1 Synopsis 17
- 2.2 The general formalism 17
- 2.3 A Dicke counter-no-go statement 22
- 2.A The Fabry-Pérot configuration 23

3 Regularization of the theory and its impact on the possibility of ultrastrong coupling 27
- 3.1 Synopsis 27
- 3.2 Possible forms of P and the single-atom Hamiltonian 28
- 3.3 Quantum electrodynamics of atoms in the multipolar picture 29
- 3.4 Appropriate choice of the transverse polarization in dipole order 31
- 3.5 The limits of coupling strength 34
- 3.A Arbitrary regularizing envelope 36

4 Depolarization shift of the superradiant phase transition 39
- 4.1 Synopsis 39
- 4.2 Regularized electric dipole picture 40
- 4.3 The electromagnetic and electronic subsystem 41
- 4.4 Dynamical instability in mean-field approximation 43

5 Theses, outlook, further developments 47

The Breakdown of Photon Blockade

6 The breakdown of photon blockade as a first-order dissipative phase transition 53
6.1 Synopsis 53
6.2 The photon-blockade-breakdown phase transition in a nutshell 53
6.3 The telegraph signal 58
6.4 Filling factor and the scaling of the drive strength 60
6.5 Dwell times 63
6.6 The role of atomic decay 67

7 Experimental realizations 69
7.1 Synopsis 69
7.2 The first experimental realization of PBB 69
7.3 Modeling the thermodynamic limit experimentally 76
7.A The full quantum model for multilevel transmons 82
7.B Semiclassical theory for a multilevel transmon 83

8 Theses, outlook 87

Computational Aspects

9 A robust adaptive quantum-jump Monte Carlo method 93
9.1 Synopsis 93
9.2 Primordial MCWF and its critique 93
9.3 Stepwise adaptive MCWF 96
9.4 Convergence 99
9.5 Comparison with the integrating method of MCWF evolution 107
9.6 A note on sampling and time averaging 111
9.A Code availability 111
9.B Quantification of the error 112

10 C++QED: a framework for simulating open quantum dynamics 115
10.1 Synopsis 115
10.2 Basic specification 115
10.3 Structure 118
10.4 High-level usage 119
10.5 Fundamental data structures 123
10.A Defining multi-level quantum systems 127

11 Theses, outlook, further developments 129

Own papers related to the Thesis 133

Bibliography 135

LIST OF FIGURES

2.1 The Fabry-Pérot configuration 24

3.1 Illustration of the Power form of the polarization field 28
3.2 Visualization of the hierarchy of lengthscales: $\lambda_A \gg \ell \gg a_0$. 33
3.3 The Dicke phase transition as a silhouette of solidification. 36

4.1 Relationship between the characteristic length scales 45
4.2 Behavior of the eigenvalues 46

6.1 Anharmonic vs. harmonic part of the spectrum 54
6.2 PBB phase diagram from the neoclassical theory 56
6.3 Comparison of phase diagrams with different scalings 57
6.4 PBB in the time domain 59
6.5 Filling factor 61
6.6 Drive strength for half-filling 62
6.7 Characteristic timescale 63
6.8 Waiting times 64
6.9 Mandel-Q in the dim periods. 66
6.10 Relationship of quantum jumps and switchings 67
6.11 The bistability cycle 68

7.1 Experimental scheme and level scheme 70
7.2 Spectrum with 3-level atoms 72
7.3 Comparing experimental results with simulations 73
7.4 Further experimental results 74
7.5 Device schematics and empty-cavity spectrum 76
7.6 Observation of photon blockade breakdown 78
7.7 The thermodynamic limit 80
7.8 The phase diagram 81
7.9 Example trajectories for different dephasing models 84
7.10 Bistability curve 85

8.1 Schematic representation of the transmission blockade breakdown phase transition 90

9.1 Cartoon of the evolution of the photon number in a single decaying harmonic-oscillator mode started from a coherent state 96
9.2 Flowchart describing a single step of our adaptive MCWF algorithm 98
9.3 A typical picture of convergence of the MCWF solution to that of the master equation 100

9.4 Deviation from exact solution as a function of the number of trajectories 101
9.5 Characteristics of MCWF evolution as a function of Δp 103
9.6 Behavior of the stepsize as a function of Δp for three sets of parameters 105
9.7 The behavior of the algorithm as witnessed by the average timestep in the case of nontrivial coherent evolution 106
9.8 Cartoon illustrating the workings of the integrating method 108
9.9 Comparison of convergence of stepwise algorithm and integrating algorithm 109

10.1 Scheme of compiled computer languages 117
10.2 Tracts of the framework and their relationships 118
10.3 The network of interactions defining the system 122

PREFACE

Quantum science has become one of the hottest topics of fundamental physics research during the past two decades, and quantum optics evolved from a specialized discipline from its origins in the 1960's to one of the main motors of this recent development. Therefore, I consider myself fortunate to have chosen this field as early as in 2001, at the incentive of Zoltán Kurucz, a fellow member of the Bolyai College, who at the time had just recently joined the group of József Janszky at the Department of Crystal Physics and Nonlinear Optics of the Research Institute for Solid State Physics and Optics of the Hungarian Academy of Sciences.

Prof. Janszky, whom I remember with gratitude, together with his group helped me with my first steps in quantum optics and in the world of scientific research that was so vividly represented by the community. This enabled me to meet Peter Domokos, and under his supervision join the cavity quantum electrodynamics group of Helmut Ritsch at the Institut für Theoretische Physik, Universität Innsbruck. During my work along the Budapest–Innsbruck axis, that is, during my master (2002-2003) and PhD (2003-2007) theses, and my postdoc years in the Ritsch group (2006-2010), I could relate to the international cream of the field, both theoretical and experimental, that had already accomplished amazing results in areas like quantum information, ion trapping, and optical lattices.

The present thesis highlights parts of my activities between 2012 and 2022, that is, the decade after my return from Innsbruck to Budapest. These years saw the advent of hybrid and artificial quantum systems, which allow for previously unattainable parameter regimes of light-matter interaction, that is the main theme of this work. In 2016, a new era of experimental quantum optics research started at the Wigner Research Centre for Physics, with the potential to provide renewed inspiration for physicists like me for decades to come.

I am grateful to all my colleagues and coauthors, but particularly to Helmut Ritsch for his incessant positive attitude, his exemplary enthusiasm towards everything that is physics, and for being part of Tyrol as my second home; and most especially to Peter Domokos for his trust in me even during times when my relationship with science was challenging, his ideas and enthusiasm, his convivial working style, and his friendship.

For the two decades of being a professional researcher, I've been happy to live a very complete life, for which I have primarily to thank my wife Viktória, and my children Borbála (b. 2006), Anna (2009), Endre (2017), and Gellért (2020).

1 INTRODUCTION

1.1 QUANTUM OPTICS – A SHORT HISTORY

Since quantum mechanics originated from the study of a thermal gas of photons in Planck's work, the history of quantum optics (Cirac & Kimble, 2017; Gerry & Knight, 2005; Fox, 2006; Bachor & Ralph, 2014) goes as far back as the origins of that greater discipline. Although quantum optics was originally understood to deal with phenomena that can be explained only by a quantum theory of light (Loudon, 2001), in an extended sense its subject is light-matter interaction in situations when one or both of these constituents is described quantum mechanically – photons and/or atoms, to paraphrase Cohen-Tannoudji et al. (1997) –, and very often it is the quantum character of the latter that has proved more important. While quantum optics originated as a specialized discipline, it went on to imbue several other fields of physics, and has eventually become one of the main pillars of the recently-emerged quantum science and technology. By today, some quantum optical systems have become the best controlled systems ever produced by mankind.

In spite of the impact of the photon concept on early quantum theory, a systematic account of quantum electrodynamics (QED) started out only in the late 1940's. Even more important for the theoretical foundations of quantum optics, non-relativistic (a.k.a. molecular) quantum electrodynamics set off in the seminal work of Power & Zienau (1959), and is still a theme today (cf. Part I of the present thesis). The 1960's brought about the birth of the theory of open quantum systems – a special gift given by quantum optics to theoretical physics at large – in the work of people like Lax, Senitzky, Haken, and Scully & Lamb[1] (Carmichael, 1993).

1. Nobel prize 1955

But quantum optics is a strongly experiment-driven discipline, and the first observations usually cited in this respect were those of Hanbury Brown and Twiss, that inspired the theory of *classical* coherence in the 1950's (Mandel & Wolf, 1995). The question of the relationship to quantum coherence arose, that lead to the quantum theory of optical coherence by Sudarshan, Glauber,[2] and others. This allowed for describing the state of light in phase space, using quasi-probability functions.

2. Nobel prize 2005

The invention of the maser and its optical analogue, the laser[3] meant a breakthrough in the experimental technology of quantum optics. Studies of whether quantization plays any role in maser operation lead to the Jaynes-Cummings model (Jaynes & Cummings, 1963), that is still one of the standard models of quantum optics theory, and will play an important role in Part II of the present thesis. Hopes that the light of a laser can be nonclassical proved to be vain, as its state can in most situations be well described by a coherent state with somewhat fluctuating amplitude. Nonetheless, the laser allowed for producing

3. Nobel prize 1964 to Townes, Basow, and Prokhorov

nonclassical light indirectly, perhaps the most striking examples being photon antibunching in single-atom resonance fluorescence, as predicted theoretically by Carmichael and Walls (Walls, 1979), and demonstrated experimentally by Kimble et al. (1977); and optical parametric processes pioneered by Louisell and Yariv.

Bell's inequalities (Bell, 1964) represent a significant advance in quantum theory, since they allow for ruling out local hidden-variable theories. First indications of their violation came from the field of quantum optics, in atomic cascades (Freedman & Clauser, 1972; Aspect et al., 1982), and subsequently in a photonic system by Ou & Mandel (1988).

Whereas quantum theory was originally applied to ensembles of particles (cf. e.g. solid-state physics), over the decades quantum optics became proficient in manipulating individual quantum systems. The first milestone on this front was the achievement of the trapping of single ions in electromagnetic fields separately by Dehmelt[4] and Wineland.[5] This allowed for an unprecedented control over the atomic internal states first manifested in resolved sideband cooling and the famous electron-shelving scheme. By today, quantum-coherent manipulation of a single or a few trapped ion(s) is routine, and has even allowed for quantum information processing in R. Blatt's group, cf. e.g. Friis et al. (2018). The group of Serge Haroche[6] developed capabilities for manipulating a system of individual Rydberg atoms coupled to microwave resonators on the single-photon, single-atom level, demonstrating Rabi oscillations, time-resolved decoherence, and quantum logic (Raimond et al., 2001). About a decade later, a full quantum toolbox using single atoms trapped in high-finesse optical microcavities was developed by the Rempe group (Reiserer & Rempe, 2015). The photonic front saw immense progress as well, quantum coherent control for quantum cryptography having been achieved on the level of even a single twin-photon pair in the Zeilinger group (Jennewein et al., 2000).

4. Nobel prize 1989

5. Nobel prize 2012

6. Nobel prize 2012

The development of laser cooling techniques,[7] chiefly for gases of alkali atoms, allowed for the preparation of cold ($\sim 100\,\mu$K) atomic samples, a prequel to the success-story of ultracold ($\lesssim 1\,\mu$K) gases, which regime was first achieved by evaporative cooling of alkali samples in magnetic traps to produce Bose-Einstein condensation.[8] This meant that the level of control that ion traps provided for single ions in the vibrational ground state of the trap was extended to macroscopic samples of neutral atoms. Via a sufficiently controlled outcoupling of atoms, the BEC allowed for the production of the so-called atom laser, a coherent state of a sequence of propagating atoms with beam-like properties that can be controlled similarly to a laser (Bloch et al., 1999), and holds great technological promises for atom interferometry. Another natural development was the production of ultracold samples in optical lattices (Greiner et al., 2002), where the demonstrated superfluid to Mott insulator phase transition has become a commonly quoted prime example of quantum simulation à la Feynman (1982), cf. also Bloch et al. (2012).

7. Nobel prize 1997 to Chu, Cohen-Tannoudji, and Phillips

8. Nobel prize 2001 to Cornell, Ketterle, and Wieman

Among the many fields imbued by quantum optics, let us mention metrology as a striking instance. Whereas atomic clocks have originated as microwave devices using thermal atomic ensembles, the introduction of optical (laser spectroscopy) techniques for state preparation and measurement in the late 1980's could lead to more than an order of magnitude improvement in accuracy (Lombardi et al., 2007). The adoption of laser-cooled atomic samples ("Cs fountain" clock) instead of thermal beams in the second half of the 1990's re-

sulted in an improvement of a similar degree. By today, the probing of certain atomic transition frequencies by atomic clocks has become the most precise measurement ever performed by mankind, a fact acknowledged in the new "quantum" SI, introduced in May 2019, that endows the unit of time with even higher significance than it had before, introducing it to the definition of even the new, "atomic" unit of mass (Schlamminger, 2018). Lately, optical frequency standards (Ludlow et al., 2015) have started to supersede microwave standards. The "quantum-logic ion clock" (Schmidt et al., 2005) uses entanglement to couple the "spectroscopy" ion to an auxiliary "logic" ion to allow for more stillness to the former by transferring manipulations to the latter. Optical lattice clocks using ultracold samples of strontium are reaching stability at the 10^{-18} level (Bloom et al., 2014). The adoption of squeezing has lead to sensitivities surpassing the standard quantum limit in several situations in metrology (Polzik et al., 1992; Hosten et al., 2016); and whereas the LIGO/VIRGO gravitational-wave detectors used techniques inspired by the experimental technology of quantum optics in mirror and resonator design from the outset (Abbott et al., 2016), advanced LIGO also uses squeezed light for enhanced sensitivity (Caves, 1980; Xiao et al., 1987; Aasi et al., 2013).

1.2 REGIMES OF LIGHT-MATTER COUPLING

In free space, the coupling of the vacuum electromagnetic field to a two-level atom leads to fundamental phenomena – Lamb shift and spontaneous emission –, whereas a populated mode "stimulates" the emission of an atom due to bosonic enhancement. These processes have been known since Einstein's rate-equation model based on considerations of thermal equilibrium, that introduced the famous A and B coefficients. Whereas the spontaneous emission rate of an atomic transition in free space is determined by fundamental constants, due to its dependence on the density of electromagnetic modes, it can be modified by boundary conditions, as found by Purcell (1946). An eminent way of doing this is to place the atoms between mirrors or in cavities (Kleppner, 1981), in a setting first realized experimentally by Goy et al. (1983) and Hulet et al. (1985). The Purcell effect is commonly cited as the starting point of the field of cavity quantum electrodynamics (CQED, cf. Haroche & Kleppner (1989)).

Spontaneous emission is, however, irreversible, so that excitation on the single-quantum level is not controlled in the above phenomena. A paradigm that came to the fore during the last two decades of the past millennium is *strong coupling* between quantum systems. This means that excitation on the single- or few-quanta level can be exchanged between the subsystems several times before dissipative processes intervene to carry those quanta away, i.e. coherent quantum dynamics between the constituents can be observed. Equivalently, the modifications that the coupling makes in the energy spectrum of the free constituents are well resolved.[9]

The first realization of strong coupling came from the field of quantum optics, in the 1990's in CQED in the microwave domain, in the Haroche group. In CQED the (single-atom) strong-coupling regime can be expressed quantitatively by the inequality $C \gg 1$, where the single-atom cooperativity[10] reads $C \equiv g^2/(\kappa\gamma)$, where g is the atom-cavity coupling constant, κ is the cavity field decay rate, and γ is the atomic spontaneous emission rate. From this for-

9. It would seem that e.g. the spin-orbit coupling of the electron in a hydrogen atom is strong under this definition, since it leads to the well-resolved fine structure; but in that case the spin and the orbital motion are not really two separate physical subsystems, furthermore, the interaction cannot be controlled.

10. For N atoms it can be shown quite generally that the cooperativity scales proportional to N, that is, the coupling constant proportional to $\sqrt{N}$.

mula it can be seen that attaining strong coupling in the optical domain is much more difficult since due to the short wavelength very short cavity length (10–100 μm) is needed.[11] Since the cavity length is short, photons are reflected more often, therefore to obtain small κ extremely good mirrors are necessary (with transmission coefficient $\sim 10^{-5}$). This said, the normal-mode splitting for an atom in an optical cavity was observed already by Thompson et al. (1992). In the optical domain, where the mechanical effect of single photons on the atomic motional state is significant, strong coupling can be exploited for enhanced, *cavity* cooling and trapping schemes (Horak et al., 1997; Maunz et al., 2004). In the course of the last three decades, the strong-coupling regime of CQED has lead to capabilities involving the internal atomic states that include single-photon generation, atom-photon quantum state transfer, generation of atom-photon entanglement, quantum memory, atom-atom quantum state transfer, remote atom-atom entanglement, Bell-state measurement, quantum teleportation, nondestructive photon detection, and atom-photon quantum gate – eventually providing a full-fledged quantum interface between photons and atoms (Reiserer & Rempe, 2015).

11. Since $\kappa \propto L^{-1}$ and $g \propto L^{-1/2}$, the cavity length L drops out from the expression of C. However, since $g/\gamma \ll 1$ is itself a requirement of strong coupling, the need for a short cavity length can be seen from here as well.

For a single electromagnetic resonator mode sustained by two mirrors or in a cavity, the cooperativity on a given atomic transition depends only on the mode waist, therefore, the use of cavities with small mode volumes is essential for the realization of the strong coupling regime. Further increasing the coupling is hence impracticable on this platform. We mention in passing that a superstrong coupling regime of CQED was proposed by Meiser & Meystre (2006), which is characterized by atom-field coupling strengths of the order of the free spectral range of the cavity, resulting in a significant change in the spatial mode structure of the light field.

The phonons of the normal modes of a chain of ions trapped in a linear ion trap can be coupled by Raman transitions to the internal states, realizing the strong-coupling regime with phonons instead of photons (Wineland, 2013). Furthermore, strong coupling was realized in semiconductors (Khitrova et al., 2006), and superconducting qubits also reached this regime by the early 2000's (Wallraff et al., 2004), an essential achievement for the development of the field of circuit quantum electrodynamics (CCQED), that was to become one of the main platforms of quantum information processing during the subsequent two decades (Haroche et al., 2020).

The first decade of the new millenium saw the advent of a new, *ultrastrong coupling* regime of light-matter interaction, first proposed by Ciuti et al. (2005). This regime is characterized by the coupling strength reaching a sizable fraction of the bare frequencies of the non-interacting constituents, and was found achievable by these authors with intersubband cavity polaritons (Dupont et al., 2003), leading to fundamental phenomena like two-mode squeezed vacuum for a ground state, and the generation of correlated photon pairs in a phenomenon reminiscent of the dynamical Casimir effect (Johansson et al., 2009; Wilson et al., 2011). Several new capabilities and effects were predicted theoretically in this regime, including the on-chip quantum simulation of the Jahn-Teller model (Bourassa et al., 2009) and that of the environment-assisted quantum transport in photosynthetic complexes (Mostame et al., 2012), a single photon simultaneously and reversibly exciting several atoms (Garziano et al., 2016), and advances in quantum information processing (Wang et al., 2012; Nataf & Ciuti, 2011; Ashhab & Nori, 2010).

Reaching the ultrastrong-coupling regime became an outstanding objective in controlled laboratory systems where confined electromagnetic radiation interacts with some kind of material degree of freedom, the most promising platforms being

- superconducting quantum circuits (Devoret et al., 2007; Forn-Díaz et al., 2010; Niemczyk et al., 2010),
- semiconductor quantum wells (Anappara et al., 2009; Günter et al., 2009; Todorov et al., 2010; Scalari et al., 2012; Geiser et al., 2012; Hagenmüller & Ciuti, 2012; Todorov & Sirtori, 2014; Todorov, 2015), and
- hybrid quantum systems (Schwartz et al., 2011; Wei et al., 2013; Cottet et al., 2015).

1.3 THE ELECTRIC-DIPOLE PICTURE AND THE DICKE-HEPP-LIEB PHASE TRANSITION

The studies summarized in Part I were modivated by the Dicke-Hepp-Lieb phase transition, colloquially denoted *Dicke* or *superradiant* phase transition. The Dicke model describes an ensemble of two-level systems interacting with a radiation mode:

$$H_{\text{Dicke}} = \omega_{\text{A}} S_z + \omega_{\text{M}}\, a^\dagger a + g\left(a + a^\dagger\right) S_x, \tag{1.1a}$$

with ω_{M} the angular frequency of the mode with boson operator a, ω_{A} that of the atomic transition with collective spin operators S_{xyz}, and g the coupling strength. Proposed by Dicke (1954), cf. also Garraway (2011); Kirton et al. (2019), the model describes collective emission of light from an ensemble of atoms, predicting the so-called superradiant behavior: if the atoms are situated within a fraction of a wavelength, the emitted amplitudes will interfere constructively, leading to an amplitude proportional to N – the number of atoms –, or the intensity to N^2 (Benedict et al., 1996). Whereas superradiance was originally thought of as a transient phenomenon (Gross & Haroche, 1982), Hepp & Lieb (1973) discovered steady-state superradiance, which occurs when the atomic ensemble is coupled to a single quantized mode, as in a cavity. In that work, superradiance occurs as a thermal phase besides a normal one, the transition between the two being a second-order thermal phase transition, cf. also Wang & Hioe (1973). The condition is that for large-enough atom-field coupling strength, there exists a critical temperature where the transition occurs.

For historical accuracy, let us note that in these works the phase transition was proved for the Tavis-Cummings model,[12] which is obtained from the Dicke model on neglecting the excitation non-conserving (counter-rotating) terms (Tavis & Cummings, 1968) – that is, the rotating-wave approximation:

$$H_{\text{Tavis-Cummings}} = \omega_{\text{A}} S_z + \omega_{\text{M}}\, a^\dagger a + g\left(a\, S_+ + a^\dagger\, S_-\right). \tag{1.1b}$$

Subsequently, it was shown (Hioe, 1973; Carmichael et al., 1973; Duncan, 1974) that the phase transition survives also in the original Dicke model, the difference being a factor of 2 in the critical coupling strength:

$$N\, g^2_{\text{c,DM}} = \omega_{\text{A}}\, \omega_{\text{M}}, \qquad N\, g^2_{\text{c,TCM}} = \frac{\omega_{\text{A}}\, \omega_{\text{M}}}{4}. \tag{1.2}$$

12. The single-atom version of the Dicke model is called (quantum) Rabi model (Braak, 2011), whereas that of the Tavis-Cummings model Jaynes-Cummings model.

The thermal phase transition has a zero-temperature counterpart, which has been further elaborated in a number of studies (Narducci et al., 1973; Hillery & Mlodinow, 1985), also in connection with quantum chaos and entanglement properties (Emary & Brandes, 2003b,a; Bužek et al., 2005; Castaños et al., 2011).

The Dicke phase transition is an astonishing theoretical possibility, since it would mean that if we put a cold ensemble of atoms in a cavity and start to reduce the mode volume then at some point light would appear quite spontaneously and abruptly in the cavity. To be sure, there are practical catches, the most important being that according to Eq. (1.2) the criticality necessitates the realization of the collective ultrastrong-coupling regime, "collective" meaning that the coupling is enhanced by $\sqrt{N}$. Still, it must have been a relief for the physics community when towards the end of the 1970's papers started to appear that professed to rule out even theoretically the superradiant phase transition (Rzażewski et al., 1975; Knight et al., 1978; Birula & Rzażewski, 1979; Rzażewski & Wódkiewicz, 1991; Nataf & Ciuti, 2010; Viehmann et al., 2011; Jaako et al., 2016) – these are the so-called *Dicke no-go theorems*.

On one hand, it is important to emphasize that the no-go statements pertain to the Dicke model in its original setting, that is, natural polarizable particles (atoms/molecules) interacting with the electromagnetic field, since they touch upon the *derivation* of the Dicke model from the *a priori* nonrelativistic QED theory applied to these systems. As such, they do not concern any results derived from the Dicke model itself (such as the phase transition) or the application of the Dicke model in other settings, perhaps in a phenomenological way. Since the models (1.1) are the simplest possible models that describe the interaction of a saturable system with a harmonic oscillator mode, it is natural that it has found applications in other fields. For example, the Lipkin-Meshkov-Glick model originating from nuclear physics (Lipkin et al., 1965) is a very close relative. Much more recently, an open-system version of the Dicke model has been proposed to describe motional excitations of a Bose-Einstein condensate in a CQED setting (Nagy et al., 2010), with the phase transition experimentally demonstrated at ETH Zürich by Baumann et al. (2010). The realization of the Dicke phase transition was proposed in a multilevel-atom scheme relying on cavity-mediated Raman transitions by Dimer et al. (2007), a closely related scheme having been realized very recently by Zhiqiang et al. (2017). It has moreover been suggested that the Dicke phase transition can occur in adequately designed CCQED and hybrid systems (Nataf & Ciuti, 2010; Ciuti & Nataf, 2012; Lambert et al., 2016; Bamba et al., 2016; Zou et al., 2014).

On the other hand, the no-go statements are problematic even in their original setting, most importantly because they rely on the *a priori* Hamiltonian of the QED of nonrelativistic point charges:[13]

$$H = \sum_{\alpha} \frac{\left[\mathbf{p}_\alpha - q_\alpha \mathbf{A}(\mathbf{r}_\alpha)\right]^2}{2m_\alpha} + \frac{\varepsilon_0}{2} \int \mathrm{d}V \, (\nabla U)^2 + H_{\text{field}}. \tag{1.3}$$

The description of the interaction of dipolar matter with the electromagnetic field based on this theory[14] is known to suffer from two problems on whose account this theory is not a suitable foundation for the standard models of quantum optics listed in Eq. (1.1):[15]

13. Some of the no-go statements furthermore rely on a single-mode approximation, that will be shown inadequate in the context of the superradiant phase transition in Part I.

14. The reason why we consider this Hamiltonian *a priori* is that it can be derived from a Lagrangian that assumes the simplest possible form of light-matter interaction: $\int \mathrm{d}V \, \mathbf{j} \cdot \mathbf{A}_\perp$.

15. For a more precise formulation of these problems cf. Section 2.2.

- The canonical momentum of the charges differ from their kinetic one by a term proportional to the vector potential at the particle's position, which leads to
  - the infamous A-square term coupling all the modes and predicting the spontaneous creation and annihilation of pairs of photons, and
  - incoveniences when the particle's motion is included in the description.
- There is an instantaneous (Coulomb) interaction between the particles, which hinders the definition of atoms and molecules that we would like to think about as independent entities held together by *internal* electrostatic forces.

Partly in response to these problems, multipolar QED, the adequate foundation of the nonrelativistic quantum electrodynamics of atoms and molecules was worked out starting from the late 1950's. It is based on a unitary transformation, the Power-Zienau-Woolley (PZW) transformation (Power & Zienau, 1959; Atkins & Woolley, 1970; Woolley, 1971), leading to a theory where matter is described by a polarization field, and the displacement replaces the electric field. Though these notions call to mind macroscopic electrodynamics, the theory is microscopic, and capable to describe an arbitrary ensemble of point charges interacting with the electromagnetic field in vacuum. The PZW transformation is defined in the Hamiltonian formalism, and is independent of the choice of gauge, still, the relationship to gauge transformation was clarified (Woolley, 1974; Chernyak & Mukamel, 1995) and the Lagrangian and Hamiltonian descriptions were assessed (Woolley, 1975).

It has been a common belief in the field – suggested even by venerable textbooks – that the *a priori* picture and the PZW picture are equivalent, and the choice between them is a matter of taste. This is true in the *strictly mathematical* sense, since the two pictures are connected by canonical transformation, so they must yield the same value for all physical observables. However, the equivalence does not hold even in the theoretical physics sense, since both pictures are utterly useless without further approximations. Even the long-wavelength approximation that is fundamental in the description of atoms and molecules – we cannot have a dynamical electromagnetic field on the intra-atomic scale if we want well-defined atomic energy levels –[16] breaks the equivalence. In many experimental configurations, a two-level (or few-levels) approximation for the atoms (Barton, 1974) or a single-mode (or few-modes) approximation for the field is invoked that also depend on the picture.

16. It is interesting to note that whereas macroscopic dipole antennas tend to have sizes similar to the wavelength of their emitted radiation, atoms are much smaller than the wavelengths they emit, which makes the long-wavelength approximation possible. As we will argue in Chapter 3, cf. Eq. (3.11), this is due to the small value of the fine-structure constant.

It is a strange moment in the history of the field that this discrepancy lingered for several decades: the full-fledged adequate theory of atomic QED on one hand, the Dicke no-go theorems based on the inadequate *a priori* theory on the other. In a few instances, the Dicke model was tackled in the PZW picture (Emeljanov & Klimontovich, 1976; Kimura, 1981; Sivasubramanian et al., 2001), but it was not until Keeling (2007) that the consequences of the discrepancy were realized. He pointed out that complementing the Dicke model with terms stemming from the A-square term as in the no-go theorem of Rzażewski et al. (1975) is still not consistent because a further term of equal importance must be taken into account: the instantaneous Coulomb interaction between the charges

belonging to different atoms. His conclusion was that with this term included in the model Hamiltonian, the criticality is restored. He found that by applying a single-mode, two-level-atom truncated version of the PZW transformation on this model Hamiltonian, one exactly recovers the original Dicke model, with the modified interpretation that in this picture, the boson mode a corresponds not to a single mode of the transverse electric field, but that of the displacement field. It is the displacement field that undergoes spontaneous symmetry breaking which is shown to be due to atomic polarization only, the transverse electric field – a gauge-invariant quantity – remaining zero also in the electric-dipole gauge. A serious limitation of the approach of Keeling (2007), however, is that it is based on a single-mode approximation, and not only for the electromagnetic field but also for the polarization density, which is not adequate to describe point-like dipoles. It also implies that in this approach, we in fact cannot distinguish between electric field and displacement, anywhere in space.

In Part I we dissolve the above-described issues.[17]

- We generalize the PZW transformation for arbitrary confined geometries, and emphasize that the standard models of quantum optics must be derived from the multipolar Hamiltonian instead of the *a priori* one.
- The no-go statements are dissolved, moreover, we show that the superradiant phase in the Dicke model derived in the PZW picture yields a mean field not only in the displacement, but also in the electric field.
- We dissolve the P-square problem by regularizing the PZW transformation to arrive at a picture where the atoms interact only when their "intimacy zones" – about an order of magnitude larger than the natural size of the atom – touch.
- In this picture, a natural limit on the possibility of ultrastrong coupling between atomic matter and light presents itself. Based on this limit, we claim that the superradiant phase transition is equivalent to condensation (solidification or liquefaction).
- We calculate the depolarization shift of the phase transition point, and find it to be three times the Dicke critical density. This shift is effected by the contact interaction of the atoms when the intimacy zones touch.

17. In the case of hybrid and artificial systems, where the full microscopic description of the system is untractable, the question of the *a priori* description and the status of the no-go statements can remain an adequate one (Nataf & Ciuti, 2010; Viehmann et al., 2011; Ciuti & Nataf, 2012; Todorov & Sirtori, 2012, 2014; Todorov, 2014; Jaako et al., 2016).

1.4 THE BREAKDOWN OF PHOTON BLOCKADE

Quantum phase transitions (QPT), both first- and second-order (Vojta, 2003) have been at the forefront of physics research for half a century. The original idea of QPTs as abrupt shifts in the (pure) *ground state* of closed quantum systems as a function of some control parameter (Sachdev, 2011) appealed mostly to condensed matter physics. Dissipative phase transitions (DPT) occurring in the (in general, mixed) *steady state* of open quantum systems (Capriotti et al., 2005; Diehl et al., 2008; Nagy et al., 2010; Diehl et al., 2010; Kessler et al., 2012; Le Boité et al., 2013; Marino & Diehl, 2016; Minganti et al., 2018; Hwang et al., 2018; Gutiérrez-Jáuregui & Carmichael, 2018; Reiter et al., 2020; Soriente et al., 2021), however, broadened the scope of phase transitions to encompass meso- and later even microscopic systems, where the interaction with the environment

essentially affects the system dynamics. A DPT was first realized experimentally in a Bose-Einstein condensate interacting with a single-mode optical cavity field by Baumann et al. (2010), and they are increasingly relevant to today's quantum science and technology (Verstraete et al., 2009; Fernández-Lorenzo & Porras, 2017; Fitzpatrick et al., 2017; Garbe et al., 2020).

In view of this success, it is remarkable that in recent years yet another phase-transition paradigm could emerge, namely, *first-order* dissipative quantum phase transitions. A first-order phase transition means that two phases can coexist in a certain parameter region, like water and ice at 0 °C for a certain range of free energy. Coexistence of phases in the quantum steady state seems paradoxical, since the steady-state plus normalization conditions for the density operator constitute an inhomogeneous linear system of equations, that admits only a single solution. That is, given the Liouvillian superoperator $\mathcal{L}$ for the Markovian evolution of the system, there exists only a single normalized density operator ρ_{st} that satisfies

$$\mathcal{L}\rho_{\mathrm{st}} = 0. \tag{1.4}$$

The resolution is that a single density operator can accomodate the mixture of two macroscopically distinct phases expressing also a ratio of the two components. In the water analogy, at 0 °C we could symbolically write

$$\rho_{\mathrm{st}} = c\,\rho_{\mathrm{water}} + (1-c)\,\rho_{\mathrm{ice}}, \tag{1.5}$$

with c growing from 0 to 1 along increasing free energy.

Recently, first-order *dissipative quantum* phase transitions have been found in various systems. One such platform is clustering of Rydberg atoms described by Ising-type spin models (Ates et al., 2012; Marcuzzi et al., 2014; Overbeck et al., 2017; Roscher et al., 2018; Samajdar et al., 2021; Myerson-Jain et al., 2022), realized experimentally by Carr et al. (2013), Malossi et al. (2014), and Letscher et al. (2017). Various other systems of ultracold atoms (Labouvie et al., 2016; Ferri et al., 2021) and dissipative Dicke-like models (Gelhausen & Buchhold, 2018; Stitely et al., 2020) also exhibit signatures of a first-order DPT. Other platforms include (arrays of) nonlinear photonic or polaritonic modes (Le Boité et al., 2013; Casteels et al., 2017; Debnath et al., 2017; Rodriguez et al., 2017; Savona, 2017; Fink et al., 2018; Vicentini et al., 2018; Lang et al., 2020; Li et al., 2022), exciton-polariton condensates (Hanai et al., 2019; Dagvadorj et al., 2021), and circuit QED (Mavrogordatos et al., 2017; Brookes et al., 2021).

The Jaynes-Cummings (JC) model expressed by the Hamiltonian

$$H_{\mathrm{JC}} = \omega_{\mathrm{M}}\, a^\dagger a \,+\, \omega_{\mathrm{A}}\, \sigma^\dagger \sigma \,+\, g\big(a^\dagger \sigma + \sigma^\dagger a\big) + i\eta\big(a^\dagger e^{-i\omega t} - a\, e^{i\omega t}\big)\,, \tag{1.6}$$

(here quoted together with driving for the purposes of Part II with η the drive amplitude and ω the drive frequency) is one of the most important models in quantum science (Larson & Mavrogordatos, 2021). It is a prototype of anharmonic spectrum in the strong-coupling regime, as demonstrated in cavity (Brune et al., 1996) and circuit QED (Fink et al., 2008), and with quantum dots in semiconductor microcavities (Kasprzak et al., 2010). This anharmonicity is the basis of the photon blockade effect (Imamoğlu et al., 1997), designated in analogy with Coulomb blockade in e.g. quantum dots (recently, an analogous effect has been observed with polaritons by Ohira et al. (2021)). Photon blockade means that an excitation cannot enter the JC system from a drive tuned to

resonance with the empty resonator (or, a second excitation from a drive tuned to resonance with one of the single-excitation levels), due to the distortion of the spectrum via the coupling between the resonator and the two-level system. This blockade is, however, not absolute, as it can be broken (Carmichael, 2015; Dombi et al., 2015; Curtis et al., 2021; Pályi et al., 2012) by strong-enough driving due to a combination of multi-photon events and photon-number increasing quantum jumps, cf. Chapter 6. In an intermediary drive range, in the time domain the system alternates between a blockaded, "dim" state, and a "bright" state in which the blockade is broken, with the system residing in the high-excitation, closely harmonic part of the spectrum. In phase space, this behavior results in a bimodal steady-state distribution

$$\rho_{\mathrm{st}} = c\,\rho_{\mathrm{bright}} + (1-c)\,\rho_{\mathrm{dim}}, \tag{1.7}$$

in analogy with Eq. (1.5), with c growing from 0 to 1 with increasing η.

Bistability in the time domain or bimodality in phase space is, however, not sufficient for a first-order phase transition (Bonifacio et al., 1978). It is also necessary that the two constituents in the mixture (1.7) corresponding to the two states in the temporal bistable signal be macroscopically distinct as is the case in Eq. (1.5). As has been shown theoretically by Carmichael (2015), cf. also Chapter 6, the photon blockade breakdown (PBB) effect has such a regime, a *thermodynamic limit*, where both the timescale and the amplitude of the bistable signal goes to infinity, resulting in long-lived and macroscopically distinct dim and bright phases. Remarkably, this thermodynamic limit is a strong-coupling limit, defined as $g \to \infty$, and has nothing to do with the system size, the system remaining the same Jaynes–Cummings system consisting of two microscopic interacting subsystems.[18] In this limit, the temporal bistability is replaced by hysteresis, the state of the system being determined by the initial condition, since switching to the other state entails infinite waiting time. The passage to the thermodynamic limit, that is, the indefinite increase of g will be considered a finite-size scaling in Chapter 6. In Chapter 7, we set out to model this limit and scaling experimentally in a circuit QED system.

18. This is the reason why this phase transition has been dubbed 0-dimensional by Carmichael (2015).

Since its inception, CCQED (Blais et al., 2021) has displayed amazing capabilities, as demonstrated by the feats of quantum computation performed in arrays of such systems (Blais et al., 2020). But even single CCQED systems have continued to display rich physics, including the observation of the Bloch-Siegert shift by Pietikäinen et al. (2017), quantum-to-classical transition by Pietikäinen et al. (2019), prediction of quantum jumps by Minev et al. (2019), quantum accoustodynamics by Manenti et al. (2017), and tailored nonlinearity by Vrajitoarea et al. (2020).

In Part II, we exhibit the photon blockade breakdown effect in its first-order DPT and quantum aspects. In Chapter 6, we numerically study the finite-size scaling, proposing an appropriate scaling of the system parameters in the $g \to \infty$ thermodynamic limit. We determine finite-size scaling exponents of the timescale and the drive strength. We display the role of the well-resolved quantum-mechanical JC spectrum, and cascades of quantum jumps in the blink ON/OFF events of the bistability.

In Chapter 7, experimental realizations of the PBB effect on CCQED platforms are described, where we participated from the theoretical and numerical side. The first experimental realization (cf. Section 7.2) was done in the Wallraff

group at ETH Zürich with a coplanar resonator. Numerical modeling of their results revealed that the transmon artificial atom (generally used as a qubit) has to be described as a three-level system in order to capture some essential characteristics of the experiment.

In Section 7.3, we approach the thermodynamic limit of PBB as a first-order DPT by following the finite-size scaling over seven orders of magnitude in the characteristic timescale of the bistable signal. The indefinitely strong-coupling $g/\kappa \to \infty$ limit (where κ is the resonator linewidth) is approached by decreasing κ instead of increasing g. For the smallest κ values, the blinking timescale reaches 6 s, which is at least four orders of magnitude higher than the slowest timescale of the system ($\sim [1\,\mathrm{kHz}]^{-1}$). We experimentally determine the finite-size scaling exponent of the timescale. We sketch the phase diagram, identifying the phase coexsistence region on the drive detuning – η plane. Comparing the experimental results with full quantum-jump Monte Carlo simulations and semiclassical calculations, we assess the role of higher-lying transmon states and their phase diffusion.

1.5 COMPUTATIONAL ASPECTS

The Quantum Jump Monte Carlo (or Monte Carlo Wave-Function – MCWF)[19] method has been around since at least the late 1980s, the notion of quantum jumps being introduced in connection with intermittent fluorescence (Plenio & Knight, 1998) in works like Diósi (1985) and Javanainen (1986). The first versions of implementable algorithms were published in the early 1990s (Dum et al., 1992; Dalibard et al., 1992). In a parallel development, another kind of quantum trajectory methods, the Quantum State Diffusion has been worked out by Gisin & Percival (1992).

19. The use of the term "wave function" is not completely correct in this version of the name because the method is generally applicable for state vectors and not only for those expanded in space (which are the wave functions). Nevertheless, we continue using this customary acronym.

The Quantum Jump method can be put forward with two distinct motivations:

As a computational tool to unravel the quantum master equation into a set of quantum trajectories in order to reduce the dimensionality of the numerical problem to make larger systems tractable. In this case, it is not necessary to endow the individual trajectories with any physical meaning.

As a physical model to reflect the behavior of single realizations of small quantum systems. While quantum mechanics was originally conceived to describe ensembles, with single ions in Paul traps (Cook & Kimble, 1985) being the first examples it has in the last few decades become possible to study single realizations. In this case, the individual trajectories can be considered physical, and they will depend on the way the system is observed, in accordance with the lore of quantum measurement.

While the benefit in terms of net computational resources as compared to direct master equation simulation is not clear cut, since too many trajectories may be needed for acceptable statistics (Breuer et al., 1997); in realistic situations the system is often so big that even a single copy of the full density matrix exceeds memory limits. Then, in the ergodic case, it is still a possible solution to content oneself with finding the steady state via time averaging along a

single long trajectory. Already a single electromagnetic mode coupled to a few-level system (like in CQED) can easily fall into this category under realistic conditions (Dombi et al., 2013, 2015), but in this way it was possible to study a system consisting of two atoms coupled to a single mode (Vukics et al., 2007), or two-modes (ring cavity) coupled to a single atom (Niedenzu et al., 2010). Ergodicity could be utilized – although with heavy computational cost – even in the situations presented in Part II, that is, for a system featuring two distinct semiclassical attractors. Recently, quantum trajectories have been applied also in quantum many body contexts (Daley, 2014; Kirton & Keeling, 2017), sometimes together with tensor-network techniques.

Adaptive algorithms are very important in dynamical simulations as in general there is no way to predict an optimal stepsize, which even varies along the trajectory evolution. While in the case of deterministic problems (ordinary differential equations – ODEs), seasoned robust generic algorithms exist, the same is not true for stochastic problems (stochastic differential equations – SDEs). Such dynamics and their numerical simulation have been intensively researched during the last decades, numerous excellent papers and books can be found in the literature giving conditions on strong and weak convergence, stability, and also rates of convergence of the discretized solution (Buckwar & Riedler, 2011; Buckwar et al., 2011; Clark & Cameron, 1980; Talay, 1994). The simplest such method is the Euler-Maruyama scheme which is basically the extension of the explicit Euler method well-known from the theory of ODEs (for a more detailed description of the various numerical methods the reader is referred to Kloeden et al. (2012)). As opposed to the deterministic case, where the order of (global) convergence is 1, the order of strong convergence in the case of the Euler-Maruyama method is only 1/2. Generally, no numerical method based only on an approximation of the Brownian motion can guarantee an asymptotic convergence rate higher than that (Gaines & Lyons, 1997). For higher orders of strong convergence ($n/2$ with $n \geq 2$), the Itô-Taylor expansion yields an answer, which involves approximation of Lévy areas, i.e. integrals of Brownian motion. Unfortunately, due to the properties of the Itô integral, these schemes are more complicated than their deterministic counterparts. Usually, higher order methods are computationally very expensive, and in order to save computational time, variable stepsize for lower order methods was introduced and various results on convergence rate and the optimal choice of the stepsize were published as well (Ilie et al., 2015).

These developments are not directly relevant to MCWF because it does not consist of the integration of an SDE, but they may be utilized for Quantum State Diffusion, which does have the form of an SDE – to our knowledge, higher-order methods have not yet been tried in this case. The MCWF can be described as an SDE that consists of an ODE driven by a general Poisson-process.

In Chapter 9, we present a stepwise adaptive algorithm to simulate this process that is by principle more robust than the popular implementation of the MCWF method (Breuer & Petruccione, 1995; Homa & Diósi, 2017) that we denote the "integrating method" in this thesis, and that is used e.g. in the popular QuTiP package (Johansson et al., 2012, 2013). The increased robustness, whose main reason is that the stepwise algorithm does not depend on an algorithm for retrieving a past jump-time instant, comes at the cost of some reduction of efficiency, which however we will argue to be marginal in most usecases of interest. The algorithm here presented has been used in C++QED

(cf. Chapter 10) since the inception of that framework, both the algorithm and the framework having been originally developed for the demanding problem of simulating motional quantum degrees of freedom expanded in momentum space (Vukics et al., 2007, 2009; Niedenzu et al., 2010; Schulze et al., 2010; Niedenzu et al., 2012; Sandner et al., 2013; Winterauer et al., 2015). In this field, the robustness of our algorithm over the integrating one is especially expressed.

Apart from the parameters governing the precision of the ODE integration, the stochastic part of our algorithm is governed by the single additional dimensionless parameter Δp: the maximal allowed total jump probability per step. Another aspect of Chapter 9 is a study of convergence of ensembles of MCWF trajectories to the solution of the density operator as a function of this parameter. This being also the most important *a priori* parameter of the MCWF method, this convergence study is not specific to our algorithm, but pertains to any possible implementation of the MCWF method, including the integrating one.

In Chapter 10, we present the C++QED framework, and through this several techniques and design patterns which are essential to this framework, but should be applicable for the representation of composite quantum systems in general.

C++QED addresses the following problem: somebody who writes simulation code for a single quantum particle, mode, or spin today; tomorrow will want to simulate two or ten such systems interacting with each other. They want to reuse the code written for the single-system case, but this turns out to be rather difficult for naïvely written code, due to the algebraic structure of quantum mechanics. C++QED facilitates this task, providing a framework for representing elementary physical systems (particle motional degrees of freedom, harmonic oscillator modes, spins, etc.) in such a way that they can be immediately used as constituents of composite systems as well. Dynamical simulations (like with the MCWF method) of such, arbitrarily complex systems can be performed with a set of tools provided by the framework.

Historically, C++QED originated from the simulation of systems in CQED (hence the name of the framework). Its approach subsequently proved particularly useful in the wider context of quantum optics (Vukics et al., 2007, 2009; Niedenzu et al., 2010), as this field typically addresses systems composed of several diverse "small" subsystems interacting with each other; but also in atomic physics or quantum many-body physics (Vukics et al., 2007; Maschler et al., 2008; Nagy et al., 2009).

The framework is capable of simulating fully quantum dynamics (Schrödinger equation) of any system, provided its Hamiltonian is expressed in a finite discrete basis, and open (Liouvillean) dynamics, if the Lindblad operators are expressed in the same basis. Apart from this, the only limitation on the simulated system is its dimensionality: with present-day hardware, a typical limit is a few millions dimensions for state-vector, and a few thousands for density-operator manipulations. Since at present C++QED does not offer any special tools for addressing many-body problems, only "brute-force" calculations, this limitation means that such problems cannot be pursued very far. In terms of number of constituents, the largest system represented so far was ten qubits interacting with a single electromagnetic mode (Dombi et al., 2013).

C++QED saw a first, prototype version developed between 2006–2008, a purely object-oriented design, which was partially documented in Vukics &

Ritsch (2007). The second version, defined by the multi-array concept and compile-time algorithms, has been developed since 2008. By today it is quite mature, robust, and trustworthy, having passed thousands of tests also in real-life situations. It is an open-source project, hosted on GitHub[20], and it builds only on open-source libraries, such as the Boost library collection,[21] the GNU Scientific Library,[22] Blitz++,[23] and the Eigen template library for linear algebra.[24]

20. http://github.com/vukics/cppqed
21. http://www.boost.org
22. http://www.gnu.org/software/gsl
23. http://github.com/blitzpp/blitz
24. http://eigen.tuxfamily.org

PART I

THE ELECTRIC-DIPOLE PICTURE IN THE ULTRASTRONG-COUPLING REGIME

THE ELECTRIC-DIPOLE PICTURE IN ARBITRARY DOMAINS, AND A DICKE COUNTER-NO-GO STATEMENT

2

2.1 SYNOPSIS

In this chapter we first (Section 2.2) develop a formalism for obtaining the Power-Zienau-Wolley Hamiltonian and thence the electric-dipole picture of the quantum electrodynamics of atoms in a domain of arbitrary topology. This is an improvement over Power & Thirunamachandran (1982), which treatment was valid for a simply connected region only.

Our treatment allows us to draw conclusions regarding the controversy around the Dicke phase transition in a cavity. We are formulating a counter no-go statement in Section 2.3.

The workings of our formalism will be exemplified by the simplest confined geometry, the plane-parallel one (Fabry-Pérot resonator) in Appendix 2.A.

2.2 THE GENERAL FORMALISM

Consider a generic (possibly multiply connected) domain $\mathcal{D}$ in the three-dimensional real space bounded by (possibly several disjunct) sufficiently smooth surfaces $\partial\mathcal{D}$, which are perfectly conducting. Overall, $\mathcal{D}$ is assumed to be bounded. We have an arbitrary number of point charges coupled to the electromagnetic field confined to $\mathcal{D}$.

In the Coulomb gauge, defined by

$$\nabla \cdot \mathbf{A} = 0, \tag{2.1}$$

the *a piori* Hamiltonian of the system reads (Weinberg, 2013):

$$H = \sum_\alpha \frac{\left[\mathbf{p}_\alpha - q_\alpha \mathbf{A}(\mathbf{r}_\alpha)\right]^2}{2m_\alpha} + \frac{\varepsilon_0}{2}\int_{\mathcal{D}} \mathrm{d}V\ (\nabla U)^2 + H_{\text{field}}, \tag{2.2a}$$

with U the scalar potential, $\mathbf{p}_\alpha$ the canonical momentum of particle α conjugate to its position $\mathbf{r}_\alpha$, and

$$H_{\text{field}} = \frac{\varepsilon_0}{2}\int_{\mathcal{D}} \mathrm{d}V \left[\left(\frac{\mathbf{\Pi}}{\varepsilon_0}\right)^2 + c^2(\nabla \times \mathbf{A})^2\right], \tag{2.2b}$$

with $\mathbf{\Pi} = \varepsilon_0 \partial_t \mathbf{A}$ being the momentum conjugate to $\mathbf{A}$.[1] Since in this gauge U is tied to the charges, the second term of Eq. (2.2a) is just the electrostatic

1. Since it is often missed, we note that $\mathbf{\Pi}$ is only quasi-conjugate to $\mathbf{A}$, as their Poisson bracket is proportional not to the identity, but the projector $\mathfrak{R}$ introduced in Eq. (2.8). Hence, the Hamiltonian (2.2a) is also only of a quasi-Hamiltonian form, and to obtain a real Hamiltonian function, the transverse modes need to be invoked.

(Coulomb) energy, while the particle-field interaction is described by a term proportional to $\mathbf{p}_\alpha \cdot \mathbf{A}(\mathbf{r}_\alpha)$ in this context.

An important observation is that, *unlike in free space,* the condition (2.1) does not fix the potentials completely. The remaining freedom of choosing the potentials *within the Coulomb gauge* amounts to a freedom in choosing different constant values for U on each of the connected components of $\partial\mathcal{D}$, which will result in various configurations of capacitor fields carried by U. Our choice here will be to set

$$U|_{\partial\mathcal{D}} = 0 \quad \text{and} \quad \mathbf{A} \times \mathbf{n}|_{\partial\mathcal{D}} = 0. \tag{2.3}$$

Together with Eq. (2.1), the latter condition makes up for the vector potential satisfying both the electric and magnetic boundary conditions.[2]

The electric-dipole approximation to this Hamiltonian can be obtained in two steps.

1. (long-wavelength approximation) We assume that the individual point charges form spatially separated, well-localized clusters, that is, atoms or molecules. Then, instead of $\sum_\alpha$ there appears $\sum_A \sum_{\alpha\in A}$. We neglect all radiative effects on the intra-atomic scale, that is, we set $\mathbf{A}(\mathbf{r}_\alpha) = \mathbf{A}(\mathbf{r}_A)$, where $\mathbf{r}_A$ is the position of that atom A which incorporates the charge α.

2. We assume that the atoms have only electric dipole moment, that is, no net charge and no further electric or magnetic moments.

Upon the first assumption, we split the electrostatic term into intra- and inter-atomic parts, and take the intra-atomic part as identical to the one in free space, under the assumption that the distance of atoms from the boundary is much larger than the atomic radius. The electric-dipole order of the *a priori* Hamiltonian then reads:

$$H_{\mathrm{ED}} = \sum_A \Big[H_A - u\, \mathbf{p}_A \cdot \mathbf{A}(\mathbf{r}_A) + v\, \mathbf{A}^2(\mathbf{r}_A) + V_{\mathrm{Coul}}^{\text{dipole-self}}(\mathbf{r}_A) + \sum_B V_{\mathrm{Coul}}^{\text{dipole-dipole}}(\mathbf{r}_{A-B}) \Big] + H_{\mathrm{field}}, \tag{2.4a}$$

where u and v are constants composed of the m_αs and q_αs. The single-atom Hamiltonian reads

$$H_A = \sum_{\alpha\in A} \left(\frac{\mathbf{p}_\alpha{}^2}{2m_\alpha} + \frac{q_\alpha}{8\pi\varepsilon_0} \sum_{\substack{\beta\in A \\ \beta\neq\alpha}} \frac{q_\beta}{|\mathbf{r}_\alpha - \mathbf{r}_\beta|} \right). \tag{2.4b}$$

By this point it becomes apparent why the Coulomb gauge is a preferred choice in the quantum electrodynamics of atoms: the static part of the field effective within the charge clusters enables us to define Schrödinger-atoms with well-defined level structures. In many cases of interest the interaction with the field can be treated on a separate time/energy scale, so that the atoms retain their identity. This is going to be the main theme of Chapter 3. Another interesting gauge choice in molecular QED is the point- or Poincaré gauge, cf. Woolley (1974) and Keller (2011).

It has been tempting to take the Hamiltonian (2.4) as the starting point of cavity QED. However, this theory is fraught with the following problems, which e.g. in quantum optics, limit its usefulness in many situations:

2. The freedom of choosing the potentials within the Coulomb gauge is equivalent also to a freedom of fixing how the inclusion of the cohomological fields introduced later in Eq. (2.9), is shared between the scalar or the vector potential. With our fixing of the potentials, what we attain is that

$$U \in \mathrm{dom}(\mathrm{grad}_0) \quad \text{and} \quad \mathbf{A} \in \ker(\mathrm{div}_0),$$

that is, the electrostatic and radiative parts of the dynamics take place in the two distinct orthogonal subspaces listed later in Eq. (2.10), the cohomological components of $\mathbf{E}$ (capacitor fields) being attributed solely to $\mathbf{A}$. Note that the form of the Hamiltonian (1.3) depends on this decomposition result, since this ensures that there are separate electrostatic and radiative terms in the Hamiltonian, with no overlap between the two.

1. The canonical momentum of the atoms does not equal their kinetical momentum.

2. The A-square term couples all the modes and yields creation and annihilation of pairs of photons.

3. There is an instantaneous electrostatic interaction between remote atoms ($V_{\mathrm{Coul}}^{\text{dipole-dipole}}$) and an interaction of a single dipole with its own induced surface charges ($V_{\mathrm{Coul}}^{\text{dipole-self}}$). The former is *influenced,* while the latter is *created* by the presence of the boundaries, cf. Vukics & Domokos (2012).

In free space, these weaknesses are known to be dissolved by performing the PZW transformation on the *a piori* Hamiltonian (1.3). Here, inspired by the free-space procedure, we elevate this transformation onto a very general level, which allows for an arbitrary domain $\mathcal{D}$ and boundaries $\partial\mathcal{D}$, i.e. for a general cavity QED scenario.

The transformation that we adopt is canonical, defined by the type-2 generating function

$$G_2 \equiv \int_{\mathcal{D}} \mathrm{d}V\ \mathbf{A}\cdot\left(\mathbf{\Pi}' + \mathfrak{R}\mathbf{P}\right) + \sum_\alpha \mathbf{r}_\alpha\cdot\mathbf{p}'_\alpha, \tag{2.5a}$$

which yields a displacement of the momenta

$$\mathbf{\Pi} = \frac{\delta G_2}{\delta \mathbf{A}} = \mathbf{\Pi}' + \mathfrak{R}\mathbf{P}, \tag{2.5b}$$

$$\mathbf{p}_\alpha = \frac{\partial G_2}{\partial \mathbf{r}_\alpha} = \mathbf{p}'_\alpha + \frac{\partial}{\partial \mathbf{r}_\alpha}\int_{\mathcal{D}} \mathrm{d}V\ \mathbf{A}\cdot\mathbf{P}. \tag{2.5c}$$

At this point, $\mathbf{P}$ is an arbitrary vector, and $\mathfrak{R}$ is part of an orthogonal projector decomposition of the identity,

$$\mathfrak{Q} + \mathfrak{R} = \mathbf{id}_{L^2_{\mathrm{o}}}. \tag{2.6}$$

Here, L^2_{o} is that subspace of $L^2(\mathcal{D},\mathbb{R}^3)$, the Hilbert space of square-integrable vector fields, whose elements satisfy the normality boundary condition:

$$L^2_{\mathrm{o}}(\mathcal{D},\mathbb{R}^3) \equiv \left\{\mathbf{v}\in L^2(\mathcal{D},\mathbb{R}^3)\middle|\,\mathbf{v}\times\mathbf{n}|_{\partial\mathcal{D}} = 0\right\}, \tag{2.7}$$

which is of course nothing else than the boundary condition on the electric field (and hence the vector potential) at a perfectly conducting surface.

In order that the transformation (2.5) be canonical, $\mathfrak{R}$ must be a projector onto the divergence-free subspace of L^2_{o}:

$$\mathfrak{R} : L^2_{\mathrm{o}} \to \ker(\mathrm{div}_{\mathrm{o}}), \tag{2.8}$$

because this ensures that $\mathbf{A}$ in Eq. (2.5a) can be treated as unconstrained. Here, $\mathrm{div}_{\mathrm{o}}$ (and $\mathrm{curl}_{\mathrm{o}}$ below) are the divergence (and curl) operators over L^2, with the domain restricted to L^2_{o}. The notation 'ker' refers to the kernel of the operator, that is, the set of such vectors as are mapped onto zero by the operator. Hence, both the Coulomb-gauge and the boundary conditions on $\mathbf{A}$ can be expressed by the single condition that $\mathfrak{R}\mathbf{A} = \mathbf{A}$.

The crucial result for us to build upon here is the Helmholtz-Hodge decomposition of L^2 (Dautray & Lions, 1990; Binz & Alfred, 2010), which reads:

$$L^2(\mathcal{D},\mathbb{R}^3) = \underbrace{\mathrm{ran}(\mathrm{grad}_0)}_{\ker(\mathrm{curl}_0)} \oplus \overbrace{\mathbb{H}_2}^{\ker(\mathrm{div})} \oplus \mathrm{ran}(\mathrm{curl}), \tag{2.9}$$

where grad_0 is the gradient operator over $L^2(\mathcal{D},\mathbb{R})$ with its domain restricted to such scalar fields v as vanish on the boundaries: $v|_{\partial\mathcal{D}} = 0$. The notation 'ran' refers to the range of the operator. In free space, ($\mathcal{D} = \mathbb{R}^3$) $\mathrm{ran}(\mathrm{grad}_0) = \ker(\mathrm{curl}_0)$ (longitudinal fields) and $\mathrm{ran}(\mathrm{curl}) = \ker(\mathrm{div})$ (transverse fields) holds, and the direct sum of the two makes up for the whole $L^2(\mathbb{R}^3,\mathbb{R}^3)$. For general domains, however, the dimension of $\mathbb{H}_2$ is non-zero. The elements of $\mathbb{H}_2$ are called *cohomological fields,* and, when the electric field is in question, also *capacitor fields*.[3] On the basis of Eq. (2.9), we can assert that

$$L^2_0 = \mathrm{ran}(\mathrm{grad}_0) \oplus \ker(\mathrm{div}_0). \tag{2.10}$$

From this equation, together with Eq. (2.8) it follows that in the decomposition of the identity in Eq. (2.6), the $\mathfrak{Q}$ projector must be defined as

$$\mathfrak{Q} : L^2_0 \to \mathrm{ran}(\mathrm{grad}_0), \tag{2.11}$$

We recall that in free space $\mathfrak{Q}$ and $\mathfrak{R}$[4] project onto the longitudinal and transverse components of vector fields, respectively.

The transformed Hamiltonian reads:

$$H' = \sum_\alpha \frac{1}{2m_\alpha}\left[\mathbf{p}'_\alpha + \frac{\partial}{\partial \mathbf{r}_\alpha}\int_{\mathcal{D}} \mathrm{d}V\ \mathbf{A}\cdot\mathbf{P} - q_\alpha \mathbf{A}(\mathbf{r}_\alpha)\right]^2 + \frac{\varepsilon_0}{2}\int_{\mathcal{D}} \mathrm{d}V\ (\nabla U)^2 + \frac{\varepsilon_0}{2}\int_{\mathcal{D}} \mathrm{d}V\left[\left(\frac{\mathbf{\Pi}' + \mathfrak{R}\mathbf{P}}{\varepsilon_0}\right)^2 + c^2(\nabla\times\mathbf{A})^2\right]. \tag{2.12}$$

So far, we have not specified $\mathbf{P}$. Since according to Eq. (2.3) the scalar potential is an element of the domain of grad_0, Eq. (2.11) allows us to impose the following condition on $\mathbf{P}$:

$$\varepsilon_0 \nabla U = \mathfrak{Q}\mathbf{P}. \tag{2.13}$$

Hence, on account of Eq. (2.6) the electrostatic term in the second term of Eq. (2.12) and the term containing $\mathbf{P}^2$ in the third term combine to give $\frac{1}{2\varepsilon_0}\int_{\mathcal{D}} \mathrm{d}V\ \mathbf{P}^2$.

Condition (2.13) is *equivalent* to[5]

$$\nabla\cdot\mathbf{P} = -\rho, \tag{2.14}$$

which motivates us to identify the vector field $\mathbf{P}$, so far introduced on purely mathematical grounds, with the physical notion of the polarization density.

Besides the condition (2.13), the following condition on the other orthogonal component of $\mathbf{P}$,

$$\frac{\partial}{\partial \mathbf{r}_\alpha}\int_{\mathcal{D}} \mathrm{d}V\ \mathbf{A}\cdot\mathfrak{R}\mathbf{P} = q_\alpha \mathbf{A}(\mathbf{r}_\alpha), \tag{2.15}$$

3. The dimension of $\mathbb{H}_2$ is equal to the second Betti number of $\mathcal{D}$, that in general enough circumstances in turn equals the number of two-dimensional holes in the domain. It is zero if and only if $\partial\mathcal{D}$ is connected. In the case of a perfect Fabry-Pérot resonator, for instance (cf. Section 2.A), this subspace is one dimensional, consisting only of homogeneous fields parallel to the axis.

4. Since the explicit form of $\mathfrak{Q}$ and $\mathfrak{R}$ is not needed for our derivation, we merely note that $\mathfrak{Q}$ can be written as

$$(\mathfrak{Q}\mathbf{v})(\mathbf{r}) = -\nabla\int_{\mathcal{D}} \mathrm{d}V'\,(\nabla'\cdot\mathbf{v}(\mathbf{r}'))\mathcal{G}(\mathbf{r},\mathbf{r}'),$$

where $\mathcal{G}$ is the Dirichlet Green's function of the problem:

$$\Delta\mathcal{G}(\mathbf{r},\mathbf{r}') \equiv \delta(\mathbf{r}-\mathbf{r}') \text{ within } \mathcal{D}, \text{ and } \mathcal{G}|_{\partial\mathcal{D}} = 0,$$

whereas $\mathfrak{R}$ can be expressed with the full set of transverse modes (2.20) as

$$\mathfrak{R} = \sum_\lambda \boldsymbol{\varphi}_\lambda \otimes \boldsymbol{\varphi}_\lambda.$$

5. To prove the equivalence, we first prove (2.13)) $\Longrightarrow$ (2.14):

$$-\rho = \varepsilon_0\Delta U = \nabla\cdot\mathfrak{Q}\mathbf{P} = \nabla\cdot(\mathfrak{Q}+\mathfrak{R})\mathbf{P} = \nabla\cdot\mathbf{P},$$

where the first equality is the Poisson equation, the second is obtained by applying the ∇ operator on both sides of Eq. (2.13), the third is on account of $\nabla\cdot\mathfrak{R}\mathbf{P} = 0$, while the fourth reflects Eq. (2.6). To prove (2.14) $\Longrightarrow$ (2.13) we proceed as

$$0 = \nabla\cdot(\varepsilon_0\nabla U - \mathbf{P}) = \nabla\cdot(\varepsilon_0\nabla U - \mathfrak{Q}\mathbf{P}),$$

where the first equality follows from Eq. (2.14) and the Poisson equation, while in the second we applied again $\nabla\cdot\mathfrak{R}\mathbf{P} = 0$. It follows that the vector in parenthesis on the right-hand side is both in $\mathrm{ran}(\mathrm{grad}_0) = \mathrm{ran}(\mathfrak{Q})$, and $\ker(\mathrm{div}_0)$, which, on account of Eq. (2.10), cannot be true but for the zero vector, so that $\varepsilon_0\nabla U = \mathfrak{Q}\mathbf{P}$ must hold.

would make the first term of H' simplify. However, this condition cannot be met exactly, since the left-hand side has zero curl with respect to $\mathbf{r}_\alpha$, which is not true for the right-hand side. Nevertheless, we show that within the electric-dipole approximation to be performed in the next step, both conditions can be satisfied.

At this point, let us summarize that under the condition (2.15), the Hamiltonian would have the form

$$H' = \sum_\alpha \frac{\mathbf{p}_\alpha'^{\,2}}{2m_\alpha} + \frac{1}{2\varepsilon_0}\int_{\mathcal{D}} \mathrm{d}V\ \mathbf{P}^2 - \frac{1}{\varepsilon_0}\int_{\mathcal{D}} \mathrm{d}V\ \mathbf{D}\cdot\mathbf{P} + H'_{\text{field}}, \tag{2.16}$$

where the kinetic term manifests the coincidence of the canonical momentum $\mathbf{p}'_\alpha$ with the kinetic momentum of particle α, eliminating problem (1) listed after Eq. (2.4). We introduced the displacement field $\mathbf{D} \equiv \varepsilon_0\mathbf{E} + \mathbf{P}$, which, on account of $\mathbf{\Pi} = \varepsilon_0\partial_t\mathbf{A} = -\Re\mathbf{E}$ satisfies $\mathbf{\Pi}' = -\Re\mathbf{D} = -\mathbf{D}$.[6] The second equality holds because of Eq. (2.14) and Gauss' law. H'_{field} is formally equivalent to (2.2b), the only difference being the transformed field momentum.

We now move from the description of point charges towards that of atoms in this picture. The polarization field is $\sum_A \mathbf{P}_A$, and since the atoms are spatially separated,

$$\int_{\mathcal{D}} \mathrm{d}V\ \mathbf{P}^2 = \sum_A \int_{\mathcal{D}} \mathrm{d}V\ \mathbf{P}_A^2, \tag{2.17}$$

therefore the first two terms of Hamiltonian (2.16) give the internal energy of the atoms. In the electric-dipole approximation of atoms

$$\mathbf{P}_A(\mathbf{r}) = \left(\sum_{\alpha\in A} q_\alpha \mathbf{r}_\alpha\right)\delta^<(\mathbf{r}-\mathbf{r}_A) \equiv \mathbf{d}_A\,\delta^<(\mathbf{r}-\mathbf{r}_A), \tag{2.18}$$

$\mathbf{d}_A$ being the electric dipole moment of atom A. The function $\delta^<$ behaves as a delta function over a spatial scale that is larger than the size of the atoms, while on the intra-atomic scale it is *defined* such that condition (2.14) be satisfied.[7] With this definition, condition (2.15) is met under our assumption that $A(\mathbf{r}_\alpha) = A(\mathbf{r}_A)$.

With the two conditions being satisfied, we can proceed from Hamiltonian (2.16) to obtain the electric-dipole Hamiltonian in this picture:

$$H'_{\text{ED}} = \sum_A \left(H'_A - \mathbf{d}_A\cdot\frac{\mathbf{D}(\mathbf{r}_A)}{\varepsilon_0}\right) + H'_{\text{field}}, \tag{2.19a}$$

where the single-atom Hamiltonian has the form:

$$H'_A = \sum_{\alpha\in A} \frac{\mathbf{p}_\alpha'^{\,2}}{2m_\alpha} + \frac{1}{2\varepsilon_0}\int_{\mathrm{supp}(\mathbf{P}_A)} \mathrm{d}V\,\mathbf{P}_A^2. \tag{2.19b}$$

In the second term, the domain of the integration can be restricted to the support of $\mathbf{P}_A$, so that unless the atom is very close to any of the boundary surfaces or other atoms, the single-atom Hamiltonian is not affected by the presence of the boundaries or other atoms at all. Chapter 3 will have it as one of its main themes how far this individualistic picture of atoms can hold, and what are its consequences on the largest achievable atom-field coupling strength.

6. It is a source of confusion, but the attentive reader will have realized that despite the appearance of a displacement field, we are still dealing with microscopic electrodynamics, and all this is really just a different way of describing the same things.

7. Clearly, for a nonzero dipole moment, the charges cannot be at exactly the same position.

The notion of an atom has not remained invariant under the PZW transformation, as the potential term in the Hamiltonian (2.19b) is *a priori* very different from what we are used to. In Section 3.2 we are discussing possible forms of the polarization field, and their impact on the single-atom Hamiltonian, together with regularization strategies in situations where such are needed. Here, we will merely assume that a level-scheme similar to that of a Schrödinger-atom can be defined also in the new single-atom Hamiltonian, and it is possible to restrict such a scheme to simple level structures (two-level, lambda, etc.) in the situations where this is possible for the single-atom Hamiltonian (2.4b).[8] Importantly, the new Hamiltonian (2.19), is free from the problems listed above. Here,

1. the canonical momentum coincides with the kinetic one
2. the awkward A-square term has disappeared, as have
3. the two Coulomb terms, describing atom-atom and atom-boundary interaction.

In H'_{ED}, the boundary enters only via the displacement field $\mathbf{D}$, and the atoms interact only in a manifestly retarded way, via the radiation field.

For quantizing the theory, we introduce the transverse modes as solutions to the constraint vectorial Helmholtz equation:[9]

$$\nabla \times \nabla \times \boldsymbol{\varphi}_\lambda = \frac{\omega_\lambda^2}{c^2}\boldsymbol{\varphi}_\lambda, \text{ with } \nabla \cdot \boldsymbol{\varphi}_\lambda = 0 \text{ and } \boldsymbol{\varphi}_\lambda \times \mathbf{n}\big|_{\partial\mathcal{D}} = 0. \tag{2.20}$$

The vector potential $\mathbf{A}$ can be expanded in terms of these (dimensionless) modes:

$$\mathbf{A} = \sum_\lambda \sqrt{\frac{\hbar}{2\varepsilon_0 V \omega_\lambda}}\left(\boldsymbol{\varphi}_\lambda a_\lambda + \boldsymbol{\varphi}_\lambda^* a_\lambda^\dagger\right), \tag{2.21a}$$

where a_λ is the annihilation operator of the corresponding mode, ω_λ is its frequency, and V is the volume of the domain. As noted above, in the PZW picture the conjugate momentum is related to $\mathbf{D}$ simply as

$$\mathbf{D} = -\boldsymbol{\Pi}' = i\sum_\lambda \sqrt{\frac{\hbar\varepsilon_0\omega_\lambda}{2V}}\left(\boldsymbol{\varphi}_\lambda a_\lambda - \boldsymbol{\varphi}_\lambda^* a_\lambda^\dagger\right). \tag{2.21b}$$

2.3 A DICKE COUNTER-NO-GO STATEMENT

We are now ready to systematically introduce the single-mode approximation, which is fundamental to the standard models of cavity QED (1.1). Our analysis has shown that even in the presence of boundaries, when the possibility of a single-mode approximation arises at all, we still need the full mode expansion (2.20) for the cancellation of the A-square and the dipole-dipole interaction terms. Once this is done, in the new picture we can safely pick out one of the modes $\boldsymbol{\varphi}_\lambda$. This is at variance with the approaches of Knight et al. (1978) and Keeling (2007). In fact, the single mode approximation is much more adequate in the new picture by principle, since in the original picture, the A-square term intercouples all the modes.

The standard models of quantum optics can be derived with the additional assumption: the two-level approximation for the atoms. With this, the atomic

8. The resonances of the *full interacting system* are of course at the same frequencies regardless of the picture. On the other hand, when truncating the system degrees of freedom (e.g. atomic two-level approximation, single-mode approximation for the field, as in standard models of quantum optics (1.1)), we obtain physically different models in different pictures.

9. It can be proven that the set of the transverse modes, that is, the eigenvectors corresponding to non-negative eigenvalues span $\ker(\mathrm{div}_0)$, and that the subspace of zero-frequency modes coincides with $\mathbb{H}_2$, that is, $\omega_\lambda = 0$ if and only if $\boldsymbol{\varphi}_\lambda \in \mathbb{H}_2$. Hence, on this degenerate finite dimensional subspace $\mathbb{H}_2$, an arbitrary basis can be chosen.

ensemble can be treated as a spin $N/2$, with spin operators $S_\pm$, S_x, etc. This yields models like the Dicke and (with an additional rotating-wave approximation) the Tavis-Cummings in the new picture, where the three terms correspond one by one to the terms of the full microscopic Hamiltonian (2.19) in the same order. The coupling coefficient in the new picture reads

$$g_A(\mathbf{r}_A) = \sqrt{\frac{\omega_@}{2\hbar\varepsilon_0 V}}\langle 0|\mathbf{d}_A|1\rangle \cdot \boldsymbol{\varphi}_@(\mathbf{r}_A), \tag{2.22}$$

where $|0\rangle$ and $|1\rangle$ denote the two atomic states. Note that it is proportional to the square root of the frequency of the selected mode, in contrast to the original picture, where the form (2.21a) of the vector potential gives a coupling coefficient proportional to the inverse of the square root of the frequency.

The important point here is that no *term* of the Hamiltonian (2.19) had to be neglected, so that the A-square – direct coupling between the modes – or P-square problems – direct electrostatic coupling between the atoms – (Bamba & Ogawa, 2014) do not appear in this treatment. This is in contrast to a treatment based on the original picture, where Dicke no-go statements were formulated based on the presence of the A-square term (Rzażewski et al., 1975; Nataf & Ciuti, 2010), or on a single-mode description (Knight et al., 1978). Our analysis in this chapter displays that these arguments are irrelevant when the Dicke model is derived from the PZW picture, so that there is no such obstacle for the Dicke phase transition to occur in a light-matter system. The consequences of the P-square term will be further assessed in Chapters 3 and 4.

There remains to clarify the connection between the (purely transverse) displacement field $\mathbf{D}$ and the transverse part of the electric field $\mathbf{E}^\perp$.[10] We address the question whether a spontaneous mean field beyond the Dicke critical point in a single mode of $\mathbf{D}$ yields a field in $\mathbf{E}^\perp$, that is, true radiation, or this spontaneous mean field can be accommodated purely by the $\mathbf{P}$ field, cf. the relation

$$\mathbf{D} = \varepsilon_0\mathbf{E}^\perp + \mathbf{P}^\perp. \tag{2.23}$$

Since every dipole $\mathbf{P}$ is surrounded by a cloud of $\mathbf{P}^\perp$ and $\mathbf{P}^\parallel$ fields (of opposite signs), both vanishing inverse cubically with increasing distance from the dipole due to the relation $\mathbf{P}^\parallel = -\varepsilon_0\mathbf{E}^\parallel$ and that $\mathbf{P}^\perp = -\mathbf{P}^\parallel(\mathbf{r})$ everywhere outside the point-like dipoles, a mean field in a mode of $\mathbf{D}$ (whose spatial distribution is determined by the mode function alone) might be carried by $\mathbf{P}^\perp$ *only around the dipoles,* while far from the dipoles its carrier must be $\mathbf{E}^\perp$. This means that the phase transition in the Dicke model that we obtain *in the PZW picture* must result in a spontaneous mean field in the *gauge-invariant* observable $\mathbf{E}^\perp$. These considerations also show that a single mode of the field in the new picture (where the modes expand the $\mathbf{D}$ field, cf. Eq. (2.21b)) are in general composed of all the modes in the original picture.

10. In this paragraph, adapted from Vukics & Domokos (2012), we assume a quasi-free-space situation when the dipoles are far from the boundaries, so that we use the longitudinal and transverse fields instead of the general projectors $\mathfrak{R}$ and $\mathfrak{Q}$.

2.A THE FABRY-PÉROT CONFIGURATION

To exemplify the above general formalism, we consider one of the simplest confined geometries, the perfect Fabry-Pérot cavity, that is, two parallel infinite planes of perfect conductors in the $x-y$ plane. Hence, the axis of the cavity lies in the z direction. The left mirror is situated at $z = 0$, and the length of the

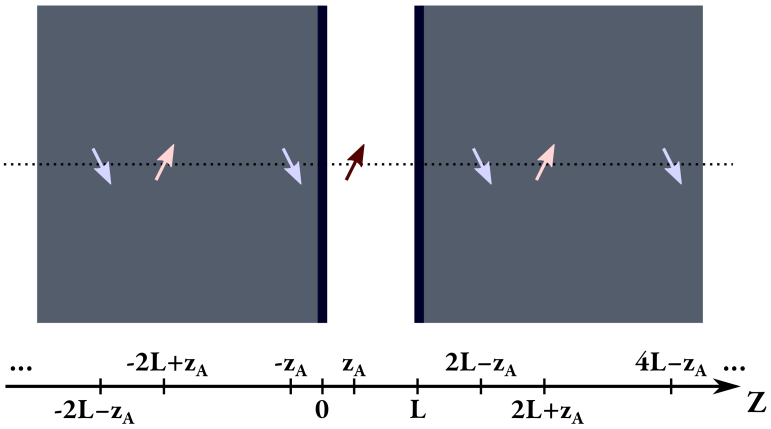

Figure 2.1: The Fabry-Pérot configuration with a single dipole within the cavity together with its image dipoles indicated in bleached colors.

cavity is L (cf. Fig. 2.1). In this case,

$$\mathcal{D} = \left\{\mathbf{r} \in \mathbb{R}^3 \middle| 0 < z < L\right\} \text{ and } \partial\mathcal{D} = \left\{\mathbf{r} \in \mathbb{R}^3 \middle| z = 0 \text{ or } z = L\right\}. \tag{2.24}$$

2.A.1 *Radiative part of the field*

The boundary conditions are:

$$\hat{\mathbf{z}} \times \mathbf{E} = 0 = \hat{\mathbf{z}}\,\mathbf{B} \quad \text{at the mirrors,} \tag{2.25}$$

and the mode functions satisfying these read (Meschede et al., 1990):

$$\boldsymbol{\varphi}^{\mathrm{E}}_{\mathbf{k}}(\mathbf{r}) \equiv \hat{\mathbf{k}}_\perp \times \hat{\mathbf{z}}\, \sin(k_n z)\, e^{i\mathbf{k}_\perp \mathbf{r}_\perp}, \tag{2.26a}$$

$$\boldsymbol{\varphi}^{\mathrm{M}}_{\mathbf{k}}(\mathbf{r}) \equiv \frac{1}{k}\left(k_\perp \cos(k_n z)\, \hat{\mathbf{z}} - i k_n \sin(k_n z)\, \hat{\mathbf{k}}_\perp\right) e^{i\mathbf{k}_\perp \mathbf{r}_\perp}. \tag{2.26b}$$

They are designated transverse electric (TE) and magnetic (TM) modes, respectively, with reference to the direction of the fields related to the $\mathbf{k}$ vector. We have introduced

$$\mathbf{r} \equiv z\hat{\mathbf{z}} + \mathbf{r}_\perp, \quad \mathbf{k} \equiv k_n \hat{\mathbf{z}} + \mathbf{k}_\perp, \quad \mathbf{r}_\perp, \mathbf{k}_\perp \perp \hat{\mathbf{z}}, \quad k_n \equiv \frac{n\pi}{L}. \tag{2.27}$$

Note that the polarizations are fixed by the direction of $\mathbf{k}_\perp$, while in the case of $\mathbf{k}_\perp = 0$ we are left with two sinusoidal modes of orthogonal polarization, which can be chosen arbitrarily in the transverse direction of the cavity. The dispersion relation reads:

$$\omega_k^2 \equiv c^2\left(k_n^2 + k_\perp^2\right) \equiv c^2 k^2. \tag{2.28}$$

Furthermore, the mode functions satisfy the transversality condition:

$$\nabla \cdot \boldsymbol{\varphi}^{\mathrm{E,M}} = 0. \tag{2.29}$$

For $k_n = 0$, the TE modes vanish identically, so that we are left with TM modes only. The latter, if $k_\perp = 0$ as well, describes a homogeneous field parallel

to the axis, which is the only cohomological field configuration in the Fabry-Pérot geometry. That is,

$$\mathbb{H}_2 = \left\{\boldsymbol{\varphi}^{\mathrm{M}}_{\mathbf{k}=0}\right\}. \tag{2.30}$$

The projector on $\ker(\mathrm{div}_0)$ reads

$$\mathfrak{R} = \sum_{\mathbf{k}} \left\{\boldsymbol{\varphi}^{\mathrm{E}}_{\mathbf{k}} \otimes \boldsymbol{\varphi}^{\mathrm{E}}_{\mathbf{k}} + \boldsymbol{\varphi}^{\mathrm{M}}_{\mathbf{k}} \otimes \boldsymbol{\varphi}^{\mathrm{M}}_{\mathbf{k}}\right\} = \frac{S}{(2\pi)^2} \int \mathrm{d}^2 k_\perp \left\{\sum_{n=1}^{\infty} \boldsymbol{\varphi}^{\mathrm{E}}_{\mathbf{k}} \otimes \boldsymbol{\varphi}^{\mathrm{E}}_{\mathbf{k}} + \sum_{n=0}^{\infty} \boldsymbol{\varphi}^{\mathrm{M}}_{\mathbf{k}} \otimes \boldsymbol{\varphi}^{\mathrm{M}}_{\mathbf{k}}\right\}. \tag{2.31}$$

2.A.2 *Electrostatic part of the field*

In this geometry, the electrostatic (Dirichlet) Green's function can be easily obtained in Descartes coordinates with the method of image charges, while in cylindrical coordinates we quote the formula given in p. 109 of Gray & Mathews (1966):[11]

$$\begin{aligned}\mathcal{G}(\mathbf{r},\mathbf{r}') &= -\frac{1}{4\pi}\sum_n \left(\frac{1}{|\mathbf{r}-\mathbf{r}'-2nL\hat{\mathbf{z}}|} - \frac{1}{|\mathbf{r}-\mathbf{r}'_\perp+(z'-2nL)\hat{\mathbf{z}}|}\right) \\ &= 2\int_0^\infty \mathrm{d}\lambda\, \frac{\sinh(\lambda(L-z))\sinh(\lambda z')}{\sinh(\lambda L)}\, J_0\Big(\lambda\sqrt{r_\perp^2 - r_\perp'^2 - 2r_\perp r'_\perp\cos(\phi-\phi')}\Big),\end{aligned} \tag{2.32}$$

in the last line $z \geq z'$, otherwise z and z' has to be interchanged. It can be clearly seen that $\mathcal{G}$ vanishes if either z or z' equals 0 or L. The form in the first line is the expression of the method of point charges.

* * *

Using the above forms, it can be shown explicitly that the completeness relation (2.6) holds with the forms given in note 4. With moderate effort, this relation can be reduced to the identity (22) of Vukics & Domokos (2012), that was proved in that paper.

11. This geometry is an exactly solvable problem, since in addition to Green's function, the mode structure and the dispersion relation are also known exactly.

REGULARIZATION OF THE THEORY AND ITS IMPACT ON THE POSSIBILITY OF ULTRASTRONG COUPLING

3

3.1 SYNOPSIS

In this Chapter we survey the consequences of the description developed in Chapter 2. We discuss possible forms of the polarization field, and show why the P-square term appearing in Eq. (2.19b) can be a problem. We present an alternative definition of the polarization field which gives a meaningful potential term in the single-atom Hamiltonian and, at the same time, retains the advantage that there is no direct electrostatic interaction between atoms sufficiently apart. The proposed definition will allow for exploring the limits of ultrastrong coupling between atomic matter and light.

We acknowledge that the definition of the PZW transformation has a freedom: the choice of the transverse part of the polarization field. We identify the restrictions this field has to meet, and define the transverse part of the polarization field generated by spatially distinct, well-localized, neutral charge clusters (atoms or molecules). With this definition, the passage to the multipolar picture is a class of transformations parametrized by a single wave-number-cutoff parameter. We show how to define bounds for the cutoff wave number on intuitive physical basis:

the lower bound comes from the required disappearance of the A-square term, while

the upper bound from that the potential term in Hamiltonian (2.19b) be only a slightly perturbed Coulomb potential.

With this appropriate choice, we arrive at a picture (regularized electric-dipole – RED – picture) where the atoms interact exclusively via the radiation modes of the electromagnetic field by means of photon emission and absorption processes. Since the instantaneous electrostatic dipole-dipole Coulomb interaction between spatially distinct atoms is canceled, the atoms have well-defined resonances regardless of the presence of other atoms. The necessary requirement is that the atoms do not approach each other within the distance corresponding to the cutoff; i.e., they all are surrounded by what we can call an *intimacy zone*.

The RED picture is thus unsuited for describing molecule formation or solidification. This is to be noted because our results indicate that the superradiant quantum phase transition accompanied by ferroelectric ordering of the

Figure 3.1: Illustration of the Power form of the polarization field for a single point charge reproduced from Cohen-Tannoudji et al. (1997) p. 281. The real charge distribution (a) is a point charge q_α at $\mathbf{r}_\alpha$. It is equivalent (b) with the reference charge distribution (q_α at O) plus n dipoles $q_\alpha \mathbf{r}_\alpha / n$. The Power form of the polarization field for this situation is obtained as the limit $n \to \infty$.

atoms in the dipolar Hamiltonian (most simply in the Dicke model) blends into that commonly observed phase transition, which is solidification. Nevertheless, sufficiently far from the regime of molecule formation, the RED picture can be used to evaluate the limitation of ultrastrong coupling within the Dicke and related models.

3.2 POSSIBLE FORMS OF P AND THE SINGLE-ATOM HAMILTONIAN

In the previous chapter, we introduced the field $\mathbf{P}$, as a replacement of the charge density in describing the "matter" part of the system. To be more precise, the polarization field describes not a charge density proper, but the displacement of a charge density with respect to a reference charge density:[1]

$$\nabla \cdot \mathbf{P} = -\rho + \rho_{\mathrm{ref}}. \tag{3.1}$$

A natural form of the polarization field is the Power form.[2] For a set of point-like charges, it reads (cf. also Fig. 3.1):

$$\mathbf{P}(\mathbf{r}) = \sum_\alpha q_\alpha \left(\mathbf{r}_\alpha - \mathbf{r}_\alpha^{(\mathrm{o})}\right) \int_0^1 \mathrm{d}u\, \delta\left(\mathbf{r} - \mathbf{r}_\alpha^{(\mathrm{o})} - u\left[\mathbf{r}_\alpha - \mathbf{r}_\alpha^{(\mathrm{o})}\right]\right), \quad \text{with} \tag{3.2a}$$

$$\rho_{\mathrm{ref}}(\mathbf{r}) = \sum_\alpha q_\alpha\, \delta\left(\mathbf{r} - \mathbf{r}_\alpha^{(\mathrm{o})}\right), \tag{3.2b}$$

In the case of neutral atoms, the most convenient choice for the reference distribution is that all the charges belonging to a single atom be localized in the nucleus of the atoms. (This leads to an identically zero reference distribution.) Then,

$$\mathbf{P}(\mathbf{r}) = \sum_A \sum_{\alpha \in A} q_\alpha (\mathbf{r}_\alpha - \mathbf{r}_A) \int_0^1 \mathrm{d}u\, \delta(\mathbf{r} - \mathbf{r}_A - u[\mathbf{r}_\alpha - \mathbf{r}_A]), \tag{3.3}$$

where $\mathbf{r}_A$ is the position of the nucleus of atom A. Besides being intuitive, this form has the advantage that it satisfies the separability condition (2.17) exactly. However, it has the serious disadvantage that the $\mathbf{P}^2$ term, appearing in the PZW Hamiltonian (2.16) or in the single-atom Hamiltonian (2.19b), contains a distribution squared. Indeed it is a common belief that the A-square

1. In case of a non-trivial reference charge density, the displacement field is no longer purely transverse:

$$\nabla \cdot \mathbf{D} = \nabla \cdot \{\varepsilon_0 \mathbf{E} + \mathbf{P}\} = \rho - \rho + \rho_{\mathrm{ref}} = \rho_{\mathrm{ref}},$$

a relation familiar from macroscopic electrodynamics.

2. This is a simplified account, for a recent retelling of all the intricacies of the full story, cf. Woolley (2020)

problem just resurfaces as the P-square problem in the PZW picture, and the transformation doesn't solve anything (Bamba & Ogawa, 2014).

Since Power & Zienau (1959), this problem was conventionally treated by a procedure inspired by renormalization. Another possibility is to endow the point charges with finite extension, considering them spheres or discs facing the center of the corresponding atom, so that the infinitesimal filaments of nonzero polarization in the form (3.2a) become finite tubes. This, however, leads to an atom picture similar to quark confinement, hence fundamentally deviating from the normal Schrödinger atom: in this case each electron would interact only with the atomic center, but with a force that would grow linearly with the distance from the center. Electrons would interact with each other only when their corresponding tubes intersect.

In the following we give a straightforward regularization proceduce that leads only to a perturbation of the Schrödinger atom.

3.3 QUANTUM ELECTRODYNAMICS OF ATOMS IN THE MULTIPOLAR PICTURE

Let us rewrite the Hamiltonian in the multipolar picture (2.16) for the purposes of this chapter as

$$H = H_{\mathrm{EM}} + H_{\mathrm{kin}} + \frac{1}{2\varepsilon_0}\int \mathrm{d}V\, P^2 - \frac{1}{\varepsilon_0}\int \mathrm{d}V\, \mathbf{P}\cdot\mathbf{D}, \tag{3.4}$$

where H_{EM} is the Hamiltonian of the free electric field, H_{kin} is the kinetic energy of the atoms, and $\mathbf{D}$ is the (purely transverse) electric displacement field. $\mathbf{P}$ is the polarization field, which plays a crucial role in this picture. This satisfies the relation

$$\nabla\cdot\mathbf{P} = -\rho, \tag{3.5}$$

that connects the polarization field to the charges, however, since $\nabla\cdot\mathbf{P} = \nabla\cdot\mathbf{P}^{\parallel}$, it relates *only* to the longitudinal component of the field.[3] Equivalently:

$$\mathbf{P}^{\parallel} = -\varepsilon_0\mathbf{E}^{\parallel}, \tag{3.6}$$

meaning that the part of the electric field which is attached to the charges and follows their motion instantaneously (the so-called "near field"), is incorporated into the polarization field, that represents the material component of the interacting system.

Besides $\mathbf{P}^{\parallel}$, the other orthogonal component of $\mathbf{P}$ is the transverse component, $\mathbf{P}^{\perp}$, which is source-free and normal to the boundaries, that is, it can either be written as curl of another vector field normal to the boundaries, or is cohomological, cf. Eq. (2.9). We emphasize again that the transverse component of the polarization field *is not determined by the charges* in such a direct way as Eq. (3.5) for the longitudinal one. Instead, it has to obey a set of conditions in order that the multipolar picture be really useful. The first comes from the requirement of the "elimination of the A-square term" to electric-dipole order, cf. Eq. (2.5c), that we expect from this picture:

$$\frac{\partial}{\partial\mathbf{r}_\alpha}\int \mathrm{d}V\, \mathbf{P}^{\perp}\cdot\mathbf{A} = q_\alpha\,\mathbf{A}(\mathbf{r}_A), \quad \forall\alpha\in A, \tag{Cond. I}$$

3. In contrast to Chapter 2, in this chapter we are not concerned with topological issues any more, so by longitudinal we simply mean that the field can be written as gradient of a scalar field vanishing on the eventual boundaries. Conversely, a transverse field is divergence-free and normal to the boundaries.

where $\mathbf{r}_A$ is the position of that atom A to which the particle α with position $\mathbf{r}_\alpha$ and charge q_α, belongs. This makes the kinetic momentum coincide with the canonical one up to a magnetic term – the so-called Röntgen term, cf. Section IV.C.4.c in Cohen-Tannoudji et al. (1997) and Vukics et al. (2021) –, which we neglect here.

The next condition is necessary for eliminating the electrostatic dipole-dipole interaction between the atoms in this picture, which means that the medium can be considered as independent atoms (elimination of cross-coupling in the P-square term). It requires that $\mathbf{P}_A$, the polarization field corresponding to any single atom A have finite support around the atomic position, so that the full polarization can be written as $\mathbf{P} = \sum_A \mathbf{P}_A$. The size of the support can be a parameter that for instance will play an important role with our choice of $\mathbf{P}^\perp$ in Section 3.4. This fact of finite support we express here with the help of the "long-wavelength" delta function as:

$$\mathbf{P}_A(\mathbf{r}) \simeq \mathbf{d}_A \delta_<(\mathbf{r} - \mathbf{r}_A). \tag{Cond. II}$$

Through the example of our choice of $\mathbf{P}^\perp$, in Section 3.4 we will discuss why and in what sense the equality is only approximate here. For the moment it is sufficient that the field $\mathbf{P}_A$ should describe a well-localized dipole when regarded on a lengthscale much larger than the atomic size.

Under this last condition, and assuming the atoms distant enough from each other that the supports of their respective $\mathbf{P}_A$ fields do not overlap, the third term of the Hamiltonian (3.4) – the potential term – can be written as per atom:

$$U \equiv \frac{1}{2\varepsilon_0} \int \mathrm{d}V\, P^2 = \frac{1}{2\varepsilon_0} \sum_A \int \mathrm{d}V\, P_A^2 \equiv \sum_A U_A, \tag{3.7}$$

which means that the only interaction between different atoms is the indirect one via the displacement field $\mathbf{D}$, that involves the emission and absorption of photons, included in the Hamiltonian (3.4) by its last term. This leads us to the final condition that $\mathbf{P}_A^\perp$ has to satisfy for each atom A. The potential corresponding to atom A can be separated into parts generated by the longitudinal and the transverse part of the polarization field, where the longitudinal part can be identified – this follows from Eq. (3.6), cf. also Section I.B.5.a in Cohen-Tannoudji et al. (1997) – as the Coulomb potential term:

$$U_A = \frac{1}{2\varepsilon_0} \int \mathrm{d}V \left(P_A^\parallel\right)^2 + \frac{1}{2\varepsilon_0} \int \mathrm{d}V \left(P_A^\perp\right)^2 \equiv U_A^{\mathrm{Coul}} + \Delta U_A. \tag{3.8}$$

Then, the last condition is that the potential generated by the transverse part be only a perturbation to the normal Coulomb potential, because we do not want to upset atomic physics as it has been worked out over the last century based in leading order on the electrons experiencing the Coulomb potential as they orbit the nucleus.

$$\Delta U_A \text{ is only a perturbation to } U_A^{\mathrm{Coul}}. \tag{Cond. III}$$

In Section 3.5, we exhibit the consequences of these conditions on the possibility of ultrastrong coupling between atoms and the electromagnetic field.

3.4 APPROPRIATE CHOICE OF THE TRANSVERSE POLARIZATION IN DIPOLE ORDER

The following form for the transverse part of the polarization field we demonstrate below to optimally fulfill the set conditions:

$$\mathbf{P}_A^{\perp}(\mathbf{r}) = \boldsymbol{\delta}_<^{\perp}(\mathbf{r}-\mathbf{r}_A)\,\mathbf{d}_A, \tag{3.9a}$$

where $\mathbf{d}_A = \sum_{\alpha\in A} q_\alpha \mathbf{r}_\alpha$ is the dipole moment of atom A, and we have used the long-wavelength part of the transverse delta function, most conveniently defined by a Lorentzian cutoff in k-space at the cutoff wavenumber k_{M}:[4]

$$\widetilde{\boldsymbol{\delta}}_<^{\perp}(\mathbf{k}) = \frac{1}{(2\pi)^{3/2}}\left(\mathbf{id}_{\mathbb{R}^3} - \frac{\mathbf{k}\circ\mathbf{k}}{k^2}\right)\frac{k_{\mathrm{M}}^2}{k^2+k_{\mathrm{M}}^2}, \tag{3.9b}$$

where we have assumed $\mathbf{r}_A = 0$ for the single atom A that we are going to consider henceforth in this Section. Using the real-space form of this, we get for $r \gtrsim k_{\mathrm{M}}^{-1} \equiv \ell$

$$\mathbf{P}_A^{\perp}(\mathbf{r}) = \frac{\gamma(r)}{4\pi r^3}\left[\frac{3\,(\mathbf{r}\cdot\mathbf{d}_A)\,\mathbf{r}}{r^2} - \mathbf{d}_A\right], \quad \text{with} \quad \gamma(r) = 1-\left(1+k_{\mathrm{M}}r+\frac{k_{\mathrm{M}}^2 r^2}{2}\right)e^{-k_{\mathrm{M}}r}. \tag{3.9c}$$

As it is apparent, this is just the electric field of a dipole, so that this choice of $\mathbf{P}_A^{\perp}$ cancels the dipole order of the longitudinal component (3.6), outside a distance $\sim \ell$. This makes that the support of $\mathbf{P}_A = \mathbf{P}_A^{\parallel} + \mathbf{P}_A^{\perp}$ is indeed finite in dipole order, that is, the atoms interact only in quadrupole order, which we are neglecting here. Hence, (Cond. II) is fulfilled up to dipole order, which we consider sufficient for our purposes here, and is in accordance with the neglect of the Röntgen term above.[5] This is the sense in which the equality in (Cond. II) is fulfilled only approximately: up to dipole order and without a region of radius ℓ around the atom. This latter is the *intimacy region* of an atom: the interaction between different atoms simplifies substantially to the indirect interaction mediated by the radiation field modes only if they do not penetrate each other's intimacy region.

This is also a point where our approach manifestly deviates from the original Power-Zineau-Woolley approach, since with Power's original definition of the polarization field (3.2a), it exactly vanishes outside of zero-measure regions within the atom – on the other hand, (Cond. III) is impossible to fulfill with that choice of the polarization field.

In our case, the cutoff wavenumber k_{M} is not a renormalization parameter, but parametrizes a class of allowed transformations. In the following, we use the remaining two conditions (Cond. I) and (Cond. III) to define an interval for k_{M}.

3.4.1 *Lower limit of cutoff*

The lower limit comes from (Cond. I) as follows. Taking the free-space traveling-wave expansion of the vector potential $\mathbf{A}(\mathbf{r}) = \int d^3k \sum_\epsilon \left[\boldsymbol{\alpha}_\epsilon(\mathbf{k})\, e^{i\mathbf{k}\cdot\mathbf{r}} + \text{c.c.}\right]$, and substituting into the LHS of (Cond. I) with our choice of $\mathbf{P}^{\perp}$ (3.9a), we obtain

$$\int \mathrm{d}V\, \frac{\partial \mathbf{P}^{\perp}}{\partial \mathbf{r}_\alpha}\mathbf{A} = q_\alpha \int d^3k\, \frac{k_{\mathrm{M}}^2}{k^2+k_{\mathrm{M}}^2}\sum_\epsilon\left[\boldsymbol{\alpha}_\epsilon(\mathbf{k}) + \text{c.c.}\right] \equiv q_\alpha \mathbf{A}_<(0). \tag{3.10}$$

4. In Appendix 3.A we show that the concrete form of the regularization function, chosen in Eq. (3.9b) as a Lorentzian for simplicity, is in fact immaterial as to the physical consequences of the obtained models, all that matters is the size of the support of this envelope, that we denote ℓ, with $\ell = k_{\mathrm{M}}^{-1}$ for our choice here.

5. This is because for a hydrogen-like atom, both this term and the quadrupole term of the electrostatic interaction is $\mathcal{O}([a_0 k_{\text{radiation}}]^2)$, while the dipole term would be $\mathcal{O}(a_0 k_{\text{radiation}})$, a_0 being the Bohr radius (cf. Section 3.4.2), for which $a_0 k_{\text{radiation}} \ll 1$ holds.

That is, if $\boldsymbol{\alpha}_e(\mathbf{k}) \approx 0$ for $k \geq k_M$ in the course of the dynamics, so that we can write $\mathbf{A}_<(0) = \mathbf{A}(0)$, then (Cond. I) is fulfilled. Hence the lower limit for k_M:

$$k_M \gg k_{\text{radiation}}. \qquad \text{(cutoff lower limit)}$$

In simple terms, the atom has to be small compared to the wavelength of populated modes, represented by $k^{-1}_{\text{radiation}}$. This is usually termed the dipole approximation, or, more precisely, the long-wavelength approximation. In the case of a hydrogen atom and optical frequencies, there are roughly 3 orders of magnitude between the atomic size and the characteristic wavenumber of the atomic transitions. This can be seen by expressing the characteristic transition frequency with fundamental constants as $\hbar\omega_A = \frac{3}{8} m_e c^2 \alpha^2$, and using $m_e c\alpha = \hbar/a_0$ to obtain

$$k_A = \frac{3\alpha}{8}\frac{1}{a_0}, \tag{3.11}$$

where α is the fine-structure constant, and k_A determines the wavenumber of the relevant resonant radiation modes ($k_{\text{radiation}} \sim k_A$).

The long-wavelength approximation is an elementary requirement for atom optics, because in this field we need well-defined atoms with level structures determined by a static potential, and radiative effects on the atomic scale are treated as mere perturbations.

3.4.2 *Upper limit of cutoff*

The upper limit comes from (Cond. III) as follows. With our choice of the transverse polarization field (3.9a), we can take the potential resulting from $\mathbf{P}^\perp$ seriously as a physically significant potential. This is in contrast to Power's choice (3.2a), since in that case the "perturbation" is infinite and calls for renormalization. The finite and regular potential ΔU_A in Eq. (3.8) resulting from the proposed polarization field $\mathbf{P}^\perp$ is

$$\Delta U_A = \frac{1}{2\varepsilon_0}\int d^3k \left|\widetilde{\mathbf{P}}^\perp_A\right|^2 = \frac{k_M^3}{24\pi\varepsilon_0} d_A^2. \tag{3.12}$$

This potential term manifests that the atom is defined in the multipolar picture differently from the one in the original picture, i.e., the canonical transformation shifts the boundary between atom and field.

To keep our discussion as simple as possible, the effect of this potential will be calculated in the example of the 1s state of the hydrogen atom by time-independent perturbation theory. To be able to do quantum physics, the potential has to be treated as an operator acting on the Hilbert space of the atom's constituents. Here, this consists in considering the positions of the atomic constituents appearing in $\mathbf{d}_A$ as quantum operators. For the hydrogen atom, $\mathbf{d} = e\,\mathbf{r}$, where $\mathbf{r}$ is the relative coordinate, so that the perturbing potential reads

$$\Delta U_{\text{hydrogen}} = \frac{e^2 k_M^3}{24\pi\varepsilon_0} r^2. \tag{3.13}$$

The 1s wave function of the electron is $\Psi_{1s}(\mathbf{r}) = e^{-r/a_0}/\left(\sqrt{\pi} a_0^{3/2}\right)$, where a_0 is the Bohr radius. The first-order perturbation reads:

$$E^{(1)}_{1s} = \langle 1s|\,\Delta U_{\text{hydrogen}}\,|1s\rangle = \frac{e^2 k_M^3}{24\pi^2\varepsilon_0 a_0^3}\int d^3r\, r^2 e^{-\frac{2r}{a_0}} = \frac{e^2 k_M^3 a_0^2}{8\pi\varepsilon_0}. \tag{3.14}$$

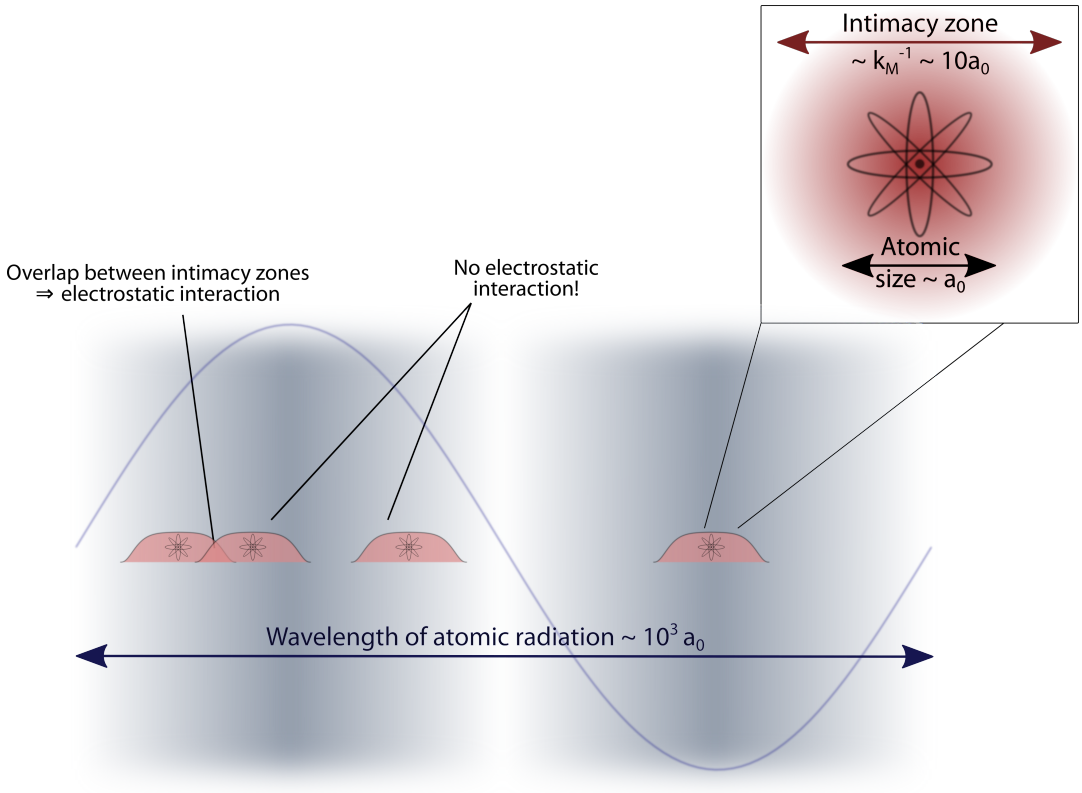

Figure 3.2: Visualization of the hierarchy of lengthscales: $\lambda_A \gg \ell \gg a_o$.

Let us compare this energy to the binding energy of the hydrogen atom, the Rydberg energy. We find the following remarkably simple expression:

$$\frac{E_{1s}^{(1)}}{\mathrm{Ry}} = (k_M a_o)^3 \,. \tag{3.15}$$

Hence (Cond. III) is translated to an upper limit of the cutoff wavenumber as

$$k_M^3 \ll (a_o)^{-3}. \qquad \text{(cutoff upper limit)}$$

The hierarchy of the lenghtscales appearing in this discussion is exhibited in Fig. 3.2. The cubic power in this expression makes that e.g. a cutoff of $k_M \approx 1/(2\,a_o)$ already gives about 0.1 for the energy ratio (3.15). That is, an intimacy region compressed to nearly the atomic size can be chosen without significantly altering the usual Coulomb potential form of the atomic Hamilton operator. We note that the Lamb shift is of the same order of magnitude as ΔU_A (Power & Zienau, 1959; Milonni, 1976), but it should be treated separately, since it comes from the *interaction with the vacuum field,* that is, the last term of Hamiltonian (3.4).

With the transverse polarization fulfilling all the conditions considered above, the single-atom Hamiltonian in (2.19) assumes a familiar form to read

$$H_A = \sum_{\alpha \in A} \frac{p_\alpha^2}{2m_\alpha} + U_A. \tag{3.16}$$

3.5 THE LIMITS OF COUPLING STRENGTH

We are now in the position of addressing the question what is the maximum coupling strength achievable between the atomic medium and a radiation field mode. The limitation arises from the requirement that the interatomic distance in the many-atom ensemble must respect the intimacy region of the individual atoms. For the collective coupling of atoms to light in the models (1.1), the figure of merit pertaining to ultrastrong coupling is the ratio

$$\mathcal{F} \equiv \frac{Ng^2}{\omega\,\omega_{\mathrm{A}}}, \tag{3.17}$$

where N is the number of atoms, ω is the frequency of a radiation mode, ω_{A} is the resonance frequency associated with a relevant electronic transition within an atom, and g is the electric-dipole coupling constant. The coupling g depends on the mode geometry and the oscillator strength of the atomic transition, cf. Eq. (2.22):

$$g^2 = \frac{\omega\, d^2}{2\hbar\varepsilon_{\mathrm{o}} V}, \tag{3.18}$$

where V is the mode volume and d is the dipole moment of the atomic transition along the mode polarization. Note that the use of all the microscopic parameters (d, ω_{A}, etc.) is justified here by the lack of cross-coupling in the "P-square term" of Eq. (3.4): without electrostatic atom-atom interaction, the presence of other atoms does not alter the atomic level structure.

The figure of merit can be expressed in two instructive forms. Firstly:

$$\mathcal{F} = \frac{N}{V}\,\lambda_{\mathrm{A}}^3\,\frac{3}{8\pi^2}\,\frac{1}{Q}, \tag{3.19a}$$

where we use the quality factor of the atomic resonance $Q \equiv \omega_{\mathrm{A}}/\gamma$ with $\gamma = \omega_{\mathrm{A}}^3 d^2/(6\pi\varepsilon_{\mathrm{o}} c^3)$ being the linewidth (half width at half maximum) and λ_{A} the wavelength. This form expresses that the density N/V must be large to compensate for the large quality factor of an atomic resonance in the denominator (for alkali atoms this is $\sim 1.2 - 1.5 \cdot 10^8$). In order to get deeper insight into scaling laws, we consider transitions between hydrogen-like ground and excited states, and find the second form:

$$\mathcal{F} = \frac{N}{V} 16\pi a_{\mathrm{o}}^3\,, \tag{3.19b}$$

where a_{o} is the Bohr radius. That is, in order to have $\mathcal{F} \sim 1/4$, the atomic medium should be so dense that one atom occurs per about 4 Bohr radius cube. Let us make explicit the *Dicke critical density*

$$n_{\mathrm{D}} = \frac{\hbar\omega\varepsilon_{\mathrm{o}}}{2d^2}, \tag{3.20}$$

that can be calculated from Eq. (3.17) by setting $\mathcal{F} = 1/4$.[6]

This density is noticeably close to the limit allowed by the maximum of the cutoff parameter k_{M} given by (cutoff upper limit), i.e., $\ell \approx 2\,a_{\mathrm{o}}$, indicating an interatomic distance just around 4 Bohr radius. This means that we can approach the critical-coupling point in the ultrastrong regime with an ensemble of independent atoms. However, this happens at the density when the intimacy regions of adjacent atoms touch. Further increasing the density, the independent-atom model breaks down for two different sets of reasons:

6. In order to obtain a lower estimate for the critical density, we are using the smaller of the two expressions (1.2).

	^{6}Li	Na	K	Rb	Cs
Dicke critical density (3.20) $[10^{27}/\mathrm{m}^3]$	3.33	3.33	1.88	1.77	1.32
crystalline density @ room temperature $[10^{27}/\mathrm{m}^3]$	53.6	25.4	13	10.6	8.48

Table 3.1: Comparison of the Dicke critical density and crystalline density for different alkali species. Atomic parameters from Steck (2021). The critical densities were calculated for the D lines, as these have the strongest transition dipoles, just like in the case of a ground-state hydrogen atom, the 1s-2p transition is the strongest. If we considered other transitions from the ground state, the transition frequency would increase whereas the dipole moment decrease, which would greatly increase the critical density. Hence, taking into account higher excited states would give a small numerical correction to our present results, but nothing qualitatively different.

Reasons within the RED picture: Electrostatic interactions between the atoms become relevant, that in turn modify both atomic parameters appearing in (3.20): the transition frequency, and the transition dipole. It is the subject of Chapter 4 whether the criticality survives these modifications, and if so, how much the critical density changes.

Reasons outside of the RED picture: At such a small atomic distance, the overlap between the exponentially decaying electron wavefunctions ($\propto e^{-r/a_0}$) belonging to different atoms becomes significant. Such a delocalization of electronic orbits would lead to covalent bonding between atoms, which effect is definitely excluded from the RED picture, as here the electrons do not experience the electrostatic potential of other nuclei. The role of electron-orbit delocalization at such high densities can be revealed by comparing the critical density $1.77 \cdot 10^{27}/\mathrm{m}^3$ for Rubidium to the crystalline density $11 \cdot 10^{27}/\mathrm{m}^3$. We find similar correspondences also for other species used in atom-optics experiments, cf. Table 3.1. Except for ^{6}Li, the two densities are within the same order of magnitude for all species.

One can thus conjecture that the superradiant criticality blends into the commonly known criticality of condensation (liquefaction or solidification/crystallization, depending on the species). The superradiant phase transition is a silhouette of condensation (cf. Fig. 3.3): as much a simplified picture as the RED description is simplified compared to the full physics of the condensation process, the latter involving the quantized atomic motion, the static and radiative multipoles, and exchange interactions.

Besides the similar magnitude of the densities, this claim can be supported by two further distinct arguments.

A scaling argument. As it is apparent in Eq. (3.19b), *in the RED picture,* the figure of merit depends only on atomic parameters, as the mode frequency drops out from the expression of $\mathcal{F}$ (this would not happen in the *a priori* picture). This means that the Dicke critical point ($\mathcal{F} = 1/4$) is determined by the Bohr radius (or, for alkali atoms, the corresponding atomic size), a_0. In an atom-picture based on the Coulomb potential, which is scale-less, this is the only available atomic lengthscale, which

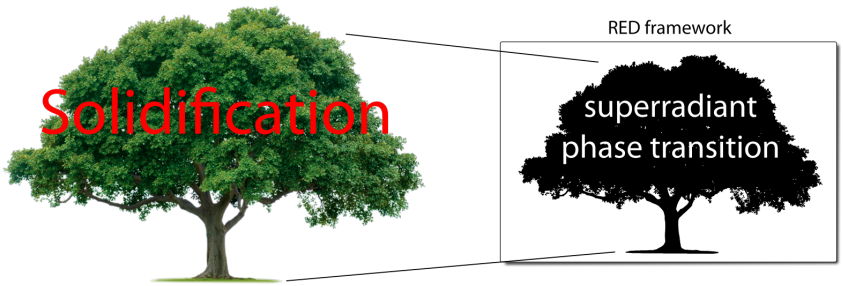

Figure 3.3: The Dicke phase transition as a silhouette of solidification.

determines also the covalent-bond distance. As there is no free parameter for nature to separately tune the Dicke critical and the solidification point, the similarity of the two is not a mere coincidence.

An argument from the macroscopic nature of the transition. Due to the above mentioned independence on the mode frequency, all the modes become superradiant at the critical point, that is, the full electromagnetic field participates in the transition.

3.A ARBITRARY REGULARIZING ENVELOPE

In this appendix, we show that the concrete form of the regularization function that in Eq. (3.9b) was chosen a Lorentzian is actually immaterial as to the physical consequences of the obtained model of light-matter interaction. In the process, we will have the opportunity to formalize more explicitly the definition of the long-wavelength approximation, and to evaluate the remainder of the A-square term. For the purposes of this derivation, let us rewrite the Hamiltonian in multipolar picture in the following form:

$$H = \sum_\alpha \frac{1}{2m_\alpha}\left(\mathbf{p}_\alpha + \frac{\partial}{\partial \mathbf{r}_\alpha}\int \mathrm{d}V\ \mathbf{A}\cdot\mathbf{P} - q_\alpha \mathbf{A}(\mathbf{r}_\alpha)\right)^2 + \frac{1}{\varepsilon_0}\int \mathrm{d}V\ \mathbf{\Pi}\cdot\mathbf{P} + \frac{\varepsilon_0}{2}\int \mathrm{d}V\left(\frac{1}{{\varepsilon_0}^2}\mathbf{\Pi}^2 + c^2[\nabla\times\mathbf{A}]^2\right) + \frac{1}{2\varepsilon_0}\int \mathrm{d}V\ \mathbf{P}^2. \tag{3.21}$$

So far, we have argued that this Hamiltonian can be better suited for the quantum electrodynamics of atoms than the original, for several reasons. However, it suffers from the presence of the last, the so-called P^2 term, that contains a distribution squared for the most straightforward choice of the polarization field, which is Power's choice (3.2a).

A solution to this problem discussed in the present chapter was based on the fact that the transverse part of the polarization field $\mathbf{P}$ is not uniquely defined. That is, while the longitudinal part (now written in k-space) is given unambigously by the charges via the Coulomb interaction as

$$\mathbf{P}^{\parallel}(\mathbf{k})\big(=-\varepsilon_0\mathbf{E}^{\parallel}(\mathbf{k})\big) = \frac{i}{(2\pi)^{\frac{3}{2}}}\frac{\mathbf{k}}{k^2}\sum_A e^{-i\mathbf{k}\cdot\mathbf{r}_A}\sum_{\alpha\in A} q_\alpha\left(e^{-i\mathbf{k}\cdot\delta\mathbf{r}_\alpha}-1\right), \tag{3.22a}$$

the transverse part has a certain freedom. In contrast to Power's choice, the regularity of the transformation was imposed by choosing

$$\mathbf{P}^{\perp}(\mathbf{k}) = \frac{\mathfrak{c}(k)}{(2\pi)^{\frac{3}{2}}}\left(\mathbb{I} - \frac{\mathbf{k}\circ\mathbf{k}}{k^2}\right)\sum_A \mathbf{d}_A\, e^{-i\mathbf{k}\cdot\mathbf{r}_A}, \tag{3.22b}$$

where we have introduced the regularizing function $\mathfrak{c}(k)$, normalized as $\mathfrak{c}(0) = 1$ and vanishing with $k \to \infty$. Here again, the label A for clusters of charges (atoms) with dipole moment $\mathbf{d}_A = \sum_{\alpha\in A} q_\alpha \mathbf{r}_\alpha$ was introduced, while $\alpha \in A$ labels the particles belonging to cluster A. The position of a cluster (center of mass or atomic nucleus) is denoted by $\mathbf{r}_A$, while the relative positions of the constituent particles by $\delta\mathbf{r}_\alpha = \mathbf{r}_\alpha - \mathbf{r}_A$. We encounter γ, the cutoff function in real space, an example for which we have seen in Eq. (3.9c), through the relation:

$$\mathfrak{c}(k) = \frac{1}{(2\pi)^3}\int \mathrm{d}V\ \gamma(r)\, e^{i\mathbf{k}\cdot\mathbf{r}}. \tag{3.23}$$

This differs from normal Fourier transformation only in the normalizing prefactor $1/(2\pi)^{3/2}$, introduced for convenience.

With this choice, we can find the Hamiltonian for N identical atoms. Here we restrict ourselves to hydrogen-like atoms with a core and a single electron labeled by c and e, respectively, but the extension to the general case is straightforward. There appears an asymmetry between the treatment of $\mathbf{r}_{c,A}$ and $\mathbf{r}_{e,A}$ because the former is identified with the position of the atom, and therefore it enters the expression (3.22b) at two places, while $\mathbf{r}_{e,A}$ only at one.

$$\begin{aligned} H = &\sum_A \frac{1}{2m_c}\left\{\mathbf{p}_{c,A} + q\big[\tilde{\mathbf{A}}(\mathbf{r}_{c,A}) - \mathbf{A}(\mathbf{r}_{c,A})\big] + (\mathbf{d}_A\cdot\nabla)\tilde{\mathbf{A}}(\mathbf{r}_{c,A}) + \mathbf{d}_A\times\big[\nabla\times\tilde{\mathbf{A}}(\mathbf{r}_{c,A})\big]\right\}^2 \\ &+ \sum_A \frac{1}{2m_e}\left\{\mathbf{p}_{e,A} - q\big[\tilde{\mathbf{A}}(\mathbf{r}_{c,A}) - \mathbf{A}(\mathbf{r}_{e,A})\big]\right\}^2 + \frac{1}{\varepsilon_0}\sum_A \mathbf{d}_A\cdot\tilde{\mathbf{\Pi}}(\mathbf{r}_{c,A}) \\ &+ \frac{\varepsilon_0}{2}\int \mathrm{d}V\left(\frac{1}{{\varepsilon_0}^2}\mathbf{\Pi}^2 + c^2\,[\nabla\times\mathbf{A}]^2\right) + \sum_A\left(U_A^{\parallel} + U_A^{\perp}\right) + \sum_{A\neq B}\left(U_{A,B}^{\parallel} + U_{A,B}^{\perp}\right), \end{aligned} \tag{3.24}$$

where $\tilde{\mathbf{A}} \equiv \gamma \star \mathbf{A}$ and $\tilde{\mathbf{\Pi}} \equiv \gamma \star \mathbf{\Pi}$ (convolution). Of the static potentials

$$U_A^{\parallel} = \frac{1}{2\varepsilon_0}\int \mathrm{d}V\ \left(\mathbf{P}_A^{\parallel}\right)^2 = \frac{1}{8\pi\varepsilon_0}\sum_{\substack{\alpha,\beta\in A\\ \alpha\neq\beta}}\frac{q_\alpha\, q_\beta}{\left|\mathbf{r}_\alpha - \mathbf{r}_\beta\right|} \tag{3.25a}$$

is the intra-atomic and

$$U_{A,B}^{\parallel} = \frac{1}{2\varepsilon_0}\int \mathrm{d}V\ \mathbf{P}_A^{\parallel}\cdot\mathbf{P}_B^{\parallel} = \frac{1}{8\pi\varepsilon_0}\sum_{\alpha\in A,\beta\in B}\frac{q_\alpha\, q_\beta}{\left|\mathbf{r}_\alpha - \mathbf{r}_\beta\right|} \tag{3.25b}$$

is the inter-atomic Coulomb potential while the terms stemming from the perpendicular part of the P^2 term read

$$U_A^{\perp} = \frac{1}{2\varepsilon_0}\int \mathrm{d}V\ \left(\mathbf{P}_A^{\perp}\right)^2 = \frac{q^2 r^2}{3\varepsilon_0}\Gamma(0), \tag{3.26a}$$

r being the position operator of the valence electron relative to the core, and

$$U_{A,B}^{\perp} = \frac{1}{2\varepsilon_0}\int \mathrm{d}V\ \mathbf{P}_A^{\perp}\cdot\mathbf{P}_B^{\perp} = \frac{1}{2\varepsilon_0}\mathbf{d}_A\, K(\mathbf{r}_A - \mathbf{r}_B)\,\mathbf{d}_B, \tag{3.26b}$$

where $\Gamma \equiv \gamma \star \gamma$ and this function is, just like γ, normalized to unity, i.e.

$$\int \mathrm{d}V\ \Gamma(r) = \int \mathrm{d}V\ \gamma(r) = 1. \tag{3.27}$$

We have also introduced the matrix (relying on the Parseval-Plancherel identity)

$$K(\mathbf{r}) \equiv \int \mathrm{d}^3k\ \frac{\mathfrak{c}^2(k)}{(2\pi)^3}\left(\mathbb{I} - \frac{\mathbf{k}\circ\mathbf{k}}{k^2}\right)e^{i\,\mathbf{k}\cdot\mathbf{r}} = \int \mathrm{d}^3k\ \frac{\mathfrak{c}^2(k)}{(2\pi)^3}e^{i\,\mathbf{k}\cdot\mathbf{r}}$$
$$+\,\nabla\circ\nabla\int \mathrm{d}^3k\ \frac{\mathfrak{c}^2(k)}{(2\pi)^3}\frac{e^{i\,\mathbf{k}\cdot\mathbf{r}}}{k^2} = \Gamma(r)\,\mathbb{I} - \nabla\circ\nabla\int \mathrm{d}^3x'\ \Gamma(r')\,G(\mathbf{r}-\mathbf{r}'), \tag{3.28}$$

with the electrostatic (Dirichlet) Green's function

$$G(\mathbf{r}) \equiv -\frac{1}{4\pi|\mathbf{r}|}. \tag{3.29}$$

The first term after the last equal sign in (3.28) is a (regularized) contact interaction, while the physical effect of the second term is that $U^{\perp}_{A,B}$ knocks out the dipole order from $U_{A,B}$ outside of the intimacy region of the atoms.[7]

The third and fourth terms in the first line of Eq. (3.24) are magnetic terms, and the difference between the canonical and kinetic momenta in the new picture is also a magnetic term (these are the so-called Röntgen terms, cf. Section IV.C.4.c in Cohen-Tannoudji et al. (1997)). These terms are of the same order as the electric quadrupole, and hence are neglected in the (regularized) *electric-dipole* picture.

Let us denote the length scale which characterizes the size of the support of Γ (and γ) in real space by ℓ. Notice that for those modes whose wavelengths are much smaller than ℓ, we have $\tilde{\mathbf{\Pi}} \sim 0 \sim \tilde{\mathbf{A}}$ and consequently the coupling of the atoms to such modes is the same as in the original Hamiltonian. On the other hand, for modes with a wavelength much larger than the above scale, we have the usual dipole coupling, because $\tilde{\mathbf{\Pi}} \sim \mathbf{\Pi}$ and $\tilde{\mathbf{A}} \sim \mathbf{A}$, i.e. γ acts like a delta function on such scales. As a basic requisite of the theory, we would like to ensure that the intra-atomic low-energy spectrum is negligibly perturbed with respect to the Coulomb one (cf Eq. (3.26a)). It can be shown that this requires $\ell \gg a_0$, where a_0 determines the size of the atom given only Coulomb interactions between core and electron (Bohr radius). As a second simplification, we disregard the electromagnetic modes below a certain cutoff wavelength $\lambda_{\min}$. The coupling to the remaining part of the spectrum should be given by the usual dipole Hamiltonian. Taken together, the requirements are given by

$$a_0 \ll \ell \ll \lambda_{\min} \tag{3.30}$$

and the (low-energy) Hamiltonian then approximately reads

$$H = \sum_A \frac{\mathbf{p}^2_{c,A}}{2m_c} + \sum_A H_{e,A} + \sum_{A\neq B}\left(U^{\parallel}_{A,B} + U^{\perp}_{A,B}\right) + \frac{1}{\varepsilon_0}\sum_A \mathbf{d}_A\cdot\mathbf{\Pi}(\mathbf{r}_{c,A})$$
$$+\,\frac{\varepsilon_0}{2}\int \mathrm{d}V\left(\frac{1}{{\varepsilon_0}^2}\mathbf{\Pi}^2 + c^2\left[\nabla\times\mathbf{A}\right]^2\right), \tag{3.31a}$$

with the electronic Hamiltonian

$$H_{e,A} = \frac{\mathbf{p}^2_{e,A}}{2m_e} + U^{\parallel}_A(\mathbf{r}_{e,A}) + U^{\perp}_A(\mathbf{r}_{e,A}). \tag{3.31b}$$

This is just the theory obtained in the main text of this chapter, with the explicit form of the γ envelope having disappeared from the expressions.

7. Concerning K an interesting note presents itself, that sheds more light on the nature of the difference between the *a priori* and the RED pictures. The origin of $U^{\perp}$ is certainly what we would identify as radiation in the original picture: indeed, this is the (dipole-order) correction which cancels the instantaneous interaction to yield a fully retarded one. In the RED picture, however, this has nothing to do with radiation since it stems from $\mathbf{P}^{\perp}$, which is a prescribed field, cf. Eq. (3.22b). It is also worth mentioning that in the RED picture, the van der Waals interaction appears as a fourth-order photon-scattering process mediated by the radiation field, that is, it stems from the second term of the Hamiltonian (2.19), in much the same way as in the normal electric-dipole picture, cf. Section II.F.2. of Cohen-Tannoudji et al. (1998).

DEPOLARIZATION SHIFT OF THE SUPERRADIANT PHASE TRANSITION

4

4.1 SYNOPSIS

In Chapter 3, we have shown that in the RED picture, where no-go theorems are irrelevant to the possibility of the Dicke phase transition, the different atoms do not interact electrostatically – which is essential to the Dicke model –, as long as their spatial separation is large enough for their intimacy regions not to overlap.

On the other hand, it turned out that the inter-atomic distance characteristic of the critical density obtained from the Dicke model is at the limit where the atoms can no longer be treated as independent dipoles. That is, the superradiant criticality is achieved at an atom-gas density very close to the crystalline density of the given atomic species. We could even conjecture that the superradiant phase transition is nothing else but the image of condensation: as much simplified an image, as the framework of dipolar quantum electrodynamics is simplified compared to the formidable quantum many-body problem of interacting moving atoms in the quantized electromagnetic field, which should be considered in order to grasp condensation with any pretense to fullness. Furthermore, the description of the delocalization of electronic orbits (as occurs in covalent bonding or bands in a solid) requires a refined description of the higher-than-dipole multipolar terms and exchange interaction.

Nevertheless, the criticality alone and the onset of the phase transition can be captured by a much simpler model, such as the dipolar Hamiltonian with adiabatically separated atomic motion. The condition of spatially separated atoms should be released, however, in order to investigate the radiative properties of the ensemble at the high densities considered. In this regime, the instantaneous – depolarizing – atom-atom interaction, whose range in the RED picture is reduced to the atomic size scale, plays a substantial role, and is expected to shift the critical point. The physical reason of this shift is clear: assume that the atoms are spontaneously polarized along a given direction in the superradiant phase. If they are allowed to approach each other on the length scale of the atomic size – something they have to do close to and above the critical coupling strength – the interaction of two dipoles pointing along the same direction costs energy and disfavors the ordered configuration. The study of this shift is the subject of the present chapter. We complement the Dicke-model description of the dense atomic gas by incorporating the contact terms – the leftover of the instantaneous atom-atom interaction in the RED picture – accounting for the case of overlapping atoms and depolarization.

4.2 REGULARIZED ELECTRIC DIPOLE PICTURE

Let us summarize the basic expressions in the picture which has been shown to be particularly suitable to describe the quantum electrodynamics of an optically dense cloud of N well-localized atoms. The RED picture can be obtained from the *a priori* Hamiltonian by canonical transformation and the dipole approximation. The Hamiltonian then reads

$$H = \sum_{j=1}^{N} \left(\frac{\mathbf{p}_j^2}{2m} + H_{\mathrm{e},j} \right) + U - \frac{1}{\varepsilon_0} \sum_{j=1}^{N} \mathbf{d}_j \cdot \mathbf{D}(\mathbf{r}_j) + H_{\mathrm{EM}}(\mathbf{D}, \mathbf{B}) \,, \tag{4.1a}$$

where $\mathbf{r}_j$ denotes the position of the atomic center of mass, $\mathbf{p}_j$ the corresponding momentum, and $\mathbf{d}_j$ the atomic dipole moment. $H_{\mathrm{e},j}$ denotes the internal (electronic) Hamiltonian of atom j, which reflects the familiar Schrödinger atom perturbed by QED effects. The last term is the free electromagnetic field energy expressed in terms of the displacement instead of the electric field,

$$H_{\mathrm{EM}} = \frac{\varepsilon_0}{2} \int \mathrm{d}V \left(\frac{1}{{\varepsilon_0}^2} \mathbf{D}^2 + c^2 \mathbf{B}^2 \right). \tag{4.1b}$$

In the lack of free charges – that is, charges not described by the set of dipoles $\mathbf{d}_j$ –, the displacement field is purely transverse: $\mathbf{D} = \mathbf{D}_\perp$.

The coupling between field and the atoms is linear in the atomic dipole moment and the displacement field. One of the main merits of this picture is that the interaction between atoms is vastly dominated by the indirect interaction via the radiation field. The key point in the present chapter is, however, that we take into account also the residual instantaneous inter-atomic potential U. In the chosen picture, it is composed of two terms,

$$U = \sum_{i \neq j} \left(U_{i,j}^{\parallel} + U_{i,j}^{\perp} \right). \tag{4.1c}$$

The first term, $U_{i,j}^{\parallel}$, is just the Coulomb interaction between the charges belonging to different atoms, while the second term, $U_{i,j}^{\perp}$, cancels the strongest, dipole-dipole order of this instantaneous interaction outside a small region around the atoms with radius ℓ (termed the atomic "intimacy zone"). Altogether, the potential U is thus much weaker than the bare Coulomb interaction for separated atoms and is significant only to describe the contact interaction when an atom penetrates another's intimacy zone. The transverse part $U_{i,j}^{\perp}$ reads

$$U_{i,j}^{\perp}(\mathbf{r}_{ij}) = \frac{1}{2\varepsilon_0} \mathbf{d}_i \, K(\mathbf{r}_{ij}) \, \mathbf{d}_j, \tag{4.2a}$$

where $\mathbf{r}_{ij} = \mathbf{r}_i - \mathbf{r}_j$ and the matrix K is given by (cf. Eq. (3.28))

$$K(\mathbf{r}) = \Gamma(r) \, \mathbb{I} - \nabla \circ \nabla \int \mathrm{d}V' \, \Gamma(r') \, G(\mathbf{r} - \mathbf{r}'), \tag{4.2b}$$

with G the electrostatic (Dirichlet) Green's function, $\Delta G(\mathbf{r}) = \delta(\mathbf{r})$. The radially symmetric $\Gamma(r)$ is a regularizing (cutoff) function, it is normalized to unity, has a supporting volume of $\sim \ell^3$. The precise form of $\Gamma(r)$ is immaterial. Cf. Section 3.A for more details.

Let us recall again the assumptions which allow the minimal coupling Hamiltonian to be transformed to the above form. One condition is that we

consider only states where the internal energy of any given atom is low. Secondly, we apply an ultraviolet cutoff on the electromagnetic spectrum, that is, we discard parts with wavelengths smaller than some $\lambda_{\min} \gg a_0$, where a_0 determines the size of an atom in the ground state (this would be the Bohr radius for hydrogen). And lastly, the length scale characterizing $\Gamma(r)$ obeys

$$a_0 \ll \ell \ll \lambda_{\min}. \tag{4.3}$$

If we choose the cutoff wavelength to be of the order of the optical wavelength corresponding to the given atomic species, then there exists a range of values for ℓ, which satisfy the above chain of inequalities.[1]

1. As an illustration thereof, we can quote the well-known relation for hydrogen:

$$\lambda_A = \frac{16\pi}{3\alpha}\, a_0 \simeq 2000\, a_0.$$

4.3 THE ELECTROMAGNETIC AND ELECTRONIC SUBSYSTEM

4.3.1 *Adiabatic elimination of center-of-mass motion*

We simplify the model further by dropping the center-of-mass kinetic energy terms and regarding the atomic positions as time-independent (classical) *random variables* instead. This may be viewed as a Born–Oppenheimer-type approximation, which can be justified by considering the vastly different time scales operative for the electromagnetic and electronic subsystems on the one hand (characteristic timescale: inverse of linewidth $\approx$ 26 ns for the D_2 line of Rb), and the center-of-mass motion on the other (characteristic timescale: inverse of recoil frequency $\approx$ 130 μs for the D_2 line of Rb). Furthermore, it is not our ambition to follow the subsystem's dynamics through all times. Instead, our aim is to find the conditions under which the normal ground state of the remaining subsystem first exhibits a *dynamically unstable* behavior, which point we will interpret as the critical point of a phase transition. Our approach thus differs from early ones (Hepp & Lieb, 1973; Wang & Hioe, 1973) in being based explicitly on dynamical as opposed to thermodynamic considerations. In order to extract the necessary information, at some point we too will need to resort to statistical averaging over the external degrees of freedom.

4.3.2 *Linearization of atomic excitation*

Since we are interested in the stability of the normal ground state of the system, we can confine the description to the lowest-lying excitations. Accordingly, we can approximate $H_{e,j}$ by that of an isotropic harmonic oscillator with transition frequency ω_A

$$H_{e,j} = \hbar\omega_A\, \mathbf{b}_j^\dagger \cdot \mathbf{b}_j. \tag{4.4a}$$

Accordingly, the dipole moment of the jth atom we can write as

$$\mathbf{d}_j = d\left(\mathbf{b}_j + \mathbf{b}_j^\dagger\right), \tag{4.4b}$$

with $d > 0$ being the transition dipole. This may be viewed as an effective linearization of the theory close to the atomic ground state, i.e. we neglect the nonlinearity of the atomic polarizability due to saturation.

The Hamiltonian we will henceforth consider is then given by

$$H = \sum_{j=1}^{N} \hbar\omega_{\mathrm{A}}\, \mathbf{b}_j^\dagger \cdot \mathbf{b}_j + \frac{d^2}{2\varepsilon_{\mathrm{o}}} \sum_{i\neq j}^{N} \mathbf{q}_i\, u(\mathbf{r}_{ij})\, \mathbf{q}_j - \frac{d}{2\varepsilon_{\mathrm{o}}} \sum_{\nu} A_\nu \sum_{j=1}^{N} \mathbf{q}_j \cdot \boldsymbol{\varphi}_\nu(\mathbf{r}_j) + \sum_{\nu} \hbar\omega_\nu\, a_\nu^\dagger a_\nu, \tag{4.5}$$

and it can be expected to describe the electronic- and electromagnetic subsystem for durations long enough for the purpose of revealing instability. Here we use the quadratures

$$\mathbf{q}_j = \mathbf{b}_j + \mathbf{b}_j^\dagger\,, \tag{4.6a}$$

and

$$A_\nu = -i(a_\nu - a_\nu^\dagger). \tag{4.6b}$$

The direct atom-atom coupling matrix u is given by

$$u(\mathbf{r}) = K(\mathbf{r}) + \nabla \circ \nabla\, G(\mathbf{r}). \tag{4.7}$$

The second term represents the dipole order in the Coulomb interaction energy $U_{i,j}^{\parallel}$, the higher multipolar orders being neglected in accordance with the linearization in terms of the electronic degrees of freedom $\mathbf{b}_j$ in Eq. (4.4). The supporting volume of the matrix u is ℓ^3. Finally, we mention that we have introduced the set of transverse modes of the electromagnetic field $\boldsymbol{\varphi}_\nu$ normalized as

$$\int \mathrm{d}V\, \boldsymbol{\varphi}_\nu(\mathbf{r}) \cdot \boldsymbol{\varphi}_{\nu'}(\mathbf{r}) = 2\hbar\omega_\nu\, \varepsilon_{\mathrm{o}}\, \delta_{\nu,\nu'}. \tag{4.8}$$

The Hamiltonian (4.5) differs from the usual single-mode Dicke Hamiltonian in several respects:

1. All field modes below an ultraviolet cutoff are retained.

2. The atomic-position-dependence of the coupling between the atomic dipoles and the displacement field is taken into account.

3. The electronic degrees of freedom are represented by isotropic harmonic oscillators (collective excitations).

4. Most importantly, the instantaneous contact interaction energy between the atoms is accounted for (cf. second term). This term leads to depolarization since it punishes the configuration of dipoles pointing along the same direction.

In keeping with the emphasis on dynamics, we now investigate the solutions to the equations of motion corresponding to the Hamiltonian (4.5), which read

$$\ddot{\mathbf{q}}_j = -\,\omega_{\mathrm{A}}^2\, \mathbf{q}_j - \frac{2\, d^2 \omega_{\mathrm{A}}}{\hbar\varepsilon_{\mathrm{o}}} \sum_{i\neq j}^{N} u(\mathbf{r}_{ji})\, \mathbf{q}_i - \frac{d\, \omega_{\mathrm{A}}}{\hbar\varepsilon_{\mathrm{o}}} \sum_{\nu} A_\nu \boldsymbol{\varphi}_\nu(\mathbf{r}_j) \tag{4.9a}$$

$$\ddot{A}_\nu = -\,\omega_\nu^2 A_\nu - \frac{d\, \omega_\nu}{\hbar\varepsilon_{\mathrm{o}}} \sum_{j=1}^{N} \mathbf{q}_j \cdot \boldsymbol{\varphi}_\nu(\mathbf{r}_j). \tag{4.9b}$$

4.3.3 *Coarse graining approximation*

We will now make use of the conditions (4.3) and imagine the total volume V divided into disjoint cells $\delta V(\mathbf{r})$ centered around the points labeled $\mathbf{r}$, each cell being much larger than the support ℓ of the regularization function $\Gamma(r)$, but much smaller than the cube of the minimal wavelength, that is

$$\ell^3 \ll \delta V \ll \lambda_{\min}^3. \tag{4.10}$$

Using the first inequality – which makes that the *bulk* of any two cells, even if they are neighboring, do not interact, the support of the interaction being ℓ^3 – we neglect the instantaneous interaction of dipoles which belong to *different* cells. Thus in (4.9a), we restrict the second term to interaction between atoms only in the same cell, that is

$$\ddot{\mathbf{q}}_j = -\omega_{\mathrm{A}}^2 \mathbf{q}_j - \frac{2d^2\,\omega_{\mathrm{A}}}{\hbar\varepsilon_0} \sum_{\substack{\mathbf{r}_k \in \delta V(\mathbf{r}) \\ k \neq j}} u(\mathbf{r}_{jk})\,\mathbf{q}_k - \frac{d\,\omega_{\mathrm{A}}}{\hbar\varepsilon_0} \sum_{\nu} A_\nu \boldsymbol{\varphi}_\nu(\mathbf{r}). \tag{4.11}$$

In the last term, we used a long wavelength approximation based on the second inequality in (4.10), which makes that the mode function varies slowly on the lengthscale of a single cell.

In a similar spirit, in Eq. (4.9b) we may approximate

$$\sum_{j=1}^{N} \mathbf{q}_j \cdot \boldsymbol{\varphi}_\nu(\mathbf{r}_j) \simeq \sum_{\mathbf{r}} n(\mathbf{r})\,\mathbf{q}(\mathbf{r}) \cdot \boldsymbol{\varphi}_\nu(\mathbf{r})\,\delta V(\mathbf{r}), \tag{4.12}$$

where we have introduced the cell-averaged generalized coordinate

$$\mathbf{q}(\mathbf{r}) = \frac{1}{\delta N(\mathbf{r})} \sum_{\mathbf{r}_j \in \delta V(\mathbf{r})} \mathbf{q}_j, \tag{4.13a}$$

as well as the cell density

$$n(\mathbf{r}) = \frac{\delta N(\mathbf{r})}{\delta V(\mathbf{r})}, \tag{4.13b}$$

with $\delta N(\mathbf{r})$ being the number of particles in the given cell. Later we will assume $\delta N(\mathbf{r}) \gg 1$ so that its statistical fluctuations be negligible.

4.4 DYNAMICAL INSTABILITY IN MEAN-FIELD APPROXIMATION

It is at this point that we make use of statistical considerations and resort to a mean-field type approximation. We shall restrict our attention to such dynamical modes where for all j with $\mathbf{r}_j \in \delta V(\mathbf{r})$ we can assume $\mathbf{q}_j \simeq \mathbf{q}(\mathbf{r})$. The existence of such states requires that to a good approximation the sum

$$\sum_{\substack{\mathbf{r}_k \in \delta V(\mathbf{r}) \\ k \neq j}} u(\mathbf{r}_{jk}) \tag{4.14}$$

be independent of the index j, i.e. the spatial configuration of dipoles surrounding any given one can be assumed to be identical on the scale ℓ set by the

interaction, which is guaranteed if every dipole is interacting simultaneously with a large number of others within the same cell. Adopting this hypothesis, we may substitute for the sum in (4.11) its conditional expectation value

$$\sum_{\substack{\mathbf{r}_k \in \delta V(\mathbf{r}) \\ k \neq j}} u(\mathbf{r}_{jk})\, \mathbf{q}_k \to n\, \mathbf{q} \int \mathrm{d}^3 x_k \; g(r_{jk}) u(\mathbf{r}_{jk}), \tag{4.15}$$

where $g(r)$ denotes the radial distribution function of the atomic centers, which we regard as a given. As a result we obtain

$$\ddot{\mathbf{q}} = -\omega_{\mathrm{A}}^2 (1+\varsigma)\mathbf{q} - \frac{d\,\omega_{\mathrm{A}}}{\hbar \varepsilon_0} \sum_\nu A_\nu \boldsymbol{\varphi}_\nu(\mathbf{r}), \tag{4.16a}$$

$$\ddot{A}_\nu = -\omega_\nu^2 A_\nu - \frac{n\, d\, \omega_\nu}{\hbar \varepsilon_0} \sum_{\mathbf{r}} \mathbf{q}(\mathbf{r}) \cdot \boldsymbol{\varphi}_\nu(\mathbf{r}), \tag{4.16b}$$

here the summation in the last term is over the cells, and we have neglected the statistical fluctuations of δN. The contact interaction in the mean-field approximation amounts to a density-dependent transition frequency shift ς, which is given by

$$\varsigma = \frac{1}{3} \frac{n}{n_{\mathrm{D}}} \int \mathrm{d}V \; g(r) \;\; \mathrm{Tr}\{u(\mathbf{r})\}. \tag{4.17}$$

It is the linear system (4.16) that we subject to dynamical stability analysis. Due to homogeneity of the system of equations, the homogeneous state ($\mathbf{q} = 0,\ A_\nu = 0$) is always a solution, but it may become unstable at a certain critical parameter set. The stability analysis consists in finding the complex eigenfrequencies (s) of the system, and looking for that point in the parameter space when at least one of these eigenfrequencies start to have a positive real part, signalling the appearance of an exponentially runaway solution (dynamical instability). The point of our whole course here is that the critical point of instability is identified with that of the phase transition. A runaway solution for at least one of the field amplitudes A_ν is identified with the onset of superradiance.

Owing to its linearity, the system (4.16) may be conveniently transformed into algebraic equations by means of a Laplace transformation with the result that

$$A_\nu(s) = \frac{J_\nu(s)}{D_\nu(s)}, \tag{4.18}$$

where s denotes the complex frequency,

$$D_\nu(s) = 1 - \frac{n}{n_{\mathrm{D}}} \frac{\omega_\nu^2 \omega_{\mathrm{A}}^2}{[s^2 + \omega_\nu^2][s^2 + \omega_{\mathrm{A}}^2(1+\varsigma)]}, \tag{4.19}$$

and J_ν subsumes all terms containing the initial conditions. The eigenfrequencies $\{s_\nu\}$ of the system are determined by the condition $D_\nu(s_\nu) = 0$. One can check that, without the frequency shift ς, the eigenfrequencies vanish just for the density $n = n_{\mathrm{D}}$.

To proceed, we calculate the frequency shift ς from Eq. (4.7),

$$\mathrm{Tr}\{u(\mathbf{r})\} = 3\Gamma(r) - \int \mathrm{d}V' \; \Gamma(r')\, \Delta G(\mathbf{r} - \mathbf{r}') + \Delta G = 2\Gamma(r) + \delta(\mathbf{r}), \tag{4.20}$$

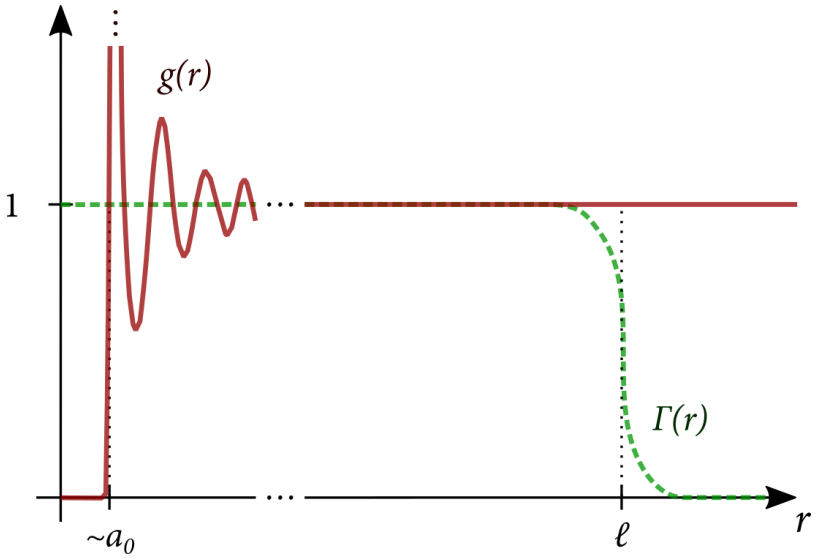

Figure 4.1: Relationship between the characteristic length scales of the radial distribution function g (solid red line) and the regularizing function Γ (dashed green line). The former, overshooting the value 1 and oscillating on the short scale $\sim a_0$, is a generic form characteristic of hard-core repulsive interparticle potentials, with a core size $\sim a_0$. (In the case of a Lennard-Jones potential, the first peak may reach as high as 3.)

where, in the second line we have used the defining property of the Green's function: $\Delta G(\mathbf{r}) = \delta(\mathbf{r})$. We hence obtain

$$\varsigma = \frac{n}{n_D}\left(\frac{2}{3}\int \mathrm{d}^3x\, g(r)\Gamma(r) + \frac{1}{3}g(0)\right). \tag{4.21}$$

The second term in the parentheses stems from the dipole part of the Coulomb interaction and does not in fact contribute because due to short range repulsion, we certainly have $g(0) = 0$. To deal with the first term, we note that on the scale given by ℓ, the ensemble of atoms may be regarded as spatially uniform, because the scale on which the radial distribution function varies around unity is clearly of the order of a_0. The relationship between characteristic spatial scales of g and Γ is sketched in Figure 4.1. Thus, due to (4.3), we can use the normalization of Γ to conclude that

$$\int \mathrm{d}^3x\, g(r)\Gamma(r) = 1 + O(a_0/\ell). \tag{4.22}$$

Hence, to within the accuracy of the model,

$$\varsigma = \frac{2}{3}\frac{n}{n_D}. \tag{4.23}$$

It is important to notice that the precise form of $\Gamma(r)$, which, as we have mentioned above, is immaterial with regard to the quality of the approximation of the model, does not influence the eigenfrequencies of the system and thus has no effect on the question of stability either. This is as it should be because we associate dynamical instability with the occurrence of an observable phenomenon, namely, a phase transition, and therefore no dependence on arbitrary quantities can be tolerated.

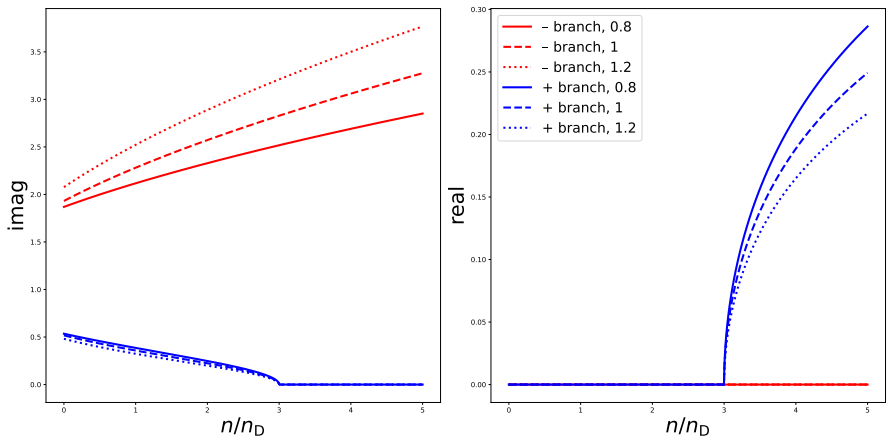

Figure 4.2: Behavior of the eigenvalues $s_{\nu,\pm}$ for three different frequency ratios: $\omega_A/\omega_\nu = 0.8,\ 1,\ 1.2$. The criticality is captured by the + branch becoming real positive at the critical density $n_c = 3n_D$.

The eigenfrequencies of the system are found to be

$$\frac{s_{\nu,\pm}^2}{\omega_A\,\omega_\nu} = -\,S(\omega_A,\omega_\nu) \pm \sqrt{S(\omega_A,\omega_\nu)^2 + \left(\frac{1}{3}\frac{n}{n_D} - 1\right)}, \quad \text{with} \tag{4.24a}$$

$$S(\omega_A,\omega_\nu) = \left[\omega_A^2(1+\varsigma) + \omega_\nu^2\right]/(2\omega_A\omega_\nu). \tag{4.24b}$$

Hence we find for every mode index ν that as long as $n < n_c$, where

$$n_c = 3\,n_D, \tag{4.25}$$

the RHS is negative, so there exist four imaginary eigenfrequencies, an upper and a lower branch reflected on the origin, and the system is *stable*. As the density increases, the lower branch $s_{\nu,+}$ softens, that is, the two eigenfrequencies $s_{\nu,+}$ approach 0 along the imaginary axis, and depart along the real axis in opposite directions. The point where they reach 0 is the critical point where the homogeneous solution ($\mathbf{q} = 0,\ A_\nu = 0$) becomes unstable. This occurs at $n = n_c$ and the homogeneous solution is *unstable* for $n > n_c$. This story is illustrated in Fig. 4.2.

Therefore, we conclude that the model predicts a phase transition at a critical density which is three times the Dicke critical density. The considerable shift of the critical density stems from the depolarization effect due to the contact interaction in the dense atomic gas.

In summary, let us emphasize again that in the course of our analysis of the criticality in the RED Hamiltonian, we have retained all the modes of the electromagnetic field. In the present picture, the Dicke critical density (3.20) depends only on atomic parameters.[2] This means that all the modes become critical at the same point, that is, reaching the critical density of atoms, a superradiant field starts to build up in all the electromagnetic modes. In this sense, the superradiant phase transition is a macroscopic effect in the RED Hamiltonian. The depolarization shift by a factor of 3 pushes the superradiant critical density even closer to the condensed matter density, further supporting our identification of the Dicke phase transition as a silhouette of the macroscopic process of condensation.

2. The reason for this is that in the present picture, the atom-mode coupling coefficient g is proportional to the square root of the mode frequency, and hence the mode frequency drops out from the expression of the critical coupling. This is not the case in the original picture, where the coupling coefficient is proportional to the square root of the *inverse* of the mode frequency.

THESES, OUTLOOK, FURTHER DEVELOPMENTS

5

Thesis I (Vukics et al., 2014) Relying on the Helmholtz-Hodge decomposition, we have generalized the Power-Zienau-Woolley transformation for domains of arbitrary topology, that is, the most general possible cavity quantum electrodynamics situation. We have shown that the elimination of the A-square term and the intstantanous interaction between charge clusters known from the free-space case holds in any such geometry as well. The single-mode standard models of quantum optics (Dicke and Tavis-Cummings models) can hence be obtained by a term-by-term mapping to the microscopic Hamiltonian. In consequence, the basis of no-go argumentations concerning the Dicke phase transition with atoms in electromagnetic fields dissolves. We have shown that the Dicke model, when based on the PZW picture, predicts a mean field in the gauge-invariant quantity of the transverse electric field in the superradiant phase.

Thesis II (Vukics et al., 2015) We have proposed a form for the transverse polarization field of atomic/molecular media that removes the P-square problem in the PZW picture – the problem of squares of delta functions appearing in the single-particle Hamiltonian – without resorting to renormalization techniques. This form entails a new parameter with the dimension of length, that we have identified with the radius of an intimacy zone for the particles: outside of the intimacy zones, the instantanous inter-particle dipole-dipole interaction vanishes. We have identified the conditions that the transverse polarization field has to fulfill, and on the basis of these conditions we have given lower and upper bounds for the size of the intimacy zone, the former on the order of the particle size, the later on the order of the wavelength.

Thesis III (Vukics et al., 2015) Assessing the critical particle density for alkali atoms in the PZW picture, we have found that it is close to the condensation density. We have found arguments in support of the claim that the Dicke superradiant phase transition is a silhouette of the macroscopic phase transition of condensation: the former is as much a simplified image of the latter as the electric-dipole Hamiltonian is a simplified model with respect to the immensely complex quantum many-body problem underlying condensation, involving electromagnetic interactions in all multipole orders, delocalization of electronic orbits, and particle motional degrees of freedom.

Thesis IV (Grießer et al., 2016) In a mean-field model, we have calculated the depolarization shift of the superradiant phase transition, that is, the phase

transition occurring in a Dicke-type model based on the regularized electric-dipole Hamiltonian. This model differs from the Dicke model by the inclusion of all the electromagnetic modes (since all of them become superradiant at the same critical particle density), and of the short-range electrostatic interaction between such particles as approach each other to the touching of the intimacy zones. We have found that the extended – more realistic – model has a critical density at 3 times the Dicke critical density, pushing it even closer to the condensation density.

Since our contribution to the field presented in this Part, several related review papers have appeared: in ultrastrong coupling (Forn-Díaz et al., 2019; Le Boité, 2020; Peraca et al., 2020), in Dicke physics (Kirton et al., 2019), and in superradiant phase transitions (Larson & Irish, 2017). The ultrastrong coupling regime is now considered divided into two sections, with

- "ultrastrong" proper referring to the case when $g/\omega \gtrsim 0.1$, and
- the *deep strong coupling* regime, when $g/\omega \gtrsim 1$.

The deep strong coupling regime has been experimentally realized very recently with superconducting qubits by Yoshihara et al. (2017) and with electron cyclotron resonance by Bayer et al. (2017). Another recently emerged field very promising in this respect is cavity magnonics (Flower et al., 2019), where a coupling ratio $g/\omega \sim 0.6$ has been achieved by Golovchanskiy et al. (2021).

During the history of molecular QED, it has been suggested early on by Woolley (1974) and Babiker & Loudon (1983) that the PZW transformation can be formulated as a gauge transformation. Especially in the Lagrangian theory it is easy to show that a transformation to the Poincaré gauge on the Coulomb-gauge Lagrangian brings about a Lagrangian whose corresponding Hamiltonian is formally equivalent to the PZW one. Up to this day there has been a debate concerning gauge freedom/invariance (Garziano et al., 2020; Settineri et al., 2021; Savasta et al., 2021), its breakdown (De Bernardis et al., 2018), and gauge ambiguities (Di Stefano et al., 2019; Stokes & Nazir, 2019; Rouse et al., 2021), partly in connection with ultrastrong coupling. Recently, Rousseau & Felbacq (2017) even claimed that the PZW theory is inconsistent, based on considerations of gauges.

The fact is that the PZW theory is completely gauge invariant, and the equivalence with Poincaré gauge is only partial, which is especially transparent in the Hamiltonian formulation. It can be derived from a fully gauge invariant theory (Vukics et al., 2021), and the final Hamiltonian, containing only the physical fields is also gauge invariant. The correctness of the theory was further reasserted (Andrews et al., 2018; Woolley, 2020), together with its relevance to quantum optics, quantum chemistry (Flick et al., 2017; Schäfer et al., 2020), and resonance energy transfer (Salam, 2018).

It has been noted that the unitary equivalence between the *a priori* and PZW pictures is broken when approximations are done to obtain the standard models of quantum optics – the few-mode approximation for the field and few-level approximation for the atoms –: the models do not describe the same physics in the two pictures, and the difference gets especially pronounced on

approaching ultrastrong coupling. Although the PZW picture was formulated as *the* theory for the quantum interaction of the electromagnetic field with atoms or molecules from the outset, and the term-by-term correspondence was a very strong indication in this respect, it has remained a question in which picture the quantum optical models perform better. Recently, it was shown by De Bernardis et al. (2018) that in most situations the PZW picture is preferable in approximating the full physics. Discussions of the impact of the A-square term on the possibility of the superradiant phase transition nevertheless continue to resurface up to this day (Andolina et al., 2019; Wang et al., 2020).

Despite the occasional controversies regarding the fundamental aspects the field has continued to see great interest during the last few years. Ultrastrong light-matter coupling was studied from the thermodynamic point of view by Pilar et al. (2020) to find strong modifications of extensive thermodynamic quantities. Ultrastrong coupling between plasmons of a nanorod array and optical cavity photons was achieved at ambient conditions and without magnetic fields (Baranov et al., 2020), and vibrational ultrastrong coupling between plasmons and phonons was demostrated using epsilon-near-zero nanocavities (Yoo et al., 2021). A non-perturbative approach to the interaction of an electron gas with a cavity field that is valid for all coupling strengths was worked out by Ashida et al. (2021).

Non-classicality of the Dicke model has been studied in connection with an excited-state quantum phase transition (Zhu et al., 2019), two-photon correlations (Xu et al., 2020), and on hybrid lattices (Zhu et al., 2020). Whereas earlier realizations of the Dicke superradiant phase transition relied on driven-dissipative systems (Baumann et al., 2010; Nagy et al., 2011; Brennecke et al., 2013), it has recently been suggested that it can be realized as an *equilibrium* phase transition in a 2D electron gas coupled to a cavity in the presence of Rashba spin-orbit coupling (Nataf et al., 2019), or as the paramagnetic-to-ferromagnetic phase transition in a solid sample confined within a cavity formed by metallic mirrors (Ashida et al., 2020). The phase diagram of an extended Dicke model representing dipolar matter interacting with a cavity mode was outlined using exact numerical methods (Schuler et al., 2020). Superradiance with 10 qubits and subradiance with 8 qubits was demostrated in a superconducting quantum circuit with variable coupling strength and qubit number (Wang et al., 2020). Finally, metrological applications of the superradiant phase transition were designed by Garbe et al. (2020), suggesting that the divergent susceptibility close to the critical point can be exploited to achieve arbitrarily high precision, a plus that must be counterweighed by the increasing protocol duration due to critical slowing down.[1]

1. Literature review closed in October 2021

PART II

THE BREAKDOWN OF PHOTON BLOCKADE

THE BREAKDOWN OF PHOTON BLOCKADE AS A FIRST-ORDER DISSIPATIVE PHASE TRANSITION

6

6.1 SYNOPSIS

In this Chapter we study the photon-blockade breakdown (PBB) scheme in its dissipative-phase-transition and quantum aspects.

For the PBB bistability to become a phase transition, an appropriate thermodynamic limit is needed, which is approached in a finite-size scaling from a finite system. This abstract thermodynamic limit is the $g \to \infty$ limit, where both the bistability timescale and the separation of the attractors become macroscopic. We construct an approriate finite-size scaling of the system parameters, and numerically determine the finite-size scaling exponent of the timescale. We assess the nonclassicality of the attractors, and identify the central role of cascades of quantum jumps in the switching processes.[1]

The numerical studies presented in this Chapter took about *half a year* on a virtual computational cluster in an OpenStack cloud environment (MTA Cloud).

1. Both the DPT and this latter feature contrast the PBB bistability with the bistable flourescence signal observed in the electron-shelving scheme (Nagourney et al., 1986; Bergquist et al., 1986), where very long but still microscopic timescales remain to determine the signal, and single quantum jumps switch between the macroscopically separable states.

6.2 THE PHOTON-BLOCKADE-BREAKDOWN PHASE TRANSITION IN A NUTSHELL

6.2.1 *The driven-lossy Jaynes–Cummings model*

The simplest possible system exhibiting the photon-blockade-breakdown effect is composed of a two-level system coupled to a harmonic oscillator. The two-level system can be an atom or artificial atom, whereas the oscillator can represent a single lossy mode of the radiation field or a longitudinal mode of a stripline resonator. We describe this interaction within the driven Jaynes-Cummings model, i.e., using the electric-dipole coupling and the rotating-wave approximation (RWA), cf. Eq. (1.6).[2]

Assuming resonance between the mode and the atom, i.e. $\omega_{\mathrm{M}} = \omega_{\mathrm{A}}$, and going into a frame rotating at the drive frequency, one gets a formally time-independent Hamiltonian,

$$H = -\Delta \left(a^\dagger a + \sigma^\dagger \sigma\right) + ig\left(a^\dagger \sigma - \sigma^\dagger a\right) + i\eta\left(a^\dagger - a\right) , \qquad (6.1)$$

where the detuning $\Delta = \omega - \omega_M$ is a tunable parameter of the drive. The mode is that of a high-finesse resonator and is subject to loss. Similarly, the two-level system can have decay through spontaneous emission.[3] These incoherent

2. We note that due to the strong coupling required for the PBB effect, we are close to the validity limit of the RWA. A quantum-to-classical transition in a similar system without the conventional rotating-wave approximation has been reported in Pietikäinen et al. (2017, 2019).

3. In CCQED, cf. Chapter 7, the phase noise of the atomic levels usually dominates the population decay.

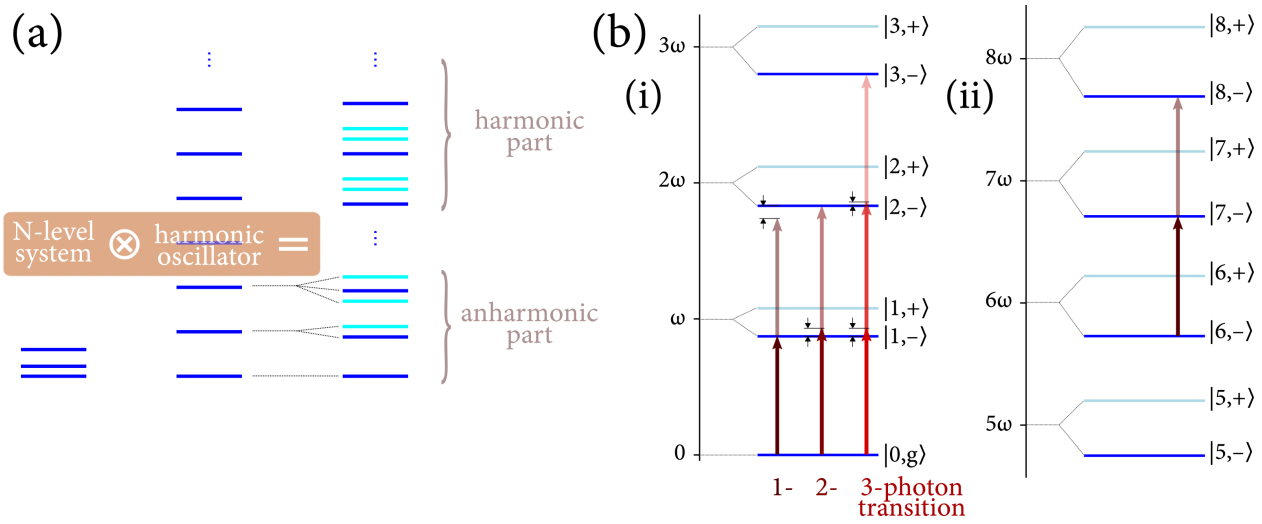

Figure 6.1: (a) In a quantum system consisting of a finite-level system strongly coupled to a harmonic oscillator, the lower part of the spectrum is anharmonic, but there are always higher-lying harmonic subsets of the spectrum. (b) The Jaynes-Cummings spectrum is a prototype of this behaviour (this part of the figure is to scale). Panel (i): the anharmonic part of the spectrum. An excitation tuned to a 1-photon transition misses the second rung of the ladder by a significant amount. That tuned to a 2- and 3-photon transition, misses the first rung and the first and second rung, respectively. Panel (ii): closely harmonic part of the spectrum. An excitation tuned to the transition between $|6,-\rangle$ and $|7,-\rangle$ is closely resonant also with the transition between $|7,-\rangle$ and $|8,-\rangle$ (the detuning is invisible on the figure's scale). As it is easy to verify from the formula (6.4), the difference in level-spacing for the '-' manifold decays as $n^{-1/2} - (n+1)^{-1/2} \approx n^{-3/2}$.

processes can be modelled by Liouvillian terms in the master equation

$$\dot{\rho} = -i[H,\rho] + \kappa\left(2a\rho a^\dagger - a^\dagger a\rho - \rho a^\dagger a\right) + \gamma\left(2\sigma\rho\sigma^\dagger - \sigma^\dagger\sigma\rho - \rho\sigma^\dagger\sigma\right) . \quad (6.2)$$

In the rest of this chapter we will consider the case $\kappa \gg \gamma$, most importantly $\gamma = 0$. The mode relaxation parameter κ defines the microscopic timescale of the problem.

6.2.2 *The photon-blockade-breakdown effect*

For weak drive strengths $\eta \ll g$, the excited eigenstates of the Hamiltonian are close to the Jaynes-Cummings dressed states

$$|n,\pm\rangle = \frac{1}{\sqrt{2}}\left(|g,n\rangle \pm |e,n-1\rangle\right) \quad (6.3)$$

with $n = 1, 2, \ldots$, and the energy levels are

$$E_{n,\pm} = n\,\omega_M \pm \sqrt{n}g\,. \quad (6.4)$$

In the strong coupling regime $g \gg \kappa$, the level shifts $\pm\sqrt{n}\,g$ with respect to the bare frequencies exceed significantly the linewidth $\sim \kappa$, so the system cannot be excited out of the ground state $|g,0\rangle$ by a near-resonant driving $\Delta \approx 0$. This is the photon blockade effect.[4]

Above a certain intensity of the driving, however, the system can be excited via higher-order (multi-photon) transition processes into the higher-lying part of the spectrum. Since one of the constituents is a harmonic oscillator, in the

4. In the literature, the 'photon blockade' sometimes denotes the effect when the first excited state with a single photon can be excited resonantly, but further excitations are suppressed due to off-resonance. This is analogous to the effect of Coulomb blockade to some extent. Here we use the term in a more general sense, where the system is blocked in the ground state, and no photons at all can be transferred to the system.

high-lying part there are harmonic subsets of the spectrum (cf. Fig. 6.1), ladders of equidistant levels which can host a coherent state with large amplitude and well-defined phase. Following a low-probability multi-photon transition into this range of the spectrum, the system gets stabilized into such a semiclassical trapping state by the competition of coherent driving and decay. Such an excitation, i.e., *the breakdown of the photon blockade* takes place in the form of a bistability. In a finite interval of the drive strength, the steady-state density operator of the system is the mixture of the 'dark' and 'bright' phases, i.e., the ground state and a highly excited coherent state of the oscillator (Carmichael, 2015; Dombi et al., 2015). As a main subject of our study, we will analyse this solution of the density matrix in detail starting from the next section. Beforehand, however, we try to capture the bistable behaviour in a corresponding classical theory.

6.2.3 *Classical phase diagram*

Following Carmichael (2015), let us first look at what the Jaynes and Cummings semiclassical (also known as 'neoclassical') equations can tell us. These are obtained by taking expectation values in Heisenberg equations of motion (e.g. $\alpha = \langle a \rangle$) and factorizing the expectations of operator products to obtain a closed set of nonlinear equations for the expectation values. Taking $\gamma = 0$, the theory leads to the self-consistent equation (valid for $\Delta < 0$), cf. Section 7.B

$$\frac{|\alpha|^2}{N_{\text{scale}}} = \left(\frac{2\eta}{g}\right)^2 \left[1 + \left(\frac{\Delta}{\kappa} - \frac{1}{\sqrt{\Delta^2\kappa^2/g^4 + |\alpha|^2/N_{\text{scale}}}}\right)^2\right]^{-1}, \qquad (6.5)$$

where we introduced the parameter $N_{\text{scale}} = g^2/4\kappa^2$. This nonlinear equation can afford different solution sets. The various domains are depicted in the phase diagram in Fig. 6.2. Below the lower boundary, the phase is the photon blockade regime, whereas above the higher boundary, the system is highly excited. In between, Eq. (6.5) has multivalued solution indicating bistability. The coordinates were chosen to be the tunable variables, i.e., the frequency and amplitude of the driving, which can serve as control parameters of the phase transition. Only the $\Delta < 0$ half-plane is shown, the positive-detuning part being the same mirrored to the $\Delta = 0$ axis.

The neoclassical result suggests an appropriate thermodynamic limit à la Carmichael (2015) and a corresponding scaling of system parameters. On fixing the timescale to the microscopic one, $\kappa = 1$, we see that a characteristic photon number is expected to scale as $\sim g^2$. Hence, the thermodynamic (infinite-system) limit is the strong coupling limit $g \to \infty$ (in contrast to previously-reported thermodynamic or classical limiting cases of quantum phase transitions in the Jaynes-Cummings and Rabi models (Hwang et al., 2015; Hwang & Plenio, 2016; Larson & Irish, 2017; Hwang et al., 2018)). Simultaneously, the drive amplitude must also be scaled up. The first guess, cf. the prefactor on the right hand side of Eq. (6.5), would be $\eta \to \infty$ such that η/g is kept invariant. This is why the quantity η/g is used for the drive amplitude on the vertical axis of the phase diagram. With this scaling, the lower boundary of the bistability phase becomes indeed independent of g: the three curves coincide perfectly. On the other hand, the upper boundaries reveal a further dependence on g. That is, the solution sets of the neoclassical equations are

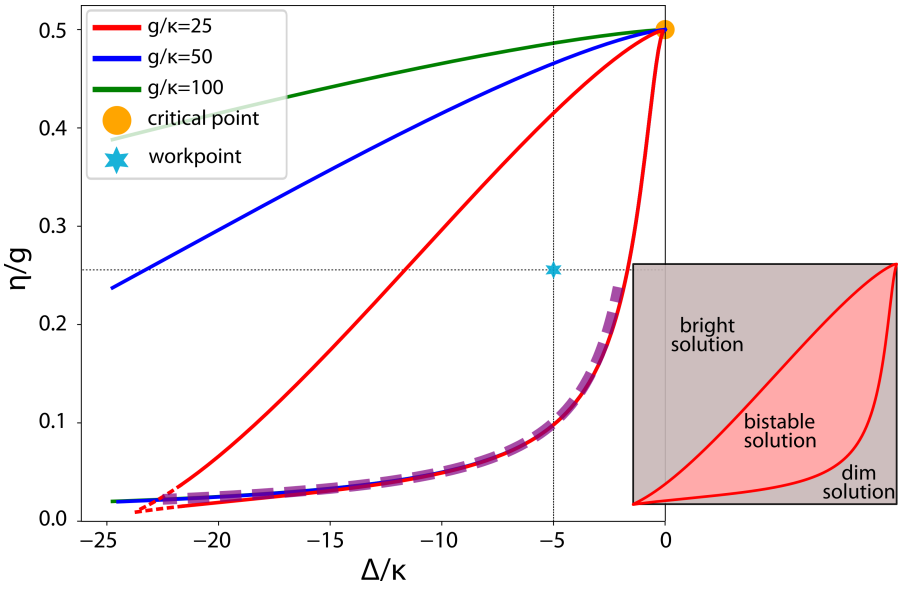

Figure 6.2: Phase diagram of the neoclassical theory based on a numerical solution of the transcendental Eq. (6.5) for three different values of the coupling constant g. The low boundaries closely overlap, the upper boundaries differ for the three values of g. As the numerics becomes very unstable when approaching the far-off-resonance closing point of the bistability region, the closing of the red curves on the left is inferred by extrapolation (dashed segments). The common closing point on the right for all g values is the spontaneous dressed-state polarization critical point. The cyan star denotes the workpoint chosen in this paper: it is at this detuning and around this drive strength that we are going to study the bistable solution for several g values. Magenta dashed line: the inference (6.7) for the lower limit of the bistability region.

not invariant under the transformation of g, $\eta \to \infty$ with $\eta/g = \text{const}$. Later, in Section 6.4 we will identify the non-trivial scaling of η which leads to a properly defined thermodynamic limit of the system. Nevertheless, since the lower boundary of the neoclassical bistability domain is invariant, and also the upper boundary does not vary strongly at $\Delta = -5\kappa$ for the g values shown in Fig. 6.2 and used in this paper, in the plots the drive strength η is given in units of g.

Finally, let us make two side remarks. Firstly, Gutiérrez-Jáuregui & Carmichael (2018) pointed out that another possible scaling deducible from the mean-field steady state equations is keeping $\Delta/g = \text{const}$. This would make that in the phase diagram Fig. 6.2, the upper limiting curves of the bistability domain would coincide, but the lower ones would differ for different g values, cf. Fig. 6.3. So, at this point the two scalings $\Delta/\kappa = \text{const}$. and $\Delta/g = \text{const}$. appear as equivalent alternatives. It can be argued that our choice is more natural in the sense that the detuning from a (bare) resonance is measured against the width of that resonance.

Secondly, there is a critical point at $\eta/g = 1/2$ on resonance $\Delta = 0$, where the lower and upper limits of the bistability region converge. It separates the solution $\alpha = 0$ with population inversion increasing from $-1/2$ to 0 from the one with $\sigma_z = 0$ and increasing α as the drive strength η is increased further. This result is in accordance with that of the full quantum treatment which can be pursued to an analytical solution in the resonant case (Alsing et al., 1992). It shows that the quasienergies coalesce in this critical point. This

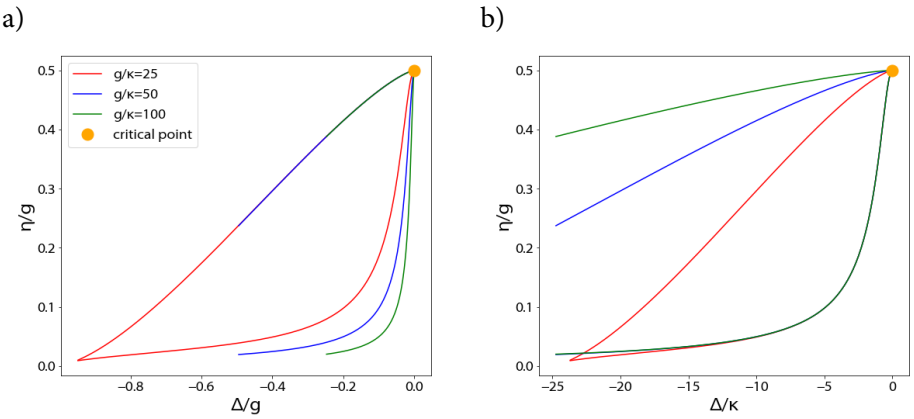

Figure 6.3: Comparison of phase diagrams with two different scalings of the detuning: (a) Δ scaled with g, and (b) with κ

critical behaviour was identified as the spontaneous dressed-state polarization by Alsing & Carmichael (1991).

6.2.4 *Bistability in the quantum solution and intuitive explanations*

Numerical simulations of the full quantum problem defined by Eq. (6.2) confirm qualitatively the phase diagram based on the neoclassical equations. The existence of a bistability regime close to resonance $|\Delta| \ll g$ has been confirmed by Dombi et al. (2015) and Carmichael (2015). The stationary density-operator solution of the master equation is then a statistical mixture of two states: the 'dim' state where the field is close to the vacuum and the atom is in the ground state, and a 'bright' state which consists of a highly excited coherent state of the field (and a completely saturated atom). On increasing the drive strength η at a fixed detuning, the relative weight of the two components is continuously varied such that the probability of the bright component goes from 0 to 1 in a finite range of η (Fink et al., 2017). The steady state is hence a continuous function of the parameters, however, there is a 'rift' between the two components of the mixture: these are classically discernible states.

The stability of the bright component for high-enough drive strength can be understood intuitively as a balance of coherent drive and spontaneous decay in a harmonic oscillator. The frequency separating adjacent dressed states $|n+1,-\rangle$ and $|n,-\rangle$ is $\omega_M - g(\sqrt{n+1} - \sqrt{n}) \approx \omega_M - g/(2\sqrt{n})$. In the limit of large photon numbers $n \to N$, this tends to a harmonic ladder in which the coherent drive η and the decay κ compete to create a coherent state with amplitude

$$\alpha = \frac{\eta}{\kappa - i\left(\Delta + \frac{g}{2\sqrt{N}}\right)} \implies N = \frac{\eta^2}{\kappa^2 + \left(\Delta + \frac{g}{2\sqrt{N}}\right)^2}, \tag{6.6}$$

where the self-consistent equation for the photon number N was obtained by taking the absolute value squared of the amplitude α. The smallest drive strength for which this equation can be satisfied is in the case of 'resonance', i.e. when the expression in the parentheses in the denominator vanishes: $\Delta = -g/(2\sqrt{N})$. The self-consistent solution is then $N = (\eta/\kappa)^2$, from which the minimum

drive strength follows as

$$\frac{\eta_{\min}}{g} \simeq \frac{\kappa}{2|\Delta|} \,. \tag{6.7}$$

This law is drawn in the thick dashed magenta line in the phase diagram in Fig. 6.2, and coincides quite accurately with the lower border of the classical bistability domain. It is remarkable that the solution of a classical equation obeys a law extracted from intuitive consideration of quantized energy levels. On further increasing the drive strength, the photon number increases, thereby leading to some detuning $\Delta + g/(2\sqrt{N}) \neq 0$ in Eq. (6.6). However, there may still be a self-consistent solution. Because the lower part of the harmonic ladder is missing (that part of the spectrum being the anharmonic photon-blockading part), there is no deterministic evolution into such a self-consistent solution. Nevertheless, the displacement operator corresponding to coherent driving contains multi-photon excitation processes, so the excitation into the near-resonant regime with a self-consistent solution can take place in a probabilistic manner.

The upper limit of the bistability domain cannot be determined from an argument as simple as the above for the lower limit. The reason is that the more we increase the drive strength η, the more the quasi-energy levels, i.e. the true eigenvalues of the Hamiltonian (1.6), differ from the dressed levels of the $\eta = 0$ Jaynes-Cummings model, since they are getting dressed also by the coherent drive (Alsing et al., 1992). However, the analytical form of the quasi-energy levels in the finite-drive strength case is not known for $\Delta \neq 0$, only for the case of $\Delta = 0$. Nevertheless, it is clear that the appearance of an η-dependence of the energy levels makes that the η/g scaling suggested by both Eqs. (6.5) and (6.6) is disrupted for large η values.

6.3 THE TELEGRAPH SIGNAL

Not only the classical phase diagram, but even the steady-state density operator solution of the full quantum problem defined by Eq. (6.2) does not describe all the relevant aspects of our phase transition. In the following we prove by numerical simulation that the components of the mixture become robust classical attractors in the thermodynamic limit. To this end, we need to unravel the density operator into the time domain, so that we can extract the dwell timescales, we can show their divergence, and we can determine the relevant exponents. To this end, we use the quantum trajectories generated by the Monte-Carlo wavefunction method. In principle, the ensemble average of many trajectories yields a density operator evolving in time towards the steady-state one. However, in the ergodic case (which will be our assumption here), the temporal averaging of the stochastic state vectors along a single long quantum trajectory yields the same steady-state density operator. Therefore it makes sense to consider a trajectory as an actual evolution under continuous measurement with an ideal photodetector.

Obviously, due to the large difference in the photon numbers, the components of the mixture correspond to very distinct output signals. The photon number is continuously monitored via the photons outcoupled into the κ loss channel. The classical distinguishability of large photocurrent versus dark counts amounts to a projection of the quantum state into only one of the com-

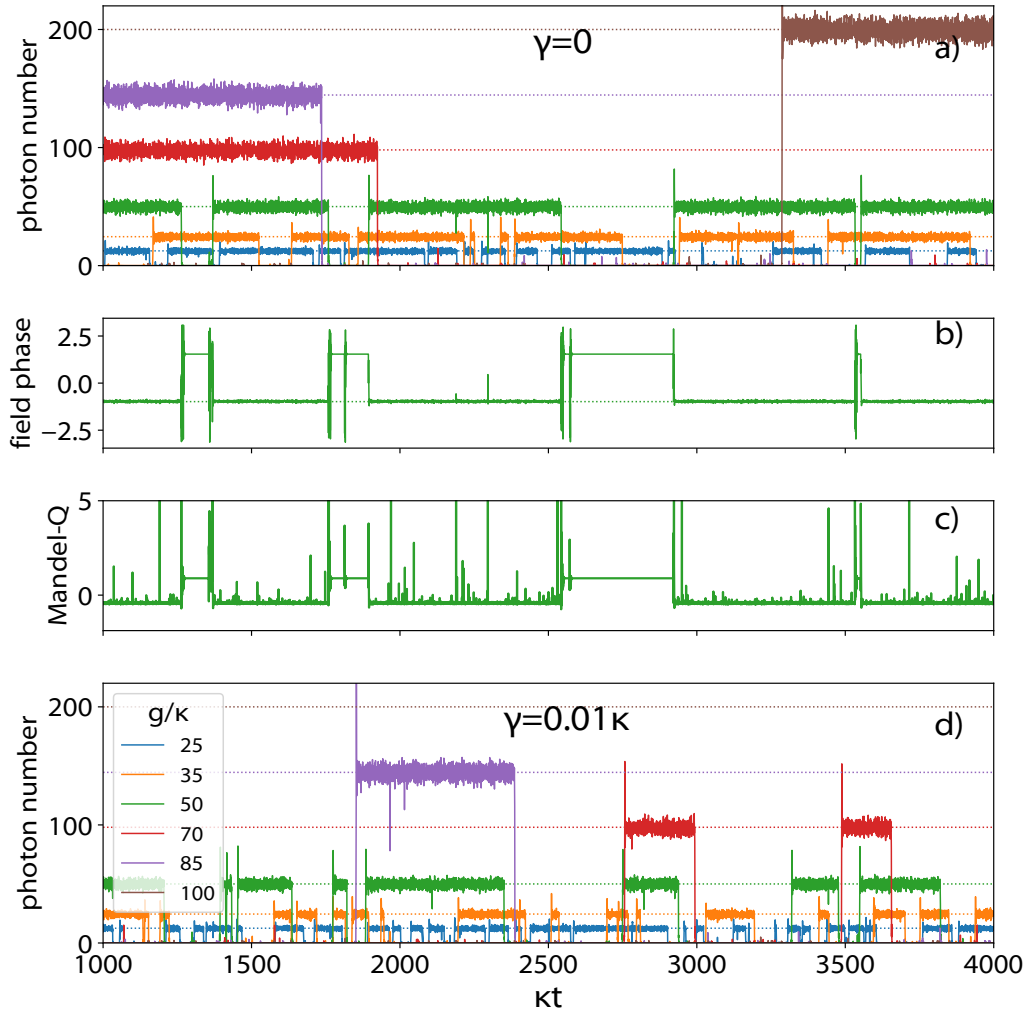

Figure 6.4: Example trajectories showing the blinking behaviour with different g values (color code is the same throughout). Parameters: $\Delta = -5\kappa$, $\eta = g/4$ (corresponding to the cyan star in Fig. 6.2). The dotted lines in panels a) and d) represent the estimate $g^2/(2\Delta^2)$ for the photon number, following from Eq. (6.6). Panel b) shows the phase of the field along the green trajectory of panel a) ($g = 50\kappa$), assuming a coherent state. The dotted green line is the field phase expected from Eq. (6.6), that is, the phase of the complex number $\left(\kappa - i\left[\Delta + g/(2\sqrt{N})\right]\right)^{-1}$, substituting the bright-state photon number $N = 50$ that can be read from panel a). We see that the coincidence with the simulated field phase in the ON periods is very good. Panel c) displays the Mandel-Q parameter along the same trajectory, exhibiting a larger nonclassicality for the OFF periods than the ON periods, which we will discuss in Section 6.5. Throughout this chapter, the numerics was performed with C++QED: a C++/Python framework for simulating open quantum dynamics, cf. Part III.

ON value	a	
blink-on rate	μ	$=$ (dwell time in OFF period $)^{-1}$
blink-off rate	λ	$=$ (dwell time in ON period $)^{-1}$
filling factor	$\mathcal{F} = \frac{\mu}{\mu+\lambda}$	
expectation value	$\langle X\rangle = \frac{a\mu}{\mu+\lambda}$	
variance	$\mathrm{var}\{X\} = \frac{a^2\mu\lambda}{(\mu+\lambda)^2}$	
temporal correlation	$\langle X(t), X(t')\rangle = e^{-(\mu+\lambda)\lvert t-t'\rvert}\,\mathrm{var}\{X\}$	
characteristic timescale	$\tau = (\mu+\lambda)^{-1}$	

Table 6.1: Characteristics of the telegraph process in the random variable X in the special case when the OFF value is 0.

ponents at a time. This is shown in Fig. 6.4, where the instantaneous photon number along quantum trajectories is plotted for various coupling strengths g. The bright and dark periods alternate sharply in the form of a telegraph signal. Detailed analysis of the statistical data shows that the presented signals are indeed very accurately (even to the limit of numerical accuracy) described by a telegraph process.[5] This means that such trajectories have essentially three parameters: the amplitude of the bright period and the rates of blink-on and -off, μ and λ, respectively, since a telegraph process is nothing else than the composition of two temporal Poisson processes with exponential waiting-time distribution. Hence, the waiting time for a blink-on (the inverse of the blink-on rate μ) equals the dwell time in the dim period, the same being true for blink-off and the bright period. The characteristics of the telegraph process are summarized in Table 6.1.

5. In particular, what we do is to define a binary signal from the somewhat noisy trajectories whose model is depicted in Fig. 6.4, simply by assigning the value 1 to the time instants where the photon number is higher than half of the temporal average and 0 to the others. On this binary signal $X(t)$ we verify the fulfillment of the relation $\mathrm{var}\{X\} = \langle X\rangle(1-\langle X\rangle)$, that is characteristic of the telegraph process (cf. Table 6.1). We find agreement up to 10^{-14} precision.

The trajectories for different coupling constants g in Fig. 6.4 are generated using the drive strength $\eta/g = 1/4$ kept invariant, while fixing the detuning $\Delta = -5\kappa$. Hence all these curves correspond to the single point denoted with the cyan star in the phase diagram Fig. 6.2 within the bistability domain. The photon number increases with increasing g. The numerics shows that the bright state has the photon number $N \approx g^2/(2\Delta^2)$, the corresponding dotted straight lines fitting nicely on the noisy numerical record. This N is twice the photon number at the lower boundary of the bistability range of the neoclassical theory. Interestingly, this analytical estimate satisfies the simple classical relation (6.6) with high accuracy, which suggests that the intuitive picture of near-resonantly driving an equidistant ladder holds even at such drive strength far above the lower boundary of the bistability domain. The same is suggested by Fig. 6.4(b), where the field phase is plotted together with an estimate from the same Eq. (6.6), once more to yield excellent agreement (cf. the figure caption for details).

Since $N_{\mathrm{scale}} \propto g^2$, the photon number measured in units of N_{scale} proves to be invariant for the different curves. On the other hand, the dwell times in the attractor states increase significantly with increasing g. This reveals that there is a thermodynamic limit in which the phases become robust, the telegraph signal disappears, to be replaced by a hysteresis-like behaviour in a genuine first-order phase transition.

Figure 6.4(d) shows that the addition of a small amount of atomic decay ($\gamma = 0.01\kappa$) does not lead to a qualitative change of the conclusions above. The photon number of the ON period remains the same as with $\gamma = 0$, however, atomic decay does noticeably decrease the dwell time in this attractor.

6.4 FILLING FACTOR AND THE SCALING OF THE DRIVE STRENGTH

In the bimodal steady-state density operator, the weights of the components vary through the bistability domain, in particular, on increasing the drive strength the 'dim' state component vanishes gradually in favour of the 'bright' state. In the time domain, the telegraph signal manifests this form of transition through the variation of the filling factor which is theoretically $\mathcal{F} = \frac{\mu}{\mu+\lambda}$. The trajectories in Fig. 6.4 show that the filling factor varies for the telegraph signals with different g. This is confirmed in Fig. 6.5. Panel (a) shows the monotonous increase of $\mathcal{F}$ as a function of η/g for a set of g values. The curves are shifted

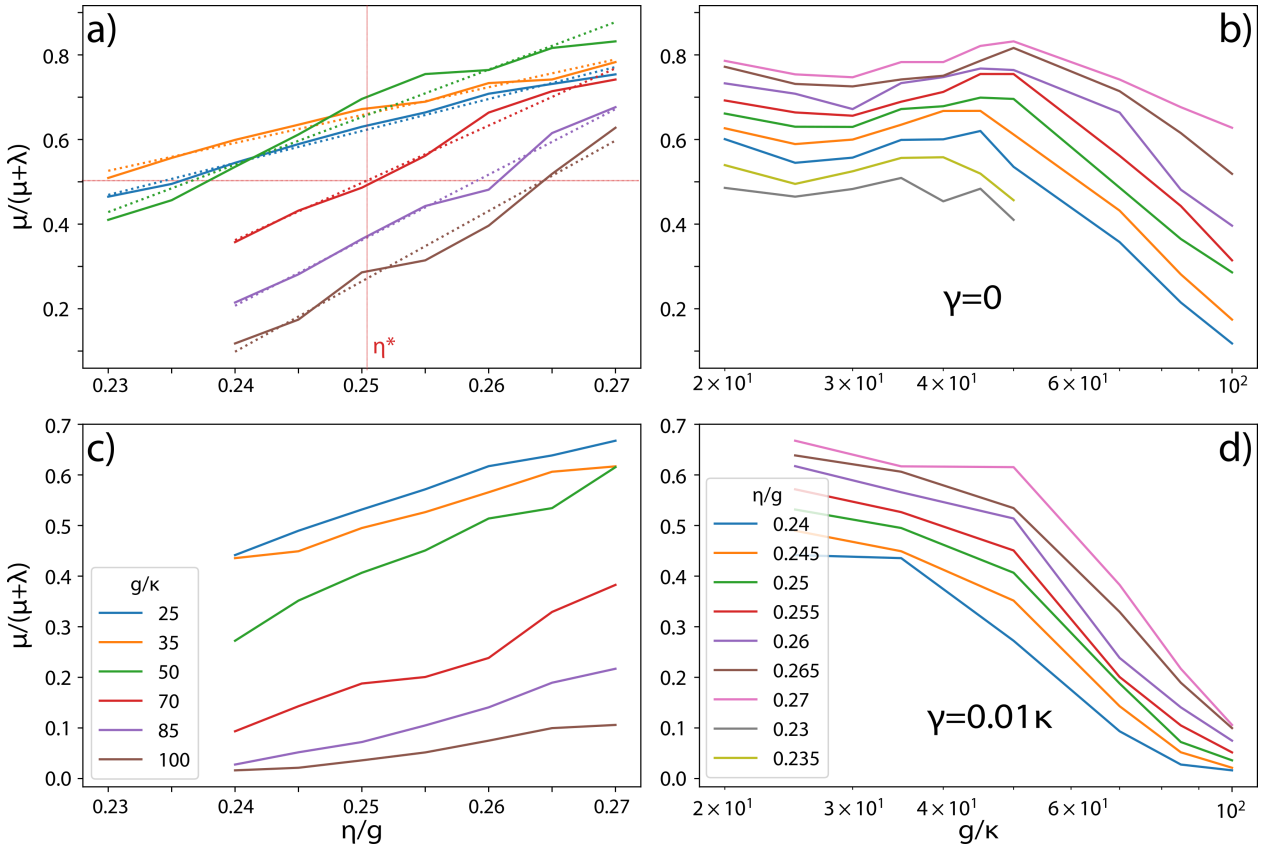

Figure 6.5: Filling factor of the bright periods (cf. Table 6.1) as a function of η/g and g/κ without (panels a and b) and with a small (panels c and d) atomic decay $\gamma = 0.01\kappa$. Color code is the same in the upper and lower row. Panel a): the dotted lines indicate linear fits in order to determine η^*, the drive strength leading to half filling. The value of η^* is indicated for the coupling strength $g = 70\kappa$.

with respect to each other. This dependence is made explicit in panel (b), where g is varied while η/g is kept at various fixed values. The filling factor is constant in the range of smaller g values, whereas $\mathcal{F}$ decreases in the range of larger coupling strengths. For example, the green line represents a closely constant filling factor around $2/3$ up to $g \approx 50\kappa$, but if g is increased further, the filling factor drops.[6]

It follows then that the scaling of the drive strength η such that η/g is kept invariant does not preserve the self-similarity of the telegraph signal. Scaling to the thermodynamic limit means that the system keeps a self-similar behaviour, only scaled up in time and brightness of the ON state. Since the latter two scale with the single parameter g, there is the parameter η left at our disposal to ensure self-similarity during the upscale, which, in the case of such a simple process as the telegraph one, cannot mean anything else than keeping the filling factor constant. As the most obvious choice, we pick the case when the filling factor is 0.5.

Since the concept of self-similarity is a difficult one in the present context, let us employ a more pictorial explanation. Upscaling means that we are looking on the system's time evolution through a telescope that via the turn of a *single* knob (here, increasing g, the single scaling parameter), increases its angle of

6. The reason why the curves span different ranges in panels (a) and (b) is that we needed to use different ranges of η for different g values in order to find the value of η^*.

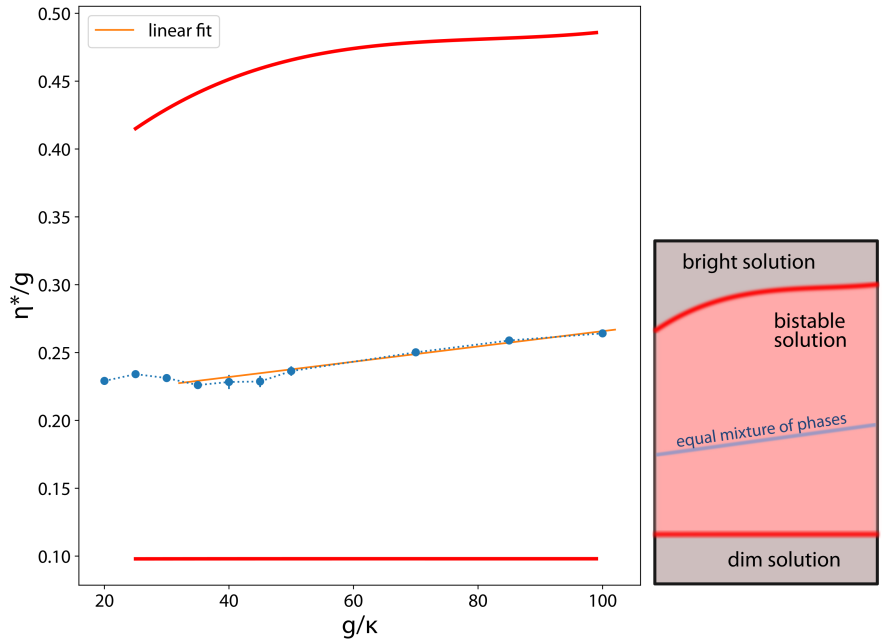

Figure 6.6: The drive strength η^* leading to half filling of the telegraph signal as a function of g, i.e., the equal mixture of the two phases in the steady-state density matrix. Solid red curves represent the phase boundaries of the bistability domain from the classical theory.

view both in time and photon number,[7] but keeps projecting the image on the same ocular area. (Hence, it has an increasingly coarse resolution both in time and photon number.) This is like the "zoom" functionality on modern camera objectives. It is very important that we are aiming at a single-parameter scaling theory, that is, we have to find a rule for how to change the other parameters of the system (here, only η) as a function of the scaling parameter g during the upscale, i.e. how to "scale η with g". The rule that defines such a one-dimensional manifold in the parameter space as the upscale orbit is: *self-similarity*. Self-similarity means that we require the image of the system's time evolution on the ocular of the telescope to remain the same during this procedure. In the case of such a simple process as the telegraph signal, the filling factor is the single parameter that determines the image in such a telescope. Hence, the preservation of self-similarity means that we are keeping the filling factor constant (namely 0.5) during the upscaling.

Therefore, in order to determine the correct scaling of η in the thermodynamic limit, we have to find the drive strength for each g value (denoted $\eta^*(g)$ in the following) that leads to half filling. Looking at Fig. 6.5(a), we observe that an approximate linear interpolation (linear fit) captures appropriately the behaviour of the $\mathcal{F}(\eta)$ curves for the different g values in the range of interest. Hence, we use such an interpolation to determine $\eta^*(g)$. As an example, in the plot we show for the red curve ($g = 70\kappa$) the corresponding η^*. In Fig. 6.6, we plot the function $\eta^*(g)$, embedded in the bistability domain that we have calculated similarly to Fig. 6.2. With this numerical result *we defined the appropriate finite size scaling*. As it turns out, a linear fit reproduces quite exactly the behaviour of η^* for $g \gtrsim 50\kappa$, which indicates that the correct scaling of the drive strength in the thermodynamic limit is $\eta \sim g^2$.[8]

7. The increase in these two dimensions is not necessarily at the same rate, e.g. here the the photon number increases under the fairly obvious rule g^2, while the timescale as g^ν, where ν is one of the finite-size scaling exponents that we want to find.

8. It is possible that if we had included Δ in the scaling as suggested by Gutiérrez-Jáuregui & Carmichael (2018) (Δ/g = const.), then the η/g = const. scaling would have been sufficient to preserve self-similarity. However, to answer this question rigorously, we would need to repeat the whole numerical work for that scaling also.

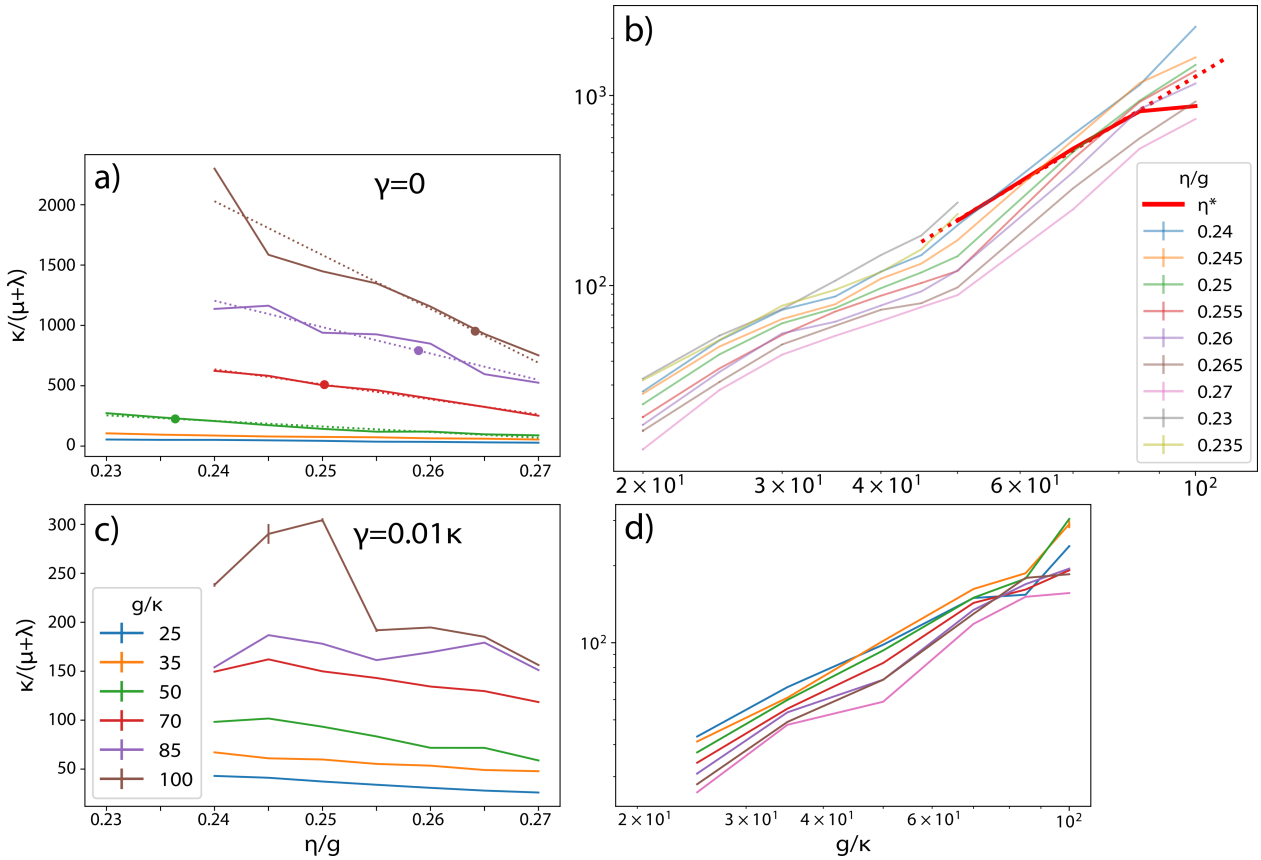

Figure 6.7: The characteristic timescale of the bistable blinking process given by the inverse of $\mu + \lambda$. The points in panel a) correspond to the values of η^* for the different g values where half-filling of the telegraph signal is achieved. In panel b), the solid red curve designates the timescale at η^* as a function of g, that is, the timescale in the correct finite-size scaling when the telegraph process is kept at half filling during the passage to the thermodynamic limit. The dotted line shows a log-log linear fit on the values leaving out $g = 100\kappa$. The exponent resulting from the fit is roughly 2.2. Panels c) and d): timescale with finite atomic decay $\gamma = 0.01\kappa$.

6.5 DWELL TIMES

6.5.1 *Characteristic timescale of the telegraph signal*

Figure 6.7 presents the characteristic timescale of the bistable blinking process. This is defined as the inverse of the sum of blinking rates $\mu+\lambda$, which is extracted from an exponential fit on the numerically calculated temporal self-correlation of the signal (cf. Table 6.1). We use the unit of κ so that the large difference is manifested in the figure: the characteristic times are orders of magnitude above the microscopic timescale κ^{-1}. On increasing the drive strength η in the presented range, the average dwell time decreases because of the increase of the rate μ of blink-on, in conjunction with the increase of the filling factor. Points represent the values of η^* where the telegraph signal has half-filling.

From the point of view of the thermodynamic limit, the dependence of the characteristic timescale on g is the most relevant (Fig. 6.7(b)). We show the increasing timescale over two orders of magnitude of the coupling constant g for various values of η/g. This g range is given by computational limitations, nevertheless, it is enough to demonstrate *the power-law scaling* of the increase

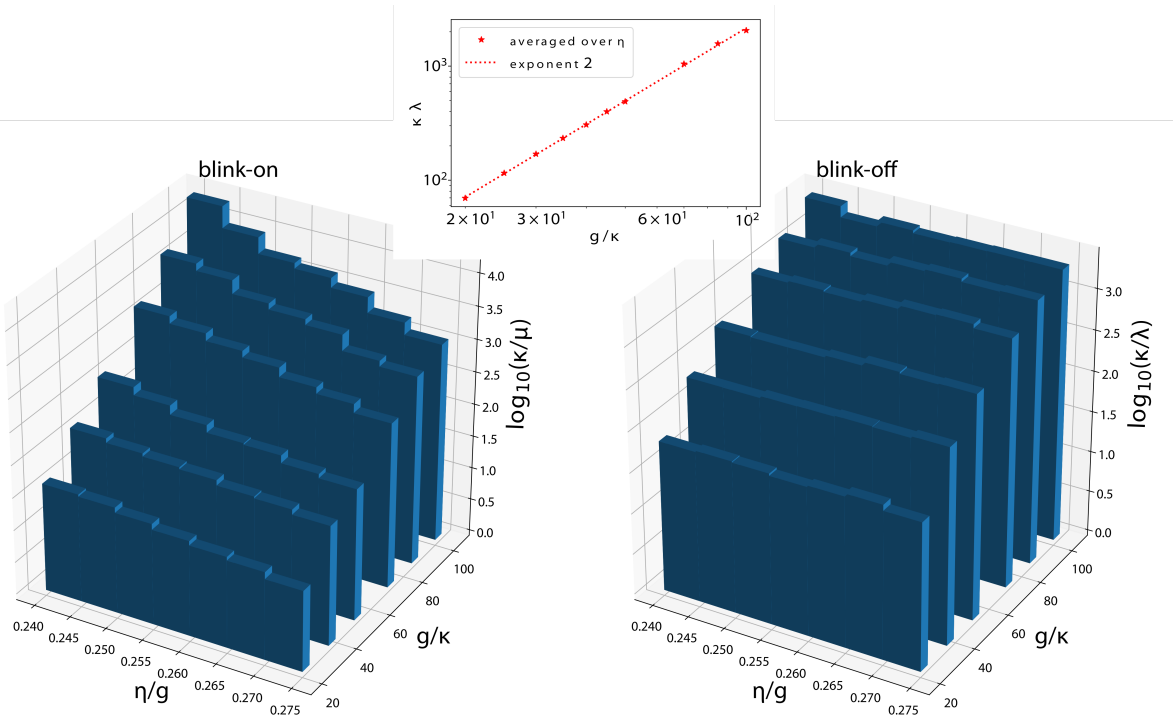

Figure 6.8: Waiting time for blink-on (μ^{-1}) and blink-off (λ^{-1}). Inset: λ values averaged over η as a function of g, with an exponential fit with exponent 2.

of the timescale and to determine the exponent. To obey the correct self-similar scaling detailed in Section 6.4, we have to find the timescale for the drive strength $\eta^*(g)$ for the different g values. To this end, we again use a linear fit on the curves of η-dependence, which captures the behavior quite correctly (cf. dotted lines in the panel (a), with the η^* values depicted with big dots of the corresponding colour). The timescale change under finite-size scaling $\tau(g, \eta^*(g))$ is shown in the thick, solid, red line in Fig. 6.7(b). A linear fit in the log-log scale leads to the numerical estimate of 2.2 for the finite-size scaling exponent of the characteristic time. The point $g = 100\kappa$ was omitted from the fitting because the dwell times were systematically underestimated due to truncation of the trajectories for the long but finite simulation time.

Figure 6.8 is devoted to the numerical analysis of the rates of blink-on and -off, μ and λ, respectively, which sheds light on the physical processes leading to switching between the robust classical attractor states in the finite-size system. These are calculated from combining the above-discussed characteristic timescale with the filling factor. For both rates, the increase of g implies a reduction, in agreement with the expectedly growing stability of phases on approaching the thermodynamic limit.

6.5.2 *Blink-off process*

The downward process is initiated by a single photon loss (detection) event. This is because there is a chance that the state residing in the ladder $|n, -\rangle$ gets

projected into the ladder $|n,+\rangle$ under such an event (Carmichael, 2015), since

$$a\,|n,\pm\rangle = \frac{\sqrt{n}+\sqrt{n-1}}{2}\,|n-1,\pm\rangle + \frac{\sqrt{n}-\sqrt{n-1}}{2}\,|n-1,\mp\rangle \approx \sqrt{n}\,|n-1,\pm\rangle + \frac{1}{4\sqrt{n}}\,|n-1,\mp\rangle\,. \quad (6.8)$$

Once such a jump occurs, there is a downward cascade of photon escapes, because while our (red-detuned) drive was closely resonant with the high-lying part of the $|n,-\rangle$ ladder, resulting in an approximately coherent state in this part, it is off-resonant with the $|n,+\rangle$ ladder (which would be resonant with the drive blue-detuned with the same amount), so on this ladder there is no drive to compensate the photon loss. The passage downward consists of a quick cascade of many jumps amounting to an exponential decay.

Although a single ladder-switching quantum jump initiates the blink-off, the likelihood of such a rare jump vanishes completely in the $g, N \to \infty$ thermodynamic limit. The rate of ladder switching scales as κ/N,[9] and as we saw above, the bright-state photon number scales as g^2 in the thermodynamic limit. This suggests the exponent 2 for the finite-size scaling of the blink-off timescale, which is verified in the inset of Fig. 6.8 to very good accuracy. This downward jump rate λ is largely independent of η, that only slightly influences the photon number in the bright phase.

9. From Eq. (6.8), the total jump rate scales as κN, while the probability of a ladder switch to occur within a jump is $\propto 1/N^2$

6.5.3 *Blink-on process*

On the other hand, the switching from the dim to the bright phase is induced by the external driving and thus is sensitive to η, as can be seen in the left panel of Fig. 6.8. The upward process is suppressed by the off-resonance of low-lying quasi-energy levels (anharmonic part of the spectrum). Therefore, it is easy to understand that the larger the coupling g, the larger the shift of the levels from resonance and the smaller the blink-on rate. In the dim phase, the state of the bosonic mode is close to the vacuum, however, there must be a small deviation from that due to the driving. The state is a non-classical superposition with positive Mandel-Q parameter (super-Poissonian photon statistics). The Mandel-Q parameter measuring the nonclassicality of the field state reads

$$Q = \frac{\mathrm{var}(a^\dagger a) - \langle a^\dagger a\rangle}{\langle a^\dagger a\rangle}, \quad (6.9)$$

where the averaging can be performed either as a quantum average on the actual state vector of the field to reflect the nonclassicality at a given time instant, or also over time. The Q parameter is zero for a classical field state (coherent state). In Fig. 6.4(c), Q is calculated as a time-dependent quantum average, and we observe that the nonclassicality is stronger in the dim phase than in the bright one. This is consistent with our picture that the bright phase consists of an approximately coherent state on the manifold $|n,-\rangle$.

The state in the dim period has the property that the projection of the wavefunction after a photon detection increases the weight of a high-excitation component.[10] While in the dim state there is a negligible amount of excited photon component generated by the η driving, triggered by a single quantum jump (which is very rare on account of the very low dim-state photon number),

10. It is straightforward to show that for pure states of a mode, the positivity of the Mandel-Q parameter, which is what we have in the dim phase, is equivalent to the nonclassical situation that a photon escape from the mode *increases* its photon number. Assuming that the state of the mode before a quantum jump is $|\Psi\rangle$, a photon escape results in the state

$$|\Psi'\rangle = a\,|\Psi\rangle\,/\sqrt{\langle N\rangle}$$

with photon number:

$$\langle N\rangle' = \langle\Psi|\,a^\dagger a^\dagger a\,a\,|\Psi\rangle\,/\,\langle N\rangle = \langle\Psi|\left(a^\dagger a\,a^\dagger a - a^\dagger a\right)|\Psi\rangle\,/\,\langle N\rangle = \langle N^2\rangle\,/\,\langle N\rangle - 1.$$

The condition for a non-intuitive (photon-number-increasing) jump reads:

$$\langle N\rangle' > \langle N\rangle\,.$$

This inequality is *equivalent* to the inequality

$$Q = \left(\langle N^2\rangle - \langle N\rangle^2 - \langle N\rangle\right)/\langle N\rangle > 0.$$

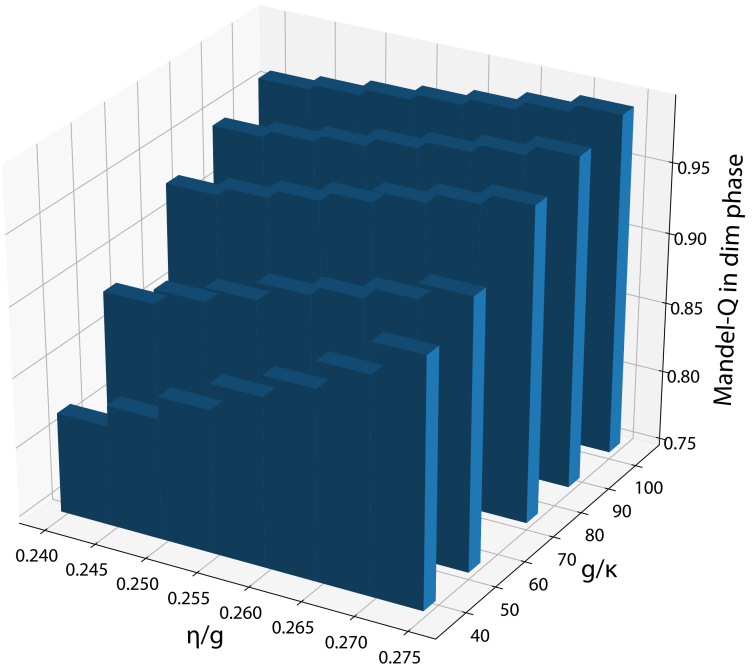

Figure 6.9: Mandel-Q parameter of the field averaged over time in the dim periods.

it can grow in an exponential runaway process for subsequent photon detections. So the blink-on also takes place in the form of a cascade of quantum jumps.

In Fig. 6.9, we plot the field Q parameter averaged over time, but only in the dim periods.[11] The overall trend is that the nonclassicality of the field in the dim phase increases both with increasing η and g, and the dependence flattens out for large g at a value close to 1. Hence, the dim phase remains nonclassical also in the thermodynamic limit.

Let us try to model the dim state of the field in the following form:

$$|\Psi\rangle = \sqrt{1-\varepsilon^2}\,|0\rangle + \varepsilon\,|\varphi\rangle\,, \tag{6.10}$$

where ε is a small number and $|\varphi\rangle$ is a state orthogonal to the vacuum state. The photon count rate $\kappa\langle a^\dagger a\rangle = \kappa\,\varepsilon^2\,N_\varphi$ can be made very small with $\varepsilon \to 0$, where $N_\varphi = \langle\varphi|a^\dagger a|\varphi\rangle$ is the mean photon number associated with the component $|\varphi\rangle$ superposed on the vacuum. At the same time, the Mandel-Q parameter of the state (6.10) is found to be independent of ε in the limit $\varepsilon \ll 1$: one finds $Q_\Psi = Q_\varphi + N_\varphi$. That is, it depends only on the properties of the state $|\varphi\rangle$. Note that (i) $N_\varphi > 1$ because the vacuum component is missing from photon number expansion of $|\varphi\rangle$, and (ii) the Mandel-Q parameter is always limited below 1 in Fig. 6.9. These two observations imply that the state $|\varphi\rangle$ is a nonclassical state with negative Mandel-Q factor.

11. Note that a time average of the Mandel-Q calculated for the instantaneous pure states of trajectories does not reproduce the Q of the time-averaged density operator, since the dependence of Q on the density operator is not linear. The aim of our usage is to substantiate that the quantum state of the mode in the dim periods is of the form (6.10), where *a photon escape increases the photon number of the mode.*

6.5.4 *Cascades of quantum jumps switch between attractors*

A study of the photon-number evolution along a single trajectory together with sufficiently resolved quantum jump events confirms the above picture both for the blink-on and -off events, cf. Fig. 6.10. In panel (a) we see that a

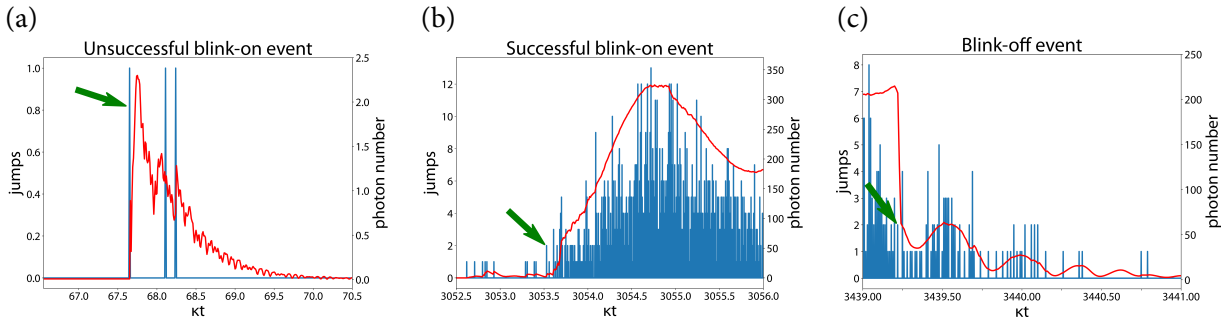

Figure 6.10: Photon-escape quantum jumps (blue) and the evolution of instantaneous photon-number expectation values (red) during blink-on and -off events. Green arrows indicate the photon escapes that trigger the switching events. The time-resolved depictions of quantum jumps are histograms with bin sizes $0.01/\kappa$ for (a) and $0.001/\kappa$ for (b,c).

single photon escape (marked with the green arrow) triggers a shootup of the photon number from the dim state, in accordance with the super-Poissonian photon statistics of the dim state. However, in this event the surge is not strong enough to break the blockade. Panel (b) depicts a successful breakthrough event where we also see that the buildup of the full bright-state photon number incurs a *probabilistic cascade of quantum jump events*. In panel (c) also a single quantum jump triggers the collapse of the bright state (green arrow at the sudden drop of photon number), followed by a normal ringdown of the photon number with rate κ, involving several further photon escapes. This proves our above claim that the telegraph signal observed here differs essentially from the electron-shelving scheme: though there is a trigger single-photon escape (quantum jump), the switch between the dim and bright phases is driven by a cascade of quantum jumps.

The physics of the entire cycle of the bistable switching in the time domain is summarized on Fig. 6.11.

6.6 THE ROLE OF ATOMIC DECAY

The condition $\gamma = 0$ is essential in the neoclassical theory, since the derivation of the transcendental Eq. (6.5) relies heavily on the fact that the length of atomic pseudo-spin is conserved, $\langle\sigma_x\rangle^2 + \langle\sigma_y\rangle^2 + \langle\sigma_z\rangle^2 = 3/4$. Allowing $\gamma \neq 0$ hence leads to qualitatively different behaviour since this conservation law is broken.

Yet, for very small γ values, the behavior of the full quantum model does not seem to be qualitatively affected: as we have shown in the course of this chapter in passing, the photon-blockade-breakdown effect can be observed in the case of a finite but small γ.

The effect of an atomic decay in the bright state, i.e., on a high-lying coherent state can be assessed similarly to the above:

$$\sigma\,|n,\pm\rangle = \frac{1}{\sqrt{2}}\left(|n-1,\pm\rangle + |n-1,\mp\rangle\right). \tag{6.11}$$

This means that in the event of an atomic decay, there is a $1/2$ probability of a ladder switch. Hence, a γ on the order of κ would wipe out the bistability, since a blink-on would immediately be followed by a collapse of the bright state. The bistability manifests itself most clearly when $\gamma = 0$, the case that we most concentrated on.

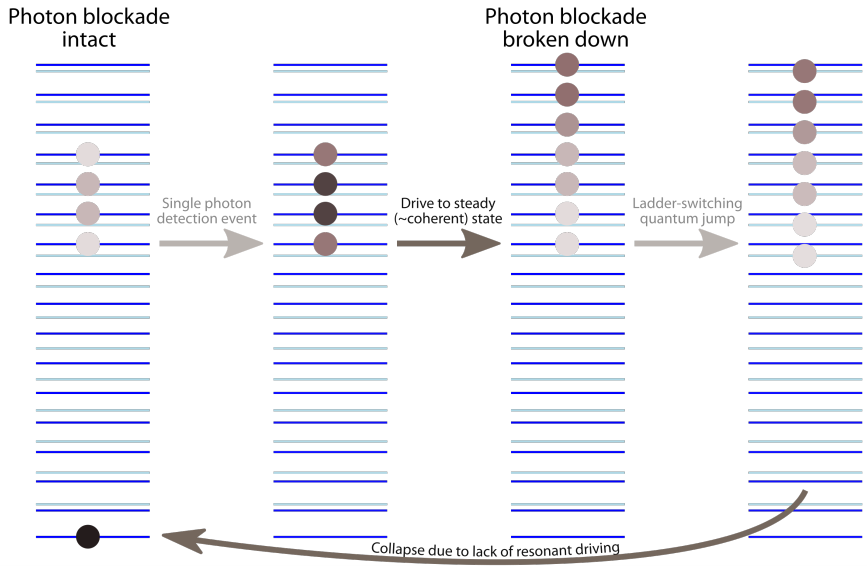

Figure 6.11: The cycle of the bistable switching from left to right: 1) The dim state with most of the population in state $|0\rangle$, and some tunnelled over the nonlinearity barrier to higher parts of the ladder to create the superposition state (6.10). 2) A single (very rare) photon-escape event erases the $|0\rangle$ component of the dim state to result in a state situated in the closely-harmonic part of the ladder. 3) The pump resonant with the '+' manifold creates a closely coherent state. 4) A rare ladder-switching quantum jump event (6.8) transfers the state to the off-resonant '-' manifold, whence it decays due to the lack of resonant driving to the dim state.

If $\gamma \ll \kappa$, which case we exposed in passing in Figs. 6.4, 6.5 and 6.7, the atomic decay emerges as a competing timescale for high-enough bright-state photon numbers, resulting overall in smaller characteristic times and filling factors. With respect to the phase transition, the system is relevant only as long as the microscopic timescale of spontaneous emission is longer and thus is dominated by the shorter macroscopic timescale τ of the phase stability.

EXPERIMENTAL REALIZATIONS

7

7.1 SYNOPSIS

In order to obtain well-resolved attractors of the switching behavior in the time domain, we need a high degree of anharmonicity in the lower part of the Jaynes-Cummings ladder, that is, very strong coupling between the mode and the two-level system. Whereas the necessary coupling strength doesn't seem achievable with (a single or a few) natural atoms in optical resonators, it has become feasible with superconducting quantum electronic circuits, that is, in the field of circuit quantum electrodynamics (CCQED), which offers large dipole coupling strengths (Fink et al., 2009) and long coherence times for multiple superconducting artificial atoms embedded in high-quality bulk or on-chip microwave cavities (Blais et al., 2021).

The realization of the photon-blockade-breakdown phase transition on this platform is the theme of the present chapter. The first experimental realization (Section 7.2) took place in the Wallraff group (Quantum Device Lab, ETH Zürich) in 2015–2016, whereas the experimental modelling of the finite-size scaling to the thermodynamic limit (Section 7.3) in the Fink group (Quantum Integrated Devices, IST Autria) in 2019-2021.

7.2 THE FIRST EXPERIMENTAL REALIZATION OF THE PHOTON-BLOCKADE BREAKDOWN

One platform that has become widespread in realizing finite-level systems (most notably, qubits in superconducting quantum computers) is the capacitively shunted superconducting charge qubit, a.k.a. *transmon* qubit (Koch et al., 2007; Paik et al., 2011). The experimental device and setup used for the results of this Section is similar to the one in Mlynek et al. (2012) and consists of three frequency-tunable transmons positioned at the anti-nodes of the first harmonic voltage standing wave resonance of a coplanar superconducting resonator at frequency $\omega_M/(2\pi) = 7.024\,\mathrm{GHz}$, see Fig. 7.1(a).

7.2.1 Description of the transmon-resonator system

The transmon is characterized, on the plus side, by a flat charge dispersion, but, on the minus side, also by a limited absolute anharmonicity of

$$\Delta_{an} \equiv \omega_{fe} - \omega_{eg} \simeq -E_C/\hbar \tag{7.1}$$

Here, $|g\rangle$, $|e\rangle$ and $|f\rangle$ are the first three levels of the artificial atom, see Fig. 7.1(b) which all take important parts in the dynamics of the presented experiments.

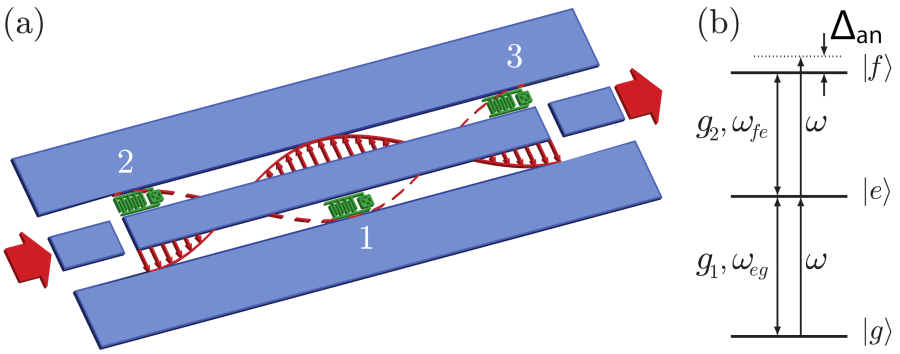

Figure 7.1: (a) Scheme of the driven coplanar waveguide resonator (blue) coupled to up to 3 transmon artificial atoms (green). An external drive (red) is applied via the input capacitor, and the coherent transmission is detected via the output capacitor. (b) Level scheme of one artificial atom indicating the parameters of Hamiltonian (7.9).

$E_C/h = (459, 359, 358)$ MHz are the charging energies and

$$g_1/(2\pi) = (-52.7, 55.4, 55.8)\,\text{MHz} \tag{7.2}$$

the single-photon $|g\rangle \to |e\rangle$ transition to resonator coupling strengths of the atoms 1, 2 and 3. Similar to a harmonic oscillator, the coupling strength of the second excited level can be approximated (Koch et al., 2007) as $g_2 \simeq \sqrt{2}g_1$. Using externally applied and locally concentrated magnetic fields one can control the flux Φ through the individual transmon SQUID loops and change their Josephson energy $E_J(\Phi)$. This allows to independently control the transmons' transition energies $\hbar\omega_{eg} \simeq \sqrt{8E_C E_J(\Phi)} - E_C$, and in particular to tune them in and out of resonance with the microwave resonator. For the most part of this Section we study the situation where two of the three artificial atoms are far detuned ($\omega_{eg} \ll \omega_M$) and thus effectively not interacting with the microwave resonator.

The Hamiltonian and Liouvillian of the system are discussed in detail in Section 7.A. In the present Section, we consider the resonant case, that is, when both the mode and the drive have the same frequency as the $|g\rangle \to |e\rangle$ transition, as displayed in Fig. 7.1(b). The resonator is characterized by a FWHM linewidth of $\kappa/\pi = 0.47$ MHz. The resonator decay is the main decay channel of the system, since the estimated transmon dephasing and depolarization rates satisfy

$$\kappa \gg \gamma_\phi \gg \gamma_1, \tag{7.3}$$

the second inequality being a general characteristic of the transmon. Since g_1 and g_2 are much larger than the decay rates, we expect a well-resolved spectrum of the interacting system. Without the third transmon level $|f\rangle$ (setting $g_2 = 0$ formally), we would get back to the situation described in Chapter 6, which favors the photon-blockade dim state up to large drive strengths.

7.2.2 *The case of a weakly coupled third level*

Assume now that the $|e\rangle \to |f\rangle$ transition is only very weakly coupled to the resonator, that is $0 \neq g_2 \ll g_1$. The Jaynes-Cummings spectrum for the two-level system $|g\rangle$ and $|e\rangle$ is then only slightly perturbed and the dressed states

$|\pm, n\rangle$ can be easily identified in the full spectrum, cf. Fig. 7.2(a). The ground state is the $|g, 0\rangle$ state and the first excited state manifold is $|\pm, 1\rangle$ exhibiting the vacuum Rabi splitting $2g_1$. Starting from the second excited manifold, there is a third level in each manifold in which the dominant component is the $|f\rangle$ state due to the small coupling $g_2 \ll g_1$. Therefore, this additional manifold $|f, n\rangle$ forms a closely equidistant ladder resonant with the photon frequency ω, which is capable of eliminating the photon-blockade effect via the following mechanism.

The off-resonant states $|\pm, 2\rangle$ get weakly populated by two-photon transitions, and a small fraction of this anyway small population leaks into this harmonic part of the spectrum, which is then resonantly driven within the manifold $|f, n\rangle$. This component of the wavefunction is thus coherently displaced in the photon mode on the timescale of κ^{-1}. The displacement is counteracted by resonator loss and leads to a steady state, which is a coherent state with an amplitude η/κ and phase locked to the phase of the driving field. Just like in optical pumping, the total state of the system is gradually pumped into this *trapping state*. The bottleneck formed by the initial two-photon transition and the weak $|\pm, 2\rangle \to |f, 0\rangle$ coupling only increases the time it takes for the system to be pumped into this trapping state. The three-level atom in a resonator with the third level weakly coupled to the other two leads thus to a steady-state bright transmission identical to that of a resonantly driven empty mode. Paradoxically, an infinitesimally coupled $|f\rangle$ state destroys the photon-blockade effect – but leads to infinite relaxation time.

7.2.3 *Increasing the coupling of the third level*

When the coupling g_2 is increased to $g_1 \lesssim g_2$ the atomic state $|f\rangle$ hydridizes significantly with the other states $|g\rangle$, $|e\rangle$. The two atomic transitions coupled to the mode form a spectrum which can be sufficiently anharmonic in the low-excitation part, as shown in Fig. 7.2(b), so that the system is blocked into the dim state up to high driving strengths at resonant driving $\Delta = 0$.

Figure 7.3(a) presents a histogram of the calculated transmitted field intensity as a function of g_2 in the range between the two limiting cases, $g_2 = 0$ and $g_1 \lesssim g_2$. As expected, small g_2 gives rise to a full transmission of the resonant driving power, the photon number fluctuates around the mean $\langle a^\dagger a \rangle \approx (\eta/\kappa)^2 = 700$. Larger fluctuations and the residual population in the low photon states, close to the origin $g_2 \approx 0$ of the plot, is merely an effect of the finite simulation time. On the other hand, it is also confirmed that the three-level atom with $g_2 > g_1$ switches off the transmission, i.e., it restores the photon blockade. The histogram is prepared from the ensemble of intensity values recorded at many randomly chosen instants while the system is in steady state. Just like in Chapter 6, the numerical simulations were performed using the C++QED framework, cf. Part III. The photon-mode basis was truncated at the Fock state $n = 3600$ and it took several weeks to generate a histogram at a single value of g_2/g_1 by sampling a 0.5 ms long trajectory at every µs.

The important feature of the histogram in Fig. 7.3(a) is the transition domain manifested by a bimodal distribution of intensities. Experimentally we are exactly in the center of this transition regime with $g_2/g_1 \simeq \sqrt{2}$.

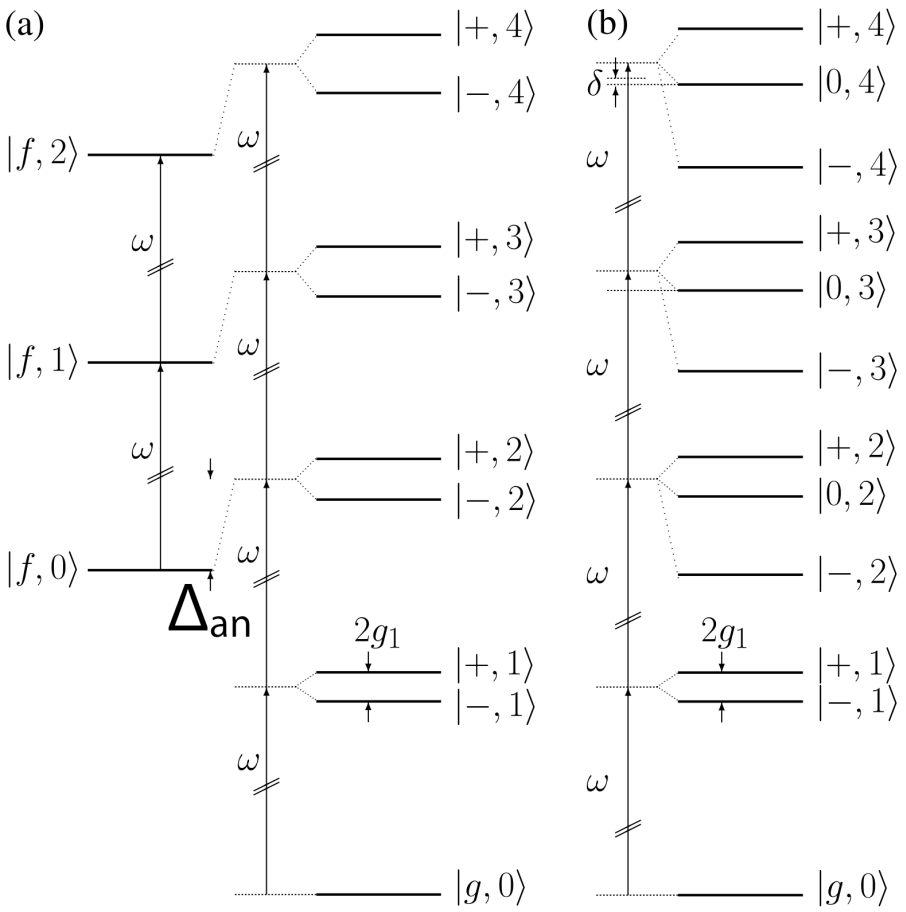

Figure 7.2: (a) The spectrum of the coupled atom-resonator system with the third atomic state $|f\rangle$ only weakly coupled to the middle one $|e\rangle$, that is, $g_2 \ll g_1$. In (a) the $|\pm, n\rangle$ denote the usual two-level-atom Jaynes-Cummings model dressed states combining $|g, n+1\rangle$ and $|e, n\rangle$. For the definition of Δ_{an}, cf. Eq. (7.1). (b) The spectrum of the coupled atom-resonator system with the experimental parameters $g_2 \simeq \sqrt{2}g_1$. In (b) the multiplets $|\{-, 0, +\}, n\rangle$ correspond to the eigenstates of the Hamiltonian (7.8) in the n-excitation manifold. δ represents the mismatch of ω with respect to the transition frequency between the states $|0, 3\rangle$ and $|0, 4\rangle$, which is an order of magnitude larger than the linewidth.

7.2.4 *The spectrum for different input powers*

Figure 7.3(b) presents measured spectra for different input probe powers varied over 4 orders of magnitude where all 3 transmons are in resonance with the mode. Here P_{in} refers to the input power at the resonator input and P_{out} refers to the digitizer input at room temperature. At low input powers corresponding to much less than a single intra-resonator photon on average, we observe the well known splitting of the coupled multi-qubit single-photon state as in Agarwal (1984). Here we observe no additional resonances which validate that the system is initialized in its quantum ground state rather than a thermal state (Fink et al., 2009).

At intermediate powers we observe a rich structure in the transmission spectrum, which is determined by multi-qubit multi-photon transitions. The power broadening of the multi-photon resonances can be observed. The situation is even more complicated due to the additional transmon levels which lead to an asymmetry of the observed spectra (Fink et al., 2008; Bishop et al., 2009).

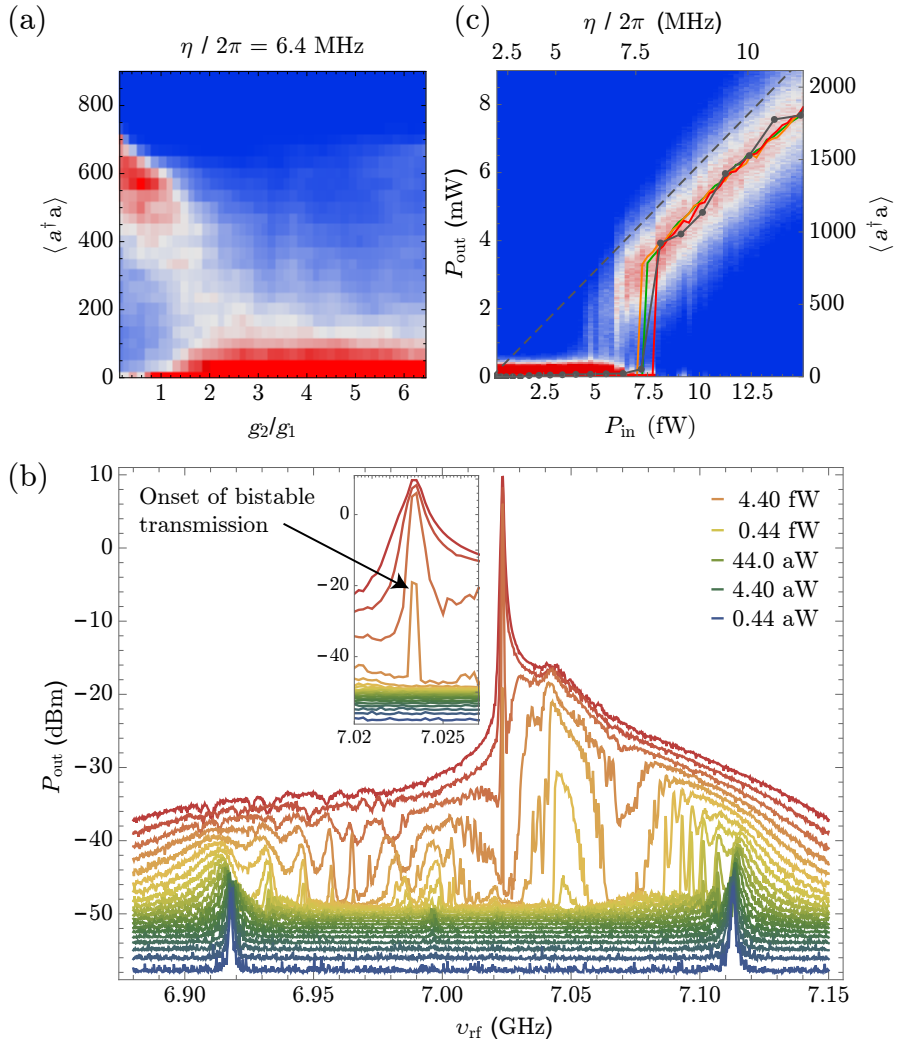

Figure 7.3: (a) Simulated histogram of the output intensity as a function of the coupling constant g_2 for $\eta/(2\pi) = 6.4$ MHz with red representing high probability and blue indicating zero probablility. (b) Measured spectra for input powers from $P_{in} = 0.44 \times 10^{-18}$ W (blue) to 25×10^{-15} W (red) with all 3 atoms in resonance with the mode. P_{in} and P_{out} refer to the resonator input power and digitizer input power respectively. For better visibility the shown spectra are offset by 1.6 nW from each other. The sharp transmission peak shown in the inset appears stochastically. In this particular measurement (orange line at 4.4 fW input power) we observe only two frequency points with small but finite switching probability and we sample over multiple switching events resulting in a certain mean detected power. At lower drive power no transmission is observed (no switching). At higher drive powers the transmission peak approaches the resonator linewidth and scales linearly with input power (no switching again). (c) Measured histogram of the detected power as a function of the resonator input power for a single transmon (density plot). The most likely photon numbers (line plots) are extracted from this measurement (red) and two similar measurements taken with 2 (orange) and 3 qubits (green) in resonance with the mode. Simulation results for the single qubit case are shown with connected black symbols for comparison. The dashed line is for reference and represents the response of the empty resonator with $\langle a^\dagger a \rangle = (\eta/\kappa)^2$.

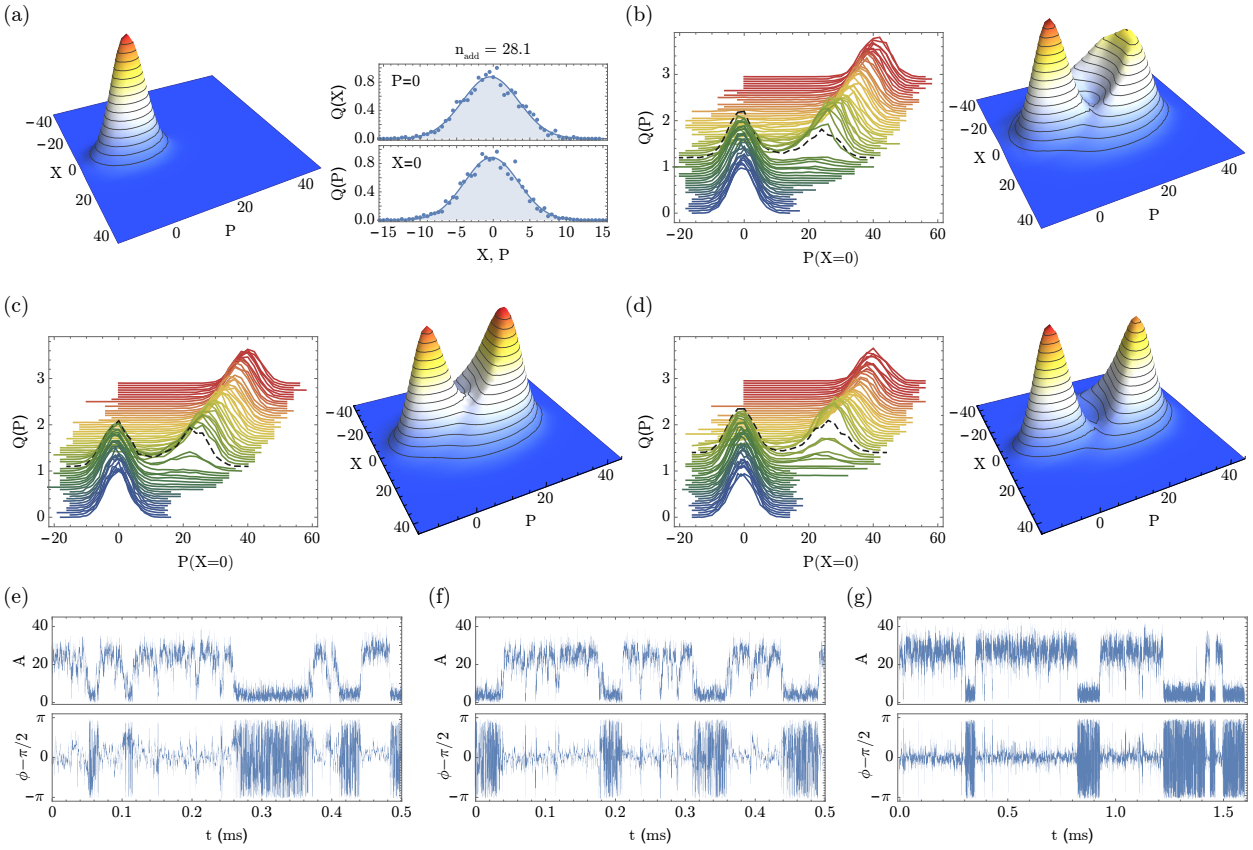

Figure 7.4: (a) Measured Q-function of the vacuum field for very low drive power $\eta/(2\pi) = 1.4$ MHz in the photon blockade regime (left) and Gaussian fit along the two field quadratures X and P. The fit reveals a thermal state due to the added amplifier noise with $n_{\mathrm{add}} = 28.1$. (b) The waterfall plot shows line cuts of the measured Q-functions where $X = 0$ as the drive strength is increased from $\eta/(2\pi) = 1.4 \rightarrow 11$ MHz for a single transmon in resonance with the mode (left). A vertical offset of 0.05 between the line plots has been used for better visibility. The complete Q function for the critical drive strength $\eta/(2\pi) = 7.1$ MHz, which is indicated by the dashed black line on the left. (c) The same measurement for transmons 1 and 2 in resonance and the critical drive strength $\eta/(2\pi) = 6.8$ MHz. (d) The same for transmons 1, 2 and 3 in resonance and the critical drive strength $\eta/(2\pi) = 7.7$ MHz. (e)-(g) The real-time single-shot record of the transmitted output field amplitude and phase for one (e), two (f) and three (g) atoms in resonance with the mode.

More importantly however, the frequency region around the bare resonator frequency remains dim over a large range of input powers.

At a certain power, corresponding to about 500 intra-resonator photons, we observe a sudden narrow transmission peak at the bare resonator frequency. This transmission peak is observed to be switching stochastically for a certain range of constant input powers. At much higher input powers the spectrum resembles that of an empty resonator without atoms. This transition to the classical regime has been studied in the dispersive limit with coherent drive where the photon number is $\sim 10^5$ by Reed et al. (2010), as well as in the resonant case with broadband thermal radiation (Fink et al., 2010).

In order to resolve the dynamics of the process leading to the sharp transmission peak, we record the resonator transmission at the bare resonator frequency for 60 different input powers. In each case we measure a single-shot real-time-

record of both field quadratures and repeat these measurements for one, two and three transmons in resonance with the resonator mode. Experimentally the transmitted tone is amplified with a commercial HEMT amplifier, down-converted with an IQ mixer and digitized with a time-resolution of 40 ns for a total time of 1.6 ms. This corresponds to a filter bandwidth of 25 MHz, much smaller than the vacuum Rabi splitting and small enough to filter out most low lying and comparably low power multi-photon transitions. The density plot shown in Fig. 7.3(c) shows the likelihood to detect a particular output power as a function of a large range of input powers, carefully mapping out the transition from the dim to the bright multi-photon phase of the system.

7.2.5 The steady-state density operator and behavior in the time domain

The measured histogram clearly shows an input power region between 4.5–7.5 fW with two distinct solutions. For smaller powers we observe no transmission (photon blockade) and for higher powers the resonator transmission scales linearly with the input power (this is close to the empty-resonator solution). The red line-plot indicates the most likely output power for this measurement and agrees very well with the simulated results shown in black. The simulation results are based on independently measured parameters, see also Mlynek et al. (2012), and provide a calibration for the drive amplitude η shown on the top horizontal axis of Fig. 7.3(c) and the mean intra-resonator photon number $\langle a^\dagger a \rangle$ shown on the right hand vertical axis. The total attenuation of 86 dB agrees with our expectations based on independent measurements and is sufficient to protect the resonator from room temperature thermal radiation. The orange and green lines show the results of identical measurements with two and three atoms in resonance with the mode. The characteristic switching power is slightly shifted, but the single- and multi-atom cases appear very similar.

A full characterization of the steady-state of the resonator field can be given by the Husimi Q quasiprobability distribution, see Fig. 7.4. For small drive strength the system is in the photon blockade regime and the Q function is that of the vacuum state. Due to the added noise of the amplifier chain we expect a convolution of the Q-function vacuum state with a thermal state and a Gaussian fit to the measured distribution (cf. Fig. 7.4a) yields an added noise photon number of 28.1 as referenced to the resonator output. This corresponds to a total system noise temperature of 9.5 K, in line with our expectations due to losses in the output line and the noise specifications of the used amplifiers.

Figure 7.4(b–d) show the experimental results for one, two and three atoms in resonance, respectively. The waterfall plots explicitly show the photon blockade breaking transition indicated by the sudden change of the Q function peak position as the drive power is increased from low (blue) to high drive strength (red). The right hand plots depict the entire Q function within the bistability region, i.e. for the data sets marked by dashed black lines on their left. In all three cases the Q function shows a clear bimodal structure with two solutions. Due to the large intra-resonator photon number in the bimodal switching regime of $\sim 500 - 700$, we can clearly resolve the double-peaked Q-function demonstrating the mixture of the vacuum state and the highly excited state with well-defined amplitude and phase.

Fig. 7.4(e-g) display the bistable behavior in the time domain, showing a general picture similar to the numerically generated trajectories in Fig. 6.4.

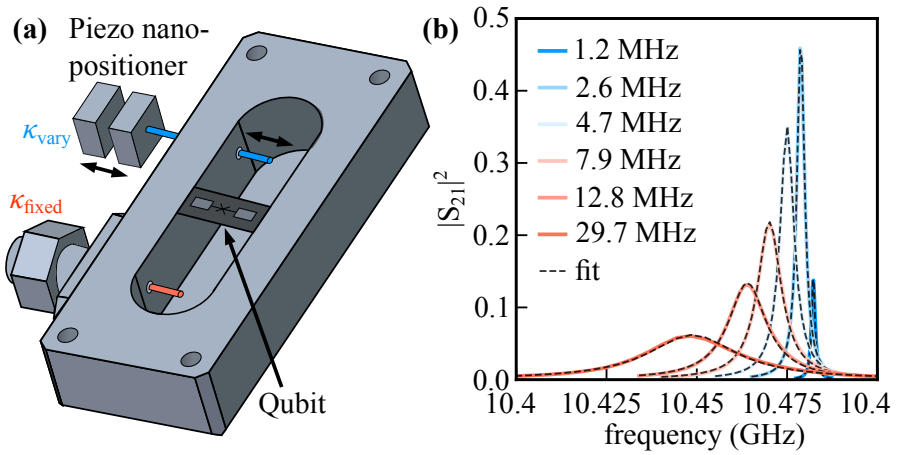

Figure 7.5: (a) Schematics of the experimental device for modeling the thermodynamic limit. It consists of a superconducting transmon qubit fabricated on a silicon substrate that is placed at the antinode of the fundamental mode of a 3D copper cavity. The cavity has fixed length (salmon) and an in-situ variable length pin coupler port (blue). (b) Measured cavity transmission spectra with the qubit far detuned for different coupler positions (color coded) together with Lorentzian fits (dashed) and the extracted $\kappa/2\pi$ values, cf. Eq. (7.4).

Whereas the bright states are characterized by a fixed-phase resonator field, the phase of the dim state is completely chaotic in the experiment due to technical noise.

7.3 MODELING THE THERMODYNAMIC LIMIT EXPERIMENTALLY

The basic idea of the experimental approach of the thermodynamic limit is that the finite-size scaling parameter g/κ (cf. Chapter 6, in particular Fig. 6.7b) is increased not by increasing g, which is not possible in CCQED, but by decreasing κ. This procedure has the inherent limitation that when κ reaches the order of magnitude of the transmon relaxation rates, then the transmon decay channels start to significantly impact the dynamics, as was demonstrated for γ in Chapter 6. However, the transmon used in this experiment is of such high quality, that it will be possible to follow the scaling of the characteristic timescale to the thermodynamic limit over seven orders of magnitude (well into the order of several seconds!) before hitting this limitation.

In order to be able to change κ *in situ*, i.e., without removing the device from the dilution refrigerator, here a 3D microwave resonator is used in contrast to the previous Section. Whereas the studies in Section 7.2 were based on archive data after the dismantling of the experiment, here the device was specifically designed for the purpose of studying the finite-size scaling of PBB, so that the synergy between theory and experiment could be much stronger.

The numerical studies presented in this Section took about *a full year* on a virtual computational cluster in an OpenStack cloud environment (MTA Cloud).

7.3.1 *The experimental system*

The experimental setting incorporates a transmon qubit placed at the anti-node of the standing wave of a 3D copper-cavity, as shown in Fig. 7.5(a), that can be flux-tuned by applying a B-field via a millimeter-sized superconducting bias coil mounted at the outside cavity wall. The transmon qubit has a maximum Josephson energy $E_{\mathrm{J,max}}/h \approx 48\,\mathrm{GHz}$, charging energy $E_{\mathrm{C}}/h \approx 382\,\mathrm{MHz}$ and a resulting maximum transition frequency between its ground and first excited states of $\omega_{\mathrm{A}}/2\pi \approx 12.166\,\mathrm{GHz}$. When the transmon ground to first excited state transition is tuned in resonance with the cavity mode at $\omega_{\mathrm{R}}/2\pi \approx 10.4725\,\mathrm{GHz}$, the directly measured coupling strength between the single photon and the qubit transition is as high as $g/2\pi = 344\,\mathrm{MHz}$, which is only about a factor of 3 below the ultrastrong coupling regime, cf. Chapter 5. The relatively high absolute anharmonicity between subsequent transmon state transitions is $\alpha/h \approx -418\,\mathrm{MHz}$ at this flux bias position.

The cavity has two ports, of which the input pin coupler position is fixed with an external coupling strength of $\kappa_{\mathrm{fixed}}/2\pi \approx 500\,\mathrm{kHz}$. The output coupler is attached to a cryogenic piezo nano-positioner, which allows to adjust the pin length extending into the cavity. With this tunable coupler the coupling strength can be varied in situ in a wide range $\kappa_{\mathrm{vary}}/2\pi \approx 20\,\mathrm{kHz} - 30\,\mathrm{MHz}$. The internal cavity loss at low temperature is $\kappa_{\mathrm{int}}/2\pi \approx 600\,\mathrm{kHz}$, which is achieved by electro-polishing of the high conductivity copper surface before cooldown to 10 mK in a dilution refrigerator.

All four scattering parameters are measured with a vector network analyzer to calibrate the measurement setup and the cavity properties when the qubit is far detuned from the cavity resonance. Figure 7.5(b) shows transmission measurements fitted with the scattering parameter S_{21} derived from the input-output theory of an open quantum system (Gardiner & Collett, 1985):

$$S_{21} = \frac{\sqrt{\kappa_{\mathrm{fixed}}\kappa_{\mathrm{vary}}}}{\kappa/2 - i(\omega - \omega_{\mathrm{R}})}. \tag{7.4}$$

From these fits, we extract all loss rates that add up to the total cavity linewidth $\kappa = \kappa_{\mathrm{fixed}} + \kappa_{\mathrm{vary}} + \kappa_{\mathrm{int}}$ also indicated in Fig. 7.5(b).

Time-domain characterization measurements confirm that the qubit is Purcell-limited and homogeneously broadened at the flux sweet spot (Houck et al., 2008), where the measured coherence times are $T_1 \approx 0.5\,\mu\mathrm{s}$ and $T_2 \approx 1\,\mu\mathrm{s}$. When the qubit frequency is tuned far below the resonator frequency $\omega_{\mathrm{A}}/2\pi \approx 6.083\,\mathrm{GHz}$ by applying an external magnetic field, the measured coherence times are $T_1 \approx 18.14\,\mu\mathrm{s}$ and $T_2 \approx 0.496\,\mu\mathrm{s}$, which we attribute to a higher Purcell limit due to the larger detuning as well as a drastically increased flux noise sensitivity. On resonance $\omega_{\mathrm{A}} = \omega_{\mathrm{R}}$, where the following experiments were performed, the energy relaxation is therefore fully dominated by cavity losses. The measured vacuum Rabi peak linewidth changes with and without the qubit in resonance are in agreement with a small amount of flux noise induced dephasing expected at that flux bias position.

In Section 7.2 the third transmon level was shown to play an important role in the dynamics. Here, due to the much (~ 6 times) increased coupling strength, but transmon anharmonicity remaining similar, even higher transmon levels come into play.

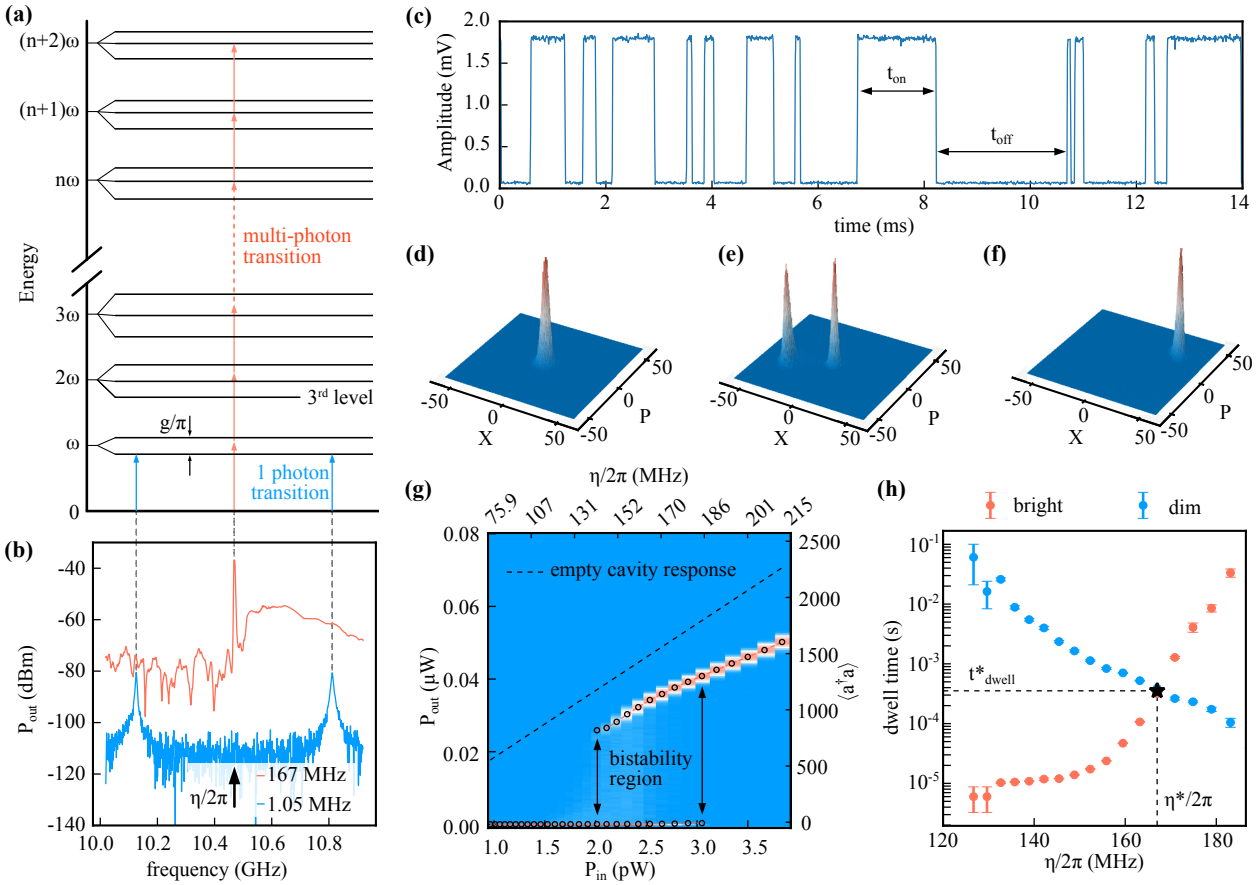

Figure 7.6: Observation of photon blockade breakdown at $g/\kappa \approx 39$. (a) The Jaynes-Cummings ladder for a three-level atom illustrating the PBB effect in the frequency domain: single-photon (blue) and multi-photon (salmon) transitions are indicated according to the measured spectrum at the Rabi-split frequencies and near resonance, respectively. (b) Measured transmission spectra at strong resonant coupling at applied external drive strengths 1.05 MHz and 167.01 MHz, where the vacuum Rabi spectrum and a sharp peak appearing close to the cavity mode frequency are observed, respectively. (c) Bistability in the time domain, with dwell times in the OFF and ON states. (d-f) Measured histograms in quadrature space – proportional to Q functions convolved with amplifier noise with added noise photons $n_{\text{amp}} \approx 9.2$, for the dim phase at $\eta/2\pi = 105$ MHz, for the bistable phase at intermediate drive strength 167 MHz, and for the bright state at higher drive strength 210 MHz, respectively. (g) Histograms of output power arranged vertically in color code as a function of input power, with the bistability region indicated by histograms with two maxima. The maxima indicated by circles trace out a typical bistability curve, cf. Fig. 7.10 in the appendix. (h) Dwell times in the dim (t_{off}) and bright states (t_{on}) as functions of η, with the dwell-time and drive amplitude corresponding to half-filling ($t_{\text{off}} = t_{\text{on}}$) indicated with asterisk.

7.3.2 *Results*

Fig. 7.6 summarizes the observation of the effect in the just described experimental setup in (a-b) the frequency and (c) the time domain, (d-f) in the language of the Q-function, and (g) as a bistability curve. Panel (h) displays how the half-filling drive amplitude η^* is determined, cf. also Section 6.4.

The modeling of the upscaling to the thermodynamic limit together with the determination of the scaling exponents is summarized in Fig. 7.7. We note that all the measured exponents differ significantly from the simulated ones in Chapter 6. The scaling law $|\alpha|^2 \propto (g/\kappa)^2$ came from the 2-level neoclassical theory, cf. Eq. (6.5). Therefore, a deviation from that can come from even the presence of the other transmon levels. In Section 6.5.2, the blink-off rate could be calculated from the rate of ladder-switching quantum jumps, and was found to be proportional to $\kappa/|\alpha|^2$, so the waiting time for a blink-off is $|\alpha|^2/\kappa$, therefore it scales as g^2/κ^3.[1] The deviation from this in the experiment can be due to the counter-rotating terms and the hybridized decay channels, which together make that the blinking mechanism is different from the simple Jaynes-Cummings case that we had in the theory chapter.

1. In the simulation, cf. Fig. 6.7, we measured the timescale-exponent $(\kappa\tau) \propto (g/\kappa)^{2.2}$, which is very close to this.

Fig. 7.7(b-d) displays simulation results that have been obtained with the `C++QED` framework. The details of the simulation are similar to Chapter 6 and Section 7.2, cf. also Section 7.A and Part III. Here, in the simulation we probe different numbers of levels for the transmon, and try different models for the dephasing of the higher transmon levels. It is clear from all the panes (b-d) that the more transmon levels we include, the better the simulation data fits the experiment. Even higher levels of the transmon seem to play an important role than the third level as in Section 7.2. This can be attributed to the stronger coupling – which coupling in the case of the transmon moreover increases for transitions between higher-lying transmon levels, cf. Eq. (7.7) –, that compensates for the increased detuning of these higher levels.

For the dephasing of higher-lying transmon levels, with dephasing rate $\gamma_\phi = 2\pi\left[\frac{1}{T_2} - \frac{1}{2T_1}\right]$, three different models have been tried: (1) $\gamma_\phi = 0$ for a baseline, (2) γ_ϕ increasing linearly with level ordinal, and (3) γ_ϕ increasing proportionally to the charge dispersion (Bishop et al., 2009) – a much quicker-than-linear increase. Results from this latter are not shown here because the trajectories are qualitatively different from the experimental ones. The general tendency deducible from the figure is that increasing the number of transmon levels improves the correspondence between simulation and experiment, and so does the inclusion of γ_ϕ. This is especially prominent in the η (or, photon-number) scale, cf. Fig. 7.7(c-d).

Regarding the exponents, the simulation data hint at a similar picture we outlined above: the exponent of the photon number seems to depend on the number of transmon levels, whereas that of the dwell time is independent of this, and closely reproduces the exponent obtained in Chapter 6. That is, the exponent of the timescale is more robust, as it depends only on such traits of the model (rotating-wave approximation and bare subsystem decay channels) as are more fundamental than the number of levels.

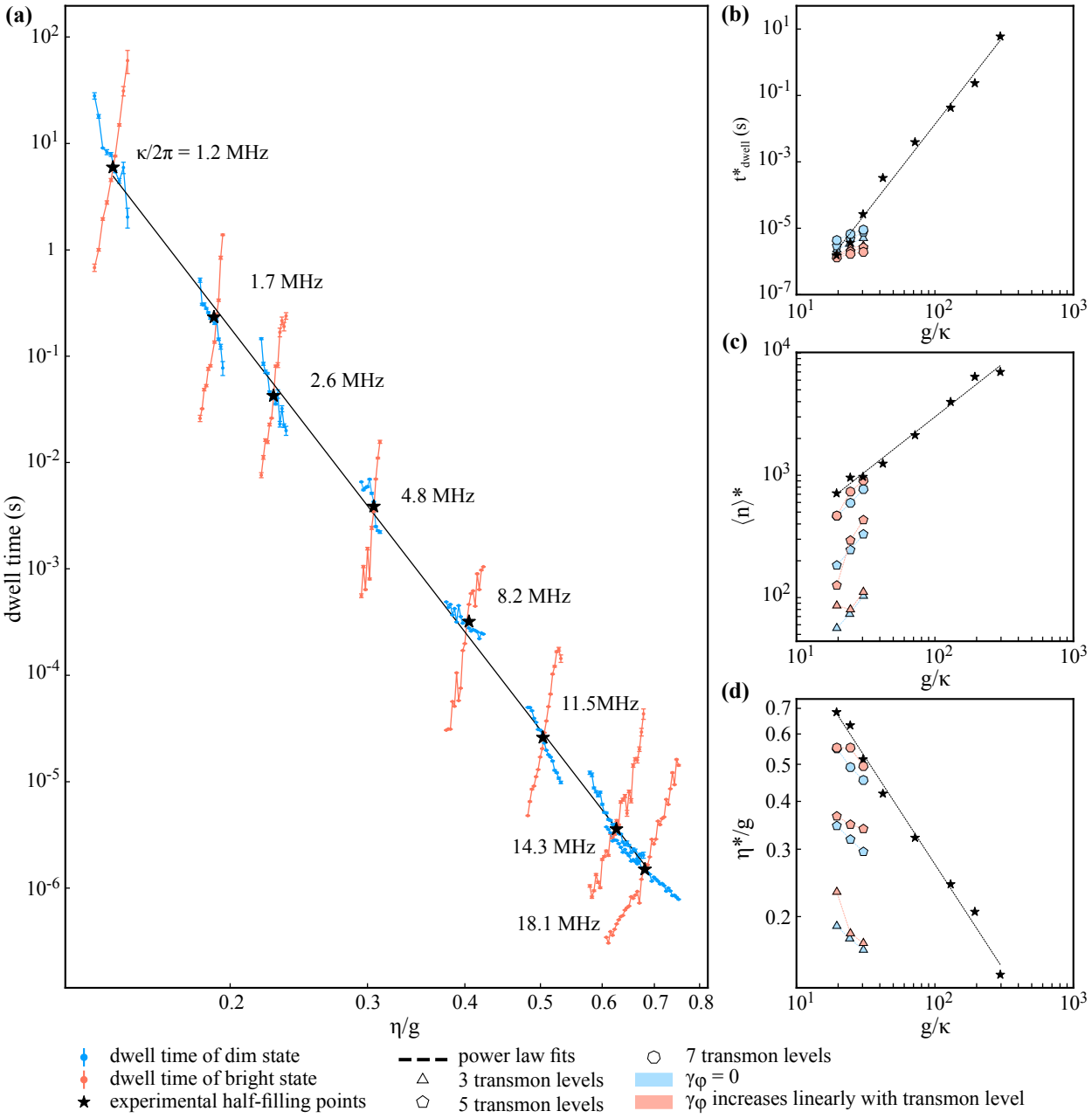

Figure 7.7: Finite-size scaling towards the thermodynamic limit. (a) Measured dwell times in dim (blue) and bright (salmon) states are shown as functions of η/g for different values of κ. Black stars denote half-filling values where the fillings of dim and bright states are equal. A power law fit (dashed line) yields $t^*_{\mathrm{dwell}} \propto (\eta^*/g)^{-10.3\pm0.2}$. (b)-(d) Scaling of dwell time, resonator photon number and input drive strength in units of g at half filling. Fitting on the experimental data, we find dwell time increasing as $(g/\kappa)^{5.4}$, the average number of intra-cavity photon number as $(g/\kappa)^{0.89}$ and η^*/g decreasing as $(g/\kappa)^{0.56}$. We compare these experimental values with QJMC simulations (polygons with color code) for κ = 11.5, 14.3, and 18.1 MHz. The simulations include 3, 5, or 7 transmon levels both without transmon dephasing noise (light blue) and with dephasing increasing linearly with the level number (light red) – for details of the simulation cf. the text and Section 7.A. By increasing the number of transmon levels included in the simulations, the correspondence with the experimental data improves.

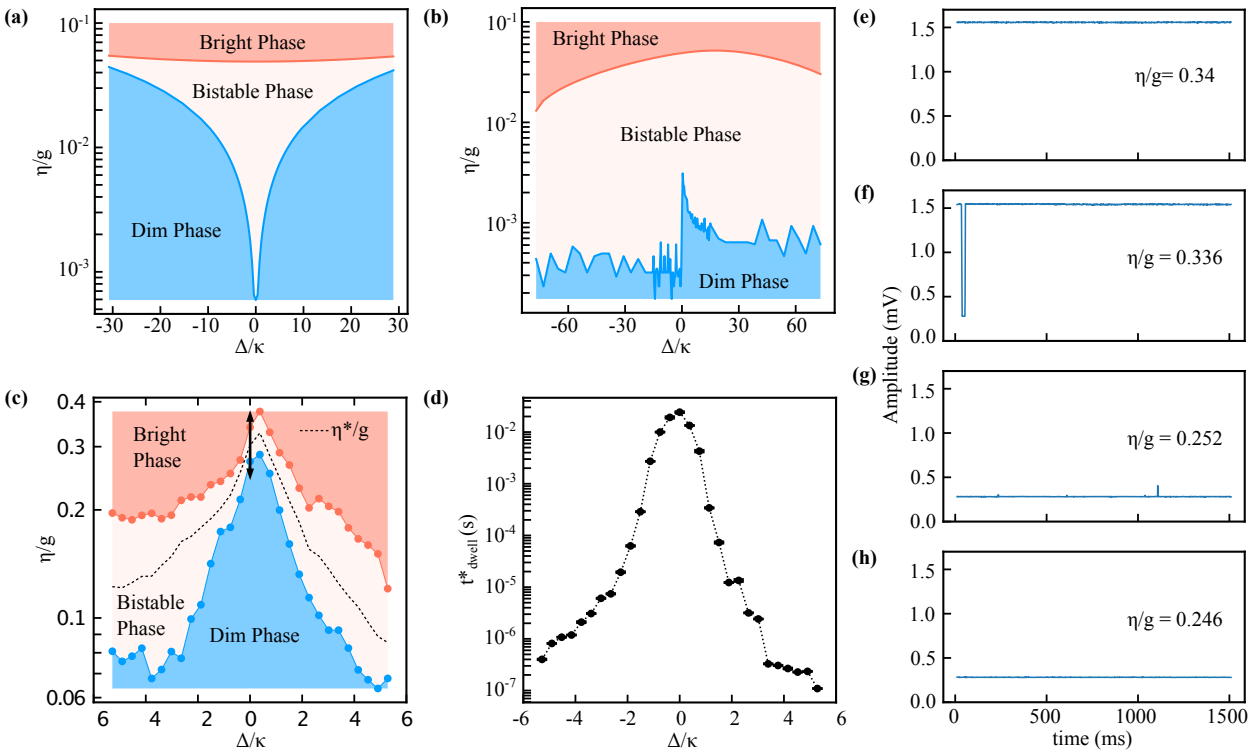

Figure 7.8: The phase diagram at $g/\kappa \approx 132$. Phase diagram on the Δ–η plane obtained from semiclassical (Maxwell-Bloch) equations for (a) two and (b) three transmon levels with values for the parameters γ_1 and γ_{phi} according to the experiment. In panel (b), the noisy lower boundary of the bistable phase results from numerics. (c) Phase diagram obtained from the experimental data. (d) Experimental dwell time at half filling as a function of the detuning of the drive. (e)-(h) shows the experimentally observed telegraph signals at different η values at $\Delta = 0$ in order to determine the boundaries of the bistability region. In this particular case, the bistability region can be observed within the range of η from 85.6 till 115.5 MHz.

7.3.3 *The phase diagram*

Finally, the phase diagram of the process has been sketched experimentally at one of the closest points to the phase transition we can have, one of the highest values of the finite-size scaling parameter: $g/\kappa = 132.3$. For this, we introduce a further parameter: Δ, the detuning of the drive from the resonance of the bare subsystems:

$$\Delta \equiv \omega - \omega_A = \omega - \omega_R. \tag{7.5}$$

Phase diagrams on the Δ–η plane as calculated from the semiclassical theory (for details, see Section 7.B) are displayed in Fig. 7.8(a,b) for a 2- and a 3-level transmon, respectively. On panel (c), the experimentally measured phase diagram is displayed. On pane (d), the experimental dwell time is shown as a function of the new parameter Δ, exhibiting a drop of about 5 orders of magnitude between resonance and $\Delta = \pm 6\kappa$.

Comparing the phase diagrams (a-c), one can see that the semiclassical 2-level case completely fails to capture the essential features of the experiment. The 3-level case is qualitatively better especially in the upper limiting curve of the bistability region, as it reproduces the overall resonance-like dependence on the detuning, and the asymmetry with respect to the $\Delta = 0$ line. However, the shape of the lower limiting curve is not correctly captured by this theory.

In fact, the 3-level semiclassical theory is unable to reproduce the finite dim phase around resonance that we observe experimentally.

This comparison with the semiclassical theory underlines that the well-resolved spectrum of the strongly coupled transmon-resonator system with more than two transmon levels plays an essential role in this experiment.

7.A THE FULL QUANTUM MODEL FOR MULTILEVEL TRANSMONS

The basic Hamiltonian for a multi-level system interacting with a driven mode reads ($\hbar = 1$):

$$H = \sum_u \Big[h_u \left|u\right\rangle \left\langle u\right| + i\Big(g_{u+1}\, a \left|u+1\right\rangle \left\langle u\right| - \text{h.c.}\Big)\Big] + \omega_\text{M}\, a^\dagger a + i\left(\eta\, e^{-i\omega t}\, a^\dagger - \text{h.c.}\right). \tag{7.6}$$

Here, u indexes the transmon levels, and we assume that only transitions between adjacent levels couple to the mode, with coupling coefficient g_{u+1}. The h_us are the bare transmon energies, ω_M is the bare mode frequency, and η and ω are the drive amplitude and frequency, respectively.

The Hamiltonian is written in the rotating-wave approximation. This is justified as long as the coupling strength does not reach the Bloch-Siegert regime of ultrastrong coupling, meaning 10 $g_1 \lesssim h, \omega_\text{M}$ (Forn-Díaz et al., 2019), which holds for the experimental systems studied in this Chapter. For the coupling coefficients we use the standard relation for transmons

$$g_{u+1} = \sqrt{u+1}\, g_1. \tag{7.7}$$

For a comprehensive theory of the transmon cf. Bishop (2010); Blais et al. (2021); Schreier et al. (2008)

Transforming to the frame rotating with ω, we obtain a time-independent Hamiltonian with $\Delta \equiv \omega - \omega_\text{M}$:

$$H = \sum_u \Big[(h_u - u\,\omega) \left|u\right\rangle \left\langle u\right| + i\Big(g_{u+1}\, a \left|u+1\right\rangle \left\langle u\right| - \text{h.c.}\Big)\Big] - \Delta\, a^\dagger a + i\left(\eta\, a^\dagger - \text{h.c.}\right). \tag{7.8}$$

Here, putting $h_0 = 0$, and assuming the 0–1 transition resonant with the mode ($h_1 = \omega_\text{M}$), we obtain a simple form for the bare transmon Hamiltonian, which we list for the first 3 levels:

$$H_\text{transmon} = -\Delta \left|1\right\rangle \left\langle 1\right| - (2\Delta - \Delta_\text{an}) \left|2\right\rangle \left\langle 2\right| + \text{contribution of higher levels,} \tag{7.9}$$

where $\Delta_\text{an} \equiv h_2 - 2\,h_1$ is the anharmonicity of the third level, which is related to the charging energy.

Let us turn to dissipation, which we describe with the Liouvillian

$$\mathcal{L}\rho = \sum_i \left(L_i\, \rho\, L_i^\dagger - \frac{1}{2}\left\{L_i^\dagger L_i, \rho\right\}\right) \equiv \left(\mathcal{L}_\text{mode} + \mathcal{L}_\text{relax} + \mathcal{L}_\text{dephase}\right)\rho \tag{7.10}$$

Let us look at the three kinds of dissipative channels in detail:

Resonator decay, $\mathcal{L}_\text{cav}$ This is described by the jump operators $L_- = \sqrt{2\,(n_\text{th}+1)\,\kappa}\, a$ and $L_+ = \sqrt{2\,n_\text{th}\,\kappa}\, a^\dagger$. Here n_th is the number of thermal photons, which can be neglected in our system, so the second kind of quantum jumps (absorption of thermal photons) does not exist.

Energy relaxation of the transmon, $\mathcal{L}_{\text{relax}}$ In analogy with the coupling to the resonator mode, we assume that this occurs only as transitions between adjacent levels. It is described by the jump operators $L_{u+1\to u} = \sqrt{\gamma_{u+1\to u}}\,|u\rangle\langle u+1|$. In the simulation, we take $\gamma_{u+1\to u}$ equal for all levels, and we identify it with γ_1 in cQED.

Dephasing of the transmon, $\mathcal{L}_{\text{dephase}}$ This is also defined separately for all transmon levels, and its jump operator for level v is

$$L_{\phi,v} = \sqrt{\gamma_{\phi,v}}\left(\sum_{u\neq v}|u\rangle\langle u| - |v\rangle\langle v|\right) = \sqrt{\gamma_{\phi,v}}\big(\mathbf{1} - 2\,|v\rangle\langle v|\big),$$

so it simply flips the phase of level v by π. Modeling the behavior of the dephasing for different transmon levels is nontrivial. We consider three possibilities:

1. $\gamma_{\phi,v} = 0$ for all v. This is only to get a theoretical baseline of dephasing-free behavior.
2. Linear growth as $\gamma_{\phi,v} = v\,\gamma_{\phi,v=1}$, where the dephasing $\gamma_{\phi,v=1} = 2\pi\times 6.25$ kHz in the experiment according to the above convention of γ_ϕ.
3. Dephasing proportional to the charge dispersion of the transmon levels (Bishop et al., 2009).

Example trajectories for the three possibilities are displayed in Fig. 7.9. It is apparent that model 3 leads to very noisy trajectories that do not reproduce qualitatively the experimentally observed behavior of stabilized attractors. Therefore, we omitted this possibility from the quantitative comparison presented in the main text.

In the simulation, for each physical parameter set, several trajectories are run with different random number generator seeds. Relying on the assumption of ergodicity, these trajectories are concatenated for a single long trajectory for each parameter set, which is then used for dwell-time statistics. Since each trajectory is started from the ground state, this method has a bias toward the dim state (breaching of ergodicity), which is the stronger, the larger the blinking time with respect to the simulation time.

The full quantum simulations were implemented within the C++QED simulation framework, cf. Part III, and took about a year on a 64-core virtual cluster defined within an OpenStack Cloud environment (http://science-cloud.hu/).

7.B SEMICLASSICAL THEORY FOR A MULTILEVEL TRANSMON

From the master equation $\dot\rho = [H,\rho]/(i\hbar) + \mathcal{L}\rho$ we can derive equations for the expectation values of the operators a and $\sigma_{uv} = |u\rangle\langle v|$. In the case of a two-level system, this simply reproduces the Maxwell-Bloch equations, with the added complication of the qubit dephasing. Here, we list the equations for

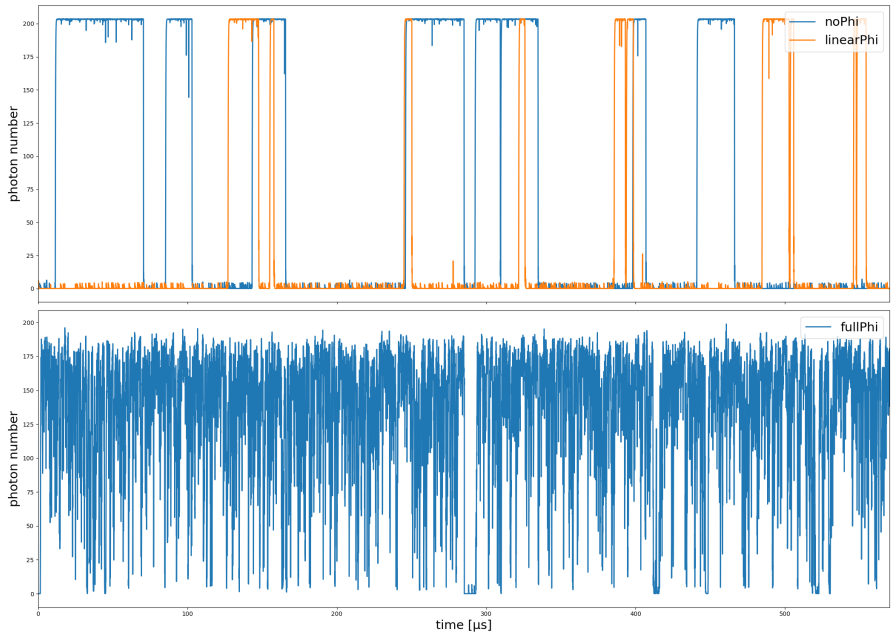

Figure 7.9: Example trajectories for the three possibilities for modelling charge dispersion for higher transmon levels enumerated in the text (labelled here "noPhi", "linearPhi", and "fullPhi", respectively). All other parameters are identical for the three trajectories. It is apparent that the "fullPhi" case leads to qualitatively incorrect results with very strong noise and vague, only partially stabilized attractors.

a three-level transmon, which still leads to an algebraically tractable scheme. In this case, 6 equations are needed for a complete system:

$$\dot{\alpha} = (i\Delta - \kappa)\alpha + \eta - g_1 s_{ge} - g_2 s_{ef} \tag{7.11a}$$

$$\dot{s}_{ge} = (i\Delta - \gamma_1)\, s_{ge} - g_1 \left(s_{ee} - s_{gg}\right) \alpha - g_2 s_{gf}\, \alpha^* \tag{7.11b}$$

$$\dot{s}_{gg} = \gamma_1 s_{ee} - 2 g_1 \mathfrak{Re}\{\alpha^* s_{ge}\} \tag{7.11c}$$

$$\dot{s}_{ef} = \left(i\left[\Delta - \Delta_f\right] - \left[\gamma_1 + 4\left(\gamma_{\phi,1} + \gamma_{\phi,2}\right)\right]\right) s_{ef} + g_2 \left(s_{ee} - s_{ff}\right)\alpha + g_1\, \alpha^*\, s_{gf} \tag{7.11d}$$

$$\dot{s}_{ee} = 2\, g_1\, \mathfrak{Re}\{\alpha^* s_{ge}\} - 2\, g_2\, \mathfrak{Re}\{\alpha^* s_{ef}\} - \gamma_1 s_{ee} + \gamma_1 s_{ff} \tag{7.11e}$$

$$\dot{s}_{gf} = \left(i\left[2\Delta - \Delta_f\right] - \left[\gamma_1 + 4\gamma_{\phi,2}\right]\right) s_{gf} - g_1\, \alpha\, s_{ef} + g_2\, \alpha\, s_{ge} \tag{7.11f}$$

Here $\alpha = \langle a \rangle$, and $s_{uv} = \langle \sigma_{uv} \rangle$. The system is completed with the completeness relation $s_{gg} + s_{ee} + s_{ff} = 1$. We are interested in the steady state, which can be obtained by zeroing the left hand side of the equations, that leads to an inhomogeneous nonlinear set of equations.

We do not need to solve the full set of equations. Instead, we can obtain a single implicit equation for only the intensity $|\alpha|^2$ as follows. First we define the complex dispersive shift

$$\Sigma\left(|\alpha|^2\right) = -\frac{g_1 s_{ge} + g_2 s_{ef}}{\alpha}, \tag{7.12}$$

second from Eq. (7.11a) in steady-state we express α explicitly. As we will show below, Σ depends only on powers of $|\alpha|^2$, and not on other combinations of α and α^*. Therefore, the equation for the intensity can be written as

$$|\alpha|^2 = \frac{|\eta|^2}{\left|\Sigma\left(|\alpha|^2\right) + (i\Delta - \kappa)\right|^2} \tag{7.13}$$

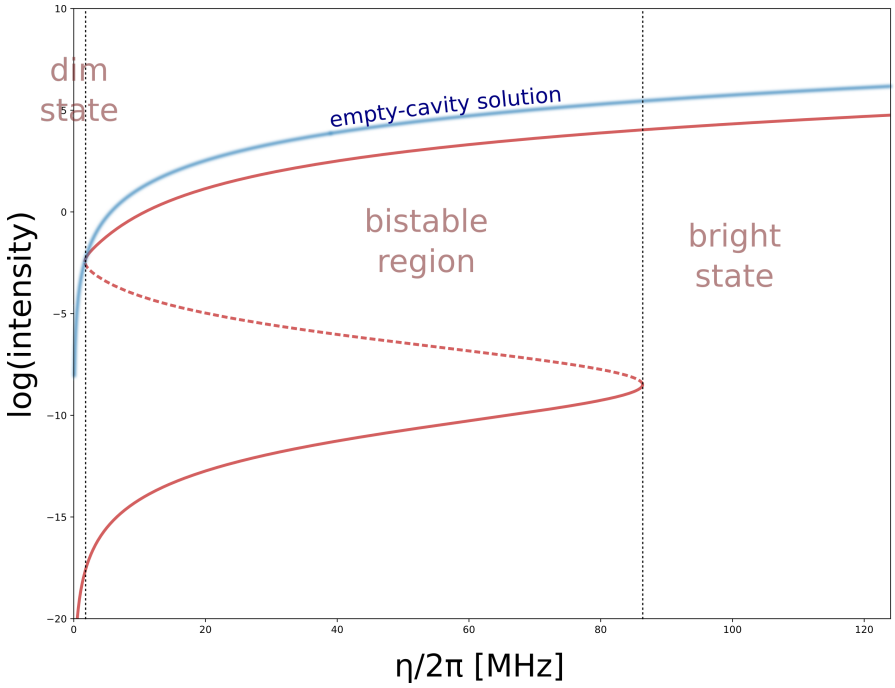

Figure 7.10: Typical bistability curve for the intensity as a function of the drive amplitude at the real system parameters and detuning $\Delta/(2\pi) = 10$ MHz. The bistable region is in fact signalled by a threefold (with some parameters even fivefold) solution, but the branch plotted in dashed line is non-physical, since the intensity decreases with increasing drive power. The empty-cavity solution is plotted for zero detuning, and we can observe that the solution curve concurs with it in the bright state, the difference being due to finite detuning.

What we have to show for the validity of Eq. (7.13) is that the solutions of s_{ge} and s_{ef} have the form of an $|\alpha|^2$-dependent expression multiplied by α. The polarizations can be expressed as functions of the populations multiplied with α from Eqs. (7.11b), (7.11d) and (7.11f) in steady state. When these solutions are substituted into the steady-state population equations (7.11c) and (7.11e), the factor α in the solutions together with α^* in those equations give an $|\alpha|^2$. Hence, the populations can be expressed from these equations as functions only of the intensity, and when these are substituted back into the solutions of the polarizations, we obtain the necessary form for these latter.

A typical solution of Eq. (7.13) exhibiting bistability is displayed in Fig. 7.10. The semiclassical theory is inferior to the full quantum-trajectory solution described in Section 7.A in at least two respects:

1. Dealing with (possibly multi-valued) steady state solutions, it does not provide information on timescales.

2. Whereas the set of three complex polarizations and two populations in Eq. (7.11) give a complete picture of the transmon in itself, the mode is represented only by a single amplitude. This means that the theory cannot account for nonclassical states of the mode and transmon-mode entanglement.

THESES, OUTLOOK

8

Thesis V (Vukics et al., 2019) We have formulated a paradigm of first-order dissipative phase transitions (DPT). According to this paradigm, a first-order DPT does not contradict the requirement that a dissipative quantum system governed by Liouvillian evolution has a unique steady-state density operator for all values of external parameters. The property of first-order phase transitions that several phases can coexist in certain domains of the parameter space holds in the dissipative quantum case without the need for a multi-valued solution for the steady-state density operator. The key to this is that a single density operator can accomodate multiple coexsisting phases as a mixture of macroscopically distinct states. However, the steady-state density operator in itself does not give information about the stability of phases, or non-equilibrium phenomena, such as hysteresis. To access such effects, we have invoked the temporal unraveling of the steady-state density operator in the language of quantum trajectories. Quantum trajectories enable the study of bistabilities developing into first-order dissipative quantum phase transitions in a thermodynamic limit where the macroscopically distinct attractors become stable phases, and the system exhibits perfect hysteresis in the coexistence domain.

Thesis VI (Vukics et al., 2019) As a prime example of the paradigm described in Thesis V, we considered the photon-blockade-breakdown phase transition, which occurs in the driven-dissipative Jaynes-Cummings model with strong coupling between the two-level system and the harmonic oscillator. For a certain range of drive strength, the stationary solution in the time domain corresponds to a bistability of classically distinguishable states. By unraveling the stationary solution into quantum trajectories, we resolved the nature of coexistence of phases: the temporal bistability is a finite-size precursor of what in the thermodynamic limit is a first-order dissipative quantum phase transition. Contrary to formerly known quantum phase transitions in the Rabi or Jaynes-Cummings models, here the thermodynamic limit is a strong-coupling limit, where the system remains the same bipartite microscopic quantum system, but both the bistability timescale and the separation of the attractors becomes macroscopic. We constructed an appropriate scaling of the system parameters such that the bistable telegraph signal remains self-similar along the passage to the thermodynamic limit, and calculated the finite-size scaling exponents numerically. The numerical studies took half a year in a cloud-based 64-core computational cluster.

Thesis VII (Vukics et al., 2019) We have demonstrated that the photon-blockade breakdown is an inherently quantum effect. This remains true even in the thermodynamic limit, i.e. the thermodynamic limit is not a classical limit.

This is because the well-resolved discrete spectrum of an interacting bipartite (atom-mode) quantum system is essential for the effect since the two attractors (phases) live in different regions of this spectrum. In the thermodynamic limit it is the increased anharmonicity of the spectrum due to the increased coupling which accounts for the increasing stability of the attractors. The dim phase is a significantly non-classical state with the property that photon escapes *increase* the photon number in the mode (super-Poissonian photon statistics). We have demonstrated that blink-on and -off processes are triggered by cascades of quantum jumps. We have shown that depolarization and dephasing of the atomic transition is detrimental for long-living attractors.

Thesis VIII (Fink et al., 2017; Sett et al., 2022) The photon-blockade breakdown effect has been demonstrated in circuit cavity quantum electrodynamics systems with transmons. The spectral, time-domain, and quasi-probability-distribution signatures of the bistability have been directly observed. We have shown that the necessary coupling strength is so high that the anharmonicity of the transmon is not sufficient for it to act as a qubit: higher-lying transmon levels enter the dynamics, with essential modifications to the spectrum and hence the parameter domains where the effect is accessible. The thermodynamic limit has been modeled experimentally by modifying the resonator loss rate while keeping the coupling strength constant. The finite-size scaling of the characteristic timescale has hence been followed over seven orders of magnitude. The phase diagram on the detuning – drive strength plane has been determined experimentally, and found to exhibit qualitative differences from a semiclassically calculated phase diagram. The numerical studies supporting the experiment took a full year in a cloud-based 64-core computational cluster.

Since Part II of the thesis contains the most recent results, in contrast to Chapters 5 and 11, here there is no need for a literature review of "further developments". A review of recent literature can be found in Section 1.4. Rather, we give an outlook below.

The comparison of our simulation data with the experimental results, especially in Section 7.3, where the simulation data doesn't depend on any fitting parameters, suggests that the fully quantum modelling of the transmon needs to be refined. Even though the ultrastrong coupling (Bloch-Siegert) regime is not reached, we can suspect that what we observe is the breakdown of the conventional modelling of the qubit-mode system with the Jaynes-Cummings model and the separate qubit and mode dissipation channels. The modelling can be improved in both of these aspects:

Coherent evolution the rotating-wave approximation is expected to break down in the ultrastrong-coupling regime, so that the Jaynes-Cummings model needs to be supplemented. We note that the Bloch-Siegert shift has recently been observed in circuit QED by Pietikäinen et al. (2017).

Incoherent evolution the standard quantum optics master equation Eq. (7.10) neglects the qubit-mode interaction in its treatment of the coupling to the environment. This assumption has been shown to break down in the ultrastrong-coupling regime (Beaudoin et al., 2011).

The photon blockade breakdown bistability represents an important first step towards exploring quantum criticality in the many-photon / high-drive-power regime. A detailed understanding of quantum phase transitions in circuit QED could play an important role for the controlled simulation and stabilization of peculiar phases of finite size open quantum systems. In the future, one could study entanglement and the details of the time dynamics using auto-correlation measurements (Lang et al., 2011). With better qubit coherence times and quantum limited amplifiers, phase multi-stability (Delanty et al., 2011) and squeezing (Peano & Thorwart, 2010) may be realizable.

Besides its fundamental interest as a quantum-classical phase transition, the PBB bistability / first-order DPT also promises applications. Since single quantum jumps were shown to trigger the switching from the (nonclassical) dim state to the (closely classical) bright state, cf. Fig. 6.10, our system can be considered as a quantum-jump amplifier, where ultimately a macroscopic microwave device (outside the fridge) is getting switched by microscopic quantum events (inside the fridge). An interesting prospect is controlling the switching behavior, that can be envisaged either in a parametric way, but preferably with another strongly coupled quantum system. In the latter case the bistability can act as a readout device with high signal-to-noise ratio, for ultra low power signal processing in photonics (Kerckhoff et al., 2011) or classical frontend-processing for quantum computers (Andersen & Mølmer, 2015). The capability of preparing the system on the verge of a phase switching could make it applicable in quantum metrology/sensing, in line with the arising paradigm for the application of (first-order) QPTs/DPTs (Fernández-Lorenzo & Porras, 2017; Raghunandan et al., 2018; Yang & Jacob, 2019; Heugel et al., 2019).

Finally, we note that in the cold-atom cavity QED laboratory at the Wigner Research Centre for Physics started in 2016, an effect dubbed "transmission blockade breakdown" (TBB) has been observed by Clark et al. (2021) that can be regarded as a many-body counterpart of PBB. Here also, an abrupt transition occurs between a "dim" and a "bright" phase of the cavity field, where the former is caused by dispersive interaction with the atoms in one of the states of the ground-state hyperfine manifold of rubidium-87, cf. Fig. 8.1.

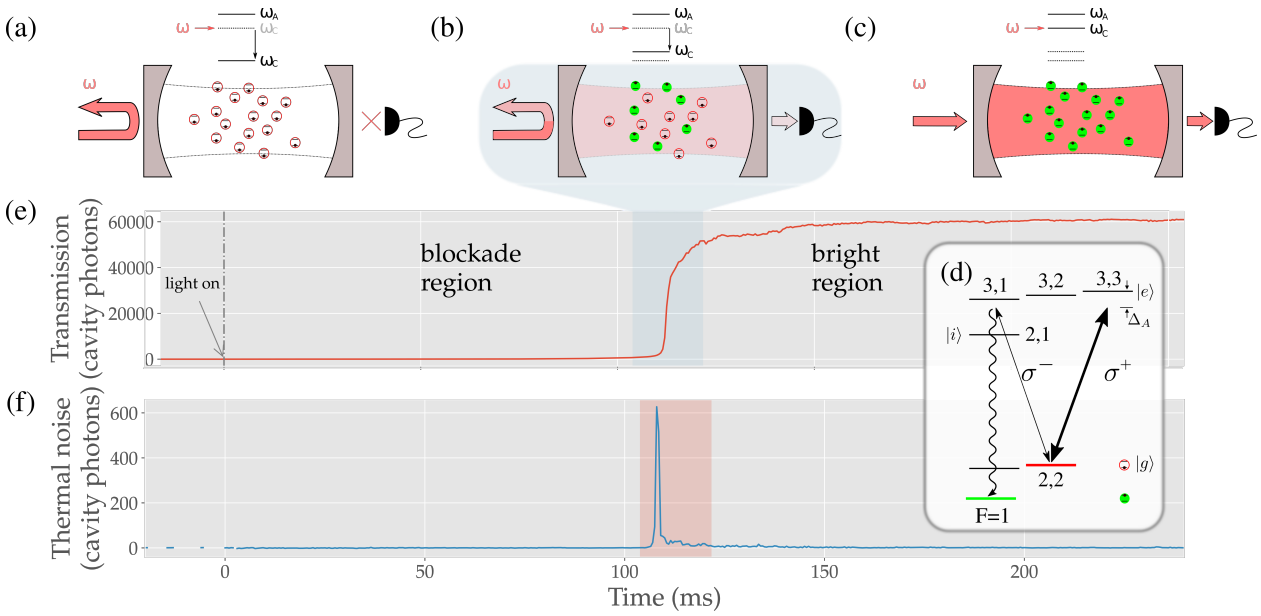

Figure 8.1: Schematic representation of the transmission blockade breakdown phase transition. Atoms can be in (a) 'red' or (c) 'green' states, blocking or permitting the light transmission through the cavity, respectively. In the transition domain (b), the atoms are in a mixture of these states. Upper level schemes show the cavity mode frequency with respect to the angular frequency of the pump laser, ω and in panel (d), red and green states are identified with the hyperfine states of ^{87}Rb (only a part of the $5^2S_{3/2} \leftrightarrow 5^2P_{5/2}$ structure is shown). Far-off-resonance σ^--polarized light provides an excitation path that assists the escape of the atoms from the blockading state, $|g\rangle$ to the $F = 1$ manifold of the electronic ground state. Atoms are first weakly excited to an intermediary state, $|i\rangle = |F = 2, m_F = 1\rangle$, before spontaneously decaying to the manifold which is optically dark with respect to the cavity mode. The time evolution of the transmitted intensity is plotted in (e), exhibiting the switch from blockaded to transparent phase around 100 ms after turning on the cavity drive. It is expressed in units of cavity photon number deduced from the detected photon flux. The transition is accompanied by the increase in cavity field fluctuations, represented in (f), in terms of thermal photon numbers extracted from the statistics of the transmitted light.

PART III

COMPUTATIONAL ASPECTS

A ROBUST ADAPTIVE QUANTUM-JUMP MONTE CARLO METHOD

9

9.1 SYNOPSIS

In this chapter we first describe the original MCWF algorithm and its issues that we set out to address with our adaptive algorithm. The latter is described in detail in Section 9.3. Section 9.4 is devoted to the numerical study of the convergence of ensembles of trajectories computed by our adaptive algorithm to the solution of the master equation. We will see (Section 9.4.1) that the problem of a finite-temperature harmonic oscillator mode driven purely by photon exchange with the bath is the most demanding of the simple generic examples, due to a kind of bosonic enhancement of the noise. In the case of a nontrivial Hamiltonian (Section 9.4.2), a contention between the ODE stepsize-control heuristic and our superimposed heuristic of jump-probability control takes place. In Section 9.5, we compare our algorithm to the integrating algorithm (Breuer & Petruccione, 1995; Homa & Diósi, 2017) of MCWF evolution, showing some realistic usecases that favor our method (Section 9.5.1). Finally, we share some insights about sampling and time averaging (Section 9.6).

9.2 PRIMORDIAL MCWF AND ITS CRITIQUE

The MCWF method aims at unravelling a master equation into a statistical ensemble of stochastic quantum trajectories, whose initial condition is a corresponding ensemble of state vectors that appropriately samples the initial density operator. Besides being a useful theoretical tool for reducing the dimensionality of the numerical problem, it furthermore reflects the – physically unrealistic – situation when an experimenter is in full control of any single copy (realization, experimental run) of the physical system, both in terms of controlling possible pure-state initial conditions and observing all the possible quantum jumps (e.g. photon decays) the system undergoes over time.

A master equation in the Born-Markov approximation in the most general – so-called Lindblad – form reads:

$$\dot{\rho} = \frac{1}{i\hbar}[H,\rho] + \sum_m \left(J_m \rho J_m^\dagger - \frac{1}{2}\left\{ J_m^\dagger J_m, \rho \right\} \right) \equiv 2\,\mathfrak{Re}\left\{ \frac{H_{\mathrm{nH}}}{i\hbar}\rho \right\} + \sum_m J_m \rho J_m^\dagger, \tag{9.1a}$$

where with the second equality we have defined the non-Hermitian "Hamiltonian"

$$H_{\mathrm{nH}} \equiv H - \frac{i\hbar}{2}\sum_m J_m^\dagger J_m. \tag{9.1b}$$

The J_m operators are called *quantum jump* – or *Lindblad,* or *reset,* or *collapse* – operators, and their maximum number is one less than the square of the dimension of the physical system (Manzano, 2020).

The state-vector initial condition $|\Psi(0)\rangle$ of a single trajectory is taken from an ensemble that appropriately samples the initial density operator $\rho(0)$ (in general, we need many state vectors from this ensemble and many trajectories *for each state-vector initial condition*). In its original form, the MCWF algorithm to evolve $|\Psi(t)\rangle$ to $|\Psi(t+\delta t)\rangle$ can be listed as follows.

1. The state vector is evolved according to the nonunitary dynamics

$$i\hbar\frac{d\,|\Psi\rangle}{dt} = H_{\mathrm{nH}}\,|\Psi\rangle\,. \tag{9.2a}$$

In the next derivations we will neglect the terms including $(\delta t)^2$ and higher powers. Then

$$|\Psi_{\mathrm{nH}}(t+\delta t)\rangle = \left(1-\frac{iH_{\mathrm{nH}}\,\delta t}{\hbar}\right)|\Psi(t)\rangle\,. \tag{9.2b}$$

Since H_{nH} is non-Hermitian, this new state vector is not normalised. The square of its norm reads

$$\begin{aligned}&\langle\Psi_{\mathrm{nH}}(t+\delta t)|\Psi_{\mathrm{nH}}(t+\delta t)\rangle\\ &\quad= \langle\Psi(t)|\left(1+\frac{iH_{\mathrm{nH}}^{\dagger}\,\delta t}{\hbar}\right)\left(1-\frac{iH_{\mathrm{nH}}\,\delta t}{\hbar}\right)|\Psi(t)\rangle \equiv 1-\delta p,\end{aligned} \tag{9.2c}$$

where δp reads

$$\begin{aligned}\delta p = \delta t\,\frac{i}{\hbar}\,\langle\Psi(t)|\,H_{\mathrm{nH}}-H_{\mathrm{nH}}^{\dagger}\,|\Psi(t)\rangle \equiv \sum_m \delta p_m,\\ \text{with}\quad \delta p_m = \delta t\,\langle\Psi(t)|\,J_m^{\dagger}J_m\,|\Psi(t)\rangle \geq 0.\end{aligned} \tag{9.2d}$$

Note that the timestep δt should be small enough that this first-order calculation be valid. Finding the appropriate δt is the main theme of this chapter. In particular, we require that

$$\delta p \ll 1. \tag{9.3}$$

This is important in order that the probability of *two jumps* occuring in the same timestep be negligible. The primordial MCWF algorithm is first order in the sense that it cannot deal correctly with events like this. Higher order MCWF algorithms have been developed by Steinbach et al. (1995), but they require a combinatorically increasing number of jump operators in order to account correctly for every possible multi-jump event.

2. A possible quantum jump with total probability δp. For the physical interpretation of such a jump, cf. Dum et al. (1992) and Dalibard et al. (1992). Choose a random number $\mathfrak{r}$ between 0 and 1, and if $\delta p < \mathfrak{r}$ – which should mostly be the case – no jump occurs and for the new normalised state vector at $t+\delta t$ take

$$|\Psi(t+\delta t)\rangle\Big|_{\text{no jump}} = \frac{|\Psi_{\mathrm{nH}}(t+\delta t)\rangle}{\sqrt{1-\delta p}}. \tag{9.4}$$

If $\mathfrak{r} < \delta p$, on the other hand, a quantum jump occurs, and the new normalised state vector is chosen from among the different state vectors $J_m |\Psi(t)\rangle$ with probability distribution $\Pi_m = \delta p_m / \delta p$:

$$|\Psi(t+\delta t)\rangle\Big|_{m\text{th jump}} = \sqrt{\delta t}\frac{J_m |\Psi(t)\rangle}{\sqrt{\delta p_m}}. \tag{9.5}$$

These steps can be easily shown to reproduce the master-equation evolution to first order in δt. Let us consider the delta of a state-vector diad on a single trajectory:

$$\begin{aligned}
&\rho_{1\text{traj}}(t+\delta t) = |\Psi(t+\delta t)\rangle\langle\Psi(t+\delta t)| \\
&= (1-\delta p)\,|\Psi(t+\delta t)\rangle\langle\Psi(t+\delta t)|\Big|_{\text{no jump}} + \sum_m \delta p_m\,|\Psi(t+\delta t)\rangle\langle\Psi(t+\delta t)|\Big|_{m\text{th jump}} \\
&= |\Psi_{\text{nH}}(t+\delta t)\rangle\langle\Psi_{\text{nH}}(t+\delta t)| + \delta t \sum_m J_m |\Psi(t)\rangle\langle\Psi(t)| J_m^\dagger \\
&= \left(1 - \frac{iH_{\text{nH}}\,\delta t}{\hbar}\right)|\Psi(t)\rangle\langle\Psi(t)|\left(1 + \frac{iH_{\text{nH}}^\dagger\,\delta t}{\hbar}\right) + \delta t \sum_m J_m\,\rho_{1\text{traj}}(t)\,J_m^\dagger \\
&= \rho_{1\text{traj}}(t) + \delta t\left(\frac{H_{\text{nH}}}{i\hbar}\rho_{1\text{traj}}(t) - \rho_{1\text{traj}}(t)\frac{H_{\text{nH}}^\dagger}{i\hbar}\right) + \delta t \sum_m J_m\,\rho_{1\text{traj}}(t)\,J_m^\dagger + \mathcal{O}(\delta t^2) \quad \blacksquare
\end{aligned} \tag{9.6}$$

This derivation displays that the first term in the rightmost part of Eq. (9.1) describes the no-jump evolution. It is a non-Hermitian evolution, because an open system is open not only at the moments of jumps, but always: the no-jump periods also leak information about the system. Hence, the no-jump evolution in general cannot remain Hermitian. Conversely, the second term in the same part of Eq. (9.1) alone is responsible for the quantum jumps.

This algorithm has several issues:

1. The no-jump evolution reduces to the Euler method of ODE evolution, which is inadequate for all but the most trivial problems.

2. The quantum jump takes finite time, since in a timestep δt, we *either* make an ODE step, *or* perform a jump. This is because in the right-hand side of Eq. (9.5), we use the unevolved state vector. Whether a jump should take a finite time has been discussed in the literature – cf. e.g. Plenio & Knight (1998) Sec. IV.C –, but here we present a strong argument that it should not.

   Let us consider a decaying harmonic-oscillator mode started from a coherent state. If we allowed jumps to take a finite time, then a single trajectory would deviate from the solution of the master equation as displayed in Fig. 9.1 (cf. the figure caption for detailed explanation). Since coherent states are (the most) classical states, we do not want to allow such a deviation, since physically a classical evolution is expected for a single trajectory as well as for the master equation or any sub-ensembles.

3. Timestep is not adaptive. This is a problem already in ODE, but in MCWF it creates the additional problem that the satisfaction of the condition Eq. (9.3) remains uncontrolled.

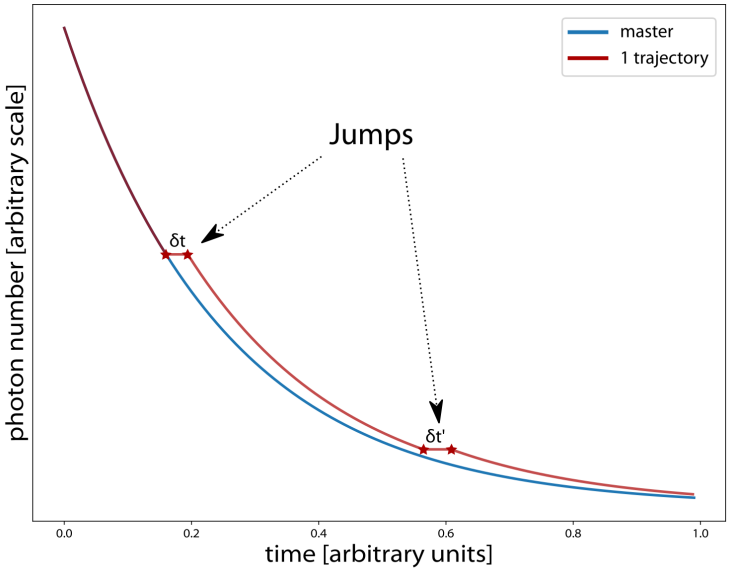

Figure 9.1: Cartoon of the evolution of the photon number in a single decaying harmonic-oscillator mode started from a coherent state. Since the coherent state is an eigenstate of the jump operator (cf. Section 9.4 with $n_{\mathrm{Th}} = 0$ for the mathematical scenery of this situation), the state remains coherent throughout, only with decaying amplitude. The blue line represents the correct solution obtained from the master equation. The red line is a single trajectory in the case when we allow jumps to take finite time. In this case, every jump introduces a temporal shift equal to the actual timestep with respect to the correct solution because the state is unchanged under a jump, the coherent state being eigenstate to the jump operator. Of course, in the timestep $\to 0$ limit, the correct behavior is recovered, however, a systematic error is introduced with finite stepsize by the incorrect treatment of jumps.

9.3 STEPWISE ADAPTIVE MCWF

While the integrating algorithm of MCWF evolution sidesteps these issues thanks to its peculiar treatment of jumps (cf. Section 9.5), we aimed at a *stepwise adaptive* algorithm that rectifies them. By 'stepwise' we mean that the possibility of one of the quantum jumps to occur is accounted for in each timestep.

1. Instead of the 1st order Euler ODE step, we use a higher order adaptive method.[1] Regarding timestep control, such a routine expects a timestep δt_{try}, which is the timestep to try in the actual step, and yields

   a) δt_{did}, the timestep actually performed

   b) δt_{next}, which is the timestep to try in the next step

   When used sequentially, δt_{try} is always equated to the δt_{next} obtained in the previous step. It is important that

   $$\delta t_{\mathrm{did}} \leq \delta t_{\mathrm{try}}, \tag{9.7}$$

   that is, the stepper is not allowed to overshoot the suggestion obtained from the step before, while δt_{next} can be bigger than δt_{did}, providing a mechanism for increasing the timestep.

1. A general-purpose choice used also in this chapter is the Runge-Kutta Cash-Karp stepper, which is fifth order with embedded fourth order error estimator.

2. ODE evolution is not optional during a timestep (this follows partly from item 1), but an ODE step is always taken, and at the end of that step, it is decided whether or not a quantum jump is taken *in addition* in the same timestep. The jump itself is instantaneous.

3. Timestep is naturally adaptive stemming from item 1, so we need to control the fulfillment of condition (9.3). For this, we introduce a new parameter Δp of the algorithm representing the maximum allowed total jump probability in a timestep. Clearly, we expect the algorithm to work correctly if

$$\Delta p \ll 1. \tag{9.8}$$

   The behavior of MCWF as a function of Δp is the main theme of the remainder of this chapter.

Our adaptive algorithm can then be summed up in the form of a flowchart as in Fig. 9.2. Superposed on the ODE stepsize-control heuristic, we use a two-layer heuristic: upon calculating the jump rates after the H_{nH} evolution,

1. the timestep guess fed back to the ODE stepper at the beginning of the next step is abridged by Δp-control as:

$$\delta t_{\mathrm{next}} \leq \frac{\Delta p}{r_{\mathrm{tot}}}, \tag{9.9}$$

   where $r_{\mathrm{tot}} = \sum_m r_m$ is the total jump rate. The problem here is that a Δp-overshot is handled only in the next step.

2. if it is found that the total accumulated probability in the given step is too high, i.e. $r_{\mathrm{tot}}\, \delta t_{\mathrm{did}} > \Delta p'$, with some $\Delta p' > \Delta p$, then the step is rejected and we go back to the beginning of the given step by restoring the state vector to a copy cached at time t. In general, the internal state of the ODE stepper needs to be cached and restored as well. The next step is tried with timestep reduced as

$$\delta t_{\mathrm{next}} = \frac{\Delta p}{r_{\mathrm{tot}}}, \tag{9.10}$$

Layer 2, introduced as a safety measure, requires additional resources (although usually negligible compared to the several copies of the state vector the ODE stepper has to store internally during a step), and our experience is that its usefulness is very difficult to quantify in real-life situations. Hence, in the following we will only study the effects of the 1st layer of control, and switch off the 2nd one (this can always be done by choosing a very large $\Delta p'$ value).

One last important difference of our algorithm compared to the original must be noted: we perform an *exact* renormalization of the state vector just before calculating the jump rates. Keeping the norm constant can be a very strong stabilizing condition for the ODE evolution, in certain problems that we will discuss in Section 9.5.1. In these problems, experience has shown that the exact renormalization can stabilize an otherwise unstable ODE evolution, or make an otherwise very small timestep bigger. The need for exact renormalization in this sense means that the integrating method, which lets the norm evolve freely and monitors its value to determine the jumps is hindered.

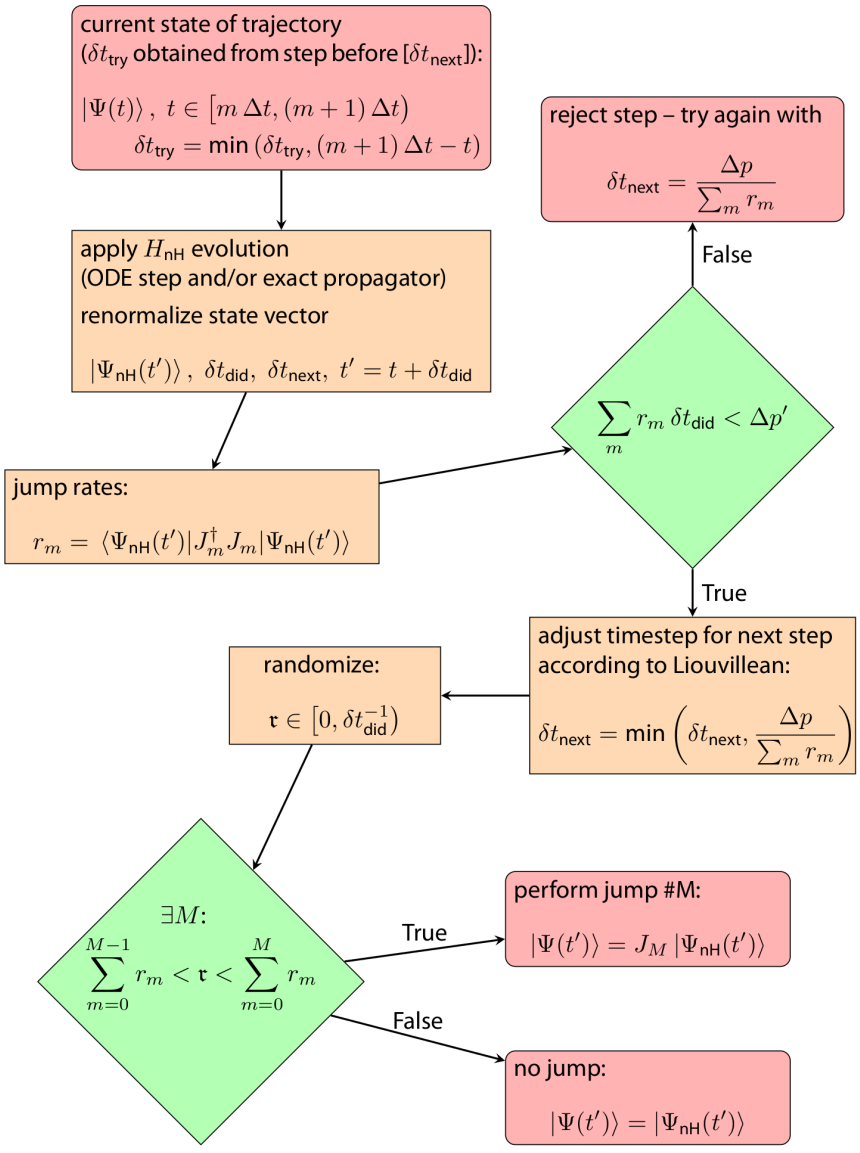

Figure 9.2: Flowchart describing a single step of our adaptive MCWF algorithm. Besides the physical parameters and those governing the ODE evolution, the parameters of the algorithm are Δt, Δp, and $\Delta p'$. The two-layer control makes sense only if $\Delta p' > \Delta p$.

It is easy to verify that the first-order-in-δt derivation of the master-equation evolution presented in Eq. (9.6) is unchanged by our modifications to the algorithm, which remains of order 0.5 despite the fact that the order of the ODE stepper can be higher. This is because the handling of the quantum jumps is essentially unchanged: we allow at most one jump per timestep.

For each timestep, we define a maximum time that the stepper is allowed to reach. This is important in order to define time instants during the trajectory at which the trajectory is sure to stop. These are defined as

$$\text{sampling times} \equiv u\,\Delta t \quad \text{with} \quad u \in \mathbb{N}. \tag{9.11}$$

Hence, at these points all the trajectories of an ensemble can be brought together e.g. for ensemble averaging (due to adaptive stepping, the trajectories have different times after fixed number of steps). As we shall see below, Δt is an important parameter that in principle pertains to the convergence of the method.

9.4 CONVERGENCE

To study the convergence properties of the adaptive MCWF as a function of Δp, we choose a very simple system: a single harmonic-oscillator mode interacting with a finite-temperature reservoir. If a denotes the annihilation operator of the mode excitations, the jump operators read:

$$J_0 = \sqrt{2\kappa(n_{\mathrm{Th}}+1)}\,a \qquad \text{(photon emission)}, \tag{9.12a}$$

$$J_1 = \sqrt{2\kappa\, n_{\mathrm{Th}}}\,a^\dagger \qquad \text{(photon absorption)}. \tag{9.12b}$$

We set the timescale such that $\kappa = 1$.

The mode can be driven by a coherent drive, that we will consider resonant with the mode frequency, in which case we find a time-independent Hamiltonian in the frame rotating with the frequency of the drive:

$$H = i\hbar\,\eta\left(a^\dagger - a\right), \tag{9.13}$$

where η is the Rabi frequency of the drive. The non-Hermitian Hamiltonian reads:

$$H_{\mathrm{nH}} = -i\hbar\,\kappa(2n_{\mathrm{Th}}+1)\,a^\dagger a + i\hbar\,\eta\left(a^\dagger - a\right). \tag{9.14}$$

The coherent drive tends to impose a coherent steady state even on a single trajectory, which is stabilized also by the photon emission (eigenstate of J_0), the photon absorption being the only mechanism acting against it.

9.4.1 Pure Δp-control

Let us first study the case of $\eta = 0$ and Fock-state initial condition, which is the most demanding of simple examples. One reason for this is that in the lack of coherent driving, the just discussed stabilization mechanism on a single trajectory is absent. The other reason is a manifestation of bosonic enhancement: the photon exchange with the reservoir is the more intense, the larger the photon number the mode already has. Therefore, the photon number along a single trajectory fluctuates wildly, with cascading absorptions

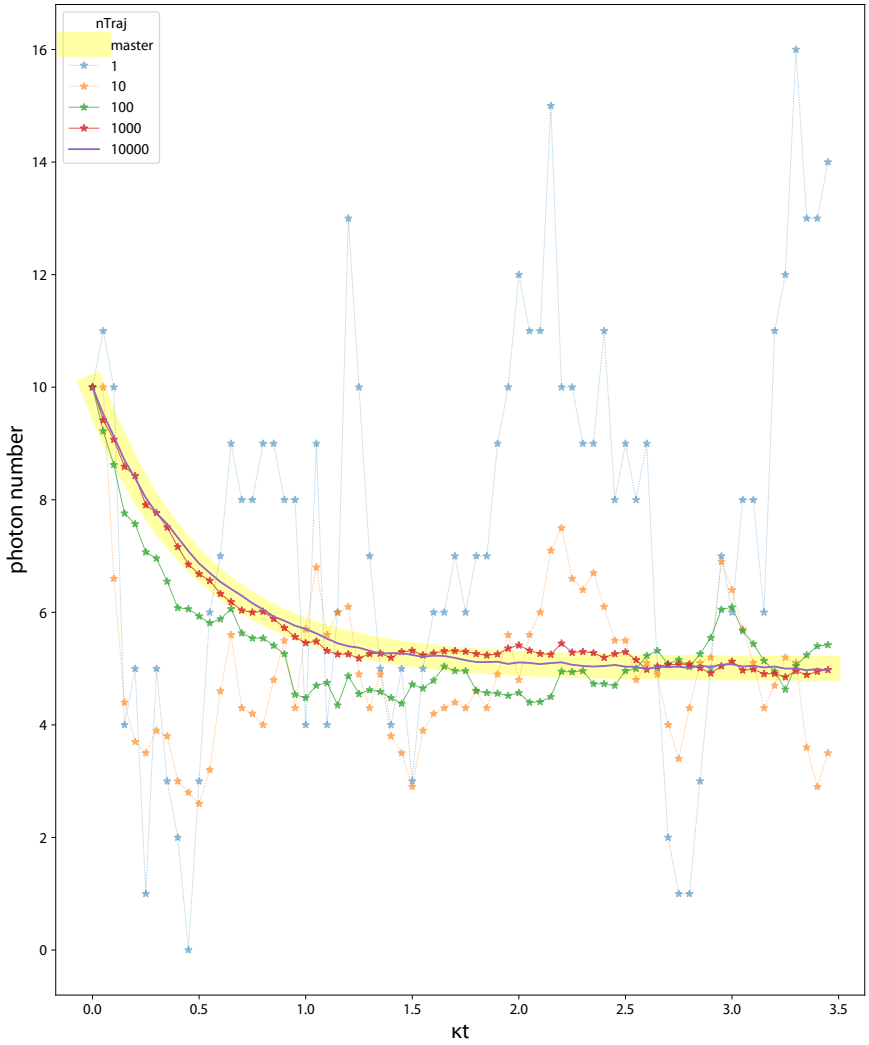

Figure 9.3: A typical picture of convergence of the MCWF solution to that of the master equation (midline of the yellow stripe) as a function of the number of trajectories. A single trajectory fluctuates wildly, without any appreciable relaxation of the initial state to the steady one. Even with 10^3 trajectories we see significant deviations, but the average of 10^4 trajectories fits nicely. Parameters: $n_{\mathrm{Th}} = 5$, $|\Psi(0)\rangle = |10\rangle$, $\Delta p = 0.1$, $\Delta t = 0.05$.

and emissions. To illustrate this, and give the reader a taste about the number of trajectories needed for acceptable convergence, we display the time evolution of the average photon number over trajectory ensembles of various sizes in Fig. 9.3. Here, $n_{\mathrm{Th}} = 5$ and $|\Psi(0)\rangle = |10\rangle$, so that the photon number along the master-equation evolution stays in the interval between 5 and 10. Yet, in ensembles on the order of one million trajectories, we have encountered single trajectories that overshoot a Fock-state cutoff of 200!

The lack of driving and the Fock-state initial condition means that the MCWF method is drastically simplified to a classical Markov chain in Fock space, since in this case the mode state will remain a number state throughout the evolution. The process could be treated exactly by using random numbers with exponential distribution for the waiting time till the next jump, and simply hopping from one jump to the next in time. However, when regarded as a

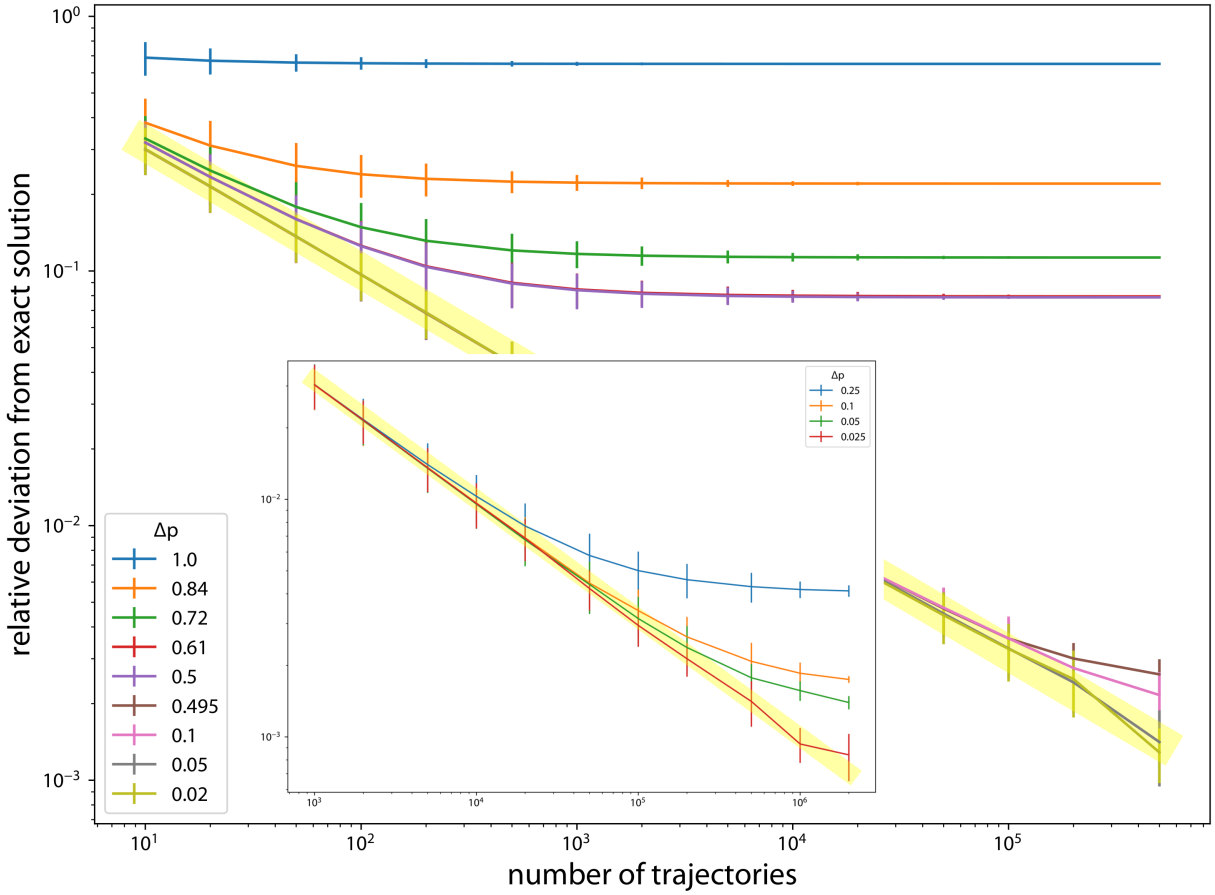

Figure 9.4: Same parameters as in Fig. 9.3, but with varying Δp. The midline of the yellow stripe is the line $\frac{1}{\sqrt{\text{number of trajectories}}}$, which coincides with a linear fit (in log-log scale) on the curve for $\Delta p = 0.02$. The three features to be noted in the Figure are: (1) the general trend of bettered convergence with decreasing Δp; (2) the flattening out of the curves with increasing number of trajectories, which occurs at the larger number of trajectories, the smaller Δp we have; (3) the critical behavior at $\Delta p_c = 0.5$ (the curve for $\Delta p = 0.61$ virtually coincides with the one at 0.5!), below which there is a sharp drop in the deviation. The inset exposes the flattening-out behavior on a more suitable scale. These three features are explained in the text. To avoid misunderstandings, we note that here and throughout this chapter, we use artificially big values of Δp in order to magnify the effect of finite Δp for the purpose of presentation. In practice, we use values on the order of 10^{-2}.

special case of our adaptive algorithm with the superimposed criterion of equally distributed sampling times, the behavior becomes nontrivial.

Our main result is displayed in Fig. 9.4. Here we plot the deviation of trajectory ensembles from the exact (master-equation) solution as a function of the size of the ensemble. The deviation is measured by

$$\text{deviation}(f,g) \equiv \frac{2\|f-g\|}{\||f|+|g|\|}, \quad \text{with} \quad \|f\| \equiv \int_0^T \mathrm{d}t\, |f(t)|, \tag{9.15}$$

where f and g are functions of time over the interval $[0, T]$, these are the expectation values of the physical quantities along the trajectory.

The general trend that a decreasing Δp betters the convergence is obvious, although we observe a striking critical behavior at $\Delta p_c = 0.5$: for larger Δp

values, the curve flattens out to a relatively high value with increasing number of trajectories and the curve already at $\Delta p = 0.61$ is virtually indistinguishable from the limiting curve at Δp_c. On the other hand, for values smaller than the critical, the Δp-dependence can be captured only with a number of trajectories on the order of hundreds of thousands: the larger Δp, the smaller the number of trajectories for which the curves start to flatten out.

The MCWF method has two layers of errors. The first layer comes from discretization: the jumps can happen only at the endpoints of the timesteps. It is easy to see that the probability of a single jump happening evaluated at the end of the timestep is always smaller than what would come from the exact exponential waiting-time distribution, so that due to discretization the number of jumps gets smaller than the exact value. The second layer comes from the missed multi-jump events due to the first-order nature of the method, which also amounts to a smaller number of jumps than what we would have on an exact jump trajectory. As exposed in Section 9.B, both these kinds of error scale with the square of an average timestep, which in turn scales with Δp^2.

The fact that the lower Δp-curves in Fig. 9.4 follow a line $\frac{\text{const.}}{\sqrt{\text{number of trajectories}}}$ (where the constant happens to be 1 within the errorbars of a least-square fit) up to a certain limiting number of trajectories, is a manifestation of the law of large numbers, given that the trajectories are independent. So what we observe in this region is the statistical error of averaging a finite set of independent trajectories. The flattening-out as a function of the trajectory number starts when this statistical error reaches the same order of magnitude as the intrinsic error of the method explained above, which of course happens with the larger number of trajectories, the smaller Δp we use. However, even though our statistics is large, we do not seem to be able to verify the Δp^2-dependence of the intrinsic error in the figure.

Let us return to the critical behavior, which is further exposed in Fig. 9.5, where we plot certain average characteristics of the trajectories as a function of Δp, the criticality being present in each. On panel (f), we can see that for $\Delta p > \Delta p_c$, the method even misses the correct number of average jumps, and even the difference between the two kinds of jumps is rendered incorrectly. (This latter is obtained trivially: since the system starts form the 10-photon state, and the steady state is the 5-photon state [$= n_{\text{Th}}$], the average difference should be 5.) It should be noted that the number of MCWF steps continues its steep increase for subcritical Δp values (cf. panel [e]), while the quality of convergence doesn't increase appreciably (cf. panel [a]).

The "smoking-gun evidence" for the cause of the critical behavior is presented by the green lines on all panels and by panels (b,c):

The green lines While in Fig. 9.5, the sampling time $\Delta t = 0.05$, for the green lines we chose $\Delta t = 0.25$, and see that the criticality disappears with this choice.

Panel (b) The timestep averaged over the trajectory drops sharply at the critical point.

Panel (c) The possibility of taking full Δt steps ceases at the critical point (curve drops to exactly 0 for $\Delta p < \Delta p_c$).

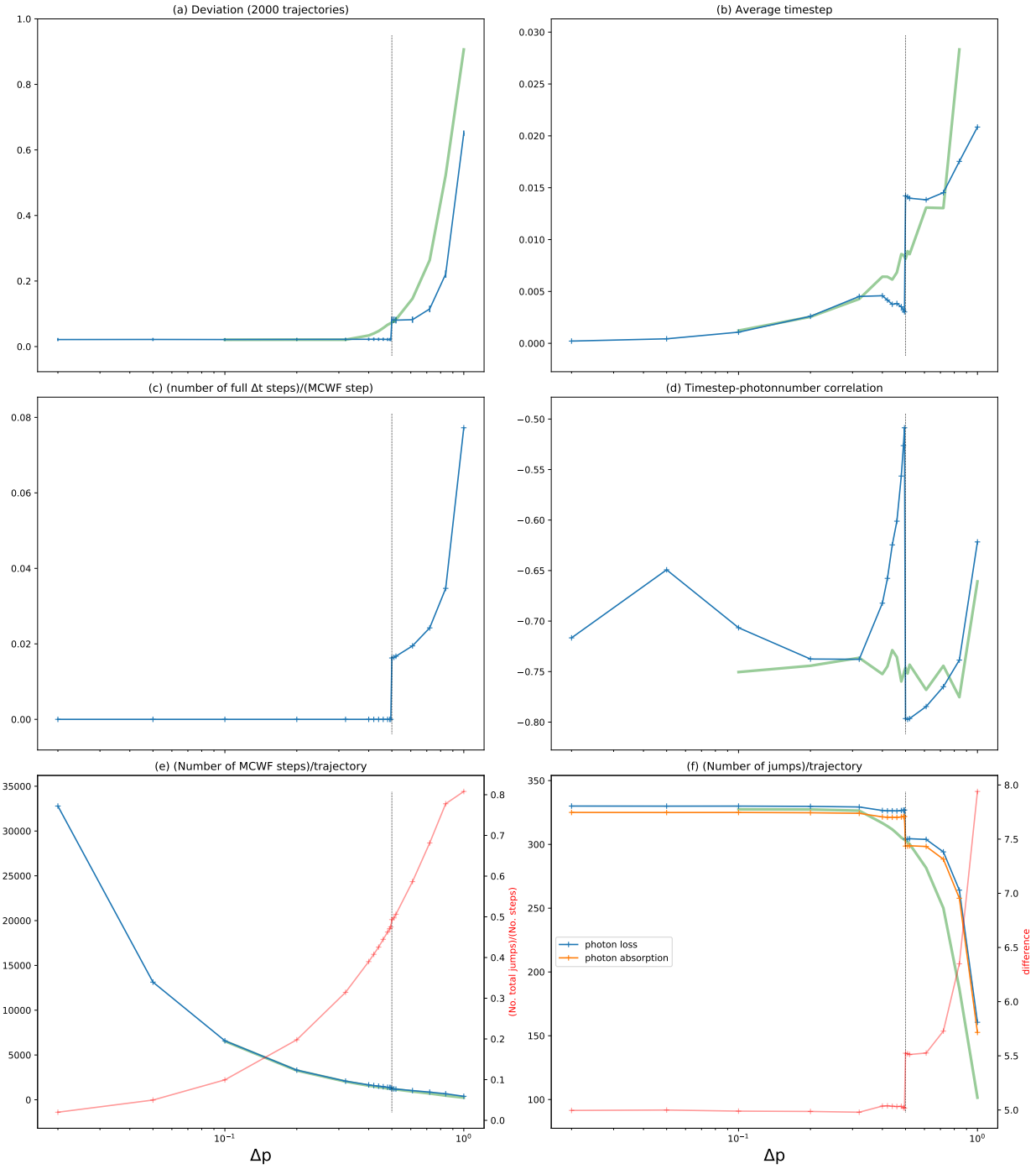

Figure 9.5: Important characteristics of MCWF evolution as a function of Δp with same parameters as in Fig. 9.4. The discontinuity observed on the panels is explained in detail in the text. For the green lines, $\Delta t = 0.25$, and they are plotted in order to show the behavior without discontinuity. In panel (f), the green line represent the mean of the two kinds of jumps. The average timestep on panel (b) and the correlation between the stepsize and the photon number in panel (d) are taken along a trajectory and over the full ensemble of trajectories as well.

In conclusion, the criticality depends strongly on Δt, being related with the possibility of taking full Δt steps. Let us explain: In our present case, when the timestep is controlled purely by the relation Eq. (9.10), we can determine the condition for the system to be able to take a full Δt step when in the Fock state n:

$$\Delta t \leq \frac{\Delta p}{r_{\mathrm{tot}}(n)} = \frac{\Delta p}{2\kappa\left[(n_{\mathrm{Th}}+1)\,n + n_{\mathrm{Th}}(n+1)\right]} = \frac{\Delta p}{2\kappa\left[(2n_{\mathrm{Th}}+1)\,n + n_{\mathrm{Th}}\right]}. \tag{9.16}$$

This gives a critical Δp value for each Fock state for the case when the equality sets in:

$$\Delta p_{\mathrm{c}}(n) = 2\kappa\,\Delta t\left[(2n_{\mathrm{Th}}+1)\,n + n_{\mathrm{Th}}\right]. \tag{9.17}$$

The smallest Δp value given by this is for $n = 0$, which gives us the value of the critical point observed in the figure as:

$$\Delta p_{\mathrm{c}} = \Delta p_{\mathrm{c}}(0) = 2\kappa\, n_{\mathrm{Th}}\,\Delta t, \tag{9.18}$$

equaling 0.5 for the parameters used in Figs. 9.3 to 9.5. Why does the cessation of the possibility of taking full Δt steps cause a drop in the average timestep and a feature also in the other characteristics plotted in Fig. 9.5? Assume the system has just undergone a sampling at time $u\,\Delta t$ with some $u \in \mathbb{N}$, and it is in the oth Fock state at this instant. Then, for supercritical Δp, it will directly jump to the next sampling time instant $(u+1)\Delta t$, while for a Δp value just below Δp_{c}, it will take a step just short of this next sampling time instant, so that it needs to take a very small step to finish the full Δt interval. It is the appearance of such small fragmentary steps that make the average timestep drop at the critical point.

The drop in the deviation of an ensemble of trajectories from the master-equation solution can also be explained from the drop seen in panel (b). In fact, the quality of convergence of the MCWF depends not directly on Δp, but on the average stepsize: the smaller the timestep, the less probable we miss jumps via two-jumps-per-timestep events, hence, the better our (first-order) MCWF is. The dependence on Δp is only via the dependence on the timestep.

The sharp feature in panel (d) at Δp_{c} can also be explained. Generally, the higher the photon number, the smaller steps we have to take, so that overall, the timestep-photonnumber correlation must be negative, which is what we see. The lower the Δp, the stricter the stepsize control, so that the correlation with the photon number should increase in modulus, that is actually the case for $\Delta p > \Delta p_{\mathrm{c}}$. At the critical value, the small fragmentary steps appear, whose size is largely independent of the photon number, hence the sudden drop in the modulus of the correlation.

On changing parameters, the above picture of the criticality is confirmed. First of all, the green lines in Fig. 9.5 represent the case $\Delta t = 0.25$, where the criticality disappears because $\Delta p_{\mathrm{c}} > 1$ according to Eq. (9.17). In Fig. 9.6 we present three further cases: for $\Delta t = 0.05$ as above, but $n_{\mathrm{Th}} = 4$ and 6 the critical point is given as 0.4 and 0.6; while in the case of $\Delta t = 0.015625$ and $n_{\mathrm{Th}} = 5$, Eq. (9.17) even predicts two critical points below 1, since $\Delta p_{\mathrm{c}}(0) = 0.15625$ and $\Delta p_{\mathrm{c}}(1) = 0.5$. These predictions are confirmed by the figure.

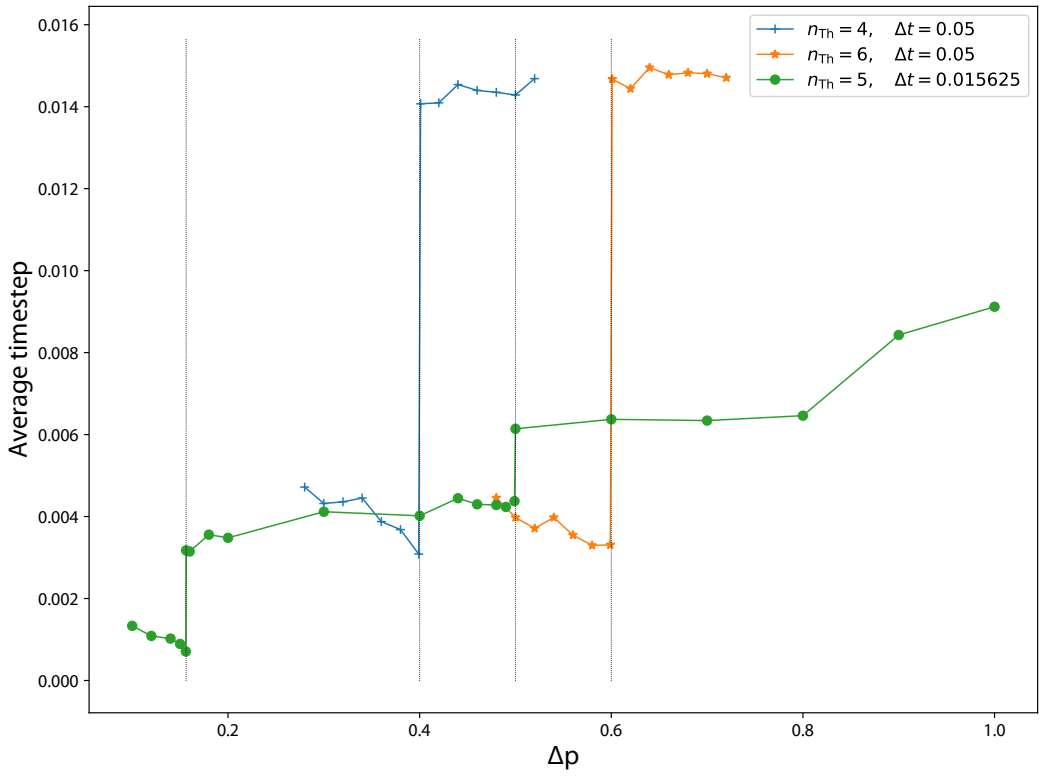

Figure 9.6: Behavior of the stepsize as a function of Δp for three sets of parameters. The criticality (which is even doubled for the green line) follows the prediction of Eq. (9.17).

9.4.2 *Contention with ODE-control*

Let us look at how the above picture is modified if the mode is driven coherently with amplitude η, that is, the Hamiltonian (9.13) is nontrivial, meaning a nontrivial ODE evolution with its own internal stepsize control. This control will contend with our superimposed Δp-control.[2]

In many situations of physical interest, a generic behavior that was noticed already in (Vukics et al., 2005) is that off-diagonal elements of the density matrix converge slower than diagonal ones. In the present case this makes that the phase of the field converges worse than the amplitude, which we have found difficult to prove in a clear-cut way. A possible physical interpretation of this behavior could be that the photon loss measures the photon number. This suggests that a homodyne detection could result in opposite behavior, however, this we could not prove either in a distilled way.

In Fig. 9.7(a) we display the average timestep as a function of Δp with three different values of η. The dashed lines are predictions based on Eq. (9.10) assuming pure Δp-control:

$$\overline{\delta t}_{\Delta p\text{-controlled}} = \Delta p \, \overline{\frac{1}{r_{\mathrm{tot}}}} = \Delta p \, \overline{\frac{1}{2\kappa\big((2n_{\mathrm{Th}}+1)a^\dagger a + n_{\mathrm{Th}}\big)}}, \tag{9.19}$$

where the overline means averaging over time along one trajectory and averaging over (an ensemble of $2 \cdot 10^4$) trajectories as well.

The main message of the figure is that for small Δp, Δp-control dominates, so that the curves overlap with Δp-controlled timestep, while for increasing Δp,

2. For the sake of clarity, we remark that *a priori*, jumps never come without a Hamiltonian to reckon with in the form of the non-Hermitian part, cf. Eq. (9.1b). Furthermore, this part scales with system parameters and state in the same way as the total jump probability. In the case when this "obligatory" part of H_{nH} is diagonal in the working basis, it can be treated with an exact propagator (this is what C++QED does), so that it does not burden the ODE stepper. In the case studied in Section 9.4.1, when the state remains a Fock state all along, this term moreover amounts to nothing more than a trivial norm factor, which anyway disappears during the renormalization after each timestep. So in this case it is possible to completely disregard this "coherent" part of the evolution. In more involved uses, when the working basis cannot be chosen in such a way that the non-Hermitian part be diagonal, the ODE-control will dominate the timestep control due to the just mentioned scaling argument, and the superimposed Δp-control will intervene only at exceptional moments. The same is true when other parts of the Hamiltonian have the largest characteristic frequencies.

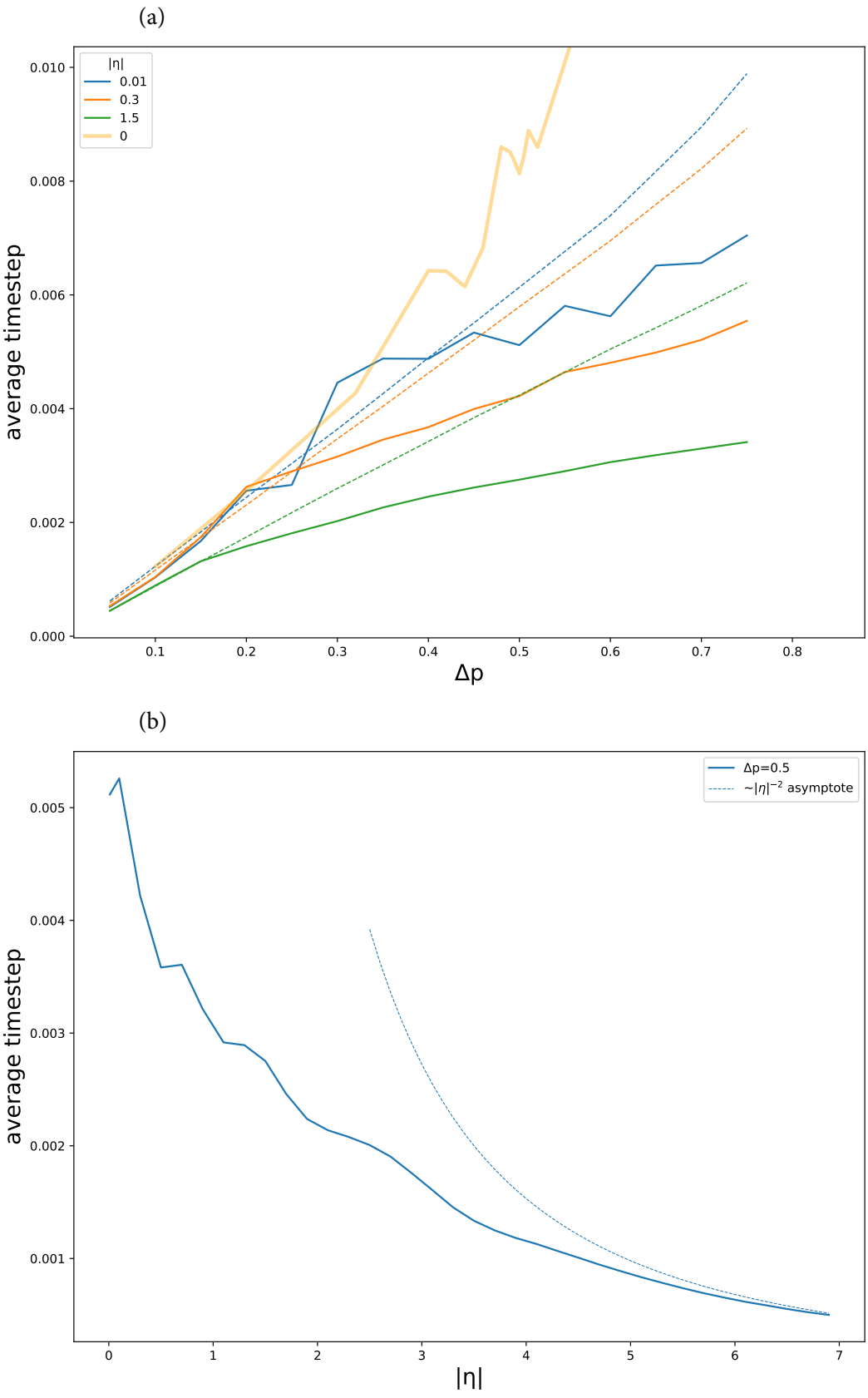

Figure 9.7: The behavior of the algorithm as witnessed by the average timestep in the case of nontrivial coherent evolution. Same physical system and parameters as in Fig. 9.4, but with finite driving amplitude η. In panel (a), the dashed lines are predictions from Eq. (9.19), with the same color code as for the solid lines.

ODE-control takes over, so that the curves flatten out, the timestep becoming independent of Δp. ODE-control depends on the largest frequency present in the system, the resulting stepsize scaling with the inverse of this frequency. This means that this control is the stricter, the larger the frequencies present in the system. This is the reason why the larger the η, the lower the Δp value at which the curves start to flatten out. For the same reason, the stepsizes are generally smaller for increasing η.

For large enough η values, pure ODE-control is established, as exhibited in panel (b) of the same figure. Here we plot the dependence of the timestep on $|\eta|$ for a rather large Δp value. We observe that the curve asymptotically coincides with the dashed one which represents a $\propto |\eta|^{-2}$ decrease. The reason for this is that in this simple case, the largest frequency in the system scales with η^2, since in the Hamiltonian (9.13), the mode amplitude is also proportional to η.

9.5 COMPARISON WITH THE INTEGRATING METHOD OF MCWF EVOLUTION

In the implementation of the MCWF method, there is another main stream, which we will refer to as "integrating" in contrast to our (adaptive) "stepwise" method. In this algorithm, the norm of the state vector is let to decrease under the evolution by H_{nH}. A random number $\mathfrak{r} \in [0, 1)$ is drawn at the beginning, and as the state-vector norm reaches this number, a jump is introduced. At this point, the distribution of jumps p_m is calculated, and the nth jump is performed where n is the smallest integer satisfying $\sum_{i=1}^{n} p_i \geq \mathfrak{r}$. It can be shown that the norm-loss equals the accumulated jump probability (hence the name "integrating method") under a very general set of conditions. The workings of the method together with the typical error that it involves are illustrated in Fig. 9.8. One needs to define a set of sampling times t_n where the norm will be compared against $\mathfrak{r}$. It is a non-trivial issue what is a good sampling interval. The source of the error of the method is that when we notice that the norm has shrunken below $\mathfrak{r}$ at time t_n, then we are already after the real time instant of the jump. Therefore, we need a mechanism to retrieve the jump time instant together with the state of the system at that time in order to perform the jump. When using linear interpolation, the error will be $|t_@ - t_*|$, which somehow scales with the sampling time interval.

One of the advantages of the method is that it enables the use of multistep methods for the ODE evolution part, although the multistepper has to be exited now and again to check the norm of the state vector, and eventually retrieve the jump time instant and perform the jumps.

The `mcsolve` routine of QuTiP (Johansson et al., 2012, 2013), uses the integrating method, the jump time within a supplied norm tolerance being retrieved by bisection root-finding combined with linearization (Paul Nation, private communication). The parameters of this algorithm are the norm tolerance (default: 0.001) and the number of maximum iterations of the root-finding algorithm (default: 5).

Our stepwise method is more conservative, conceptually simpler and more robust in the sense that it does not rely on a heuristic for retrieving the jump time instance, hence it is immune against failures of such a heuristic (for which

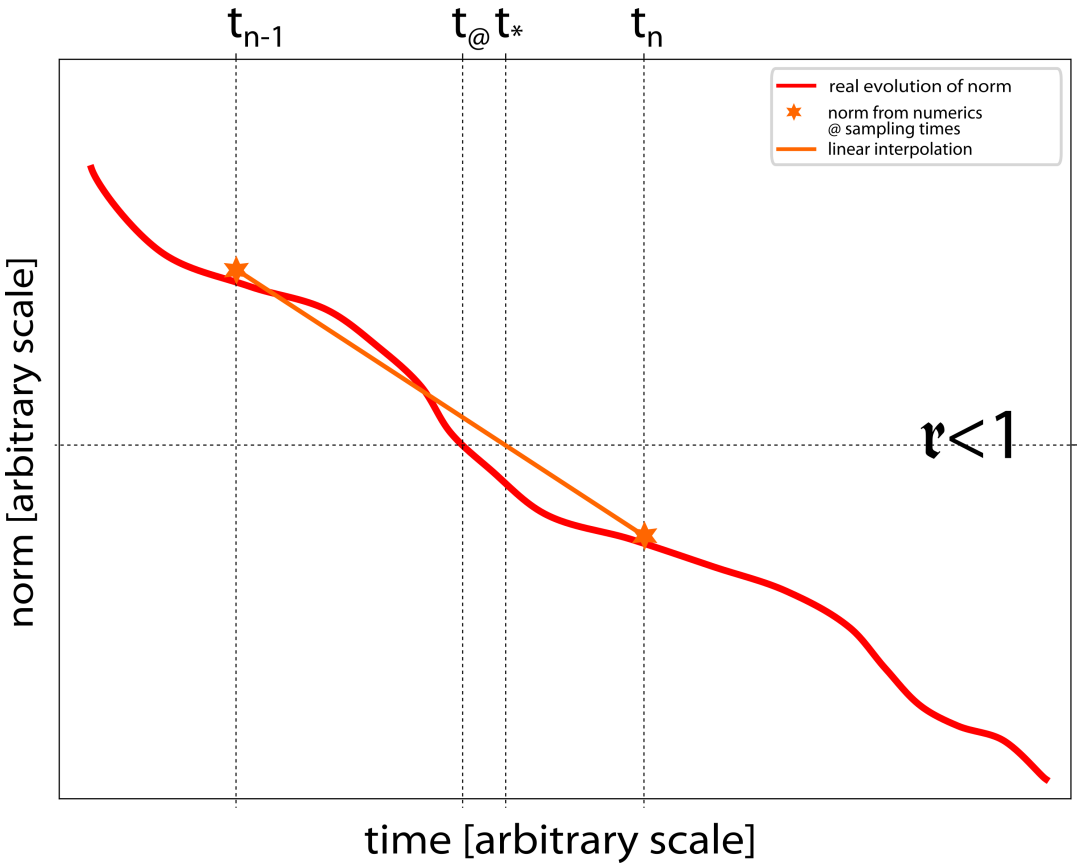

Figure 9.8: Cartoon illustrating the workings of the integrating method. t_ns are the sampling time instants when the state-vector norm is compared against the previously drawn random number r. $t_@$ would be the time instant of the jump according to the real evolution of the norm, while t_* is the jump time instant retrieved by the algorithm when using the most primitive retrieval method: linear interpolation.

there are specific error messages in QuTiP).[3] However this comes at the price of a certain reduction of performance, which is twofold:

1. The stepsize is bounded in each timestep due to the Δp-criterion, while in the integrating method it is solely the ODE stepper which controls the stepsize. This difference, however, disappears in the case when the ODE-control dominates the timestep-control, which in our experience is the case in most real-life situations (cf. Section 9.4.2).

2. The jump probabilities have to be evaluated in each timestep, instead of just calculating the norm. This overhead on the other hand can become negligible if the evaluation of the Hamiltonian (which is done several times per step within the ODE solver) is significantly more expensive, which is the case in most real-life examples we encountered so far.

Let us make two more notes of comparison favoring our method.

1. The integrating method requires more parameters for controlling the error of the MCWF, since besides the norm tolerance, further parameters are required for the routine dedicated to retrieve the time instance of the jump (e.g. number of iterations). Furthermore, the parameters controlling the specific error of the first-order MCWF are intertwined

3. According to the developers (Paul Nation, private communication), in all the usecases encountered so far, the jump time was found within the default tolerance in at most 3 iterations.

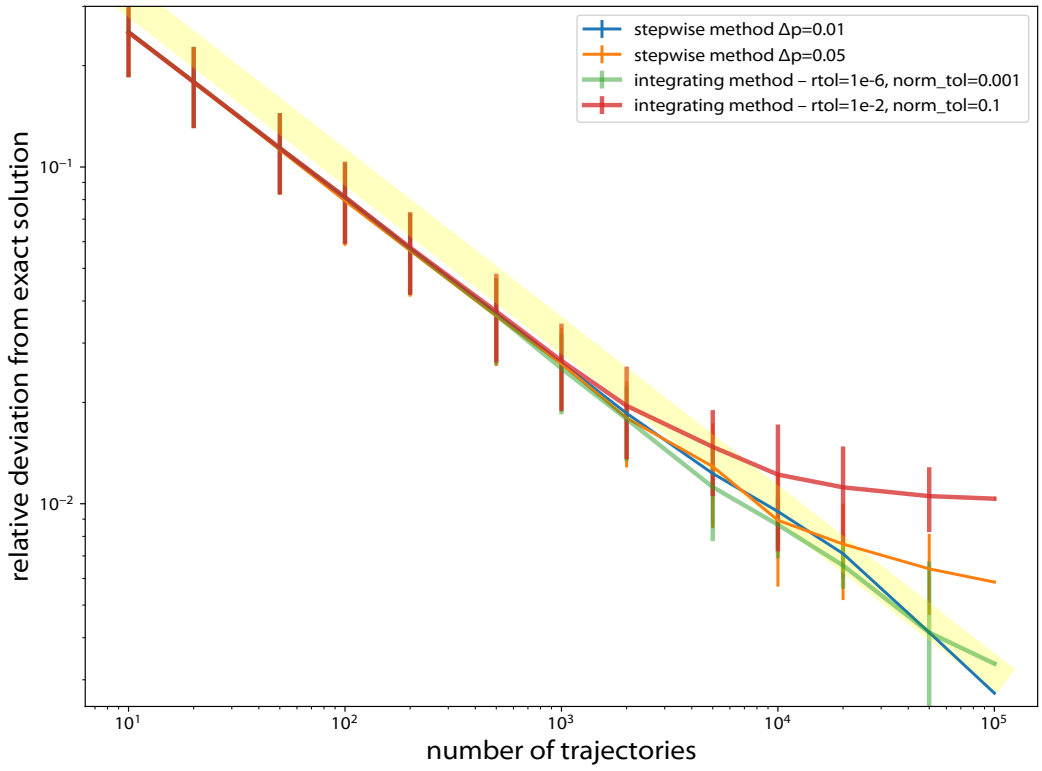

Figure 9.9: Comparison of the convergence of our adaptive stepwise algorithm with two different Δps and the integrating algorithm as implemented in QuTiP with two different sets of precision parameters. The physical system is the same as in Section 9.4.2, with same parameters as in Fig. 9.7. The yellow stripe is the same as in Fig. 9.4.

with the parameters controlling the sampling, since the larger the sampling intervals, the larger the overshoot of the real jump moment. This is in contrast to our single parameter Δp, and our stepsize control which is done either by the ODE stepper, or by the Δp condition, depending on which one is stricter. In our method it is also easy to estimate the maximum probability of two jumps occuring in a single time step, since assuming $\Delta p \ll 1$, this is given by Δp^2.

2. The possibility of exactly renormalizing the state vector after each ODE step is lost in the integrating method. This is an important stabilizing means of the method (cf. Section 9.5.1), which is available in our algorithm.[4]

Having said all this, the convergence properties of the two methods are similar when respective appropriate parameters are chosen, as illustrated on the example of the coherently driven mode interacting with a thermal bath in Fig. 9.9. As we see, the "flattening out" behavior also appears in the case of the integrating method. Note that this method is also sensitive to the issue of double jumps, being also first order in this sense: it will miss such events when two jumps would occur within the time interval corresponding to the given norm tolerance.

4. On a final note: the concept of a single adaptive step is well-defined in our case due to the possibility of jumps being immediately accounted for in each step, making our algorithm compatible with higher-level trajectory drivers.

9.5.1 *Example usecases favoring the stepwise method*

Moving-particle cavity QED Let us consider a particle of mass m with a one-dimensional motional degree of freedom. We consider periodic boundary condition in space, meaning that the particle momentum is discretized with intervals Δk, so that it is possible to define a dimensionless "wave-number operator" for the particle $\mathbb{K} = p/(\hbar\,\Delta k)$, that has integer spectrum. The particle is moving in a single-cosine-mode optical field with wave number K that is an integer multiple of Δk. The Hamiltonian then reads:

$$H = \hbar\omega_{\mathrm{rec}}\,\mathbb{K}^2 + V\cos^2(Kx), \tag{9.20}$$

where the recoil frequency is defined as $\omega_{\mathrm{rec}} = \hbar\,\Delta k^2/(2m)$, and V is an energy scale representing the coupling between the mode and the particle. This is a numerically demanding problem because of the quadratic increase of the characteristic frequencies of the different components in particle wave-number space. The quadratic increase makes that very separate timescales appear in the simulation, resulting in very small timesteps compared to the necessary simulation time. (In general, the simulation time scales with the slowest, while the timestep with the fastest timescale.) This situation can be improved by transforming into an interaction picture defined by the kinetic part of the Hamiltonian:

$$H_{\mathrm{I}} = \frac{V}{2}\Big[e^{4i\omega_{\mathrm{rec}}(\mathbb{K}-K/\Delta k)t}e^{-2iKx} + e^{-4i\omega_{\mathrm{rec}}(\mathbb{K}+K/\Delta k)t}e^{2iKx}\Big], \tag{9.21}$$

the gain by this being that the characteristic frequency now increases only linearly with $\mathbb{K}$. This can lead to an increase by a few orders of magnitude in the timestep. However, the still large frequencies in the now explicitly time-dependent Hamiltonian can lead to instabilities in the ODE stepper. We have found that an exact renormalization of the state vector after each ODE step resolves this issue. This approach has been used with success in several situations (Vukics et al., 2005; Vukics & Domokos, 2005; Vukics et al., 2007, 2009; Schulze et al., 2010; Niedenzu et al., 2010, 2012; Sandner et al., 2013; Winterauer et al., 2015).

Non-unitary interaction picture In many situations it is worthwhile to use not only a traditional interaction picture, but an exact propagator obtained by exponentializing the full diagonal part of the non-Hermitian Hamiltonian, that is, a non-unitary interaction picture. Consider Eq. (9.14), but with off-resonant driving with detuning δ:

$$H_{\mathrm{nH}} = -\hbar[i\kappa(2n_{\mathrm{Th}}+1)+\delta]a^\dagger a + i\hbar\,\eta\left(a^\dagger - a\right). \tag{9.22}$$

Here, if we pass to a traditional interaction picture

$$H_{\mathrm{nH,I}} = -\hbar i\kappa(2n_{\mathrm{Th}}+1)a^\dagger a + i\hbar\,\eta\left(e^{-i\delta t}\,a^\dagger - e^{i\delta t}\,a\right), \tag{9.23}$$

then a term contributing high frequencies with growing excitation number remains in the form of the non-Hermitian term. It can be significantly more advantageous to eliminate this as well:

$$H_{\mathrm{nH,nU}} = i\hbar\,\eta\left(e^{[\kappa(2n_{\mathrm{Th}}+1)-i\delta]t}\,a^\dagger - e^{[-\kappa(2n_{\mathrm{Th}}+1)+i\delta]t}\,a\right). \tag{9.24}$$

We see that the frequency depending linearly on the excitation number has disappeared, which again can lead to a substantial increase in the timestep. The downside is that there appeared explicitly time-dependent terms, some of which grow while others decrease exponentially in time. This can again lead to instabilities in the ODE stepper. Here again, we have found that these instabilities are removed by an exact renormalization of the state vector after each ODE step. This approach has been used with success in several situations (Dombi et al., 2013, 2015; Fink et al., 2017).

The necessity of renormalization after each ODE step in the two situations shown in this section has the consequence that the integrating method cannot be used, since the norm remains 1 during the whole evolution.

9.6 A NOTE ON SAMPLING AND TIME AVERAGING

Because of the adaptive nature of the trajectories, there are two possibilities for sampling along the evolution of a single trajectory: one can either sample (1) in equal time intervals or (2) in equal number of steps. Sampling method (2) is better suited for following the physics of the problem along a single trajectory, since at those times where a lot of dynamics takes place, the stepsize control will choose smaller timesteps resulting in more samples than in calmer times. Moreover, it is only with method (2) that the sampling does not influence the trajectory simulation in the way we saw in Section 9.4.1.

In this connection, it is important to note that when using a single long trajectory for finding steady-state results as time averages, then with sampling method (2) the time average must be calculated with weighing with the stepsize:

$$\overline{\mathcal{O}}^{(2)} = \frac{\sum_{m\in[\text{sampling steps}]} \delta t(m)\, \langle\mathcal{O}\rangle(m)}{\sum_{m\in[\text{sampling steps}]} \delta t(m)}, \tag{9.25a}$$

where $\mathcal{O}$ is an observable and $\delta t(m)$ is the timestep done in the mth step. This is because states are correlated with stepsize (cf. Fig. 9.5(d)) and hence the density of samples, so that states resulting in smaller stepsize (e.g., states with higher photon numbers in the example of Section 9.4.1) will be overrepresented among the samples. On the other hand, with sampling method (1), stepsize-weighing must not be used:

$$\overline{\mathcal{O}}^{(1)} = \frac{\sum_{t_i\in[\text{sampling times}]} \langle\mathcal{O}\rangle(t_i)}{(\text{number of sampling times})}, \tag{9.25b}$$

where the sampling times are equally distributed in time. Confusion in this respect can result in gross misestimates of steady-state values!

9.A CODE AVAILABILITY

The algorithm presented here is available as the

```
quantumtrajectory::MCWF_Trajectory
```

class in C++QED, cf. Chapter 10. In particular, all the simulations presented here can be reproduced using the `PumpedLossyMode_C++QED` script available in the framework's distribution. A sample command line simulating a single trajectory may read:

```
PumpedLossyMode_C++QED -dpLimit 0.1 -seed 1000 -cutoff 2000 -nTh 5
```

(the parameter Δp is called `dpLimit` in the framework, for historical reasons).

9.B QUANTIFICATION OF THE ERROR

In this appendix, we give a simple quantification of the behavior of the error in Fig. 9.4.

Let us introduce some notation. Let $X(t)$ denote the photon-number as a stochastic process. In the simplest case exhibited in Section 9.4.1, when the mode is driven solely by the interaction with the thermal bath, $X(t)$ is a birth-death process with generator

$$q_{nm} = \begin{cases} \lambda_n & \text{if} \quad m = n+1 \\ -\lambda_n - \mu_n & \text{if} \quad m = n \\ \mu_n & \text{if} \quad m = n-1 \\ 0 & \text{otherwise.} \end{cases} \tag{9.26}$$

where $\lambda_n = 2\kappa(n+1)n_{th}$ and $\mu_n = 2\kappa(n_{th}+1)n$. The theory of such processes is well developed, and it is known that the process X is fully determined by its state space and its generator, furthermore one can easily determine the stationary state (if it exists), the distribution of waiting times, the probability of extinction, etc.

Let $Y(t)$ denote the discretized model. In this simple case $Y(t)$ is also a stochastic process, in particular a discrete-time Markov chain, but with different transition probabilities. Since the rate of transition is fixed between jumps, so is the timestep δt. Here the transition matrix is given by

$$p_{nm} = \mathbb{P}\big[Y(t+\delta t) = m \,\big|\, Y(t) = n\big] = \begin{cases} \lambda_n \delta t & \text{if} \quad m = n+1 \\ 1-(\lambda_n+\mu_n)\delta t & \text{if} \quad m = n \\ \mu_n \delta t & \text{if} \quad m = n-1 \\ 0 & \text{otherwise.} \end{cases} \tag{9.27}$$

Note that this matrix is a valid transition matrix if and only if $(\lambda_n + \mu_n)\,\delta t \leq 1$, furthermore that $Y(t)$ is a time-discretized version of $X(t)$. In order to understand the relaxation of the curves in the figures let us examine the quantity

$$\mathbb{E}\big[X(t+\delta t) - Y(t+\delta t) \,\big|\, X(t) = Y(t) = n\big], \tag{9.28}$$

that is, the difference of the mean of the real trajectories and that of the approximated ones at one timestep away from t, given that the trajectories coincide at time t. The expected value of Y is given by

$$\mathbb{E}\big[Y(t+\delta t) \,\big|\, Y(t) = n\big] = n + (\lambda_n - \mu_n)\,\delta t, \tag{9.29}$$

while that of X needs a little bit more effort to calculate. First we will show that

$$\mathbb{P}\big[|X(t+\delta t) - n| \geq 3 \,\big|\, X(t) = n\big] = O(\delta t^3). \tag{9.30}$$

It is known that the waiting times between two jumps of a continuous-time Markov chain are exponentially distributed and independent random variables. Consider some independent, exponentially distributed random variables T_j, $j = 1, 2, 3$ with parameters γ_j, $j = 1, 2, 3$. Then

$$\begin{aligned}&\mathbb{P}(T_1 + T_2 + T_3 < \delta t)\\ &= \frac{\gamma_1\gamma_2\gamma_3}{\gamma_1 - \gamma_2}\left[\frac{\frac{1}{\gamma_2}\left(1 - e^{-\gamma_2\delta t}\right) - \frac{1}{\gamma_3}\left(1 - e^{-\gamma_3\delta t}\right)}{\gamma_3 - \gamma_2} - \frac{\frac{1}{\gamma_1}\left(1 - e^{-\gamma_1\delta t}\right) - \frac{1}{\gamma_3}\left(1 - e^{-\gamma_3\delta t}\right)}{\gamma_3 - \gamma_1}\right] = O(\delta t^3),\end{aligned} \tag{9.31}$$

which means that the probability of a continuous time Markov chain jumping at least three times in an interval of length δt is $O(\delta t^3)$, thus

$$\begin{aligned}\mathbb{E}\big[X(t+\delta t)\,\big|\,X(t) = n\big] &= \sum_m m\,\mathbb{P}\big[X(t+\delta t) = m\,\big|\,X(t) = n\big]\\ &= \sum_{m\,:\,|m-n|\le 2} m\,\mathbb{P}\big[X(t+\delta t) = m\,\big|\,X(t) = n\big] + O(\delta t^3).\end{aligned} \tag{9.32}$$

Hence, for an at-most-second-order-in-δt calculation of the expectation, we only need to calculate the probabilities

$$\mathbb{P}\big[X(t+\delta t) = m,\ \text{in at most 2 jumps}\,\big|\,X(t) = n\big],\quad \text{with}\quad m = n,\ n\pm 1,\ n\pm 2. \tag{9.33}$$

These are found to read

$$\begin{aligned}&\mathbb{P}\big[X(t+\delta t) = n,\ \#\text{jumps} \le 2\,\big|\,X(t) = n\big]\\ &\quad= e^{-q_n\delta t} + \frac{\lambda_n\,\mu_{n+1}}{q_n - q_{n+1}}\left(\frac{e^{-q_n\delta t} - e^{-q_{n+1}\delta t}}{q_n - q_{n+1}} - \delta t\, e^{-q_n\delta t}\right)\\ &\qquad+ \frac{\mu_n\,\lambda_{n-1}}{q_n - q_{n-1}}\left(\frac{e^{-q_n\delta t} - e^{-q_{n-1}\delta t}}{q_n - q_{n-1}} - \delta t\, e^{-q_n\delta t}\right)\\ &\quad= 1 - q_n\delta t + \frac{(q_n\delta t)^2}{2} + \frac{\lambda_n\,\mu_{n+1} + \lambda_{n-1}\,\mu_n}{2}\delta t^2 + O(\delta t^3),\end{aligned} \tag{9.34a}$$

$$\begin{aligned}&\mathbb{P}\big[X(t+\delta t) = n+1,\ \#\text{jumps} \le 2\,\big|\,X(t) = n\big]\\ &\quad= \frac{\lambda_n}{q_{n+1} - q_n}\left(e^{-q_n\delta t} - e^{-q_{n+1}\delta t}\right) = \lambda_n\delta t - \frac{\lambda_n}{2}(q_n + q_{n+1})\delta t^2 + O(\delta t^3),\end{aligned} \tag{9.34b}$$

$$\begin{aligned}&\mathbb{P}\big[X(t+\delta t) = n-1,\ \#\text{jumps} \le 2\,\big|\,X(t) = n\big]\\ &\quad= \frac{\mu_n}{q_{n-1} - q_n}\left(e^{-q_n\delta t} - e^{-q_{n-1}\delta t}\right) = \mu_n\delta t - \frac{\mu_n}{2}(q_n + q_{n-1})\delta t^2 + O(\delta t^3),\end{aligned} \tag{9.34c}$$

$$\begin{aligned}&\mathbb{P}\big[X(t+\delta t) = n+2,\ \#\text{jumps} \le 2\,\big|\,X(t) = n\big]\\ &= \frac{\lambda_n\lambda_{n+1}}{q_{n+2} - q_{n+1}}\left(\frac{e^{-q_n\delta t} - e^{-q_{n+1}\delta t}}{q_{n+1} - q_n} - \frac{e^{-q_n\delta t} - e^{-q_{n+2}\delta t}}{q_{n+2} - q_n}\right) = \frac{1}{2}\lambda_n\lambda_{n+1}\delta t^2 + O(\delta t^3),\end{aligned} \tag{9.34d}$$

$$\mathbb{P}\Big[X(t+\delta t) = n-2,\ \#\text{jumps} \le 2 \,\Big|\, X(t) = n\Big]$$
$$= \frac{\mu_n \mu_{n-1}}{q_{n-2} - q_{n-1}} \left(\frac{e^{-q_n \delta t} - e^{-q_{n-1}\delta t}}{q_{n-1} - q_n} - \frac{e^{-q_n \delta t} - e^{-q_{n-2}\delta t}}{q_{n-2} - q_n} \right) = \frac{1}{2}\mu_n \mu_{n-1} \delta t^2 + O(\delta t^3), \tag{9.34e}$$

from which we obtain

$$\begin{aligned} &\mathbb{E}\Big[X(t+\delta t) - Y(t+\delta t) \,\Big|\, X(t) = Y(t) = n\Big] \\ &\qquad = \frac{\delta t^2}{2} \Big(q_n^2 + \lambda_n \mu_{n+1} + \lambda_{n-1}\mu_n + (n+1)\lambda_n (q_n + q_{n+1}) \\ &\qquad + (n-1)\mu_n (q_n + q_{n-1}) + (n+2)\lambda_n \lambda_{n+1} + (n-2)\mu_n \mu_{n-1} \Big) \\ &\qquad \sim \Delta p^2, \end{aligned} \tag{9.35}$$

where the last relation is due to Eq. (9.10). This implies that as soon as $\frac{1}{\text{number of trajectories}}$ is comparable to Δp^2, the error does not decrease by increasing the number of trajectories, a phenomenon observed in Figs. 9.4 and 9.9. We also remark that Eq. (9.35) shows the local error of the means. In the case of fixed timestep, the global error can grow up to $O(\delta t)$ as well.

C++QED: A FRAMEWORK FOR SIMULATING OPEN QUANTUM DYNAMICS

10

10.1 SYNOPSIS

C++QED grew out of my PhD work, where I simulated the quantum motion of atoms in cavity fields with *ad hoc* C codes, cf. Vukics et al. (2005); Vukics & Domokos (2005). I realised that there is a lot of know-how hidden in these codes that in a few years would become unavailable even for myself. Hence, I decided to make this know-how available for a wider community in the form of a C++ application-programming framework. C++ has proved a good choice as

- it is known to be an ideal tool for expressing complex structures, due to its multiparadigm nature;
- it is a fast language due to its being essentially C deep down;
- it has good library support due to its having been one of the most popular languages in software industry for decades;
- and it has convenient toolchains available on Linux systems used in most high-performance-computing scenarios.

In this Chapter, I sketch the basic idea, the structure, and a very little of the implementation of the framework. I present a design pattern relying on the multi-array concept that should be generic for the representation of composite quantum systems, and some further patterns of how high-level computing can be utilized in scientific computing, in physics, and, in particular, in simulations of small (open) quantum systems.

10.2 BASIC SPECIFICATION

The framework provides two types of building blocks for composite quantum systems:

1. elementary free subsystems, where "free" means that the system has only one quantum number;
2. interactions between such free systems.

Time-evolution drivers are provided for systems composed of these elements:

1. Full master-equation solution for the density operator of the system, cf. Eq. (9.1). Given that the system is represented on a discrete Hilbert space, this is a simple adaptive-stepsize ordinary differential equation (ODE) evolution, whose dimension is the square of the dimension of the system Hilbert space.

2. Monte Carlo wave-function (MCWF) trajectory for a stochastic state vector of the system, with the adaptive algorithm discussed in Chapter 9. This reproduces the Schrödinger-equation evolution in the case when the system is closed.

3. Ensemble of MCWF trajectories. Here, the trajectories are all evolved to certain time instants, cf. Eq. (9.11), at which points the approximate density operator of the system is assembled from the ensemble of stochastic state vectors:

$$\rho_{\text{ensemble}}(t) = \frac{1}{\text{number of trajectories}} \sum_{i \in \{\text{set of trajectories}\}} |\Psi_i(t)\rangle \langle \Psi_i(t)| . \tag{10.1}$$

   This density operator is then used to gain information about the state of the system, in exactly the same way as if it was obtained from a full master-equation solution.

These modules together provide a high-level C++ application-programming interface. Normally, they are assembled in high-level C++ programs (which we will refer to as *script*s throughout), which specify the system and what to do with it. Example scripts will be given in Section 10.4. Hence, in normal usage to each physical system there corresponds a program which uses the framework as a library.

The framework strives to facilitate the implementation of new building blocks. There are classes representing quantum operators with their appropriate algebra, so that e.g. to express the Hamiltonian of the paradigmatic Jaynes-Cummings interaction

$$\frac{H}{i\hbar} = g^* \sigma a^\dagger - \text{h.c.} \tag{10.2}$$

it is possible to write

```
1 tridiagMinusHC(conj(g)*sigmaop()*aop(mode).dagger()).
```

An important principle in the design and implementation of the framework was that all information which is available at compile time, should be processed at compile time. This leads to optimal separation between the two types of information, the information available at compile time and the information becoming available only at runtime, and allows for maximal exploitation of compile time. Normally, a script compiled once will be used many times for data collection.

The idea of composing systems out of elementary building blocks would fail if too many building blocks were required for realistic systems. Experience shows, however, that for a given problem domain, only a few such blocks are required for building arbitrarily complex systems in the domain. Furthermore, every such block has a clear physical meaning. The example of polarizable particles moving in optical (cavity or free) fields was presented in Sec. 5 in Vukics & Ritsch (2007).

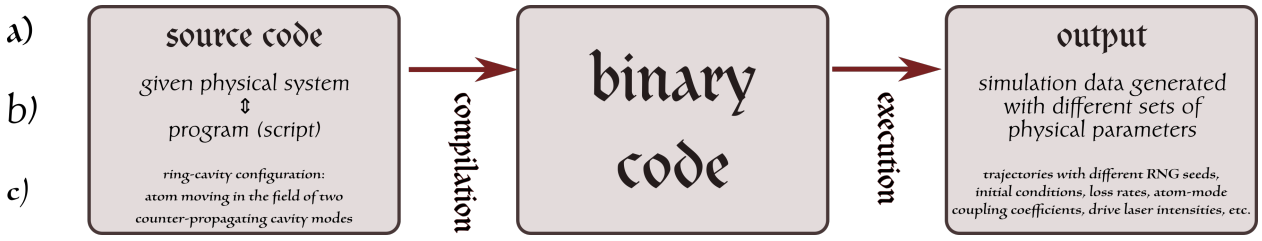

Figure 10.1: (a) General scheme of compiled computer languages, (b) how it maps on the framework, and (c) to a concrete example within the framework (cf. Fig. 10.3(a)).

10.2.1 *Compile-time algorithms*

In compiled computer languages, as sketched in Fig. 10.1, source code goes through two stages to produce output:[1]

1. the compilation resulting in an executable (binary) code and
2. the actual execution producing the data.

Usually, calculations are performed during stage 2 only, but C++ provides tools[2] to abritrarily process information available in stage 1 as well. Hence, compilation is useful not only for performing optimizations, but it is possible to shift calculations from stage 2 to here.

Let us see how compile-time algorithms come about in the definition of composite quantum systems. Such systems have several quantum numbers, and their state vector is most conveniently represented by an entity having as many indices.[3] Consider the following two possibilities:

1. The rank of the system is an information that becomes available only at runtime.[4]
2. Or, it is an information available already at compile time, the way it is treated in C++QED.

If we have two state vectors of different arity $\Psi^{(\text{rank}_1)}$ and $\Psi^{(\text{rank}_2)}$, then in the first case they have to be represented by entities of the *same type,* while in the second case they *can be different types.* Therefore, a nonsensical expression like

$$\Psi^{(\text{rank}_1)} + \Psi^{(\text{rank}_2)}$$

causes a probably fatal error in the first case, which can be detected only at runtime, possibly after a lot of calculations. In the second case, however, such an expression can be a *grammar error* prohibiting compilation. Furthermore, for indexing such a state vector, in the first case a runtime loop is needed, which is not necessary in the second case, where this loop can be unravelled at compile time.

In C++QED, since a script corresponds to a given physical system, the layout of the system is known at the time we compile the script, so that its arity is naturally also known. This then implies a lot of further compile-time calculations (cf. Section 10.5.1). Furthermore, many errors related to inconsistencies in the system layout can also be detected at compile time.

Very roughly, we can think about C++QED scripts as C++ programs which exploit the compile-time metaprogramming machinery of C++, to generate

1. In contrast, in interpreted languages like Python and JavaScript, these two stages are fused.

2. Before C++14, *the* tool was template metaprogramming (TMP), cf. Abrahams & Gurtovoy (2004), whose basic operands are the C++ *types.*

3. This is referred to as the 'rank' or 'arity' of the system or state vector: un*ary,* bin*ary,* tern*ary,* quatern*ary,* etc.

4. This is the case in the QuTiP Python package (Johansson et al., 2012, 2013).

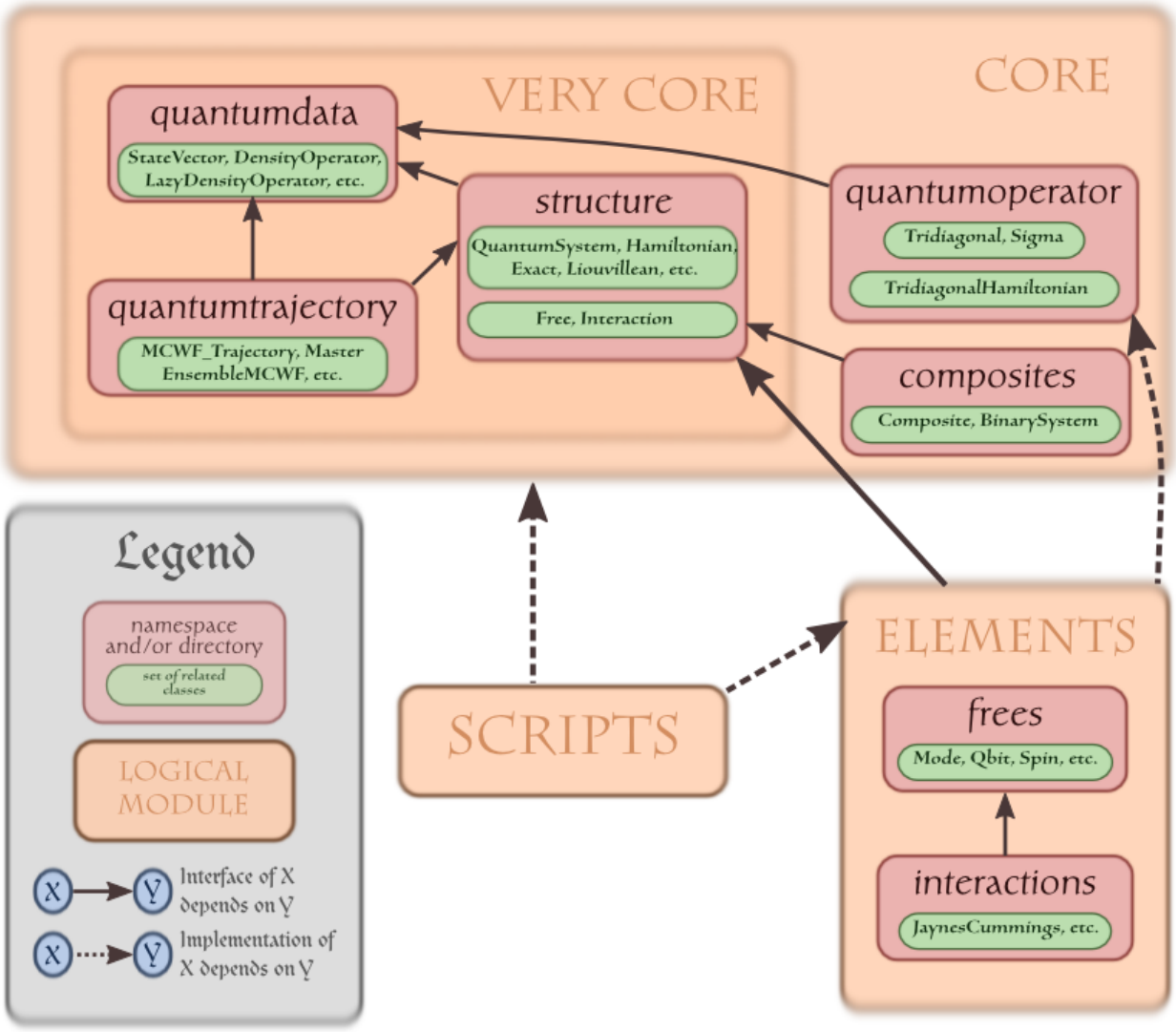

Figure 10.2: Tracts of the framework and their relationships. We display only a rudimentary list of classes, with no pretension to completeness.

(lower-level) C++ programs in such a way that in the resulting executable all compile-time information is encoded to yield a maximally effective and safe application for the given physical system.

In C++QED, compile-time resource requirement scales with the complexity of the simulated system, while runtime resource requirement scales with the total dimensionality. Hence, compile time can be best exploited when the system is composed of a lot of subsystems, all with low dimensionality. As an example, we might think of several qubits with complex interactions. For benchmarks cf. Vukics (2012).

10.3 STRUCTURE

The structure of the framework is sketched in Fig. 10.2. This structure is reflected on the build system, dependencies being strictly defined and observed throughout.

The very core is composed of the following namespaces:

`quantumdata` defines data structures. It is completely autonomous, not depending on the rest of the framework, but all the rest directly or indirectly depends on it.

`structure` defines such interfaces as quantum systems must or may present towards time-evolution drivers (or other clients). E.g. every system *must* be derived from the abstract interface class `QuantumSystem` to be usable with the time-evolution drivers. A system *may* derive e.g. from `Hamiltonian`, if its dynamics has a Hamiltonian part.

`quantumtrajectory` defines the time-evolution drivers.

The `quantumoperator` namespace constitutes a separate tract defining classes for representing special operator structures to facilitate the implementation of new elements. So far, tridiagonal and sparse matrices have been implemented: these cover most of the usecases in quantum optics.

The `Composite` class represents a quantum system with arbitrary complexity, that consists of a number of free constituents and a number of interactions with arbitrary arity between them. The class keeps track of all these constituents and what state-vector slices they need to operate on, as will be explained below.[5]

Elements come in two brands: in this tract free elements are independent, while interactions depend on frees. Most free and interaction elements are implemented with the help of special operator structures, so that their implementation depends on the `quantumoperator` tract. Both brands of elements derive from at least one of the classes in namespace `structure`.

5. `BinarySystem` is just a separate implementation for the frequent special case of composite systems composed only of two free elements with a single binary interaction between them.

10.4 HIGH-LEVEL USAGE

In the following, we give a flavor of how the concept of C++QED works in practice in the highest level interface. The highest level is a C++ program, which we call a *script* throughout. The framework is capable of saving (serializing/-marshalling) the full binary state of a trajectory, including that of the ODE stepper and random number generator (RNG), so that it is possible to resume any trajectory as if an interruption has not happened.

A script creates an executable which defines and simulates a system of a particular layout. All information pertaining to the layout of the system is processed at compile time. A script is composed of a part in which the system is specified, and another in which we do something with the system (simulate its time evolution).[6]

6. In this Section, the examples are taken from the field of (moving-particle) cavity QED, cf. Vukics & Ritsch (2007) for more information about the appearing physical elements.

10.4.1 An elementary example

The simplest case is a free system alone. Consider a lossy resonator mode, which may be driven ("pumped") with a laser. This is the same system discussed in Section 9.4, with $n_{\mathrm{Th}} = 0$. We begin with defining the system, which is trivial in this case:

```
1 PumpedLossyMode mode{delta,kappa,eta,cutoff};
```

where `cutoff` is the cutoff of the mode Fock space.

Suppose we want to simulate a single MCWF trajectory. The system is started from a pure initial state, specified as

```
quantumdata::StateVector<1> psi{mode::coherent(alpha,cutoff)};
```

that is, the mode is in a coherent state $|\alpha\rangle$. `StateVector<1>` means that it is a state vector of a *unary* system. Next, we define our `MCWF_Trajectory`:

```
quantumtrajectory::MCWF_Trajectory<1> trajectory{psi,mode,...};
```

The first two parameters are clear, but we omit a lot more parameters, pertaining to the ODE stepper, the RNG, etc.

The trajectory can be run with

```
run(trajectory,time,dt);
```

This will evolve the `trajectory` for `time`, and display information about the state of the system after every time interval `dt`. The set of information (usually a set of quantum expectation values) displayed is defined by the system.[7]

7. There is another version, where the number of (adaptive) timesteps between two displays can be specified. This is usually more suited to the physics of the problem, since the timesteps will be small when many things are happening, and this is when we want more output, too, cf. Section 9.6.

In the above, the necessary parameters must be previously defined somewhere. Parameters can come from several sources, but the most useful alternative especially in supercomputing environments is a command-line interface (CLI). This allows for a fine-grained control over what parameters the user wants to accept as default and what she wants to override. In the framework, this looks like:

```
1  #include "EvolutionHigh.h"
2  #include "Mode.h"
3
4  int main(int argc, char* argv[])
5  {
6    ParameterTable p;
7
8    evolution::Pars pe{p};       // time-evolution parameters
9    mode::ParsPumpedLossy pm{p}; // mode parameters
10
11   pe.evol=EM_MASTER; pm.cutoff=30;
12   // ... other default values may follow
13
14   update(p,argc,argv,"--"); // Parsing the command line
15
16   // ****** ****** ****** ****** ****** ******
17
18   evolve(init(pm),make(pm,QMP_UIP),pe);
19 }
```

`ParameterTable` in line 6 is the module realizing the CLI by storing all the parameters of the problem, and allowing them to be manipulated from the command line. We instantiate the actual parameters for the time-evolution driver(s) in line 8 and the mode in line 9. The command line is parsed by the `update` function in line 14. Line 18 does all the rest. It is here that we instantiate our mode, selecting the best `...Mode` class corresponding to the parameters.[8]

8. A mode can be driven or not, lossy or conservative, finite or zero temperature, and it can be represented in several quantum mechanical pictures. Each of these possibilities is represented by a class. E.g. if $\kappa = 0$, and $\eta = 0$, then we will have a `Mode`; if η is nonzero, a `PumpedMode`; and if both are nonzero, a `PumpedLossyMode`. The significance of this is that e.g. if the mode is not lossy, then it is not that the *probability* of a quantum jump will be calculated and found zero, but rather the *possibility* of a quantum jump will not even be considered during time evolution, which speeds the evolution up.

An example command line may read:

```
PumpedLossyModeScript --evol master --eps 1e-12 --dc 100 --
    deltaC -10 --cutoff 20 --eta "(2,-1)"...
```

10.4.2 *Example: a binary system*

Assume a two-level atom (qbit) interacting with a single cavity mode via the Jaynes-Cummings interaction (10.2). Both the qbit and the mode may be driven, lossy, or both.

Such a system can be represented by the `BinarySystem` class, that can be constructed like

```
auto sys=binary::make(jaynescummings::make(qbit::make(pb,qmp),
                                           mode::make(pm,qmp),
                                           pjc));
```

where `pb`, `pm`, and `pjc` are parameter objects that can be constructed similarly to the above.

In the case of a binary system, the complete layout of the system can be figured out from the single interaction element – and this is trivial. `BinarySystem` is a simplified version of `Composite` (cf. Section 10.4.3). Both are quite powerful modules, whose design reflects the basic idea behind the framework. `BinarySystem` internally handles all the loops and slicing necessary to calculate the effect of the Hamiltonian of the qbit component if it is part of a binary system (cf. Section 10.5.1). It acts and feels like any other system, like `Mode` itself, with the difference that the latter has only one quantum number, while `BinarySystem` has two.

Such a system can be evolved in the same way we saw above:

```
evolve(qbit::state0()*mode::coherent(alpha,cutoff),sys,pe);
```

where we chose to specify a concrete initial condition.

Henceforth, usage is the same as we have seen in the mode example. `BinarySystem` will reach into its constituents for the informations to display (the quantum expectation values), supplying either with the corresponding reduced density operator (cf. Section 10.5.2), which contains all information about the state of the subsystem.

10.4.3 *More complex examples*

If there are more than two free subsystems, the system can be much more complex. The number of possible interactions rises combinatorically with the number of free constituents. This is the situation where the full potential of C++QED is displayed.

Assume a system with a particle moving along the axis of a ring cavity, and interacting with two counterpropagating running-wave modes of the cavity (Niedenzu et al., 2010). Both modes are lossy, and one is also driven. This system consists of three subsystems, a particle[9] and the two modes. There are three interactions:

9. More precisely: a one-dimensional motional degree of freedom.

(1-2) The particle can absorb a photon from either of the modes and emit it in a stimulated way into the *same mode*. This yields dipole force for the particle and a corresponding light shift for the mode. It is implemented by the interaction element `ParticleAlongCavity`.

(3) The particle can emit the photon absorbed from one of the modes into the *other mode*. This yields a ternary interaction between all the free subsystems, implemented by the interaction element `ParticleTwoModes`

(a)

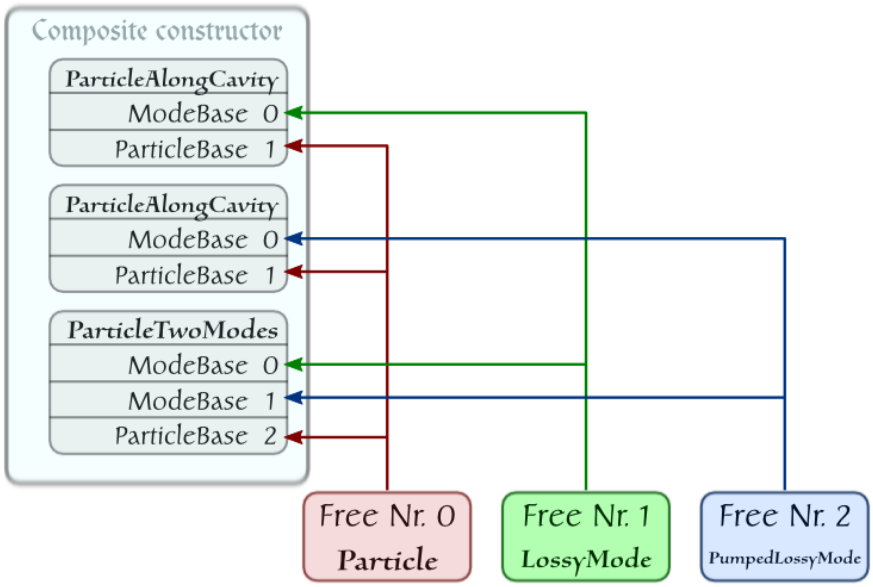

(b)

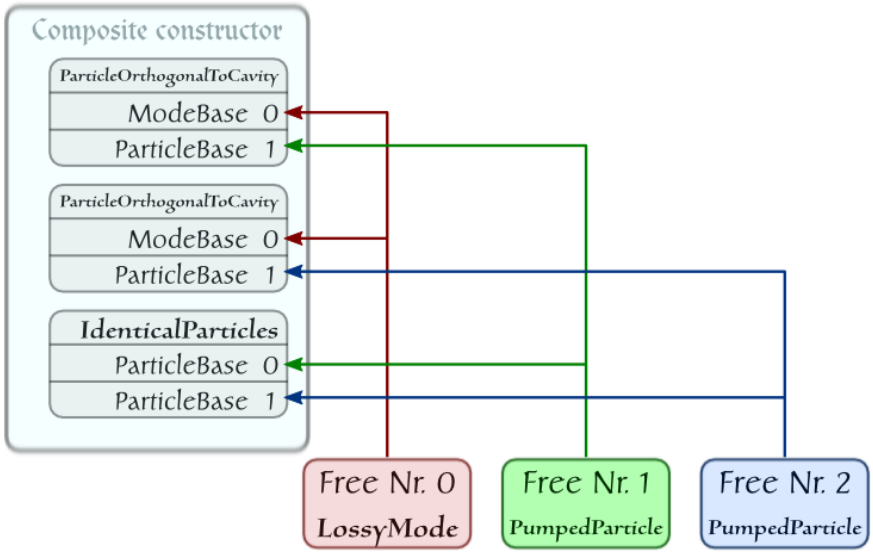

Figure 10.3: The network of interactions defining the system for (a) the ring-cavity example and (b) the self-organization example.

The system can be layed out as a simple network, as displayed in Fig. 10.3(a). The `Composite` module of the framework is designed to directly represent such a network. Assume the following definitions are in effect:

```
// Construct Frees
Particle        part {...};
LossyMode       plus {...};
PumpedLossyMode minus{...};
// Construct Interactions
ParticleAlongCavity iaP{plus ,part,...,MFT_PLUS };
ParticleAlongCavity iaM{minus,part,...,MFT_MINUS};
ParticleTwoModes    ia3{plus,minus,part,...};
```

(Here, `MFT` means the type of the mode function, and `PLUS` and `MINUS` signify that they are counterpropagating running-wave modes.) Then, the system is created by a maker function for `Composite` with a helper class denoted `_`:

```
composite::make(_<1,0>  {iaP},
                _<2,0>  {iaM},
                _<1,2,0>{ia3});
```

What we are expressing here e.g. with the specification `_<1,2,0>(ia3)` is that the 0th leg of the interaction element `ParticleTwoModes`, which is the mode `plus`, is the 1st in our row of free subsystems in the network in Fig. 10.3(a). The 1st leg, the mode `minus` is the 2nd in the row; and the 2nd leg, the particle is the 0th in the row of frees. The legs of interaction elements cannot be interchanged, and we also have to be consistent with our preconceived order of free subsystems throughout. Clearly, the three `_` objects contain all the information needed by the framework to figure out the full layout of the system. Any inconsistencies in the layout will result in a compile-time or runtime error, depending on when the information becomes available.

To end this Section, we display one more example. This exhibits a last feature reflecting a basic principle of quantum physics: if two systems are identical, they are indistinguishable. In C++QED, this means that a single object is enough to represent them. Consider two identical pumped particles moving in a direction orthogonal to the axis of a cavity sustaining a single lossy mode (Vukics et al., 2007). The layout of the system is displayed in Fig. 10.3(b). The core of a corresponding script may read:

```
LossyMode      mode{pm}; // Free0
PumpedParticle part{pp}; // Free1,2 - only one instant

ParticleOrthogonalToCavity ia{mode,part,ppc}; // only one instant

evolve(init(pm)*coherent(pp)*coherent(pp),
       composite::make(_<0,1>{ia},
                       _<0,2>{ia},
                       _<1,2>{IdenticalParticles<2>{part,...}}),
       pe);
```

10.5 FUNDAMENTAL DATA STRUCTURES

10.5.1 State vectors as multi-arrays

We first introduce basic definitions in the algebra of composite quantum systems. Here, the state vector of the system is an element of a Hilbert space $\mathcal{H}$

which is the direct product of elementary Hilbert spaces $\mathcal{H}_i$s:

$$\mathcal{H} = \bigotimes_i \mathcal{H}_i, \tag{10.3a}$$

$$|\iota\rangle \in \mathcal{H}, \tag{10.3b}$$

$$|\iota_i\rangle \in \mathcal{H}_i, \tag{10.3c}$$

$$|\iota\rangle = \bigotimes_i |\iota_i\rangle \equiv |\iota_0, \iota_1, \dots\rangle\,, \tag{10.3d}$$

so that $|\iota\rangle$ and $|\iota_i\rangle$ are basis vectors in $\mathcal{H}$ and $\mathcal{H}_i$, respectively. The number of elementary Hilbert spaces is the arity of the system.

Through an example, we define *slicing*. Assume a state vector:

$$|\Psi\rangle \equiv \sum_\iota \Psi_\iota\, |\iota\rangle \in \mathcal{H}, \tag{10.4a}$$

then a state-vector slice is a state vector in the Hilbert space of a subsystem:

$$\left|\Psi^{\langle 1,3,6,7,9\rangle}(\iota_0, \iota_2, \iota_4, \iota_5, \iota_8, \iota_{10}, \dots)\right\rangle \equiv \sum_{\iota_1,\iota_3,\iota_6,\iota_7,\iota_9} \Psi_\iota\, |\iota_1, \iota_3, \iota_6, \iota_7, \iota_9\rangle \in \bigotimes_{i=1,3,6,7,9} \mathcal{H}_i. \tag{10.4b}$$

Such a state-vector slice is defined by the *retained axes* $\langle 1, 3, 6, 7, 9\rangle$, which define the subsystem, and the *dummy indices* $(\iota_0, \iota_2, \iota_4, \iota_5, \iota_8, \iota_{10}, \dots)$. In situations when slicing occurs in the framework, the set of retained axes is an information available at compile time, while the set of dummy indices is an information becoming available only at runtime.

Slicing is recursive: a state-vector slice behaves as a state vector, only with a lower rank, and it can even be further sliced. It is in particular true that

$$\langle\iota|\Psi\rangle = \left\langle \iota_1, \iota_3, \iota_6, \iota_7, \iota_9 \middle| \Psi^{\langle 1,3,6,7,9\rangle}(\iota_0, \iota_2, \iota_4, \iota_5, \iota_8, \iota_{10}, \dots)\right\rangle. \tag{10.5}$$

Through an example, we define operator *broadcasting*.[10] Assume a linear operator:

$$A \equiv \sum_k A_{\mathrm{k},3} \otimes A_{\mathrm{k},6} \otimes A_{\mathrm{k},1} \otimes A_{\mathrm{k},9} \otimes A_{\mathrm{k},7} \in \mathfrak{L}(\mathcal{H}_3 \otimes \mathcal{H}_6 \otimes \mathcal{H}_1 \otimes \mathcal{H}_9 \otimes \mathcal{H}_7), \tag{10.6a}$$

$$\begin{aligned} &A^{\langle 3,6,1,9,7\rangle}(\mathcal{H}) \\ &\quad\equiv \sum_k (\mathbb{I}_0 \otimes A_{\mathrm{k},1} \otimes \mathbb{I}_2 \otimes A_{\mathrm{k},3} \otimes \mathbb{I}_4 \otimes \mathbb{I}_5 \otimes A_{\mathrm{k},6} \otimes A_{\mathrm{k},7} \otimes \mathbb{I}_8 \otimes A_{\mathrm{k},9} \otimes \mathbb{I}_{10} \dots) \\ &\qquad\qquad \in \mathfrak{L}(\mathcal{H}). \end{aligned} \tag{10.6b}$$

When the numbers in the angular brackets are permutations of a sequence of ordinals, this corresponds only to a permutation of the underlying elementary Hilbert spaces. Matrix elements of the broadcasted operator can then be calculated by acting with the (possibly permutated) original operator on an appropriate vector slice:

$$\langle\iota|\, A^{\langle 3,6,1,9,7\rangle}(\mathcal{H})\, |\Psi\rangle = \langle \iota_1, \iota_3, \iota_6, \iota_7, \iota_9|\, A^{\langle 1,2,0,4,3\rangle} \left|\Psi^{\langle 1,3,6,7,9\rangle}(\iota_0, \iota_2, \iota_4, \iota_5, \iota_8, \iota_{10}, \dots)\right\rangle. \tag{10.7}$$

Due to the recursivity of slicing, the state vector of a composite quantum system is most conveniently represented computationally by a multi-array of complex numbers. The multi-array concept can be defined as: the possibility of

10. *Slicing* and *broadcasting* have become standard terminology in multi-array libraries, like the NumPy Python package.

1. indexing the array with as many indices as the rank of the array;
2. slicing the array in a recursive way: any slice also behaves as a multi-array;
3. creating views (both constant and non-constant) of the array without actually touching the storage in memory. Any view again behaves as a multi-array.

Our principal tool to work with state vectors is a range that contains the slices of a multi-array corresponding to all possible combinations of the retained indices:

```
template<int... RetainedAxes, typename MultiArray>
auto slicesRange(MultiArray);
```

Slice iteration is at the heart of the framework, as it is indispensable to implement composite quantum systems. Quite generally, by iterating through the slices corresponding to all the combinations of indices not belonging to the given subsystem (dummy indices), it can be used to implement operator broadcasting. Sticking to the example of Eq. (10.7), assume that the function

```
void actWithA(StateVector<5>&);
```

implements the action of operator A on a state vector of rank 5. Then the action on the extended Hilbert space can be calculated as

```
void broadcastA_to11Dims(StateVector<11>& psi)
{
  for_each(slicesRange<3,6,1,9,7>(psi),actWithA);
}
```

Observe the one-to-one correspondance between this piece of code and the entities in Eq. (10.7).

At this point, it becomes apparent how compile-time algorithms come about in the framework. Here we need to calculate the "permutated operator" $A^{\langle 1,2,0,4,3\rangle}$ *at compile time.* Rather than touching the operators defined as functions, this permutation is done on the multi-array, resulting in a multi-array *view* with permutated indices, so that we do not need to actually move data around. This example shows that the use of multi-arrays and compile-time algorithms go hand-in-hand in our problem.

10.5.2 Lazy density operator

In a quantum-simulation framework, clients should be able to write code for calculating quantum expectation values from quantumdata, independently of whether this data is represented by state vectors or density operators, in orthogonal or non-orthogonal bases. One obvious solution is relying on the formula

$$\langle A\rangle = \mathrm{Tr}\{A\rho\} \tag{10.8}$$

(A being an observable and ρ the density operator of the system), to write code only for the density-operator case, and fall back to this in the state-vector case as well, by calculating a dyad from the state vector. However, this is wasteful since usually not all the matrix elements of ρ are needed for calculating the expectation value. Furthermore, for large dimensionality, this solution may

become unaffordable in terms of memory: for large systems, we may afford to store $|\Psi\rangle$, but not $|\Psi\rangle\langle\Psi|$.

The solution adopted for this problem in the framework is represented by the class `LazyDensityOperator`. This class provides a common interface for all the four kinds of quantumdata to calculate quantum expectation values from their data: state vector or density operator, in orthogonal or non-orthogonal bases.[11] Here, "laziness" means that in the case of state vectors only those elements of the density operator are calculated that are actually asked for. `LazyDensityOperator` is an abstract interface, which gets implemented by classes like `StateVector`, `DensityOperator`, and their non-orthogonal counterparts.

The semantics of `LazyDensityOperator` can be understood through the following examples:

Unary system Assume a mode represented in Fock basis with ladder operator a. To calculate the quantum expectation value

$$\langle a^2 \rangle = \mathrm{Tr}\{a^2\rho\} = \sum_i \sqrt{i(i-1)}\,\rho_{i;i-2}, \tag{10.9}$$

one can write the following function:

```
auto calculateASqr(const LazyDensityOperator<1>& m)
{
  complex res;
  for (int i=2; i<m.getTotalDimension(); ++i)
    res+=sqrt(i*(i-1))*m(i,i-2);
  return res;
}
```

Binary system Assume two modes represented in Fock bases with ladder-operators a and b, respectively. To calculate the quantum expectation value

$$\langle a^\dagger b \rangle = \mathrm{Tr}\{a^\dagger b\rho\} = \sum_{i,j} \sqrt{(i+1)j}\,\rho_{(i,j);(i+1,j-1)}, \tag{10.10}$$

one can write the following function:

```
auto calculateADaggerB(const LazyDensityOperator<2>& m)
{
  const auto dim{m.getDimensions()};

  complex res;
  for (int i=0; i<dim[0]-1; ++i) for (int j=1; j<dim[1]; ++j)
    res+=sqrt((i+1)*j)*m({i,j},{i+1,j-1});
  return res;
}
```

We note that analogously to state vectors, `LazyDensityOperator` must also be sliced because for calculating quantum expectation values of subsystem-observables (e.g. in composite systems), the partial-trace density operator is needed. For the partial trace, however, only such elements of the full density operator are needed, as are diagonal in the dummy indices.

11. In the case of non-orthogonal bases, we adopt the covariant-contravariant formalism, and provide services for "pulling" indices. An important usecase in quantum optics is a set of coherent states as an approximately complete basis for a mode in a certain segment of its Hilbert space (Krämer & Ritsch, 2012).

10.A DEFINING MULTI-LEVEL QUANTUM SYSTEMS

In this Appendix, we sketch a generic element of C++QED, which provides a framework for representing multi-level quantum systems, e.g. atoms or ions of arbitrary level structure. Coherent driving, loss, and interaction with harmonic-oscillator modes can also be defined. The framework is defined in the header files

- `elements/frees/MultiLevel.h` and
- `elements/interactions/MLJC.h`,

the latter acronym standing for **m**ulti-**l**evel **J**aynes-**C**ummings.

An N-level system is characterized by a set of basis vectors

$$|i\rangle\,, \quad i = 0 \ldots N-1. \tag{10.11}$$

Coherent driving – e.g. with laser light – of a transition between two levels i and j is described by the Hamiltonian:

$$H_{\text{driving } i-j} \propto \eta_{ij}\,|j\rangle\,\langle i| - \text{h.c.}, \tag{10.12}$$

$$H_{\text{coupling } i-j} \propto g_{ij}\,a\,|j\rangle\,\langle i| - \text{h.c.}, \tag{10.13}$$

where in the second line the external driving has been replaced by a harmonic-oscillator mode with ladder operator a, resulting in a Jaynes-Cummings coupling. (This corresponds to the situation when a driving laser is replaced by a cavity mode.) Decay of level j to level i can be described by the Lindblad operator

$$J_{j\to i} = \sqrt{2\gamma_{ij}}\,|i\rangle\,\langle j|\,, \tag{10.14}$$

where γ_{ij} is the decay rate.

The `MultiLevel` framework in C++QED is designed in such a way that a set of drivings, couplings to harmonic-oscillator modes, and decays can be defined *at compile time* as lists of pairs of i and j levels. From these lists, the framework assembles the Hamiltonian of the system *at compile time* as a sum of terms like (10.12) and (10.13), and the Lindblad operators as a set of operators like (10.14). Then, the values of parameters like η_{ij}, g_{ij}, and γ_{ij} for all the pairs such defined can be specified at runtime. The rationale of this arrangement is that such pairs of levels as are never expected to be driven or coupled (or lossy), will not pollute the Hamiltonian with terms which would turn out to be zero at runtime. (Or, if the pair is not specified in the list of decays, it will not be considered when trying for quantum jumps.)

The script `scripts/Ca40InCavity.cc` demonstrates the syntax and usage. This script represents a $^{40}Ca^{+}$ ion interacting with a cavity mode as described e.g. in Barros et al. (2009). In this case, the $4^2S_{1/2}$, $3^2D_{3/2}$, and $4^2P_{1/2}$ levels of the ion constitute an eight-level system, with two driven transitions, six transitions coupled to the cavity mode, and ten decaying transitions.

Another important usecase is circuit quantum electrodynamics with transmons, where the strong coupling to the resonator and the insufficient nonlinearity of the transmon means that one must take into account more than two transmon levels, making it a multilevel system, cf. Chapter 7.

THESES, OUTLOOK, FURTHER DEVELOPMENTS

11

Thesis IX (Kornyik & Vukics, 2019) We have developed a stepwise adaptive MCWF algorithm controlled by a single specific parameter: the maximum allowed total jump probability per timestep, Δp. We have studied the convergence behavior of the MCWF method depending on this parameter. We have found that the dependence of the deviation of the MCWF from the exact solution proportional to the square root of the inverse of the number of trajectories flattens out, which happens at the larger number of trajectories, the smaller the Δp. This behavior we attributed to the inherent errors of the first order MCWF method, namely

1. time discretization and
2. missing multi-jump events,

both of which are $O(\delta t^2)$ errors, meaning that they scale as Δp^2. We have found and characterized a discontinuous behavior of the method as a function of Δp in the pure Δp-controlled regime, which we have attributed to the way the trajectories are sampled in time. This a showcase of how sampling can modify the behavior of trajectories through influencing the stepsize, which at the same time displays the role of the average stepsize as the real regulator of MCWF convergence. In the case when a non-trivial Hamiltonian is present, we have characterized the contention between Δp- and ODE-control, finding that ODE-control will take over when those characteristic frequencies of the system that do not participate in the loss increase. The takeover of ODE-control is signalled by that the average timestep becomes determined by the largest non-loss-related characteristic frequency of the system, becoming independent of Δp.

Thesis X (Vukics, 2012; Sandner & Vukics, 2014) We have developed and maintained C++QED: a C++ framework for simulating open quantum dynamics. The design is based on leveraging the multi-array concept for representing the quantum state (state vector or density operator) of composite quantum systems. The knowledge of the arity of the system at compile time entails the utilization of compile-time algorithms for processing the layout of composite quantum systems at compile time, hence cutting on runtime. The framework provides a high-level interface where users can compose arbitrarily complex interacting composite quantum systems from elementary free subsystems – e.g. harmonic-oscillator modes, qubits, particle motional degrees of freedom –, and interactions between them – e.g. Jaynes-Cummings, x-x interaction. C++QED provides a separate framework for defining multi-level systems (e.g. for atoms

of complex level structure) with an arbitrary set of drivings, couplings to electromagnetic modes, and radiative losses assembled at compile time. During its history of more than a decade, C++QED has formed the basis of about 20 research papers, and has proved particularly useful in supercomputing environments.

The formalism for describing open quantum systems is seeing refinements up to this day. The connection between strong symmetries and conservation laws on individual trajectories was clarified by Munoz et al. (2019), while in the case of a weak symmetry of the Liouvillean, it was shown how a symmetric Hamiltonian and jump operators connecting only the symmetry eigenspaces with a fixed eigenvalue ratio can be constructed to simplify evolution on a single trajectory (Macieszczak & Rose, 2021). An important recent paradigm is time-delayed quantum coherent feedback (Grimsmo, 2015): in cascaded quantum systems with the growth of the network it becomes increasingly important to account for the situation when an output field of one of the subsystems influences one of its inputs at a later time. Quantum trajectory methods to deal with this situation have been developed during recent years (Német, 2019; Crowder et al., 2020). Simulation methods for open quantum *many-body* systems incorporating also quantum trajectories have seen great progress during the last decade (Weimer et al., 2021). Recently, a "numerically exact" treatment of many-body self-organization in a cavity became possible (Halati et al., 2020).

On the mathematical-physics front, quantum trajectories were extended to the case of arbitrary system-environment coupling by Donvil & Muratore-Ginanneschi (2021), exhibiting interference of distinct realizations of quantum trajectories in the strong-coupling case. In numerical analysis, structure-preserving numerical schemes were developed by Cao & Lu (2021), taking advantage on special algebraic properties of Lindblad master equations.[1]

1. Literature review closed in October 2021

Regarding implementations, whereas around the inception of the `C++QED` framework the main simulation tool for open quantum systems used by quantum opticians was the rather inefficient Matlab Quantum Optics Toolbox (Tan, 1999), during the past decade two new tools appeared: the very popular QuTiP in Python (Johansson et al., 2012, 2013), and QuantumOptics.jl (Krämer et al., 2018) in Julia, a new numerical language. Whereas interpreted languages cannot be as fast as compiled ones by principle, the borderline between these two categories is becoming elusive with the just-in-time-compilation paradigm of Julia. Due partly to their languages, QuTiP and QuantumOptics.jl are tuned towards usage at the console, while `C++QED` is especially useful for batch usage in supercomputing environments.

Finally, some remarks about the future of the `C++QED` framework. One drawback of C++ for scientific applications has been the very scanty numerics in the standard library, and, what is particularly problematic for our application is that it still lacks a standard multiarray type.[2] As long as we are stuck with the Blitz library, we cannot fully embrace modern techniques. Nevertheless, the tri-annual updates to the language starting with C++11 have greatly enhanced its overall usability, and allowed us to express especially our compile-time structures in much more straightforward ways than the esotheric solutions

2. Contrast this with FORTRAN that has featured a built-in multiarray type from the very beginning, or Python, where the `ndarray` type of the NumPy library has become a *de facto* standard.

we needed to resort to when we started with C++03 in 2006. The upcoming C++23 will even include a multi-array infrastructure. A great challenge facing C++QED is the exploitation of heterogeneous architectures – graphical processing units (GPU), field-programmable gate arrays (FPGA), and eventually even quantum processors – that has become a mainstream in scientific computing during the last decade. Recent editions of the C++ standard provide several tools to facilitate deployment to these platforms. All in all, despite being more than a decade old, we can expect C++QED to see a bright future, where cleaner and more accessible structures and applicability in heterogeneous computational environments make it a tool of choice for a wider audience of quantum scientists.

OWN PAPERS RELATED TO THE THESIS

2007

Vukics, A., C. Maschler, and H. Ritsch (2007). Microscopic physics of quantum self-organization of optical lattices in cavities. *New J. Phys. 9*(8), 255.

Vukics, A. and H. Ritsch (2007). C++QED: an object-oriented framework for wave-function simulations of cavity QED systems. *Eur. Phys. J. D 44*(3), 585–599.

2009

Vukics, A., W. Niedenzu, and H. Ritsch (2009). Cavity nonlinear optics with few photons and ultracold quantum particles. *Phys. Rev. A 79*(1), 013828.

2010

Niedenzu, W., R. Schulze, A. Vukics, and H. Ritsch (2010). Microscopic dynamics of ultracold particles in a ring-cavity optical lattice. *Phys. Rev. A 82*(4), 043605.

2012

Vukics, A. and P. Domokos (2012). Adequacy of the Dicke model in cavity QED: A counter-no-go statement. *Phys. Rev. A 86*(5), 053807.

Vukics, A. (2012). C++QEDv2: The multi-array concept and compile-time algorithms in the definition of composite quantum systems. *Comp. Phys. Comm. 183*(6), 1381–1396.

2013

Dombi, A., A. Vukics, and P. Domokos (2013). Optical bistability in strong-coupling cavity QED with a few atoms. *J. Phys. B 46*(22), 224010.

2014

Vukics, A., T. Grießer, and P. Domokos (2014). Elimination of the A-square problem from cavity QED. *Phys. Rev. Lett. 112*(7), 073601.

Sandner, R. and A. Vukics (2014). C++QEDv2 Milestone 10: A C++/Python application-programming framework for simulating open quantum dynamics. *Comp. Phys. Comm. 185*(9), 2380–2382.

2015

Vukics, A., T. Grießer, and P. Domokos (2015). Fundamental limitation of ultrastrong coupling between light and atoms. *Phys. Rev. A 92*(4), 043835.

Dombi, A., A. Vukics, and P. Domokos (2015). Bistability effect in the extreme strong coupling regime of the Jaynes-Cummings model. *Eur. Phys. J. D 69*(3), 60.

2016

Grießer, T., A. Vukics, and P. Domokos (2016). Depolarization shift of the superradiant phase transition. *Phys. Rev. A 94*(3), 033815.

2017

Fink, J., A. Dombi, A. Vukics, A. Wallraff, and P. Domokos (2017). Observation of the photon-blockade breakdown phase transition. *Phys. Rev. X 7*(1), 011012.

2019

Vukics, A., A. Dombi, J. Fink, and P. Domokos (2019). Finite-size scaling of the photon-blockade breakdown dissipative quantum phase transition. *Quantum 3*, 150.

Kornyik, M. and A. Vukics (2019). The Monte Carlo wave-function method: A robust adaptive algorithm and a study in convergence. *Comp. Phys. Comm. 238*, 88–101.

2021

Fuchs, S., A. Vukics, and S. Y. Buhmann (2021). Superradiance from nonideal initial states: A quantum trajectory approach. *Phys. Rev. A 103*(4), 043712.

Vukics, A., G. Kónya, and P. Domokos (2021). The gauge-invariant Lagrangian, the Power–Zienau–Woolley picture, and the choices of field momenta in nonrelativistic quantum electrodynamics. *Sci. Rep. 11*(1), 1–11.

2022

Clark, T., A. Dombi, F. Williams, Á. Kurkó, J. Fortágh, D. Nagy, A. Vukics, and P. Domokos (2022). Time-resolved observation of a dynamical phase transition of atoms in a cavity. *Phys. Rev. A 105*, 063712.

Sett, R., F. Hassani, D. Phan, S. Barzanjeh, A. Vukics, and J. M. Fink (2022). Approaching the thermodynamic limit of a first-order dissipative quantum phase transition in zero dimension. *In preparation for Phys. Rev. X.**

*This paper has been in preparation since late 2019, but has been repeatedly delayed due to a combination of the COVID-19 pandemic and a certain lack of human resources on the experimental side. The material has already been presented in international conferences, e.g. APS March Meeting 2022 (R. Sett) and CMD29 (A. Vukics).

BIBLIOGRAPHY

Aasi, J., J. Abadie, B. Abbott, R. Abbott, T. Abbott, M. Abernathy, C. Adams, T. Adams, P. Addesso, R. Adhikari, et al. (2013). Enhanced sensitivity of the LIGO gravitational wave detector by using squeezed states of light. *Nat. Photonics 7*(8), 613–619.

Abbott, B. P., R. Abbott, T. D. Abbott, M. R. Abernathy, F. Acernese, et al. (2016). Observation of Gravitational Waves from a Binary Black Hole Merger. *Phys. Rev. Lett. 116*, 061102.

Abrahams, D. & A. Gurtovoy (2004). *C++ Template Metaprogramming: Concepts, Tools, and Techniques from Boost and Beyond (C++ in Depth Series)*. Addison-Wesley Professional.

Agarwal, G. S. (1984). Vacuum-Field Rabi Splittings in Microwave Absorption by Rydberg Atoms in a Cavity. *Phys. Rev. Lett. 53*(18), 1732–1734.

Alsing, P. & H. Carmichael (1991). Spontaneous dressed-state polarization of a coupled atom and cavity mode. *Quantum Opt. 3*(1), 13.

Alsing, P., D.-S. Guo, & H. Carmichael (1992). Dynamic Stark effect for the Jaynes-Cummings system. *Phys. Rev. A 45*(7), 5135.

Anappara, A. A., S. De Liberato, A. Tredicucci, C. Ciuti, G. Biasiol, L. Sorba, & F. Beltram (2009). Signatures of the ultrastrong light-matter coupling regime. *Phys. Rev. B 79*, 201303.

Andersen, C. K. & K. Mølmer (2015). Circuit QED Flip-Flop Memory with All-Microwave Switching. *Phys. Rev. Applied 3*, 024002.

Andolina, G. M., F. M. D. Pellegrino, V. Giovannetti, A. H. MacDonald, & M. Polini (2019). Cavity quantum electrodynamics of strongly correlated electron systems: A no-go theorem for photon condensation. *Phys. Rev. B 100*, 121109.

Andrews, D. L., G. A. Jones, A. Salam, & R. G. Woolley (2018). Perspective: Quantum Hamiltonians for optical interactions. *J. Chem. Phys. 148*(4), 040901.

Ashhab, S. & F. Nori (2010). Qubit-oscillator systems in the ultrastrong-coupling regime and their potential for preparing nonclassical states. *Phys. Rev. A 81*, 042311.

Ashida, Y., A. Imamoglu, & E. Demler (2021). Cavity Quantum Electrodynamics at Arbitrary Light-Matter Coupling Strengths. *Phys. Rev. Lett. 126*, 153603.

Ashida, Y., A. Imamoglu, J. Faist, D. Jaksch, A. Cavalleri, & E. Demler (2020). Quantum electrodynamic control of matter: Cavity-enhanced ferroelectric phase transition. *Phys. Rev. X 10*(4), 041027.

Aspect, A., P. Grangier, & G. Roger (1982). Experimental Realization of Einstein-Podolsky-Rosen-Bohm Gedankenexperiment: A New Violation of Bell's Inequalities. *Phys. Rev. Lett. 49*, 91–94.

Ates, C., B. Olmos, J. P. Garrahan, & I. Lesanovsky (2012). Dynamical phases and intermittency of the dissipative quantum Ising model. *Phys. Rev. A 85*, 043620.

Atkins, P. & R. Woolley (1970). The interaction of molecular multipoles with the electromagnetic field in the canonical formulation of non-covariant quantum electrodynamics. *Proc. R. Soc. Lond., Ser. A 319*(1539), 549–563.

Babiker, M. & R. Loudon (1983). Derivation of the Power-Zienau-Woolley Hamiltonian in Quantum Electrodynamics by Gauge Transformation. *Proc. R. Soc. London, Ser. A 385*, 1789.

Bachor, H.-A. & T. C. Ralph (2014). *A Guide to Experiments in Quantum Optics*. Wiley.

Bamba, M., K. Inomata, & Y. Nakamura (2016). Superradiant Phase Transition in a Superconducting Circuit in Thermal Equilibrium. *Phys. Rev. Lett. 117*, 173601.

Bamba, M. & T. Ogawa (2014). Stability of polarizable materials against superradiant phase transition. *Phys. Rev. A 90*, 063825.

Baranov, D. G., B. Munkhbat, E. Zhukova, A. Bisht, A. Canales, B. Rousseaux, G. Johansson, T. J. Antosiewicz, & T. Shegai (2020). Ultrastrong coupling between nanoparticle plasmons and cavity photons at ambient conditions. *Nat. Comm. 11*(1), 1–9.

Barros, H., A. Stute, T. Northup, C. Russo, P. Schmidt, & R. Blatt (2009). Deterministic single-photon source from a single ion. *New J. Phys. 11*(10), 103004.

Barton, G. (1974). Frequency shifts near an interface: inadequacy of two-level atomic models. *J. Phys. B: At. Mol. Phys. 7*(16), 2134.

Baumann, K., C. Guerlin, F. Brennecke, & T. Esslinger (2010). Dicke quantum phase transition with a superfluid gas in an optical cavity. *Nature 464*(7293), 1301.

Bayer, A., M. Pozimski, S. Schambeck, D. Schuh, R. Huber, D. Bougeard, & C. Lange (2017). Terahertz light–matter interaction beyond unity coupling strength. *Nano Lett. 17*(10), 6340–6344.

Beaudoin, F., J. M. Gambetta, & A. Blais (2011). Dissipation and ultrastrong coupling in circuit QED. *Phys. Rev. A 84*, 043832.

Bell, J. S. (1964). On the Einstein Podolsky Rosen paradox. *Phys. Phys. Fiz. 1*, 195–200.

Benedict, M., A. Ermolaev, V. Malyshev, I. Sokolov, & E. Trifonov (1996). *Superradiance: Multiatomic coherent emission*. Taylor and Francis.

Bergquist, J. C., R. G. Hulet, W. M. Itano, & D. J. Wineland (1986). Observation of Quantum Jumps in a Single Atom. *Phys. Rev. Lett. 57*, 1699–1702.

Binz, E. & R. Alfred (2010). Symplectic geometry of Maxwell theory and the photon concept. *J. Phys. Conf. Ser. 237*(1), 012006.

Birula, I. B. & K. Rzażewski (1979). No-go theorem concerning the superradiant phase transition in atomic systems. *Phys. Rev. A 19*, 301–303.

Bishop, L. S. (2010). *Circuit Quantum Electrodynamics*. Ph. D. thesis, Department of Physics, Yale University.

Bishop, L. S., J. M. Chow, J. Koch, A. A. Houck, M. H. Devoret, E. Thuneberg, S. M. Girvin, & R. J. Schoelkopf (2009). Nonlinear response of the vacuum Rabi resonance. *Nat. Phys. 5*(2), 105–109.

Blais, A., S. M. Girvin, & W. D. Oliver (2020). Quantum information processing and quantum optics with circuit quantum electrodynamics. *Nat. Phys. 16*(3), 247–256.

Blais, A., A. L. Grimsmo, S. M. Girvin, & A. Wallraff (2021). Circuit quantum electrodynamics. *Rev. Mod. Phys. 93*, 025005.

Bloch, I., J. Dalibard, & S. Nascimbène (2012). Quantum simulations with ultracold quantum gases. *Nat. Phys. 8*(4), 267–276.

Bloch, I., T. W. Hänsch, & T. Esslinger (1999). Atom Laser with a cw Output Coupler. *Phys. Rev. Lett. 82*, 3008–3011.

Bloom, B., T. Nicholson, J. Williams, S. Campbell, M. Bishof, X. Zhang, W. Zhang, S. Bromley, & J. Ye (2014). An optical lattice clock with accuracy and stability at the 10- 18 level. *Nature 506*(7486), 71–75.

Bonifacio, R., M. Gronchi, & L. A. Lugiato (1978). Photon statistics of a bistable absorber. *Phys. Rev. A 18*, 2266–2279.

Bourassa, J., J. M. Gambetta, A. A. Abdumalikov, O. Astafiev, Y. Nakamura, & A. Blais (2009). Ultrastrong coupling regime of cavity QED with phase-biased flux qubits. *Phys. Rev. A 80*, 032109.

Braak, D. (2011). Integrability of the Rabi Model. *Phys. Rev. Lett. 107*, 100401.

Brennecke, F., R. Mottl, K. Baumann, R. Landig, T. Donner, & T. Esslinger (2013). Real-time observation of fluctuations at the driven-dissipative Dicke phase transition. *PNAS 110*(29), 11763–11767.

Breuer, H.-P., W. Huber, & F. Petruccione (1997). Stochastic wave-function method versus density matrix: a numerical comparison. *Comp. Phys. Comm. 104*(1), 46 – 58.

Breuer, H.-P. & F. Petruccione (1995). Stochastic dynamics of quantum jumps. *Phys. Rev. E 52*, 428–441.

Brookes, P., G. Tancredi, A. D. Patterson, J. Rahamim, M. Esposito, T. K. Mavrogordatos, P. J. Leek, E. Ginossar, & M. H. Szymanska (2021). Critical slowing down in circuit quantum electrodynamics. *Science Advances 7*(21), eabe9492.

Brune, M., F. Schmidt-Kaler, A. Maali, J. Dreyer, E. Hagley, J. Raimond, & S. Haroche (1996). Quantum Rabi oscillation: A direct test of field quantization in a cavity. *Phys. Rev. Lett. 76*(11), 1800.

Buckwar, E. & M. Riedler (2011). Runge–Kutta methods for jump–diffusion differential equations. *Journal of Computational and Applied Mathematics 236*(6), 1155–1182.

Buckwar, E., M. Riedler, & P. Kloeden (2011). The numerical stability of stochastic ordinary differential equations with additive noise. *Stochastics and Dynamics 11*(02n03), 265–281.

Bužek, V., M. Orszag, & M. Roško (2005). Instability and Entanglement of the Ground State of the Dicke Model. *Phys. Rev. Lett. 94*, 163601.

Cao, Y. & J. Lu (2021). Structure-preserving numerical schemes for Lindblad equations. *arXiv preprint arXiv:2103.01194*.

Capriotti, L., A. Cuccoli, A. Fubini, V. Tognetti, & R. Vaia (2005). Dissipation-driven phase transition in two-dimensional Josephson arrays. *Phys. Rev. Lett. 94*(15), 157001.

Carmichael, H. (1993). *An Open Systems Approach to Quantum Optics*. Springer.

Carmichael, H. J. (2015). Breakdown of Photon Blockade: A Dissipative Quantum Phase Transition in Zero Dimensions. *Phys. Rev. X 5*, 031028.

Carmichael, H. J., C. W. Gardiner, & D. F. Walls (1973). Higher order corrections to the Dicke superradiant phase transition. *Phys. Lett. A 46*(1), 47–48.

Carr, C., R. Ritter, C. G. Wade, C. S. Adams, & K. J. Weatherill (2013). Nonequilibrium Phase Transition in a Dilute Rydberg Ensemble. *Phys. Rev. Lett. 111*, 113901.

Castaños, O., E. Nahmad-Achar, R. López-Peña, & J. G. Hirsch (2011). Superradiant phase in field-matter interactions. *Phys. Rev. A 84*, 013819.

Casteels, W., R. Fazio, & C. Ciuti (2017). Critical dynamical properties of a first-order dissipative phase transition. *Phys. Rev. A 95*, 012128.

Caves, C. M. (1980). Quantum-mechanical radiation-pressure fluctuations in an interferometer. *Phys. Rev. Lett. 45*(2), 75.

Chernyak, V. & S. Mukamel (1995). Gauge invariant formulation of molecular electrodynamics and the multipolar Hamiltonian. *Chemical physics 198*(1-2), 133–143.

Cirac, J. I. & H. J. Kimble (2017). Quantum optics, what next? *Nat. Photonics 11*(1), 18–20.

Ciuti, C., G. Bastard, & I. Carusotto (2005). Quantum vacuum properties of the intersubband cavity polariton field. *Phys. Rev. B 72*, 115303.

Ciuti, C. & P. Nataf (2012). Comment on "Superradiant Phase Transitions and the Standard Description of Circuit QED". *Phys. Rev. Lett. 109*, 179301.

Clark, J. & R. Cameron (1980). The maximum rate of convergence of discrete approximations for stochastic differential equations. In *Stochastic Differential Systems Filtering and Control*, pp. 162–171. Springer.

Cohen-Tannoudji, C., J. Dupont-Roc, & G. Grynberg (1997). *Photons and Atoms*. Wiley-Interscience.

Cohen-Tannoudji, C., J. Dupont-Roc, & G. Grynberg (1998). *Atom-Photon Interactions*. Wiley-VCH.

Cook, R. J. & H. J. Kimble (1985). Possibility of Direct Observation of Quantum Jumps. *Phys. Rev. Lett. 54*, 1023–1026.

Cottet, A., T. Kontos, & B. Douçot (2015). Electron-photon coupling in mesoscopic quantum electrodynamics. *Phys. Rev. B 91*, 205417.

Crowder, G., H. Carmichael, & S. Hughes (2020). Quantum trajectory theory of few-photon cavity-QED systems with a time-delayed coherent feedback. *Phys. Rev. A 101*, 023807.

Curtis, J. B., I. Boettcher, J. T. Young, M. F. Maghrebi, H. Carmichael, A. V. Gorshkov, & M. Foss-Feig (2021). Critical theory for the breakdown of photon blockade. *Phys. Rev. Research 3*, 023062.

Dagvadorj, G., M. Kulczykowski, M. H. Szymańska, & M. Matuszewski (2021). First-order dissipative phase transition in an exciton-polariton condensate. *Phys. Rev. B 104*, 165301.

Daley, A. J. (2014). Quantum trajectories and open many-body quantum systems. *Advances in Physics 63*(2), 77–149.

Dalibard, J., Y. Castin, & K. Mølmer (1992). Wave-function approach to dissipative processes in quantum optics. *Phys. Rev. Lett. 68*, 580–583.

Dautray, R. & J.-L. Lions (1990). *Spectral Theory and Applications*, Volume 3 of *Mathematical Analysis and Numerical Methods for Science and Technology*. Springer.

De Bernardis, D., P. Pilar, T. Jaako, S. De Liberato, & P. Rabl (2018). Breakdown of gauge invariance in ultrastrong-coupling cavity QED. *Phys. Rev. A 98*, 053819.

Debnath, K., E. Mascarenhas, & V. Savona (2017). Nonequilibrium photonic transport and phase transition in an array of optical cavities. *New Journal of Physics 19*(11), 115006.

Delanty, M., S. Rebić, & J. Twamley (2011). Superradiance and phase multistability in circuit quantum electrodynamics. *New Journal of Physics 13*(5), 053032.

Devoret, M., S. Girvin, & R. Schoelkopf (2007). Circuit-QED: How strong can the coupling between a Josephson junction atom and a transmission line resonator be? *Annalen der Physik 16*(10-11), 767–779.

Di Stefano, O., A. Settineri, V. Macrì, L. Garziano, R. Stassi, S. Savasta, & F. Nori (2019). Resolution of gauge ambiguities in ultrastrong-coupling cavity quantum electrodynamics. *Nat. Phys. 15*(8), 803–808.

Dicke, R. H. (1954). Coherence in Spontaneous Radiation Processes. *Phys. Rev. 93*, 99–110.

Diehl, S., A. Micheli, A. Kantian, B. Kraus, H. Büchler, & P. Zoller (2008). Quantum states and phases in driven open quantum systems with cold atoms. *Nat. Phys. 4*(11), 878–883.

Diehl, S., A. Tomadin, A. Micheli, R. Fazio, & P. Zoller (2010). Dynamical phase transitions and instabilities in open atomic many-body systems. *Phys. Rev. Lett. 105*(1), 015702.

Dimer, F., B. Estienne, A. S. Parkins, & H. J. Carmichael (2007). Proposed realization of the Dicke-model quantum phase transition in an optical cavity QED system. *Phys. Rev. A 75*, 013804.

Diósi, L. (1985). Orthogonal jumps of the wavefunction in white-noise potentials. *Physics Letters A 112*(6), 288 – 292.

Donvil, B. & P. Muratore-Ginanneschi (2021). Interference of Quantum Trajectories. *arXiv preprint arXiv:2102.10355*.

Dum, R., P. Zoller, & H. Ritsch (1992). Monte Carlo simulation of the atomic master equation for spontaneous emission. *Phys. Rev. A 45*, 4879–4887.

Duncan, G. C. (1974). Effect of antiresonant atom-field interactions on phase transitions in the Dicke model. *Phys. Rev. A 9*, 418–421.

Dupont, E., H. C. Liu, A. J. SpringThorpe, W. Lai, & M. Extavour (2003). Vacuum-field Rabi splitting in quantum-well infrared photodetectors. *Phys. Rev. B 68*, 245320.

Emary, C. & T. Brandes (2003a). Chaos and the quantum phase transition in the Dicke model. *Phys. Rev. E 67*, 066203.

Emary, C. & T. Brandes (2003b). Quantum Chaos Triggered by Precursors of a Quantum Phase Transition: The Dicke Model. *Phys. Rev. Lett. 90*, 044101.

Emeljanov, V. & Y. L. Klimontovich (1976). Appearance of collective polarisation as a result of phase transition in an ensemble of two-level atoms, interacting through electromagnetic field. *Physics Letters A 59*(5), 366–368.

Fernández-Lorenzo, S. & D. Porras (2017). Quantum sensing close to a dissipative phase transition: Symmetry breaking and criticality as metrological resources. *Phys. Rev. A 96*, 013817.

Ferri, F., R. Rosa-Medina, F. Finger, N. Dogra, M. Soriente, O. Zilberberg, T. Donner, & T. Esslinger (2021). Emerging Dissipative Phases in a Superradiant Quantum Gas with Tunable Decay. *Phys. Rev. X 11*, 041046.

Feynman, R. P. (1982). Simulating physics with computers. *International Journal of Theoretical Physics 21*(6), 467–488.

Fink, J. M., M. Baur, R. Bianchetti, S. Filipp, M. Göppl, P. J. Leek, L. Steffen, A. Blais, & A. Wallraff (2009). Thermal Excitation of Multi-Photon Dressed States in Circuit Quantum Electrodynamics. *Phys. Scr. T137*, 014013.

Fink, J. M., R. Bianchetti, M. Baur, M. Göppl, L. Steffen, S. Filipp, P. J. Leek, A. Blais, & A. Wallraff (2009). Dressed Collective Qubit States and the Tavis-Cummings Model in Circuit QED. *Phys. Rev. Lett. 103*, 083601.

Fink, J. M., M. Göppl, M. Baur, R. Bianchetti, P. J. Leek, A. Blais, & A. Wallraff (2008). Climbing the Jaynes–Cummings ladder and observing its nonlinearity in a cavity QED system. *Nature 454*(7202), 315–318.

Fink, J. M., L. Steffen, P. Studer, L. S. Bishop, M. Baur, R. Bianchetti, D. Bozyigit, C. Lang, S. Filipp, P. J. Leek, & A. Wallraff (2010). Quantum-To-Classical Transition in Cavity Quantum Electrodynamics. *Phys. Rev. Lett. 105*(16), 163601.

Fink, T., A. Schade, S. Höfling, C. Schneider, & A. Imamoglu (2018). Signatures of a dissipative phase transition in photon correlation measurements. *Nat. Phys. 14*(4), 365–369.

Fitzpatrick, M., N. M. Sundaresan, A. C. Y. Li, J. Koch, & A. A. Houck (2017). Observation of a Dissipative Phase Transition in a One-Dimensional Circuit QED Lattice. *Phys. Rev. X 7*, 011016.

Flick, J., M. Ruggenthaler, H. Appel, & A. Rubio (2017). Atoms and molecules in cavities, from weak to strong coupling in quantum-electrodynamics (QED) chemistry. *PNAS 114*(12), 3026–3034.

Flower, G., M. Goryachev, J. Bourhill, & M. E. Tobar (2019). Experimental implementations of cavity-magnon systems: from ultra strong coupling to applications in precision measurement. *New J. Phys. 21*(9), 095004.

Forn-Díaz, P., L. Lamata, E. Rico, J. Kono, & E. Solano (2019). Ultrastrong coupling regimes of light-matter interaction. *Rev. Mod. Phys. 91*, 025005.

Forn-Díaz, P., J. Lisenfeld, D. Marcos, J. J. García-Ripoll, E. Solano, C. J. P. M. Harmans, & J. E. Mooij (2010). Observation of the Bloch-Siegert Shift in a Qubit-Oscillator System in the Ultrastrong Coupling Regime. *Phys. Rev. Lett. 105*, 237001.

Fox, M. (2006). *Quantum Optics – An Introduction*. Oxford University Press.

Freedman, S. J. & J. F. Clauser (1972). Experimental Test of Local Hidden-Variable Theories. *Phys. Rev. Lett. 28*, 938–941.

Friis, N., O. Marty, C. Maier, C. Hempel, M. Holzäpfel, P. Jurcevic, M. B. Plenio, M. Huber, C. Roos, R. Blatt, & B. Lanyon (2018). Observation of Entangled States of a Fully Controlled 20-Qubit System. *Phys. Rev. X 8*, 021012.

Gaines, J. & T. Lyons (1997). Variable step size control in the numerical solution of stochastic differential equations. *SIAM Journal on Applied Mathematics 57*(5), 1455–1484.

Garbe, L., M. Bina, A. Keller, M. G. A. Paris, & S. Felicetti (2020). Critical Quantum Metrology with a Finite-Component Quantum Phase Transition. *Phys. Rev. Lett. 124*, 120504.

Gardiner, C. W. & M. J. Collett (1985). Input and output in damped quantum systems: Quantum stochastic differential equations and the master equation. *Phys. Rev. A 31*, 3761–3774.

Garraway, B. M. (2011). The Dicke model in quantum optics: Dicke model revisited. *Phil. Trans. R. Soc. A 369*(1939), 1137–1155.

Garziano, L., V. Macrì, R. Stassi, O. Di Stefano, F. Nori, & S. Savasta (2016). One Photon Can Simultaneously Excite Two or More Atoms. *Phys. Rev. Lett. 117*, 043601.

Garziano, L., A. Settineri, O. Di Stefano, S. Savasta, & F. Nori (2020). Gauge invariance of the Dicke and Hopfield models. *Phys. Rev. A 102*, 023718.

Geiser, M., F. Castellano, G. Scalari, M. Beck, L. Nevou, & J. Faist (2012). Ultrastrong Coupling Regime and Plasmon Polaritons in Parabolic Semiconductor Quantum Wells. *Phys. Rev. Lett. 108*, 106402.

Gelhausen, J. & M. Buchhold (2018). Dissipative Dicke model with collective atomic decay: Bistability, noise-driven activation, and the nonthermal first-order superradiance transition. *Phys. Rev. A 97*, 023807.

Gerry, C. & P. Knight (2005). *Introductory Quantum Optics*. Cambridge University Press.

Gisin, N. & I. C. Percival (1992). The quantum-state diffusion model applied to open systems. *J. Phys. A: Math. Gen. 25*(21), 5677.

Golovchanskiy, I., N. Abramov, V. Stolyarov, A. Golubov, M. Y. Kupriyanov, V. Ryazanov, & A. Ustinov (2021). Approaching Deep-Strong On-Chip Photon-To-Magnon Coupling. *Phys. Rev. Applied 16*, 034029.

Goy, P., J. M. Raimond, M. Gross, & S. Haroche (1983). Observation of Cavity-Enhanced Single-Atom Spontaneous Emission. *Phys. Rev. Lett. 50*, 1903–1906.

Gray, A. & G. B. Mathews (1966). *A Treatise on Bessel Functions and Their Applications to Physics*, pp. 109. Dover Publications.

Greiner, M., O. Mandel, T. Esslinger, T. W. Hänsch, & I. Bloch (2002). Quantum phase transition from a superfluid to a Mott insulator in a gas of ultracold atoms. *Nature 415*(6867), 39–44.

Grimsmo, A. L. (2015). Time-Delayed Quantum Feedback Control. *Phys. Rev. Lett. 115*, 060402.

Gross, M. & S. Haroche (1982). Superradiance: An essay on the theory of collective spontaneous emission. *Physics reports 93*(5), 301–396.

Günter, G., A. A. Anappara, J. Hees, A. Sell, G. Biasiol, L. Sorba, S. De Liberato, C. Ciuti, A. Tredicucci, A. Leitenstorfer, & R. Huber (2009). Sub-cycle switch-on of ultrastrong light-matter interaction. *Nature 458*(7235), 178–181.

Gutiérrez-Jáuregui, R. & H. J. Carmichael (2018). Dissipative quantum phase transitions of light in a generalized Jaynes-Cummings-Rabi model. *Phys. Rev. A 98*, 023804.

Hagenmüller, D. & C. Ciuti (2012). Cavity QED of the Graphene Cyclotron Transition. *Phys. Rev. Lett. 109*, 267403.

Halati, C.-M., A. Sheikhan, H. Ritsch, & C. Kollath (2020). Numerically Exact Treatment of Many-Body Self-Organization in a Cavity. *Phys. Rev. Lett. 125*, 093604.

Hanai, R., A. Edelman, Y. Ohashi, & P. B. Littlewood (2019). Non-Hermitian Phase Transition from a Polariton Bose-Einstein Condensate to a Photon Laser. *Phys. Rev. Lett. 122*, 185301.

Haroche, S., M. Brune, & J. Raimond (2020). From cavity to circuit quantum electrodynamics. *Nat. Phys. 16*(3), 243–246.

Haroche, S. & D. Kleppner (1989). Cavity Quantum Electrodynamics. *Physics Today 42*(1), 24–30.

Hepp, K. & E. H. Lieb (1973). On the superradiant phase transition for molecules in a quantized radiation field: the Dicke maser model. *Ann. Phys. 76*(2), 360–404.

Heugel, T. L., M. Biondi, O. Zilberberg, & R. Chitra (2019). Quantum Transducer Using a Parametric Driven-Dissipative Phase Transition. *Phys. Rev. Lett. 123*, 173601.

Hillery, M. & L. D. Mlodinow (1985). Semiclassical expansion for nonlinear dielectric media. *Phys. Rev. A 31*, 797–806.

Hioe, F. T. (1973). Phase Transitions in Some Generalized Dicke Models of Superradiance. *Phys. Rev. A 8*, 1440–1445.

Homa, G. & L. Diósi (2017). On the earliest jump unravelling of the spatial decoherence master equation. *Physics Letters A 381*(40), 3456 – 3459.

Horak, P., G. Hechenblaikner, K. M. Gheri, H. Stecher, & H. Ritsch (1997). Cavity-Induced Atom Cooling in the Strong Coupling Regime. *Phys. Rev. Lett. 79*, 4974–4977.

Hosten, O., N. J. Engelsen, R. Krishnakumar, & M. A. Kasevich (2016). Measurement noise 100 times lower than the quantum-projection limit using entangled atoms. *Nature 529*(7587), 505–508.

Houck, A. A., J. A. Schreier, B. R. Johnson, J. M. Chow, J. Koch, J. M. Gambetta, D. I. Schuster, L. Frunzio, M. H. Devoret, S. M. Girvin, & R. J. Schoelkopf (2008). Controlling the Spontaneous Emission of a Superconducting Transmon Qubit. *Phys. Rev. Lett. 101*, 080502.

Hulet, R. G., E. S. Hilfer, & D. Kleppner (1985). Inhibited Spontaneous Emission by a Rydberg Atom. *Phys. Rev. Lett. 55*, 2137–2140.

Hwang, M.-J. & M. B. Plenio (2016). Quantum Phase Transition in the Finite Jaynes-Cummings Lattice Systems. *Phys. Rev. Lett. 117*, 123602.

Hwang, M.-J., R. Puebla, & M. B. Plenio (2015). Quantum Phase Transition and Universal Dynamics in the Rabi Model. *Phys. Rev. Lett. 115*, 180404.

Hwang, M.-J., P. Rabl, & M. B. Plenio (2018). Dissipative phase transition in the open quantum Rabi model. *Phys. Rev. A 97*, 013825.

Ilie, S., K. Jackson, & W. Enright (2015). Adaptive time-stepping for the strong numerical solution of stochastic differential equations. *Numerical Algorithms 68*(4), 791–812.

Imamoğlu, A., H. Schmidt, G. Woods, & M. Deutsch (1997). Strongly Interacting Photons in a Nonlinear Cavity. *Phys. Rev. Lett. 79*, 1467–1470.

Jaako, T., Z.-L. Xiang, J. J. Garcia-Ripoll, & P. Rabl (2016). Ultrastrong-coupling phenomena beyond the Dicke model. *Phys. Rev. A 94*, 033850.

Javanainen, J. (1986). Possibility of quantum jumps in a three-level system. *Phys. Rev. A 33*, 2121–2123.

Jaynes, E. & F. Cummings (1963). Comparison of quantum and semiclassical radiation theories with application to the beam maser. *Proceedings of the IEEE 51*(1), 89–109.

Jennewein, T., C. Simon, G. Weihs, H. Weinfurter, & A. Zeilinger (2000). Quantum Cryptography with Entangled Photons. *Phys. Rev. Lett. 84*, 4729–4732.

Johansson, J., P. Nation, & F. Nori (2012). QuTiP: An open-source Python framework for the dynamics of open quantum systems. *Comp. Phys. Comm. 183*(8), 1760 – 1772.

Johansson, J., P. Nation, & F. Nori (2013). QuTiP 2: A Python framework for the dynamics of open quantum systems. *Comp. Phys. Comm. 184*(4), 1234 – 1240.

Johansson, J. R., G. Johansson, C. Wilson, & F. Nori (2009). Dynamical Casimir effect in a superconducting coplanar waveguide. *Phys. Rev. Lett. 103*(14), 147003.

Kasprzak, J., S. Reitzenstein, E. A. Muljarov, C. Kistner, C. Schneider, M. Strauss, S. Höfling, A. Forchel, & W. Langbein (2010). Up on the Jaynes–Cummings ladder of a quantum-dot/microcavity system. *Nature materials 9*(4), 304–308.

Keeling, J. (2007). Coulomb interactions, gauge invariance, and phase transitions of the Dicke model. *J. Phys.: Cond. Mat. 19*(29), 295213.

Keller, O. (2011). *Electrodynamics in the Poincaré Gauge*, pp. 477–500. Berlin, Heidelberg: Springer Berlin Heidelberg.

Kerckhoff, J., M. A. Armen, D. S. Pavlichin, & H. Mabuchi (2011). The dressed atom as binary phase modulator: towards attojoule/edge optical phase-shift keying. *Opt. Express 19*(7), 6478–6486.

Kessler, E. M., G. Giedke, A. Imamoglu, S. F. Yelin, M. D. Lukin, & J. I. Cirac (2012). Dissipative phase transition in a central spin system. *Phys. Rev. A 86*, 012116.

Khitrova, G., H. Gibbs, M. Kira, S. W. Koch, & A. Scherer (2006). Vacuum Rabi splitting in semiconductors. *Nat. Phys. 2*(2), 81–90.

Kimble, H. J., M. Dagenais, & L. Mandel (1977). Photon Antibunching in Resonance Fluorescence. *Phys. Rev. Lett. 39*, 691–695.

Kimura, M. (1981). Thermodynamics and electrodynamics of superradiant phase. *Progress of Theoretical Physics 65*(2), 437–450.

Kirton, P. & J. Keeling (2017). Suppressing and Restoring the Dicke Superradiance Transition by Dephasing and Decay. *Phys. Rev. Lett. 118*, 123602.

Kirton, P., M. M. Roses, J. Keeling, & E. G. Dalla Torre (2019). Introduction to the Dicke model: From equilibrium to nonequilibrium, and vice versa. *Advanced Quantum Technologies 2*(1-2), 1800043.

Kleppner, D. (1981). Inhibited Spontaneous Emission. *Phys. Rev. Lett. 47*, 233–236.

Kloeden, P. E., E. Platen, & H. Schurz (2012). *Numerical solution of SDE through computer experiments*. Springer Science & Business Media.

Knight, J. M., Y. Aharonov, & G. T. C. Hsieh (1978). Are super-radiant phase transitions possible? *Phys. Rev. A 17*, 1454–1462.

Koch, J., T. M. Yu, J. Gambetta, A. A. Houck, D. I. Schuster, J. Majer, A. Blais, M. H. Devoret, S. M. Girvin, & R. J. Schoelkopf (2007). Charge-insensitive qubit design derived from the Cooper pair box. *Phys. Rev. A 76*, 042319.

Krämer, S., D. Plankensteiner, L. Ostermann, & H. Ritsch (2018). QuantumOptics. jl: A Julia framework for simulating open quantum systems. *Comp. Phys. Comm. 227*, 109–116.

Krämer, S. & H. Ritsch (2012). Efficient wave function simulations in nonlinear quantum optics using an adaptive coherent state basis. In *AIP Conference Proceedings*, Volume 1475, pp. 137–139. American Institute of Physics.

Labouvie, R., B. Santra, S. Heun, & H. Ott (2016). Bistability in a Driven-Dissipative Superfluid. *Phys. Rev. Lett. 116*, 235302.

Lambert, N., Y. Matsuzaki, K. Kakuyanagi, N. Ishida, S. Saito, & F. Nori (2016). Superradiance with an ensemble of superconducting flux qubits. *Phys. Rev. B 94*, 224510.

Lang, C., D. Bozyigit, C. Eichler, L. Steffen, J. M. Fink, A. A. Abdumalikov, M. Baur, S. Filipp, M. P. da Silva, A. Blais, & A. Wallraff (2011). Observation of Resonant Photon Blockade at Microwave Frequencies Using Correlation Function Measurements. *Phys. Rev. Lett. 106*, 243601.

Lang, J., D. Chang, & F. Piazza (2020). Interaction-Induced Transparency for Strong-Coupling Polaritons. *Phys. Rev. Lett. 125*, 133604.

Larson, J. & E. K. Irish (2017). Some remarks on 'superradiant' phase transitions in light-matter systems. *Journal of Physics A: Mathematical and Theoretical 50*(17), 174002.

Larson, J. & T. Mavrogordatos (2021). *The Jaynes–Cummings Model and Its Descendants*. Institute of Physics Publishing.

Le Boité, A., G. Orso, & C. Ciuti (2013). Steady-State Phases and Tunneling-Induced Instabilities in the Driven Dissipative Bose-Hubbard Model. *Phys. Rev. Lett. 110*, 233601.

Le Boité, A. (2020). Theoretical Methods for Ultrastrong Light–Matter Interactions. *Advanced Quantum Technologies 3*(7), 1900140.

Letscher, F., O. Thomas, T. Niederprüm, M. Fleischhauer, & H. Ott (2017). Bistability Versus Metastability in Driven Dissipative Rydberg Gases. *Phys. Rev. X 7*, 021020.

Li, Z., F. Claude, T. Boulier, E. Giacobino, Q. Glorieux, A. Bramati, & C. Ciuti (2022). Dissipative Phase Transition with Driving-Controlled Spatial Dimension and Diffusive Boundary Conditions. *Phys. Rev. Lett. 128*, 093601.

Lipkin, H. J., N. Meshkov, & A. J. Glick (1965). Validity of many-body approximation methods for a solvable model. *Nucl. Phys. 62*(2), 188–198.

Lombardi, M. A., T. P. Heavner, & S. R. Jefferts (2007). NIST primary frequency standards and the realization of the SI second. *NCSLI Measure 2*(4), 74–89.

Loudon, R. (2001). *The Quantum Theory of Light*. Oxford University Press.

Ludlow, A. D., M. M. Boyd, J. Ye, E. Peik, & P. O. Schmidt (2015). Optical atomic clocks. *Rev. Mod. Phys. 87*, 637–701.

Macieszczak, K. & D. C. Rose (2021). Quantum jump Monte Carlo approach simplified: Abelian symmetries. *Phys. Rev. A 103*(4), 042204.

Malossi, N., M. M. Valado, S. Scotto, P. Huillery, P. Pillet, D. Ciampini, E. Arimondo, & O. Morsch (2014). Full Counting Statistics and Phase Diagram of a Dissipative Rydberg Gas. *Phys. Rev. Lett. 113*, 023006.

Mandel, L. & E. Wolf (1995). *Optical Coherence and Quantum Optics*. Cambridge University Press.

Manenti, R., A. F. Kockum, A. Patterson, T. Behrle, J. Rahamim, G. Tancredi, F. Nori, & P. J. Leek (2017). Circuit quantum acoustodynamics with surface acoustic waves. *Nat. Comm. 8*(1), 1–6.

Manzano, D. (2020). A short introduction to the Lindblad master equation. *AIP Advances 10*(2), 025106.

Marcuzzi, M., E. Levi, S. Diehl, J. P. Garrahan, & I. Lesanovsky (2014). Universal nonequilibrium properties of dissipative Rydberg gases. *Phys. Rev. Lett. 113*(21), 210401.

Marino, J. & S. Diehl (2016). Driven Markovian Quantum Criticality. *Phys. Rev. Lett. 116*, 070407.

Maschler, C., I. B. Mekhov, & H. Ritsch (2008). Ultracold atoms in optical lattices generated by quantized light fields. *Eur. Phys. J. D 46*(3), 545–560.

Maunz, P., T. Puppe, I. Schuster, N. Syassen, P. W. Pinkse, & G. Rempe (2004). Cavity cooling of a single atom. *Nature 428*(6978), 50–52.

Mavrogordatos, T. K., G. Tancredi, M. Elliott, M. J. Peterer, A. Patterson, J. Rahamim, P. J. Leek, E. Ginossar, & M. H. Szymańska (2017). Simultaneous Bistability of a Qubit and Resonator in Circuit Quantum Electrodynamics. *Phys. Rev. Lett. 118*, 040402.

Meiser, D. & P. Meystre (2006). Superstrong coupling regime of cavity quantum electrodynamics. *Phys. Rev. A 74*, 065801.

Meschede, D., W. Jhe, & E. A. Hinds (1990). Radiative properties of atoms near a conducting plane: An old problem in a new light. *Phys. Rev. A 41*, 1587–1596.

Milonni, P. W. (1976). Semiclassical and quantum-electrodynamical approaches in nonrelativistic radiation theory. *Phys. Rep. 25*(1), 1–81.

Minev, Z. K., S. O. Mundhada, S. Shankar, P. Reinhold, R. Gutiérrez-Jáuregui, R. J. Schoelkopf, M. Mirrahimi, H. J. Carmichael, & M. H. Devoret (2019). To catch and reverse a quantum jump mid-flight. *Nature 570*(7760), 200–204.

Minganti, F., A. Biella, N. Bartolo, & C. Ciuti (2018). Spectral theory of Liouvillians for dissipative phase transitions. *Phys. Rev. A 98*, 042118.

Mlynek, J. A., A. A. Abdumalikov, J. M. Fink, L. Steffen, M. Baur, C. Lang, A. F. van Loo, & A. Wallraff (2012). Demonstrating W-type entanglement of Dicke states in resonant cavity quantum electrodynamics. *Phys. Rev. A 86*, 053838.

Mostame, S., P. Rebentrost, A. Eisfeld, A. J. Kerman, D. I. Tsomokos, & A. Aspuru-Guzik (2012). Quantum simulator of an open quantum system using superconducting qubits: exciton transport in photosynthetic complexes. *New J. Phys. 14*(10), 105013.

Munoz, C. S., B. Buča, J. Tindall, A. González-Tudela, D. Jaksch, & D. Porras (2019). Symmetries and conservation laws in quantum trajectories: Dissipative freezing. *Phys. Rev. A 100*(4), 042113.

Myerson-Jain, N. E., S. Yan, D. Weld, & C. Xu (2022). Construction of Fractal Order and Phase Transition with Rydberg Atoms. *Phys. Rev. Lett. 128*(1), 017601.

Nagourney, W., J. Sandberg, & H. Dehmelt (1986). Shelved optical electron amplifier: Observation of quantum jumps. *Phys. Rev. Lett. 56*, 2797–2799.

Nagy, D., P. Domokos, A. Vukics, & H. Ritsch (2009). Nonlinear quantum dynamics of two BEC modes dispersively coupled by an optical cavity. *Eur. Phys. J. D 55*(3), 659–668.

Nagy, D., G. Kónya, G. Szirmai, & P. Domokos (2010). Dicke-Model Phase Transition in the Quantum Motion of a Bose-Einstein Condensate in an Optical Cavity. *Phys. Rev. Lett. 104*, 130401.

Nagy, D., G. Szirmai, & P. Domokos (2011). Critical exponent of a quantum-noise-driven phase transition: The open-system Dicke model. *Phys. Rev. A 84*, 043637.

Narducci, L. M., M. Orszag, & R. A. Tuft (1973). Energy Spectrum of the Dicke Hamiltonian. *Phys. Rev. A 8*, 1892–1906.

Nataf, P., T. Champel, G. Blatter, & D. M. Basko (2019). Rashba Cavity QED: A Route Towards the Superradiant Quantum Phase Transition. *Phys. Rev. Lett. 123*, 207402.

Nataf, P. & C. Ciuti (2010). No-go theorem for superradiant quantum phase transitions in cavity QED and counter-example in circuit QED. *Nat. Comm. 1*, 72.

Nataf, P. & C. Ciuti (2011). Protected Quantum Computation with Multiple Resonators in Ultrastrong Coupling Circuit QED. *Phys. Rev. Lett. 107*, 190402.

Niedenzu, W., R. M. Sandner, C. Genes, & H. Ritsch (2012). Quantum-correlated motion and heralded entanglement of distant optomechanically coupled objects. *J. Phys. B: At. Mol. Opt. Phys. 45*(24), 245501.

Niemczyk, T., F. Deppe, H. Huebl, E. Menzel, F. Hocke, M. Schwarz, J. Garcia-Ripoll, D. Zueco, T. Hümmer, E. Solano, et al. (2010). Circuit quantum electrodynamics in the ultrastrong-coupling regime. *Nat. Phys. 6*(10), 772–776.

Német, N. (2019). *Time-delayed coherent feedback control for open quantum systems*. Ph. D. thesis, Department of Physics, The University of Auckland.

Ohira, R., S. Kume, H. Takahashi, & K. Toyoda (2021). Polariton blockade in the Jaynes–Cummings–Hubbard model with trapped ions. *Quantum Science and Technology 6*(2), 024015.

Ou, Z. Y. & L. Mandel (1988). Violation of Bell's Inequality and Classical Probability in a Two-Photon Correlation Experiment. *Phys. Rev. Lett. 61*, 50–53.

Overbeck, V. R., M. F. Maghrebi, A. V. Gorshkov, & H. Weimer (2017). Multicritical behavior in dissipative Ising models. *Phys. Rev. A 95*, 042133.

Paik, H., D. I. Schuster, L. S. Bishop, G. Kirchmair, G. Catelani, A. P. Sears, B. R. Johnson, M. J. Reagor, L. Frunzio, L. I. Glazman, S. M. Girvin, M. H. Devoret, & R. J. Schoelkopf (2011). Observation of High Coherence in Josephson Junction Qubits Measured in a Three-Dimensional Circuit QED Architecture. *Phys. Rev. Lett. 107*, 240501.

Pályi, A., P. R. Struck, M. Rudner, K. Flensberg, & G. Burkard (2012). Spin-Orbit-Induced Strong Coupling of a Single Spin to a Nanomechanical Resonator. *Phys. Rev. Lett. 108*, 206811.

Peano, V. & M. Thorwart (2010). Dynamical bistability in the driven circuit QED. *EPL (Europhysics Letters) 89*(1), 17008.

Peraca, N. M., A. Baydin, W. Gao, M. Bamba, & J. Kono (2020). Chapter Three - Ultrastrong light–matter coupling in semiconductors. In S. T. Cundiff & M. Kira (Eds.), *Semiconductor Quantum Science and Technology*, Volume 105 of *Semiconductors and Semimetals*, pp. 89–151. Elsevier.

Pietikäinen, I., S. Danilin, K. S. Kumar, A. Vepsäläinen, D. S. Golubev, J. Tuorila, & G. S. Paraoanu (2017). Observation of the Bloch-Siegert shift in a driven quantum-to-classical transition. *Phys. Rev. B 96*, 020501.

Pietikäinen, I., J. Tuorila, D. S. Golubev, & G. S. Paraoanu (2019). Photon blockade and the quantum-to-classical transition in the driven-dissipative Josephson pendulum coupled to a resonator. *Phys. Rev. A 99*, 063828.

Pilar, P., D. De Bernardis, & P. Rabl (2020). Thermodynamics of ultrastrongly coupled light-matter systems. *Quantum 4*, 335.

Plenio, M. B. & P. L. Knight (1998). The quantum-jump approach to dissipative dynamics in quantum optics. *Rev. Mod. Phys. 70*, 101–144.

Polzik, E. S., J. Carri, & H. J. Kimble (1992). Spectroscopy with squeezed light. *Phys. Rev. Lett. 68*, 3020–3023.

Power, E. A. & T. Thirunamachandran (1982). Quantum electrodynamics in a cavity. *Phys. Rev. A 25*, 2473–2484.

Power, E. A. & S. Zienau (1959). Coulomb gauge in non-relativistic quantum electro-dynamics and the shape of spectral lines. *Phil. Trans. R. Soc. A 251*(999), 427–454.

Purcell, E. M. (1946). Spontaneous emission probabilities at radio frequencies. *Phys. Rev. 69*, 681.

Raghunandan, M., J. Wrachtrup, & H. Weimer (2018). High-density quantum sensing with dissipative first order transitions. *Phys. Rev. Lett. 120*(15), 150501.

Raimond, J. M., M. Brune, & S. Haroche (2001). Manipulating quantum entanglement with atoms and photons in a cavity. *Rev. Mod. Phys. 73*, 565–582.

Reed, M. D., L. DiCarlo, B. R. Johnson, L. Sun, D. I. Schuster, L. Frunzio, & R. J. Schoelkopf (2010). High-Fidelity Readout in Circuit Quantum Electrodynamics Using the Jaynes-Cummings Nonlinearity. *Phys. Rev. Lett. 105*, 173601.

Reiserer, A. & G. Rempe (2015). Cavity-based quantum networks with single atoms and optical photons. *Rev. Mod. Phys. 87*, 1379–1418.

Reiter, F., T. L. Nguyen, J. P. Home, & S. F. Yelin (2020). Cooperative breakdown of the oscillator blockade in the Dicke model. *Phys. Rev. Lett. 125*(23), 233602.

Rodriguez, S. R. K., W. Casteels, F. Storme, N. Carlon Zambon, I. Sagnes, L. Le Gratiet, E. Galopin, A. Lemaître, A. Amo, C. Ciuti, & J. Bloch (2017). Probing a Dissipative Phase Transition via Dynamical Optical Hysteresis. *Phys. Rev. Lett. 118*, 247402.

Roscher, D., S. Diehl, & M. Buchhold (2018). Phenomenology of first-order dark-state phase transitions. *Phys. Rev. A 98*, 062117.

Rouse, D. M., B. W. Lovett, E. M. Gauger, & N. Westerberg (2021). Avoiding gauge ambiguities in cavity quantum electrodynamics. *Scientific reports 11*(1), 1–10.

Rousseau, E. & D. Felbacq (2017). The quantum-optics Hamiltonian in the Multipolar gauge. *Scientific reports 7*(1), 1–8.

Rzażewski, K. & K. Wódkiewicz (1991). Stability of matter interacting with photons. *Phys. Rev. A 43*, 593–594.

Rzażewski, K., K. Wódkiewicz, & W. Żakowicz (1975). Phase Transitions, Two-Level Atoms, and the A^2 Term. *Phys. Rev. Lett. 35*, 432–434.

Sachdev, S. (2011). *Quantum Phase Transitions*. Cambridge University Press.

Salam, A. (2018). The unified theory of resonance energy transfer according to molecular quantum electrodynamics. *Atoms 6*(4), 56.

Samajdar, R., W. W. Ho, H. Pichler, M. D. Lukin, & S. Sachdev (2021). Quantum phases of Rydberg atoms on a kagome lattice. *PNAS 118*(4), e2015785118.

Sandner, R. M., W. Niedenzu, & H. Ritsch (2013). Subrecoil cavity cooling towards degeneracy: A numerical study. *EPL (Europhysics Letters) 104*(4), 43001.

Savasta, S., O. Di Stefano, A. Settineri, D. Zueco, S. Hughes, & F. Nori (2021). Gauge principle and gauge invariance in two-level systems. *Phys. Rev. A 103*, 053703.

Savona, V. (2017). Spontaneous symmetry breaking in a quadratically driven nonlinear photonic lattice. *Phys. Rev. A 96*, 033826.

Scalari, G., C. Maissen, D. Turčinková, D. Hagenmüller, S. De Liberato, C. Ciuti, C. Reichl, D. Schuh, W. Wegscheider, M. Beck, & J. Faist (2012). Ultrastrong Coupling of the Cyclotron Transition of a 2D Electron Gas to a THz Metamaterial. *Science 335*(6074), 1323–1326.

Schäfer, C., M. Ruggenthaler, V. Rokaj, & A. Rubio (2020). Relevance of the quadratic diamagnetic and self-polarization terms in cavity quantum electrodynamics. *ACS photonics 7*(4), 975–990.

Schlamminger, S. (2018). *Redefining the Kilogram and Other SI Units*. 2399-2891. IOP Publishing.

Schmidt, P. O., T. Rosenband, C. Langer, W. M. Itano, J. C. Bergquist, & D. J. Wineland (2005). Spectroscopy using quantum logic. *Science 309*(5735), 749–752.

Schreier, J. A., A. A. Houck, J. Koch, D. I. Schuster, B. R. Johnson, J. M. Chow, J. M. Gambetta, J. Majer, L. Frunzio, M. H. Devoret, S. M. Girvin, & R. J. Schoelkopf (2008). Suppressing charge noise decoherence in superconducting charge qubits. *Phys. Rev. B 77*, 180502.

Schuler, M., D. De Bernardis, A. Läuchli, & P. Rabl (2020). The vacua of dipolar cavity quantum electrodynamics. *SciPost Physics 9*(5), 066.

Schulze, R. J., C. Genes, & H. Ritsch (2010). Optomechanical approach to cooling of small polarizable particles in a strongly pumped ring cavity. *Phys. Rev. A 81*, 063820.

Schwartz, T., J. A. Hutchison, C. Genet, & T. W. Ebbesen (2011). Reversible Switching of Ultrastrong Light-Molecule Coupling. *Phys. Rev. Lett. 106*, 196405.

Settineri, A., O. Di Stefano, D. Zueco, S. Hughes, S. Savasta, & F. Nori (2021). Gauge freedom, quantum measurements, and time-dependent interactions in cavity QED. *Phys. Rev. Research 3*, 023079.

Sivasubramanian, S., A. Widom, & Y. Srivastava (2001). Gauge invariant formulations of Dicke–Preparata super-radiant models. *Physica A: Statistical Mechanics and its Applications 301*(1-4), 241–254.

Soriente, M., T. L. Heugel, K. Arimitsu, R. Chitra, & O. Zilberberg (2021). Distinctive class of dissipation-induced phase transitions and their universal characteristics. *Phys. Rev. Research 3*, 023100.

Steck, D. (2021). Alkali D Line Data. http://steck.us/alkalidata/. [Online; accessed 10-June-2021].

Steinbach, J., B. M. Garraway, & P. L. Knight (1995). High-order unraveling of master equations for dissipative evolution. *Phys. Rev. A 51*, 3302–3308.

Stitely, K. C., A. Giraldo, B. Krauskopf, & S. Parkins (2020). Nonlinear semiclassical dynamics of the unbalanced, open Dicke model. *Phys. Rev. Research 2*, 033131.

Stokes, A. & A. Nazir (2019). Gauge ambiguities imply Jaynes-Cummings physics remains valid in ultrastrong coupling QED. *Nat. Comm. 10*(1), 1–9.

Talay, D. (1994). *Numerical solution of stochastic differential equations*. Taylor & Francis.

Tan, S. M. (1999). A computational toolbox for quantum and atomic optics. *J. Opt. B: Quantum Semiclass. Opt. 1*(4), 424.

Tavis, M. & F. W. Cummings (1968). Exact Solution for an N-Molecule–Radiation-Field Hamiltonian. *Phys. Rev. 170*, 379–384.

Thompson, R. J., G. Rempe, & H. J. Kimble (1992). Observation of normal-mode splitting for an atom in an optical cavity. *Phys. Rev. Lett. 68*, 1132–1135.

Todorov, Y. (2014). Dipolar quantum electrodynamics theory of the three-dimensional electron gas. *Phys. Rev. B 89*, 075115.

Todorov, Y. (2015). Dipolar quantum electrodynamics of the two-dimensional electron gas. *Phys. Rev. B 91*, 125409.

Todorov, Y., A. M. Andrews, R. Colombelli, S. De Liberato, C. Ciuti, P. Klang, G. Strasser, & C. Sirtori (2010). Ultrastrong Light-Matter Coupling Regime with Polariton Dots. *Phys. Rev. Lett. 105*, 196402.

Todorov, Y. & C. Sirtori (2012). Intersubband polaritons in the electrical dipole gauge. *Phys. Rev. B 85*, 045304.

Todorov, Y. & C. Sirtori (2014). Few-Electron Ultrastrong Light-Matter Coupling in a Quantum *LC* Circuit. *Phys. Rev. X 4*, 041031.

Verstraete, F., M. M. Wolf, & J. Ignacio Cirac (2009). Quantum computation and quantum-state engineering driven by dissipation. *Nat. Phys. 5*(9), 633–636.

Vicentini, F., F. Minganti, R. Rota, G. Orso, & C. Ciuti (2018). Critical slowing down in driven-dissipative Bose-Hubbard lattices. *Phys. Rev. A 97*, 013853.

Viehmann, O., J. von Delft, & F. Marquardt (2011). Superradiant Phase Transitions and the Standard Description of Circuit QED. *Phys. Rev. Lett. 107*, 113602.

Vojta, M. (2003). Quantum phase transitions. *Reports on Progress in Physics 66*(12), 2069.

Vrajitoarea, A., Z. Huang, P. Groszkowski, J. Koch, & A. A. Houck (2020). Quantum control of an oscillator using a stimulated Josephson nonlinearity. *Nat. Phys. 16*(2), 211–217.

Vukics, A. & P. Domokos (2005). Simultaneous cooling and trapping of atoms by a single cavity-field mode. *Phys. Rev. A 72*, 031401.

Vukics, A., J. Janszky, & P. Domokos (2005). Cavity cooling of atoms: a quantum statistical treatment. *J. Phys. B: At. Mol. Opt. Phys. 38*(10), 1453.

Wallraff, A., D. I. Schuster, A. Blais, L. Frunzio, R.-S. Huang, J. Majer, S. Kumar, S. M. Girvin, & R. J. Schoelkopf (2004). Strong coupling of a single photon to a superconducting qubit using circuit quantum electrodynamics. *Nature 431*(7005), 162–167.

Walls, D. F. (1979). Evidence for the quantum nature of light. *Nature 280*(5722), 451–454.

Wang, Y., D. Ballester, G. Romero, V. Scarani, & E. Solano (2012). Validity of resonant two-qubit gates in the ultrastrong coupling regime of circuit quantum electrodynamics. *Physica Scripta 2012*(T147), 014031.

Wang, Y., M. Liu, W.-L. You, S. Chesi, H.-G. Luo, & H.-Q. Lin (2020). Resilience of the superradiant phase against A^2 effects in the quantum Rabi dimer. *Phys. Rev. A 101*, 063843.

Wang, Y. K. & F. T. Hioe (1973). Phase Transition in the Dicke Model of Superradiance. *Phys. Rev. A 7*, 831–836.

Wang, Z., H. Li, W. Feng, X. Song, C. Song, W. Liu, Q. Guo, X. Zhang, H. Dong, D. Zheng, H. Wang, & D.-W. Wang (2020). Controllable Switching between Superradiant and Subradiant States in a 10-qubit Superconducting Circuit. *Phys. Rev. Lett. 124*, 013601.

Wei, H.-S., C.-C. Jaing, Y.-T. Chen, C.-C. Lin, C.-W. Cheng, C.-H. Chan, C.-C. Lee, & J.-F. Chang (2013). Adjustable exciton-photon coupling with giant Rabi-splitting using layer-by-layer J-aggregate thin films in all-metal mirror microcavities. *Optics express 21*(18), 21365–21373.

Weimer, H., A. Kshetrimayum, & R. Orús (2021). Simulation methods for open quantum many-body systems. *Rev. Mod. Phys. 93*, 015008.

Weinberg, S. (2013). *Lectures on Quantum Mechanics*. Cambridge University Press.

Wilson, C., G. Johansson, A. Pourkabirian, M. Simoen, J. Johansson, T. Duty, F. Nori, & P. Delsing (2011). Observation of the dynamical Casimir effect in a superconducting circuit. *Nature 479*(7373), 376–379.

Wineland, D. J. (2013). Nobel Lecture: Superposition, entanglement, and raising Schrödinger's cat. *Rev. Mod. Phys. 85*, 1103–1114.

Winterauer, D. J., W. Niedenzu, & H. Ritsch (2015). Multistable particle-field dynamics in cavity-generated optical lattices. *Phys. Rev. A 91*, 053829.

Woolley, R. (1971). Molecular Quantum Electrodynamics. *Proc. R. Soc. London, Ser. A 321*, 1547.

Woolley, R. (1974). A reformulation of molecular quantum electrodynamics. *Journal of Physics B: Atomic and Molecular Physics 7*(4), 488–499.

Woolley, R. (1975). On non-relativistic electron theory. In *Annales de l'IHP Physique théorique*, Volume 23, pp. 365–378.

Woolley, R. G. (2020). Power-Zienau-Woolley representations of nonrelativistic QED for atoms and molecules. *Phys. Rev. Research 2*, 013206.

Xiao, M., L.-A. Wu, & H. J. Kimble (1987). Precision measurement beyond the shot-noise limit. *Phys. Rev. Lett. 59*, 278–281.

Xu, H.-G., C. Wang, & X.-L. Gao (2020). Two-photon statistics of nonclassical radiation in the dissipative finite-size Dicke model. *J. Phys. B: At. Mol. Opt. Phys. 53*(15), 155406.

Yang, L.-P. & Z. Jacob (2019). Engineering first-order quantum phase transitions for weak signal detection. *Journal of Applied Physics 126*(17), 174502.

Yoo, D., F. de León-Pérez, M. Pelton, I.-H. Lee, D. A. Mohr, M. B. Raschke, J. D. Caldwell, L. Martín-Moreno, & S.-H. Oh (2021). Ultrastrong plasmon–phonon coupling via epsilon-near-zero nanocavities. *Nat. Photonics 15*(2), 125–130.

Yoshihara, F., T. Fuse, S. Ashhab, K. Kakuyanagi, S. Saito, & K. Semba (2017). Superconducting qubit–oscillator circuit beyond the ultrastrong-coupling regime. *Nat. Phys. 13*(1), 44–47.

Zhiqiang, Z., C. H. Lee, R. Kumar, K. Arnold, S. J. Masson, A. Parkins, & M. Barrett (2017). Nonequilibrium phase transition in a spin-1 Dicke model. *Optica 4*(4), 424–429.

Zhu, G.-L., X.-Y. Lü, S.-W. Bin, C. You, & Y. Wu (2019). Entanglement and excited-state quantum phase transition in an extended Dicke model. *Frontiers of Physics 14*(5), 1–9.

Zhu, G.-L., H. Ramezani, C. Emary, J.-H. Gao, Y. Wu, & X.-Y. Lü (2020). Interplay of quantum phase transition and flat band in hybrid lattices. *Phys. Rev. Research 2*(3), 033463.

Zou, L. J., D. Marcos, S. Diehl, S. Putz, J. Schmiedmayer, J. Majer, & P. Rabl (2014). Implementation of the Dicke Lattice Model in Hybrid Quantum System Arrays. *Phys. Rev. Lett. 113*, 023603.